Innovative optoelectronic and photonic devices and systems for Space applications

Politecnico di Bari

Department of Electrical and Information Engineering
ELECTRICAL AND INFORMATION ENGINEERING
Ph.D. Program
SSD: ING-INF/01–ELECTRONICS

Final Dissertation

Innovative optoelectronic and photonic devices and systems for Space applications

---

by

GIUSEPPE BRUNETTI

Supervisor:

Prof. CATERINA CIMINELLI

Coordinator of Ph.D. Program:

Prof. ALFREDO GRIECO

Course n°32, 01/11/2016-31/10/2019

Department of Electrical and Information Engineering
ELECTRICAL AND INFORMATION ENGINEERING
Ph.D. Program
SSD: ING-INF/01–ELECTRONICS

Final Dissertation

Innovative optoelectronic and photonic devices and systems for Space applications

---

by

GIUSEPPE BRUNETTI:

Referees:

Prof. ALESSANDRO BUSACCA

Prof. RICHARD DE LA RUE

Supervisor:

Prof. CATERINA CIMINELLI

Coordinator of Ph.D Program:
Prof. ALFREDO GRIECO

Course n°32, 01/11/2016-31/10/2019

To my parents

There will come a day when the passage of time and the efforts of a longer stretch of human history will bring to light things that are now obscure. One lifetime, even if it can be wholly devoted to astronomy, is not sufficient for the investigation of such important matters. And just think of how we divide our tiny number of years unequally between our studies and our vices. So it will take a long succession of people to explain these matters.

There will come a day when our descendants are astonished that we did not know such obvious facts. These five stars force themselves on our attention, and, as they constantly appear in different places, make us inquisitive; but what their morning and evening risings are, what are their stations, when they move straight ahead, why they are driven backward—all this we have only just begun to understand. Whether Jupiter was rising, or setting, or retrograde—for they have applied that term to his retreating—we learned just a few years ago.

Seneca, *Naturales Quaestiones*, **VII**, 25, 4-5

Abstract

Science and Earth observation missions require high-class gyroscopes, having a resolution in the range 0.1 – 1 °/hr and a bias stability in the range 0.001 – 0.1 °/hr, for an accurate control of the satellite attitude and orbit.

High reliability, high radiation resistance, high robustness, high shock tolerance, small volume, low power consumption and reduced mass are typical requirements of new generation angular rate sensors for Space applications.

In this context, the photonic ring resonators are emerging as key building blocks. The radiation hardness of a ring resonator useful for Space applications has been investigated, demonstrating a negligible worsening of the performance under γ radiations.

In this thesis, the potentiality of an ultra-high-Q ring resonator, acting as sensitive element of a resonant micro-optic gyroscope architecture (RMOG), has been discussed, aiming to design a chip-scale, high performing gyroscope.

The key element of the proposed RMOG configuration is a Si_3N_4-based simple ring resonator with a one-dimensional photonic crystal included along the whole optical path, called as 1D-PhCRR. Its operation is based on the exploitment of the slow light effect, typical of the PhC, providing an improvement of the Q-factor respect a simple ring resonator more than 3 order of magnitude. The Si_3N_4 PhCRR with $Q > 10^9$, has been theoretically demonstrated by using a self-made mathematical model, based on the Coupled Mode Theory (CMT). This performance ensures a gyro resolution < 0.05 °/hr with a small volume (< 1 cm^3), compliant to the Space operators' requirements. The development of the 1D-PhCRR has been carried out in the framework of the European Space Agency NPI contract, that sponsor the PhD activities.

Besides its suitability for attitude and orbit control sub-systems, the PhCRR could be used to implement several functionalities in the next photonic-based generation telecom payloads and for Earth observation purpose.

Telecom satellites are the most mature Space applications. In the last decades, Space operators require flexible telecom payload that can be adapted and optimized after the launch, according to the varying user demands in terms of bandwidth, coverage, and frequency allocation. The microwave photonic represents the most suitable approach to fulfil the next-generations telecom payloads requirements.

In this context, photonic-based microwave filters have been investigated, and the design of a silicon – based PhCRR with a bandwidth B = 10.43 GHz and ER > 40 dB, acts as notch filter, has been reported. By inserting and engineering defects into the PhC section, superimposed the PhC on a ring resonator section, a Gaussian-shaped frequency response, with very steep sidewalls, has been simulated. A continuous tuning of the filtering central frequency (15 GHz), with a fast switching time (≈ 1 ns) and power consumption of 47 mW is ensured, by exploiting the free carrier plasma dispersion effect in correspondence of PhC defects.

Furthermore, the theoretical feasibility of a miniaturized Ka-band optoelectronic oscillator, based on the designed PhCRR, with a phase noise at 10 kHz offset from the carrier of about -155 dBc/Hz and an output electric power > 10 dBm has been demonstrated, that represent a remarkable improvement respect to the state-of-the-art.

The high purity of the oscillating signal has been exploited for the design of a linearly chirped microwave generator, useful for high-resolution Synthetic Aperture Radar (SAR) systems for Earth Observation, with a time-bandwidth product of 3200 and a phase noise of about -116 dBc/Hz.

The design of an ultra-compact graphene-based optical delay line useful for the beamsteering/beamforming in X-band, is reported to ensure a wide swath size of SAR systems, with high range resolution, simulating the highest figure of merit reported at the state-of-the-art.

Acknowledgments

First, I would like to thank my supervisor, Prof. Caterina Ciminelli, for having made this PhD possible. Her continuous suggestions, encouragements and support during these years represent a great value for me. Thanks for all.

Thanks to Prof. Mario N. Armenise for the fruitful discussions, by providing his well-known experience in optoelectronic topics.

Thanks to the Optoelectronics Laboratory members at the Politecnico di Bari, Prof. Francesco Dell' Olio and Mr. Nicola Sasanelli, for supporting me during these years with valuable advices and scientific suggestions. From day one, they made me feel part of the group. Although he left our group few years ago, I'd like to thank Dr. Donato Conteduca for his helpful suggestions in the research topics and the daily life, becoming a great friend.

Thanks to the European project NPI for funding several PhD activities, giving me the opportunity to cooperate with the European Space Agency (ESA). Thanks to Dr. I. McKenzie for his support and hospitality during my visit at ESTEC headquarter, where the support of Dr. A. Meoli, Dr. M. Muschitiello, Drs. A. Costantino has been very useful. Thank you. Furthermore, I'd like to thank the LioniX International BV staff (A. Leinse, E. Schreuder, R. Heuvink) to host and encourage me during the activity of chip characterization.

Thanks to my parents, Dino and Marinella. This thesis is for you, to the continuous support in every moment of my life. For everything you do, for all the suggestions and all love that you have provide me during all my life.

Thanks to my grandmothers, aunts, uncles and cousins, especially the Strippoli family, for the support during these three years.

Thanks to Roberta, to make me special. Her love, psychologically support and hard encouragement makes me able to see the everyday life from another point of view. I know you will always be there to take my hand and overcome the difficulties together.

The last but not the least, thanks to my Stars into the sky, to follow me during my life. I will never forget you and this thesis is also yours.

List of Acronyms

1D	One-Dimensional
2D	Two-Dimensional
3D	Three-Dimensional
ADC	Analog-To-Digital Converters
AOCS	Attitude and Orbit Control Sub-System
ARW	Angle Random Walk
ASIC	Application Specific Integrated Circuit
AWG	Arrayed Waveguide Gratings
BG	Bragg Grating
BPF	Pass Band Filter
BW	Bandwidth
CAGR	Compound Annual Growth Rate
CGR	Galactic Cosmic Radiation
CMOS	Complementary Metal-Oxide Semiconductor
CMT	Coupled Mode Theory
COTS	Commercial Off-The-Shelf
CROW	Coupled-Resonator Optical Waveguide
CVD	Chemical Vapour Deposition
DAC	Digital-To-Analog Converters
DAQ	Data Acquisition
DC	Duty Cycle
DFB	Distributed Feedback Laser

DOF	Degree Of Freedom
DSP	Digital Signal Processing
E/O	Electro-Optical
ECSS	European Cooperation for Space Standardization
EDFA	Erbium-Doped Fiber Amplifiers
EIM	Effective-Index Method
EM	Electro-Magnetic
EMI	Electromagnetic Interference
ENOB	Effective Number Of Bit
EO	Earth Observation
EOM	Electro-Optical Mixer
ER	Extinction Ratio
ESA	European Space Agency
FBG	Fiber Bragg Grating
FC	Frequency Converter
FDTD	Finite Difference Time Domain
FEM	Finite Element Method
FOG	Fiber Optic Gyro
FOM	Figure Of Merit
FSR	Free Spectral Range
FWHM	Full Width at Half Maximum
GEO	Geostationary Orbit
GLONASS	Global'naja Navigacionnaja Sputnikovaja Sistema
GNSS	Global Satellite Navigation System
GPS	Global Positioning System
GTO	Geostationary Transfer Orbit
HEO	Highly Elliptical Orbit
HPA	High Power Amplifier
HRG	Hemispherical Resonator Gyro
I/Q	In-Phase/Quadrature
IF	Intermediate Frequency

IL	Insertion Loss
IMPF	Integrated Microwave Photonic Filter
IMU	Inertial Measurement Unit
ISS	International Space Station
JAXA	Japan Aerospace Exploration Agency
LCMW	Linearly Chirped Microwave Waveform
LEO	Low Earth Orbit
LEOP	Launch and Early Operation Phase
LNA	Low-Noise Amplifier
LO	Local Oscillator
LPCVD	Low Pressure Chemical Vapour Deposition
MAP	Microwave Anisotropy Probe
MEMS	Micro Electro-Mechanical Systems
MEO	Medium Earth Orbit
MM	Multi-Mode
MMIC	Monolithic Microwave Integrated Circuit
MOVPE	Metal-Organic Vapour-Phase-Epitaxy
MPF	Microwave Photonic Filters
MQW	Multi Quantum Well
MWP	Microwave Photonic
MZ	Mach-Zehnder
NASA	National Astronautics and Space Administration
NMRG	Nuclear Magnetic Resonance Gyroscope
OBPF	Optical Band Pass Filter
OEO	Optoelectronic Oscillator
PAA	Phased Array Antenna
PBG	Photonic Crystal Bandgap
PC	Polarization Controller
PD	Photodetector
PhC	Photonic Crystal
PhCRR	Photonic Crystal Ring Resonator

PhCW	Photonic Crystal Waveguides
PI	Proportional Integral
PIC	Photonic Integrated Circuit
PM	Polarization Maintaining
PS	Power Splitter
RADAR	Radio Detection And Ranging
RAMZI	Ring Assisted Mach Zehnder Interferometer
RF	Radio Frequency
RFOG	Resonant Fiber Optic Gyroscope
RLG	Ring Laser Gyro
RMOG	Resonant Micro Optic Gyroscope
RMS	Root Mean Square
RPML	Recirculating Phase Modulation Loop
RR	Ring Resonator
Rx	Reception
RXTE	Rossi X-Ray Timing Explorer
SAMPEX	Solar Anomalous And Magnetospheric Particle Explorer
SAR	Synthetic Aperture Radar
SBS	Stimulated Brillouin Scattering
SCISSOR	Side-Coupled Integrated Spaced-Sequence Of Resonator
SEDS	Small Explorer Data System
SEP	Solar Energetic Particles
SM	Single-Mode
SMT	Scattering Matrix Theory
SOI	Silicon On Insulator
SS-FTT	Frequency-To-Time Mapping Technique
SW	Switch
TBWP	Time-Bandwidth Product
TE	Transverse Electric Mode
TIA	TransImpedence Amplifier
TIR	Total Internal Reflection

TM	Transvers Magnetic Mode
TMM	Transfer Matrix Method
TMT	Transmission Matrix Theory
TRL	Technology Readiness Level
TRMM	Tropical Rainforest Measuring Mission
TTDL	True-Time Delay Line
Tx	Transmission
ULLW	Ultra-Low Loss Waveguide
VCO	Voltage-Controlled Oscillator
VGA	Variable Gain Amplifier
WGM	Whispering Gallery Mode

List of Figures

1.1 Space system segments: payload and satellite platform (a), transportation segment (b) and ground segment (c). Photos and images: ESA……..... 2

1.2 Orbits classification (*LEO*: Low Earth Orbit, *GEO*: Geostationary Orbit, *MEO*: Medium Earth Orbit, *HEO*: Highly Elliptical Orbits)… 6

2.1 SRL-based gyroscope ([38] for (a), [39] for (b)), (*EO*: electro-optic; *PD*: photodiode; *BH*: buried heterostructure; *CCS:* constant current source; *A*: amplifier; *SA*: spectrum analyzer)……. 26

2.2 Resonant Micro Optical Gyroscope (RMOG) architecture, (*BS:* beam splitter, *PD:*photodetector)……... 28

2.3 Resonant Fiber Optic Gyroscope (RFOG)……. 29

2.4 Photograph of CaF_2 WGM resonator -based gyroscope [45…… 30

2.5 SiO_2 wedge resonator and a SiN waveguide as bus [57]…… 31

2.6 Schematic of the nanophotonic optical gyroscope based on reciprocal sensitivity enhancement [64], (*PC*: Polarization Controller, *MZI*: Mach-Zehnder Interferometer, *PD*: photodiode, *TIA*: TransImpedence Amplifier; *VGA*: Variable Gain Amplifier, *LPF*: Low-Pass Filter, *AMP*: amplifier, *REF*: voltage reference).……... 33

2.7 Interferometric Optical Gyroscope architecture (a), based on a Si_3N_4-based coil (b) [66], (*PD*: photodiode, *EA*: electrical amplifier, *LID*: lock-in amplifier, *WG:* waveguide, *WG C*: waveguide coil,

DAQ: Data AcQuisition, *SG*: signal generator)……..... 34

2.8 Brillouin-based gyroscope architecture [67], (*PC*: polarization controller, *PM:* phase-modulator, *PI:* proportional integral servo, *OBPF*: optical band-pass filter, *ESA:* electrical spectrum analyzer, *VCO:* voltage-controlled oscillator, *PD*: photodiode)……..... 35

2.9 (a) Schematic of the InGaAsP/InP ring resonator under test, with the map of the electric field of the TE_0 inside the bus waveguide; (b) packaged device under test; (c) schematic of the packaged device (*R*: radius, w_{wg}: waveguide width, *g*:gap, t_{wg}: waveguide thickness; t_{upper}: slab layer thickness). Reprinted with permission from [95] © The Optical Society..……... 40

2.10 (a) Overview of the measurement setup; (b) TE mode resonance spectrum; (c) Resonance detuning $\Delta\lambda_{res}$ when changing the chip temperature, (*TEC*: thermo-electric cooler, ΔT: temperature change, $\Delta\lambda_{res}$: resonance detuning). Reprinted with permission from [95] © The Optical Society..……..…. 41

2.11 AD590 output current (blue line) *vs* total absorbed dose. An output current = 298 μA guarantees a chip temperature equal to 25.0 °C, used as reference (supply voltage = 5 V). The dotted blue lines are referred to the maximum and minimum measured value. The green line is referred to the constant temperature of the chamber, where the measurements are carried out. Reprinted with permission from [95] © The Optical Society..…… 45

2.12 *S* [μA/krad] vs T_{chip} [K]. Reprinted with permission from [95] © The Optical Society..…….. 45

2.13 Temperature closed-loop control (*PID*: Proportional-Integral-Derivative; *A/D*: analog-to- digital; *D/A*: digital-to-analog)…… 46

2.14 (a) Red-shift of ring resonator resonance $\Delta\lambda_{res}$ vs total adsorbed dose. The bold red line is related to a linear fitting of the measured blue markers. (b) *ER* variation (ΔER) vs total adsorbed dose; (c) *Q*-factor variation (ΔQ) vs total adsorbed dose. The radiation and annealing activities are defined to the left and to the right of red line, respectively. Reprinted with permission from [95] © The Optical Society 47

2.14 TE resonance spectra pre- and after- irradiation ($\lambda_0 \approx 1.55$ μm; $\Delta\lambda_{max}$ is the maximum value of the laser scan across the operating wavelength λ_0 (200 MHz); $\Delta\lambda_{res}$ is the resonance detuning, caused by the radiation effect). Reprinted with permission from [95] © The Optical Society 48

2.16 PhC slab waveguide (a), relative band diagram (b) and n_g *vs* frequency at the band edge (c)..... 50

2.17 Mechanisms to obtain slow light in photonic crystals: Backscattering (a), omnidirectional reflection (b)..... 51

2.18 1D-Photonic Crystal Ring Resonator..... 52

2.19 a) Simple ring resonator, b) transmission spectrum, c) peak of resonance at λ= 1547 nm (*R*: radius, *w*: waveguide width, *g*: bus-ring gap)..... 54

2.20 a) PhCRR with air holes, b) transmission spectrum, c) band-edge peak at λ= 1559 nm (*R*: radius, *w*: waveguide width, *g*: bus-ring gap, *d*: holes diameter, *Λ*:period)..... 55

2.21 Sketch of some configurations of PhCRR proposed in literature [131, 123, 126, 132, 133, 136]..... 57

2.22 (a) 1D-Photonic Crystal, (b) grating-assisted coupling region..... 59

2.23 (a) 3D waveguiding ring in Cartesian (blue lines) and Cylindrical (red lines) coordinates. (b) 2D focus on a ring resonator section, (n_s = refractive index of inner cladding, n_t = refractive index of core, n_c = refractive index of outer cladding, R = radius of curvature, d = waveguide width)..... 60

2.24 n_{eff} *vs* curvature radius (a), α_{loss} [a.u.] *vs* curvature radius (b)……. 62
2.25 Schematic of a bent 1D-PhC…….. 63
2.26 Schematic of a bent Si_3N_4 top grating (a) and its transmission power ($|F_g^+(\theta_{max})|^2$) spectrum…… 66
2.27 Schematic of a Si_3N_4 sidewall grating (h = 100 nm, w = 2.8 µm, Λ = 525.5 nm, w_H = 3.4 µm, w_L = 2.2 µm, L = 200 µm) (a) and the comparison of the transmission power calculated by using CMT (blue line) or 2D-FDTD (red line) approach (b)…… 67
2.28 Schematic of the grating assisted-coupling region (b = bus waveguide, g = grating waveguide, n_b = refractive index of b, $n_{g1,2}$ = refractive indices of the two grating region, w_b = bus width, w_g, = grating width, g_0 = minimum gap)…….. 68
2.29 Calculated Gaussian trend of $|K_{bg}^+(z)|^2$ in the grating assisted coupling region…….. 69
2.30 Top view of a schematic diagram of the coupling region (w = 2.8 µm, Λ = 525.5 nm, w_H = 3.4 µm, w_L = 2.2 µm, gap_0 = 5.5 µm, L = 300 µm) (a) and the comparison of the transmission grating output power calculated by using CMT (blue line) or 2D-FDTD (red line) approach (b)……..... 72
2.31 Si_3N_4 – based waveguide 100 nm thick and 2.8 µm wide (*LPCVD:* Low Pressure Chemical Vapour Deposition)……. 78
2.32 Electric field normalized distribution of the TE (a) and TM (b) mode into the waveguide in Fig.2.30 ……. 78
2.33 Si_3N_4-based top grating, (Λ: period; t_H: maximum thickness; t_L: minimum thickness; d: modulation depth)…… 80
2.34 n_{effTE} *vs* waveguide thickness…… 80
2.35 1D PhCRR based on top grating, (w: waveguide width; t: waveguide thickness; t_H: grating maximum thickness; t_L: grating minimum thickness; R: radius)…….. 81
2.36 Simulated TE-polarized transmission spectrum of 1D-PhCRR based on top grating (*FSR:* Free Spectral Range)…….…….. 81

2.37 1st band edge transmission peak of Full-PhCRR based on top grating…… 82
3.1 Classification of satellite currently in orbit according to their functions……. 102
3.2 Multi-beam network approach…… 105
3.3 Simplified scheme of a photonic-based RF repeater, (*Rx*: reception; *BPF*: pass-band filter; *LNA*: low-noise amplifier; *EOM*: electro-optical modulator; *O/E*: optical-electro converter; *HPA*: high power amplifier; *Tx*: transmission). The blue building blocks are based on a photonic approach. The green building blocks are based on a standard RF approach……. 105
3.4 Configuration of the Ka-band OEO, (*DFB laser*: distributed-feedback laser; *MZI*: Mach-Zehnder Interferometer; *PhC*: photonic crystal; *PIC*: Photonic Integrated Circuit; *MMIC*: Monolithic Microwave Integrated Circuit)...……...…….. 109
3.5 *Q*-factor of the first band edge resonance *vs* ring radius, for different values of ER…… 110
3.6 Typical phase noise spectrum of an OEO…….. 111
3.7 Oscillator phase noise at 10 kHz offset from the carrier *vs* the ring radius…….. 112
3.8 Microwave photonic filter in an incoherent (a) and coherent (b) regime……. 116
3.9 (a) Schematic of the photonic crystal ring resonator with Newton distribution of the defects. Inset: Cross-section of the defect region into the PhC section. (b) Cross-section of the waveguide without PhC. (c) Top-view of the sidewall grating superimposed along a section of the ring resonator. (d) Normalized Poynting vector of TE_0 mode into the unperturbed waveguide cross-section, (t_{wg}: waveguide thickness, w_{wg}: waveguide width, L_1: ring resonator section without PhC, R: radius, w_{min}: PhC minimum width, w_{def}: PhC defect width, w_{max}: PhC maximum width, DC: duty-cycle, Λ: period, L_{def}: defect 120

length, w_{dis}: core-doping regions distance, V_g: applied voltage) [101] © 2019 IEEE…… .

3.10 (a) Silicon-based sidewall grating with defects placed according to the Newton rule; (b) Transmission spectrum of the PhC section with L_{def} = 3.11 μm, N_d = 6 and N_t = 128 [101] © 2019 IEEE …….. 122

3.11 Silicon-based rib waveguide: (Blue curve) trends of effective index change Δn_{eff}, and (Red curve) tuning loss α_{tuning} [1/m], as function of the applied voltage V_g [101] © 2019 IEEE.……...…… 123

3.12 Silicon-based sidewall grating with defects placed according to the Newton rule: (a) transmission spectra vs Δf, which is the frequency shift from the operating frequency ($f_0 \approx$ 193 THz); (b) inset of transmissions spectra vs Δf, (c) central frequency detuning, δf_c, as a function of V_g [101] © 2019 IEEE ….……..……. 124

3.13 Bottom band of the PhCRR transmission response, for several values of coupling efficiency k^2 [101] © 2019 IEEE ….……. 125

3.14 Phase response of PhCRR for (a) $k^2 \leq K_{critical}$ and (c) $k^2 \geq K_{critical}$, and phase transmission $\angle T$ contour map depending on S_{11} and S_{22} to achieve a phase linear response null at 0 (b) or π (d) [101] © 2019 IEEE……... 127

3.15 PhCRR transmission as function of Δf at three different values of ΔL_1 [101] © 2019 IEEE ….……..…….. 127

3.16 Wide transmission spectrum of PhCRR under investigation (a), with a zoom on the Gaussian-like resonance (b). Magnification on the bottom band for k^2 = 15% (c) and k^2 = 16% (d) [101] © 2019 IEEE.. 128

3.17 Transmission spectra of silicon-based sidewall gratings with N_t = 128 (a) and N_t = 256 (b) and for several values of N_d (L_{def} = 3.11 μm), designed according to Tab. 3.2 [101] © 2019 IEEE …...……... 129

3.18 Transmission spectra S_{21} of sidewall grating with N_t = 128 and N_d = 6 for several values of the L_{def}, compliant to Eq. (3.3) [101] © 2019 IEEE ……... 130

3.19 (a) Figure-of-merit *FOM* (*ER*/*BW*); (b) PhCRR radius R as a function of L_{def}, for PhCRRs with $N_t = 256$ and $N_d = 5$ (blue curve), and $N_d = 7$ (red curve). The dotted points refer to defects lengths L_{def} that are compliant to Eq. (3.3) [101] © 2019 IEEE …… 132

3.20 Detuning, δf_c, of the central frequency of the notch filter *vs* applied voltage V_g [101] © 2019 IEEE …… 133

3.21 Coupling efficiency k^2 [%] vs gap bus-ring *g* [nm] [101] © 2019 IEEE……... 133

3.22 (a) Transmission spectrum of the PhCRR with $N_t = 256$, $N_d = 7$, $L_{def} = 3.11$ µm ($k^2 = 20\%$) and Bode plot (b) of the 1st order Butteworth low pass filter (ω is the angular frequency [rad/s] and $\Delta\omega$ is the angular frequency shift from the operating angular frequency). (c) Shifting of the central frequency and ER trends as a function of the applied voltage V_g, with some examples of the transmission spectra after voltage tuning (d) ($f_0 \approx 193.2877$ THz) [101] © 2019 IEEE 134

4.1 Illustration of imaging radar geometry…….. 151

4.2 SAR operating modes: Stripmap (a), ScanSAR (b) and Spotlight (c)……... 154

4.3 Design scheme of a SAR payload. MW: microwave; A/D: analog-to-digital; Tx: transmission; Rx: reception; A: amplifier. Inset image source: RADARSAT-2 Data and Products © MacDonald Dettwiler and Associates Ltd (2009) – All Rights Reserved – RADARSAT is an official mark of the Canadian Space Agency [22]……..……... 155

4.4 Passive (a) and active (b) phased-array antenna, (*a*: attenuation stage, *RF A*.: RF amplifier, ϕ: phase shifter)…….. 158

4.5 Configuration of the graphene-based silicon Bragg grating, with the nanowire cross-section in the inset (t_{Si}: waveguide thickness, w_{Si}: waveguide width, t_{gr}: graphene thickness, t_{Al}: Al_2O_3 thickness; V_g: applied voltage; Λ: period, $L_1 - L_2$: PhC sections). Reprinted with permission from [65] © The Optical Society..... 162

4.6 Real (a) and imaginary (b) part of the effective indices in the sections with the graphene capacitor, for TE (red curve) and TM (blue curve) modes, as a function of the electrochemical potential μ_c. Reprinted with permission from [65] © The Optical Society …… 164

4.7 Time delay spectra for several values of the electrochemical potential μ_c with L_g = 2 mm. Reprinted with permission from [65] © The Optical Society …… 165

4.8 Maximum delay time τ_{max} vs voltage V_g and electrochemical potential μ_c with L_g = 2 mm. Reprinted with permission from [65] © The Optical Society ……..... 166

4.9 (a) Delay time and (b) group index spectra of 2 mm Bragg grating, applying voltage V_g = 4.363 V. Reprinted with permission from [65] © The Optical Society ……..…… 166

4.10 (a) Behaviour of τ_{max} and τ_{min} and (b) of $V(\tau_{max})$ and $V(\tau_{min})$ as a function of the grating length L_g. Reprinted with permission from [65] © The Optical Society ……. 167

4.11 (a) Delay loss (blue line) and FOM (red line) as a function of L_g. Transmission spectra at the band edge of the Bragg grating with (b) L_g = 2.3 mm ($\lambda_0 = \lambda(\tau_{max})$ = 1547.67 nm), (c) L_g = 2.6 mm ($\lambda_0 = \lambda(\tau_{max})$ = 1547.65 nm), and (d) L_g = 2.9 mm ($\lambda_0 = \lambda(\tau_{max})$ = 1547.63 nm), when $V(\tau_{max})$ and $V(\tau_{min})$ are applied to the graphene electrodes. Reprinted with permission from [65] © The Optical Society…….. 168

4.12 (a) Transmission spectrum of the Bragg grating with L_g = 2.6 mm and (b) related delay time. (c) Zoom of the transmission spectrum and (d) delay time of the first resonance peak at the band edge. Δf is the frequency shift from resonant frequency ($f_0 \approx$ 193.824 THz corresponding to $\lambda_0 \approx$ 1547.65 nm). Reprinted with permission from [65] © The Optical Society ……. 169

4.13 Tuning of the time delay as a function of the capacitor voltage. Reprinted with permission from [65] © The Optical Society ……. 170

4.14 Design scheme of linearly chirped microwave waveform (*LCMW*) generator, (*PS*: power splitter, *MZI*: Mach-Zehnder modulator, *PC*: power combiner, *OA*: optical amplifier, *PM*: phase modulator, *SW*: switch, *PD*: photodiode, *RR*: ring resonator, *RF A*: electric amplifier, *RPML*: recirculating phase modulation loop, *OEO*: optoelectronic oscillator, *PBF*: pass-band filter). Optical connections are in green, electrical ones are in blue [22]…….. 173

4.15 OEO based on a phase (a) or intensity (b) modulation approach (*PS*: power splitter, *MZI*: Mach-Zehnder modulator, *PM*: phase modulator, *PD*: photodiode, *RR*: ring resonator, *A*: electric amplifier, *PBF:* pass-band filter). Optical connections are in green, electrical ones are in blue [22] …….. 175

4.16 Phase noise trend of LCMW (output power ≈ 10 dBm) *vs* ring resonator *Q*-factor, for P_{laser} equal to 25 mW(blue) and 40 mW(red). 177

4.17 Phase noise trend *vs* ring resonator Q-factor, for OEO configurations with PM (blue curve) and MZI (red curve)…… 177

4.18 Output power of the OEO output signal for the configuration with (a) and without (b) the RF amplifier into the feedback loop……. 178

4.19 Phase noise trend of OEO with PM and PBF *vs* ring resonator *Q*-factor, for P_{laser} = 40 mW (red curve) – 80 mW (blue curve)……. 179

4.20 Driven signal of the MZI (a) and PM (b) into the RPML, with a period of 15 ns…..... 181

4.21 (a) LCMW amplitude for RPML configuration with PM driven by a parabolic waveform (see Fig. 4.20(b)); (b) Zoom on a single period of the LCMW…….. 181

4.22 10-times stepped parabolic waveform…… 182

4.23 LCMW amplitude for RPML configuration with PM driven by a 10-times stepped parabolic waveform (see Fig. 4.22)……. 182

A.1 Gyroscope input-output static characteristic…….. 198

A.2 Typical output of a gyro at rest……. 199

B.1 Sagnac ring interferometer…… 201

List of Tables

1.1 Examples of payloads and the relative missions promoted by ESA……..... 3

1.2 Many Space applications and the relative main purpose……. 6

2.1 IMUs mission requirements (✓:suitable, X: unsuitable)…….. 20

2.2 Gyro classification, in terms of bias stability and angle random walk.. 21

2.3 Comparison of gyroscope devices currently in the market [21, 24, 28-31, 34]……. 23

2.4 Comparison of the most promising RMOG technologies [41, 45, 62, 64, 66-68]……. 36

2.5 Sidewall grating performance comparison between our model and 2D-FDTD for the quasi TE-mode. …….. 67

2.6 Coupling region performance comparison between the model and 2D-FDTD approach. …….. 73

2.7 Comparison between ULLWs, proposed in literature [49, 52, 155-161]. ……. 76

2.8 Comparison between single-mode Si_3N_4 ULLWs, proposed in literature at about 1550 nm [146, 155, 162-163]……. 77

2.9 Simulated PhCRR features to obtain ER of 8 and 10 dB, and the performance of the RMOG based on the designed PhCRRs……. 83

3.1 Assumed values for the OEO key parameters …….. 111

3.2 Pascal Triangle of Binomial Coefficients B_n Related to the Number of Defects N_d [101]……..... 122

3.3 Design parameters of several PhC configurations and related PhCRRs (L_{def} = 3.11 μm) [101]……..…….. 130

3.4 Tuning performance comparison (ER_{MAX} = ER @ V_g = 0 V, ER_{MAX} = ER @ V_g = V_{MAX}) [101]…… 134

4.1 Frequency bands for SAR systems……... 148

4.2 Examples of SAR sytems for civil applications launched into the Space [5-13]…….. 150

4.3 Performance of the graphene-based Si Bragg grating with L_g = 2.6 mm [65]….……... 170

4.4 State-of-the-art of optical delay lines [65] with optical resonators [35, 45, 46, 49, 50, 53, 54] ….……. 171

Contents

Abstract ..... **i**

Acknowledgments ..... **iii**

List of Acronyms ..... **iv**

List of Figures ..... **ix**

List of Tables ..... **xviii**

1 Introduction **1**

1.1 Space system segments **2**

1.1.1 Space segment **3**

1.1.2 Transfer segment **4**

1.1.3 Ground segment **4**

1.2 Space flight mission classification **5**

1.3 Overview of the photonic-based Space applications **7**

1.4 Outline of the thesis **10**

1.5 References **10**

2 Attitude and orbit control sub-system **14**

2.1 Inertial Measurement Unit **18**

2.2 Gyroscope classification and market **20**

2.3 Gyroscope technologies **22**

2.3.1 Gyro-on-chip: Semiconductor Ring Laser **25**

2.3.2 Gyro-on-chip: Resonant Micro Optical Gyroscope **27**

2.3.3 Gyro-on-chip: emerging technologies **32**

2.3.4 Gyro-on-chip: summary..... **35**

2.4 Space qualification **36**

2.4.1 Optical characterization of the InGaAsP/InP ring resonator **39**

2.4.2 Experimental evaluation of the radiation impact on the InGaAsP/InP ring resonator 42
2.5 1D Photonic Crystal Ring Resonator 49
2.5.1 State of the art of PhCRRs 55
2.5.2 Mathematical modelling 58
2.5.2.1 CMT model of a bent 1D PhC 60
2.5.2.2 Coupler model 67
2.5.2.3 Transmission function of the 1D-PhCRR 73
2.5.3 Design 74
2.5.3.1 Technology platform selection 75
2.5.3.2 Photonic crystal Selection 79
2.5.4 PhCRR simulated performance 80
2.6 Conclusions 83
2.7 References 84

3 Telecommunication payloads 102
3.1 Photonic RF payload architecture 105
3.2 Chip-scaled optoelectronic oscillator 106
3.2.1 Resonator design 109
3.2.2 OEO performance 110
3.3 Microwave Photonic Filter 114
3.3.1 Photonic notch filter 119
3.3.2 Modelling and design of the PhCRR 120
3.3.3 Design results 129
3.4 Conclusions 135
3.5 References 136

4 Photonic-based Synthetic Aperture Radar system 148
4.1 RADAR fundamentals 151
4.2 SAR operating modes 153
4.3 Photonic-based SAR payload 155
4.3.1 Photonic ADCs 156
4.3.2 Photonic Beamformer 157
4.3.2.1 Graphene-based optical delay line 161
4.3.2.1.1 Device configuration 161
4.3.2.1.2 Numerical results 163
4.3.3 Chirped waveform Generator 171
4.3.3.1 Optoelectronic Oscillator 174

4.3.3.2 Recirculating Phase Modulation Loop……. **179**
4.3.3.3 Performance of LCMW generator…… **180**
4.4 Conclusions…….. **182**
4.5 References…… **183**

5 Conclusions **194**
5.1 Summary of accomplishments……... **194**
5.2 Critical issues ……..... **195**
5.3 Future work ……... **196**

Appendix A Gyro performance parameter **197**
References…… **199**

Appendix B Sagnac effect **200**
References……. **204**

List of publications on optoelectronic and photonic devices and systems for Space applications …….. **206**

Complete list of publications…… **210**

Chapter 1

Introduction

Since the last decades, the global Space has undergone rapid transformations. New technologies are entering the sector, paving the way to the "Space economy" growth. Focusing on the enhancement of spacecrafts performance per unit of cost, the main Space companies and agencies are interested in small satellites, and consequently, satellite constellations [1].

In this context, *photonics* represents a key enabling technology in the field of aerospace engineering [2]. It is a well-established technology in several scientific/technological areas, such as telecommunications, life science, health care, lighting and so on. Photonic technologies are demonstrating several advantages, i.e. performance improvement, good resistance to vibrations/shocks, radiation and high temperature gradients, immunity to electromagnetic interference, low power consumption, and compactness, with respect to the competing ones in monitoring of critical aerospace structures, e.g. the propulsion subsystem, space communications, RF signal generation/processing, analog-to-digital conversion, and wireless power transfer. These features make the photonic device so attractive that its worldwide market is expected to exceed 600 billion Euro in 2020 [3]. According to [4], an estimated Compound Annual Growth Rate (CAGR) of 36.4 % in the period 2016-2024 demonstrates that photonics for Space is becoming a strategic R&D sector for the global aerospace market.

Since the 1960s, the potential of photonics in Space engineering has notably grown with the use of solar cells on satellites.

Currently, optical, opto-electronic, and photonic payloads are widely used especially for Earth observation and several new payloads based on the same -

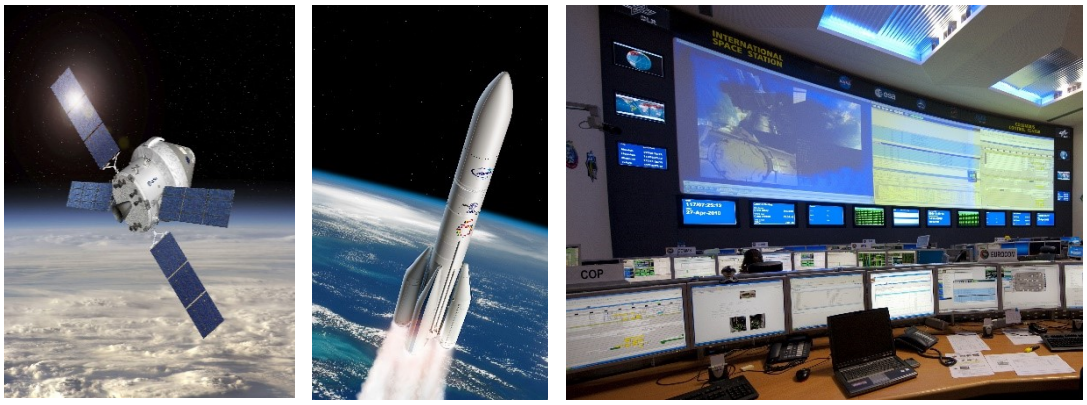

(a) (b) (c)

Fig.1.1. Space system segments: payload and satellite platform (a), transportation segment (b) and ground segment (c). Photos and images: ESA.

technologies are in the development stage. In the satellites currently in orbit, photonic components are included in some subsystems, i.e. the attitude control and the power supply sub-systems.

In this sector, several technological programs are currently ongoing in USA, Canada, Europe, Japan, and China to assess the emerging photonic technologies in terms of reliability and performance, aiming to using them in future satellites, launchers, aircrafts, helicopters, and unmanned vehicles. The aforementioned programs foster the development of free-space communications over long distances, Earth observation and navigation payloads for miniaturized satellites, high resolution measurement systems and improving the reliability and qualification of optical packaging. In the next decades, photonics will gain an important role in almost all Space system sub-systems, with remarkable benefits in terms of performance, size and mass reduction.

In this Chapter, the Space system is briefly introduced, focusing on its building blocks. Furthermore, the criteria for Space mission and orbit classification are set out, with an overview of the photonics-based Space applications.

1.1 Space system segments

A typical Space flight system consists of three system segments (Fig. 1.1), which are designed and coordinated according to the mission objectives. The

Space segment comprises the spacecraft and its payload in orbit. The transfer segment provides the transport into Space of both the satellite platform and its payload by a launcher. A ground segment is required to control and monitor the spacecraft as well as to distribute and process the payload data. The design of the ground and transfer segments and their relative costs strictly depend by the physical features of the spacecraft and the payload.

1.1.1 Space segment

The Space segment includes the payload and the satellite platform carrying it. The payload is the heart of a space flight mission, and its operation could involve the mission success or failure. The payloads features, such as mass, geometry, power and communication requirements, determines the properties of the carrying satellite platform, known as satellite bus.

A wide variety of payloads has been developed during the last decades. Some examples of payloads and the relative missions, developed by European Space Agency (ESA), have been reported in Tab. 1.1, where the most common payloads are radiometers, spectrometers, magnetometers, cameras, radar systems, transmitters, atomic clocks for navigation/positioning, transponders for satellite telecommunications, and rover vehicles [5].

Tab. 1.1: Examples of payloads and the relative missions promoted by ESA.

Payload	Application	Missions example
Cameras	• Earth Observation • Weather monitoring • Planetary exploration	• *Meteosat* • *Mars Express* • *Cosmo Sky Med 1 – 2*
Radar		
Sensors	• Earth exploration • Planetary exploration	• *CHAMP* • *ENVISAT*
Signal transmitter	• Navigation • Positioning	• *Galileo*
Atomic clock		
Lander	• Analysis of planet surfaces • Analysis of planet surfaces	• *Giotto* • *Mars Express*
Rover		

The satellite platform is formed by several sub-systems, that constitute the infrastructure on which the payload is installed. Over the mechanical system, aiming to accommodate the payload, other subsystems, such as the power supply, the attitude control, and the thermal sub-system, ensure the proper operation of the satellite, in terms of energy, attitude and temperature. Furthermore, communications systems guarantee the reception/transmission of data, processed and handled on board the spacecraft by dedicated sub-systems.

1.1.2 Transfer segment

The transfer segment includes the launch vehicle, equipped with appropriate propellants, and the launch infrastructure. Several rockets have entered the commercial market over the last years, such as *Atlas V* or *Ariane 5*.

The key elements of the launch vehicle are the mechanical structure, propellant tanks, engines, attitude control systems, and flight monitoring systems. In the launcher, chemical reactions produce very high temperature gases that expand through a nozzle. Due to the high development costs of rockets, the pool of launcher suitable for a mission profile is often very limited. Although many launchers are available for spacecraft with a mass under 2 tons and Low Earth Orbit (LEOs), satellites with a mass of more than 8 tons can only be launched by *Ariane 5*, *US Atlas V* and *Delta IV* rockets [5].

1.1.3 Ground segment

The ground segment controls and monitors the space flight mission scenario. In contrast to the spacecraft, the ground segment could be revised after the launch, at the expense of higher mission cost. It can be divided into two system elements: mission operations and the ground station network. The mission operations are designed and conducted at a control center, aiming to monitor and control the spacecraft operation.

The central part of mission operations is the flight one, which includes the management of the flight tasks and the maintenance of the spacecraft in all

mission phases. The operations activities strictly depend by the phases of preparation and execution of a mission. The riskiest step of mission operation is the Launch and Early Operation Phase (LEOP), where the spacecraft is activated and its survival should be ensured into a hazardous environment, in terms of temperature, vacuum and radiation.

The ground station network receive/transmit the data from and to the spacecraft. Several frequency bands can be used, regulated by international coordination protocols. As the mission operations, the mission profile of a ground station is also strictly dependent by the mission phase. During the LEOP, frequent and long contacts with the spacecraft are important to track its position. Global ground stations are used to ensure more frequent contact with the spacecraft.

1.2 Space flight mission classification

Space missions can be classified according to both the area of application and the operation orbit. The applications areas of Space missions are constantly growing, furnishing direct and tangible benefits to people on Earth. Many application areas, with the relative main purpose, are reported in Tab. 1.2. As example, into the scenario of hydrogeological instability, Earth observation, telecommunications and global navigation can play a vital role in preventing disaster, by providing accurate and timely information for decision-makers. In particular, Earth observation can be used to manage hazard maps and define the map areas that could be affected by tsunamis, forest fires, landslides and other natural risk. In a complementary way, the satellite telecommunication offers the possibility of transmitting warnings very quickly from one continent to another, in addition to other relevant information, while, the positioning systems are useful to understand the relative motion of tectonic plates, and then earthquakes disaster.

Tab. 1.2. Many Space applications and the relative main purpose.

Space applications	Main purpose
Meteorology	Weather forecasting
Positioning, navigation and timing	Tracking of vehicles
Military and national security uses of Space	Enhancement of the effectiveness of ground-, air-. and sea-based military force
Satellite telecommunications	Routing of voice, video, data signals
Earth observation	Observation of Earth's land and water surfaces
Space tourism	Transport of fare-paying passengers into Space

Moreover, the space flight mission can be classified according to the operating orbit, in terms of the shape and the altitude. The target mission of the spacecraft and its orbit are strictly correlated. The most used selected orbits for Space missions are around the Earth, and they could be classified in Low Earth Orbit (LEO), Geostationary Orbit (GEO), Medium Earth orbit (MEO) and Highly Elliptical Orbit (HEOs), as shown in Fig. 1.2 [5]. The LEO is a near-circular orbit with altitude ranging from 300 km to 1,500 km, while the GEO is a near-circular orbit with an altitude of about 36,000 km. The near-circular orbits at intermediate altitudes, from 1,500 km to 36,000 km, are called MEOs, while, HEOs are elliptical orbits with a distance from the Earth < 1,000 km and > 36,000 km at the perigee and apogee, respectively. The Geostationary Transfer Orbit (GTO) is a highly eccentric orbit used by a satellite as intermediate orbit before reaching the GEO orbit.

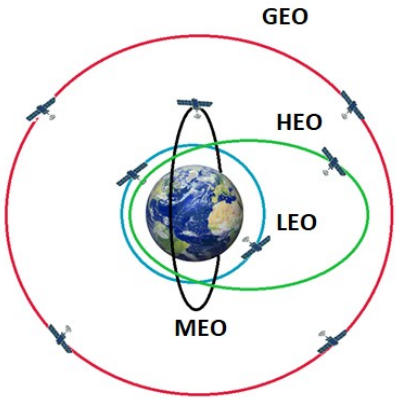

Fig. 1.2. Orbits classification (*LEO*: Low Earth Orbit, *GEO*: Geostationary Orbit, *MEO*: Medium Earth Orbit, *HEO*: Highly Elliptical Orbits).

1.3 Overview of the photonic-based Space applications

Although several photonic sub-systems represent hot R&D topics for Space companies and agencies, most of the photonic-based Space applications play important roles into Space segment currently in orbit, such as payload and satellite platform.

In particular, the photonic technology for satellite platform results already mature. Space solar cells have been used as power sources by many satellites, and they play an important role in a wide range of applications, as communications, resource investigation, and scientific research. Since their first utilization in Space, in 1958, the solar cells have been included in the power supply sub-system of all satellites.

Optical fibers have been used to interconnect sub-systems with high speed on board a spacecraft, known as box-to-box interconnects [6]. The fiber-based optical communication links provide several advantages over competing technologies, such as hardness to electromagnetic interference, low signal distortion, extremely large bandwidth, low power consumption, ease of system integration/testing, mechanical flexibility, low volume, and light weight. Currently, optical links are used for transferring or distributing data on board a spacecraft [7]. Since the 1990s, the US National Astronautics and Space Administration (NASA) have used fiber-optic data links for satellite telemetry and control applications. In particular, the control and data handling functions in Solar Anomalous and Magnetospheric Particle Explorer (SAMPEX) satellite, launched in 1992, were performed by using the optical fiber technology in the Small Explorer Data System (SEDS) [8]. Other NASA missions that exploit the optical fiber data link technology include the *Rossi X-ray Timing Explorer* (RXTE), the *Tropical Rainforest Measuring Mission* (TRMM), and the *Microwave Anisotropy Probe* (MAP). Furthermore, this technology has been also used on board the International Space Station (ISS), with an optical fiber data bus operating at 0.1 Gb/s.

Over the optical link, the fiber properties can be exploited for monitoring and sensing. The fiber Bragg grating (FBG) is one of the most promising photonic technologies for strain/temperature mapping. Since 1996, the FBG technology has

been used in Space for the monitoring of the strain on the propulsion system by NASA, ESA and Japan Aerospace Exploration Agency (JAXA). Furthermore, the performance of an FBG-based complex sensor, able to monitor pressure, temperature and strain, was evaluated in the Space environment by the ESA mission *Proba-2* [9].

Photonic devices play an important role in the attitude and orbit control sub-system (AOCS). All spacecrafts include an AOCS that monitor the attitude and produce the commands for the actuators, which change the attitude by creating torque [10]. The attitude can be detected by several sensors, able to measure both the absolute attitude, i.e. star trackers, sun sensors, earth sensors, magnetometers, and the spacecraft angular rate, i.e. gyroscope, into an inertial reference frame. Although remarkable progress in star tracker technology allows the development of gyro-less satellites for telecom purposes, e.g. *Globstar 2* and *Iridium Next* constellations [11], Earth observation and scientific missions, and rover vehicles for planet exploration, require gyroscopes with resolution in the order of 0.1°/h and 1-10 °/h, respectively. In the 1980s, this requirement was fulfilled by a highly performing vibrating gyro, the Hemispherical Resonator Gyro (HRG). HRG is a very sensitive and heavy gyro [12] and it was used on many spacecrafts, including the *CASSINI* spacecrafts, *Alphabus* and *Spacecraft 4000* [13-15].

The satellite miniaturization trend has involved the development of compact gyroscope with high performance. The photonic technology results compliant to the micro/nano satellites requirements, hence, in the last decades, photonic sensors have dominated the market of gyros for Space applications [16-17]. These devices are all based on the Sagnac effect [18], i.e. the generation of a phase (or frequency) shift between two optical beams that counter-propagate along a rotating closed path. The Ring Laser Gyro (RLG) is the first photonic gyroscope used for Space applications. Currently, it is widely used on board of launchers. In several missions, the RLG has been replaced by the Fiber Optic Gyro (FOG), with a bias drift ranging from 0.1 °/h to 0.0003 °/h, that has been used in many European Space missions (*Pleiades*, *Aeolus*, *Planck*, *Galileo*) [19]

and was mounted on board the NASA's planetary rovers for Mars exploration [20].

The technological step towards a photonic approach appears to be in a preliminary stage, although several demonstrators have proved the performance upgrade respect to the conventional counterparts. Notable example are cameras and spectrometer used in optical payload for Earth Observation: a chemistry and camera tool (ChemCam), where laser, camera and spectrograph work together, is installed on board of Mars *Curiosity* Rover, developed by NASA and launched in 2011, aiming to identify the chemical and mineral composition of rocks and soils on the Martian surface [21].

Furthermore, the requirement of data transmission/reception rate in the order of tens of Gb/s for two-way communications between satellite and ground station drives can be fulfilled by a laser communication (lasercom) technology, that shows a high level of security, ultrawide usable bandwidth, frequency reuse, mass, power consumption, and size reduction, immunity to radiation and electromagnetic interference, and absence of any frequency regulation [22]. The saving in terms of size, weight, and power consumption of the lasercom technology is mainly due the lower level of diffraction suffered by an optical beam with respect to an RF beam. Moreover, the key building blocks of the systems (laser, modulators, amplifiers, and photodetectors) for free-space optical links between satellites and between satellite and ground stations, have reached a high level of maturity, also demonstrating a correct operation in the harsh environments. The main issue of the lasercom technology regards the detrimental effects due to cloud coverage and/or fog, that could affect the link operation. Although, since the 1970s, this technology has been widely investigated by NASA, JAXA, ESA and several companies in the US, Europe, and Japan, it has only recently reached the commercialization stage. In 2007, this technology has been demonstrated inside a Russian spherical capsule, performing a bit rate of 62.5 kb/s, with a bit error rate in the range 10^{-7}-10^{-4} [23].

In the last years, a great research effort has been spent also on innovative sub-systems for on-board data pre-processing and speeding-up of availability of images. These functionalities require an A/D conversion at high resolution, and a

transmission to the on-board pre-processor at high speed. As example, a Synthetic Aperture Radar (SAR) antenna, that contains tens of radiating elements each connected to an A/D converter, ensure a data rate up to 0.1 Tb/s of the signal from the A/D converter to the on-board processor.

Although these fully photonics systems are currently at a prototype level, in the coming years, they will be able to replace the counterparts currently in orbit, providing a high bit rate data stream with a very high resolution of the image.

In conclusion, for radar, telecom and navigation payloads, the migration towards photonic technology platform is still in place and its finalisation is expected into the following decades.

1.4 Outline of the thesis

The thesis is focused on the modelling and the design of optoelectronic and photonic devices and systems for Space applications.

The next Chapter critically reviews the attitude and orbit control systems currently in orbit. Furthermore, an innovative architecture of optical gyroscope is proposed, with the relative electromagnetic model and the simulated performance.

New architectures of optical filter and microwave oscillator, suitable for telecom payloads, are presented in Chapter 3.

The design of a photonic Synthetic Aperture Radar system is the topic of Chapter 4.

The trade-offs, the future developments and the conclusions are discussed in Chapter 5.

1.5 References

[1] C. D. Jilla, and D. W. Miller, “Satellite design: past, present and future,” International Journal of Small Satellite Engineering, **8**, pp. 611-613, 1997.

[2] C. Ciminelli, F. Dell’ Olio, and M. N. Armenise, *Photonics in Space: Advanced Photonic Devices and Systems*, World Scientific, 2016.

[3] Photonic Industry Report 2013, http://www.photonics21.org/.

[4] Free Space Optics Market Global Scenario, Market size, outlook, trend and forecast, 2015-2024.

[5] W. Ley, K. Wittman, and W. Hallman, *Handbook of space technology*, **22**, John Wiley & Sons, 2009.

[6] K. A LaBel, C. J. Marshall, P. W. Marshall, P. J. Luers, R. A. Reed, M. N. Ott, C. M. Seidleck, and D. J. Andrucyk, "On the suitability of fiber optic data links in the space radiation environment: a historical and scaling technology perspective," Proc. of the 1998 IEEE Aerospace Conference, IEEE, **4**, pp. 421–434, Aspen, Colorado, USA, March 21–28, 1998.

[7] N. Karafolas, J. M. P Armengol, and I. Mckenzie, "Introducing photonics in spacecraft engineering: ESA's strategic approach," Proc. of 2009 IEEE Aerospace conference, IEEE, pp. 1-15, Big Sky, MT, USA, March 7–14, 2009.

[8] M. N. Ott, F. LaRocca, W. J. Thomes, R. Switzer, R. Chuska, and S. Macmurphy, "Applications of optical fiber assemblies in harsh environments: The journey past, present, and future," Proc. of Optical Technologies for Arming, Safing, Fuzing and Firing IV, International Society for Optics and Photonics, **7070**, p. 707009, San Diego, California, USA, August 13-14, 2008.

[9] R. V. Kruzelecky, J. Zou, N. Mohammed, E. Haddad, W. Jamroz, F. Ricci, J. Lamorie, E. Edwards, I. McKenzie, and P. Vuilleumier, "Fiber-Optic Sensor Demonstrator (FSD) for the Monitoring of Spacecraft Subsystems on ESA's Proba-2," International Conference on Space Optics – ICSO 2006, **10567**, p. 1054672D, ESTEC, Noordwijk, Netherlands, June 27–30, 2006.

[10] M. A. Aguirre, *Introduction to Space Systems: Design and Synthesis. Springer*, New York, 2012.

[11] B. N. Agrawal, and W. J. Palermo, "Angular Rate Estimation for Gyroless Satellite Attitude Control," Proc. of AIAA Guidance, Navigation, and Control Conference, p. 4463, Monterey, California, USA, August 5–8, 2002.

[12] F. Dell'Olio, T. Tatoli, C. Ciminelli, and M. N. Armenise, "Recent advances in miniaturized optical gyroscopes", Journal of the European optical society-Rapid publications, **9**, 2014.

[13] E. C. Litty, L. L. Gresham, P. A. Toole, and D. A. Beisecker, "Hemispherical resonator gyro: an IRU for Cassini," Proc. of Cassini/Huygens: A Mission to the Saturnian Systems, International Society for Optics and Photonics, **2803**, pp. 299-310, Denver, Colorado, USA, October 7,1996.

[14] O. Girard, J. M. Caron, and P. Berthier, "HRG Technology: A Promising Gyrometer Space Equipment," Proc. of the 6th International ESA Conference on Guidance, Navigation and Control Systems, **606**, Loutraki, Greece, October 17-20, 2005.

[15] N. Perriault, B. Célérier, and S. Dussy, "Medium to Low Class Gyros for Spacebus 4000 Application," Proc. of the 6th International ESA Conference on Guidance, Navigation and Control Systems, Loutraki, Greece, October 17-20, 2005.

[16] C. Ciminelli, F. Dell'Olio, G. Brunetti, D. Conteduca, N. Sasanelli, and M. N. Armenise, "Photonic technologies for nanosatellites", Proc. of Italy – Israel Workshop On Nanosatellite Technologies, Rome, Italy, April 9-10, 2018.

[17] G. Brunetti, F. Dell'Olio, D. Conteduca, M. N. Armenise, and C. Ciminelli, "Photonic Devices for Space Applications," Proc. of 26th Annual International Conference on Composites/Nano Engineering (ICCE-26), Paris, France, July 15-21, 2018. (INVITED).

[18] M. N. Armenise, C. Ciminelli, F. Dell'Olio, and V. M. N. Passaro, *Advances in gyroscope technologies*, Springer, New York, 2011.

[19] M. A. Gleyzes, L. Perret, and P. Kubik, "Pleiades system architecture and main performances," International Archives of the Photogrammetry, Remote Sensing and Spatial Information Sciences, **39**, 1, pp. 537-542, 2012.

[20] E. Udd, "The early history of the closed loop fiber optic gyro and derivative sensors at McDonnell Douglas, Blue Road Research and

Columbia Gorge Research," Proc. of Fiber Optic Sensors and Applications XIII, International Society for Optics and Photonics, **9852**, p. 985202, Baltimore, Maryland, USA, April 18-21, 2016.

[21] R. C. Wiens, *et al.,* "The ChemCam instrument suite on the Mars Science Laboratory (MSL) rover: Body unit and combined system tests," Space science reviews, **170**, 1-4, pp. 167-227, 2012.

[22] H. Hemmati, *Near-earth laser communications*, CRC press, 2009.

[23] H. Guerrero, "Optoelectronic COTS Technologies for Planetary exploration," Europlanet Meeting, Helsinki, Finland, May 26, 2011.

Chapter 2

Attitude and orbit control subsystem

The Attitude and Orbit Control Subsystem (AOCS) provides attitude information and maintains the required spacecraft attitude during all phases of the mission, e.g. spacecraft separation from the launch vehicle and operational lifetime. To proper perform its function, orbiting satellite must point in a specific direction, and, then, a control of its altitude is needed. The AOCS is the part of satellite designed to ensure the satellite control, in terms of orientation of the satellite body with respect to a reference frame.

The attitude control of the satellite includes sensors and actuators, which provide the torques necessary for producing the required attitude changes, and a feedback loop, in order to prevent an attitude unwanted change.

Since the satellites should be capable of assuming different attitudes, depending also by the operating orbit, i.e. Low Earth Orbit (LEO), Medium Earth Orbit (MEO), Geostationary Orbit (GEO), different settings are required for different situations. Each of these situations define a mode, called as “mission mode”, for the satellite’s attitude control and may require different sensors, actuators, and control logic [1].

Seven attitude modes can be identified, including initialization, commissioning, nominal operation, orbit control, safe mode, dormant mode, and deorbiting. During the “initialization” mode, the launcher releases the satellite and ends when the satellite has acquired a safe attitude. Several components useful for the nominal operation are switched-on. After this phase, the satellite finishes in a “safe-mode” where the attitude control system ensures the satellite’s secure operation for an unlimited period. After the launch, the satellite reconfigures itself

by deploying all the mechanisms not yet acted during the initialization phase and progressively switching-on, calibrating, and characterizing all the satellite's platform and instrument components ("commissioning" mode). This phase ends with the satellite in a "nominal" mode and attitude, ready to carry out all its functions. The orbit correction via thrusters is carried out during the "orbit control" mode, that lasts short periods. Sometimes in order to avoid a large power consumption, the satellite could be set in a "dormant" mode, where the satellite is minimally active, as during the *Rosetta* mission [2]. The "deorbiting" mode is activated at the end of mission, where the satellite should perform a dedicated orbit correction manoeuvres to ensure the re-entry into the Earth's atmosphere.

During these satellite modes, the attitude control systems play an important rule, determining the control approach to be used and the associated attitude control modes. The control approach can be classified as: uncontrolled, gravity-gradient, spin-stabilized, dual spin /momentum bias, and inertial control.

Some missions, called as uncontrolled, do not require any attitude control system and the orbit is controlled by a data post-processing at the ground station, as for the French *Starlette/Stella* satellites [3]. The gravity-gradient attitude control exploits the natural alignment of the satellite along a long axis, providing one reference direction and two attitude axes, but without control along the yaw direction. To prevent rotations along this axis, a supplementary attitude detection and actuation tools must be provided. This approach provides an accuracy of the order of ± 5°, which is not enough for many applications.

As in the case of gravity-gradient stabilization, spin stabilization by rotation provides a reference direction and constrains two attitude axes, resulting as a highly accurate, low cost, uncomplicated, and reliable attitude control system. Nevertheless, its rigid observation geometry makes them not suitable for several applications. In dual spin satellites, one part of it rotates with respect to the other, providing the gyroscopic inertia advantage of the spin-stabilized satellites and the flexibility of pointing for communication antenna or instruments, located in the nonrotating part of the satellite. In this case, the satellite does not rotate, but the permanently rotating momentum wheel provides the necessary momentum bias, resulting in good pointing stability and gyroscopic stiffness.

Inertially stabilized satellites guarantees the highest possible flexibility for the satellite attitude, being able to point in any direction and keep or change the pointing direction, as the mission requires. This is the broadest attitude control strategy, used in satellite for the Earth observation with fixed attitude, called as Non Agile Nadir-pointed, as *Sentinel-3* [4], or in missions that require flexibility of pointing for observing small areas with high resolution, called as Agile Nadir-pointed satellite, as *Pleiades* [5].

The selection of the control approach includes identifying the appropriate attitude sensors, actuator, torques, and the control logic to be used.

The actuators can provide torques for changing the satellite's attitude. Several approaches have been investigated during the last years, as thrusters, magnet torquer, reaction wheels, momentum wheels and control momentum gyros. Over the control approach, the choice of the proper actuator strictly depends by the mission requirements, in terms of torque amplitudes, cost and external supply availability.

The satellite's attitude control logic depends on the attitude control concept, the sensors, the actuators and attitude accuracy and agility requirements. The logic of the control loop can be digital or analog. In the case of a digital control loop, that is the widely used approach nowadays, the control logic can be implemented by the satellite's central processor or be given its own dedicated processor.

The attitude sensors sense the actual attitude status. The satellite's attitude can be measured either as absolute, with respect to a reference coordinate system, or as relative information, e.g. dedicated angles or attitude changes. The determination of the absolute attitude is based on the direction of two linearly independent vectors of a corresponding reference frame. The Earth magnetic field vector, the direction vector to the Sun, the direction vectors to stars, the direction vector to the Earth (or the angle to the Earth's horizon) and the direction vectors to the satellites of a Global Satellite Navigation System (GNSS) [6], such as US Global Positioning System (GPS) [7], Russian GLObal'naja NAvigacionnaja Sputnikovaja Sistema (GLONASS) [8], European Galileo [9] and Chinese BeiDou-2 [10], could be measured on board by using magnetometers, Sun sensors, star trackers, Earth sensors and GNSS receivers, respectively [1]. The accuracy of three-

axis attitude determination is strictly affected by the accuracy of the single measurements and the relative orientation of the vectors.

The GNSS is a system that uses satellites to provide autonomous geo-spatial positioning. It allows small electronic receivers to determine their location with high precision using time signals transmitted along a line of sight by radio from satellite. Although it is widely used in terrestrial applications, recently, the GNSS is used to assist other attitude systems, forming a cost-effective hybrid system [11].

A widely used approach in spacecraft is the attitude measurements by the inertial determination of angular differences and rotation rates. Although they need periodic alignment with absolute attitude measurements, the main advantage of the inertial measurements is the continuous and independent, of external source of the measurement values, control.

Gyroscope is the most mature technology for the attitude estimation by measuring the satellite's angular velocity in an inertial reference frame. The big advantage with respect to other attitude sensors, as Sun sensors and star trackers, is the high resolution of the output signal with a complete independence from external sources [12-13]. Gyros are most suitable for stabilizing spacecraft rotation and for bridging time spans without direct attitude measurements. As widely described into the next Paragraph, gyroscopes are mounted with motion sensors, as accelerometers (and, sometimes magnetometers) into an Inertial Measurement Unit (IMU), in order to measure and report the satellite specific force, angular rate and the orientation. IMUs are typically used to manoeuvre aircrafts, including unmanned aerial vehicles, and spacecraft, including satellites and landers.

In the last ten years, a great research effort has been focused on the migration of gyro functionalities in star tracker, improving their robustness to solar flares, non-stellar objects and dynamic conditions. For the coming years, the development is expected to be on miniaturisation to ease accommodation, cost reduction and the provision of high accuracy versions of the star trackers improving the robustness. The state of the art in terms of star tracker technology is represented by the multi head Active Pixel Sensor based Star Tracker by Sodern [14], which is largely immune to solar events and to a large variety of non-stellar objects, i.e. moon, planets, comets, and is relatively compact.

The star trackers efficiency, low cost and radiation immunity have opened the way to the integration of star trackers and gyros, called as pseudo-gyro less systems, as installed into *Iridium Next* and *Globalstar-2* constellation [15]. In these systems, a coarse gyro is used as a complement to star tracker for safe and transitions modes. Although this approach involves the reduction of the cost and the mass of the system star tracker – coarse gyro, the pseudo-gyro less approach causes an increase of the power consumption, the volume of the star tracker unit and the difficulty of thermal regulation of the star tracker unit, with a degradation of reliability. Although the pseudo-gyro less approach is technically feasible and supported by some Space operators, e.g. Thales Group [16], its potential market is extremely small, providing too little benefits with too many additional issues.

In this Chapter, an overview of gyroscopes for Space applications is reported, focusing on high performance gyros based on an ultra-high *Q*-factor cavity. The suitability of photonic high *Q*-factor cavity, used as sensitive element of resonant gyroscope, has been experimentally demonstrated. Furthermore, an innovative configuration of integrated ring resonator-based gyroscope is presented. A coupled mode theory-based mathematical model of the proposed device is reported, used for a device design compliant to the requirements of high-class gyroscopes. An ultra-high *Q*-factor and, then, a gyro resolution less than 0.05 °/h have been calculated.

2.1 Inertial Measurement Unit

The IMU is an electronic device that measures angular rate, force and sometimes magnetic field. The linear acceleration across one or three axes is detected by the accelerometer. An accelerometer can also be used to measure gravity as a downward force. The rotational motion of the body with respect to the inertial reference frame is sensed by using gyroscopic sensors. The gyroscopes could be classified as three-axis or single-axis, according to the number of sensed axis. By combining the two sets of measurements, it is possible to define the translational motion of the satellite within the inertial reference frame and so to calculate its angular position within it [13].

Ideally, IMUs are composed of a three-axes accelerometer and a three-axes gyroscope, which would be considered a six-axes IMU. They can also include an additional three-axes magnetometer, which is commonly used as a heading reference, forming the so-called nine-axes IMU. An IMU provides two to six Degrees of Freedom (DOF), which refers to the number of different ways that an object is able to move throughout the 3D space. The maximum possible is 6 DOF, which would include three degrees of translation movement across a straight plane along each axis (front/back, right/left, up/down), and three degrees of rotational movement across the x, y and z axes, called as pitch, rall and yaw, respectively.

A sensor fusion software combines the raw data from multiple sensors to provide measures of orientation and heading. A typical implementation, referred to a strap down inertial system, integrates angular rate from the gyroscope to calculate angular position. This is fused with the gravity vector measured by the accelerometers in a Kalman filter to estimate attitude [17]. The attitude could be estimated by the linear velocity and the linear position, calculated by integrating once and twice, respectively, the acceleration measurements into an inertial reference frame [12].

The accelerometers could be considered as well-consolidated devices, based on MEMS technology, i.e. *MS1000* [18] and *MS9000* [19] series by Colibrys and the accelerometers placed into IMUs Honeywell *HG4930* [20] or Northrop Grumann *LN200S* [21], or quartz, i.e. *QA2000* [22] and *QA3000* [23] series by Honeywell mounted into the IMU Honeywell *HG9900* [24], used for the attitude and orbit control in *Mars Express* [25], *LISA pathfinder* [26], and *Venus Express* missions [27].

In contrast to accelerometers, the gyroscopes are currently subject to a continue development, in terms of performance, cost and volume/mass reduction, and different types of gyros, essentially based on angular momentum conservation, as Sagnac and Coriolis effect, have been proposed in literature [13].

High reliability, high robustness, resistance to radiations, high shock tolerance, small volume, low power consumption and reduced mass make photonic gyroscopes as the most powerful motions sensors for the AOCS systems.

Tab.2.1: IMUs mission requirements (✓:suitable, X: unsuitable).

	Micro Nano IMU	**High Accuracy IMU**	**IMU for Launchers**
LEO/MEO Constellation	✓	X	X
Science Astronomy	X	✓	X
Formation Flying	X	✓	X
Exploration	✓	✓	X
Launchers	X	X	✓
Micro Nano Sat	✓	X	X
In orbit servicing	X	✓	X

The IMU classification is mainly influenced by the gyroscope performance (widely explained into the Appendix A), including Micro/Nano IMU, High Accuracy IMU and IMU for launchers. The Micro/Nano IMUs require a mass < 10 g, a power consumption < 1 W, gyro bias stability of 5 °/hr and an angular random walk of 0.1 °/√hr. The research on the high accuracy IMUs target to a power consumption < 10 W, gyro bias stability from 0.1 to 1 °/hr and an angular random walk from 0.003 to 0.01 °/√hr. The IMUs for Launchers are directly managed by common core launcher development, and the main requirement regard a very large immunity to the vibrations, to which the IMU is subject during the initialization phase. A classification of the aforementioned IMUs, according to the mission suitability, is reported in Tab. 2.1.

2.2 Gyroscope classification and market

The gyroscope has a large variety of Space applications, which impose different requirements on the sensor. The main gyro performance parameters, which are used to specify the application requirements, are the resolution, the bias drift and the Angle Random Walk (ARW), discussed in the Appendix A.

According to the performance parameters, the gyros are grouped into three main performance classes, including high, medium and coarse gyros, whose key features are reported into Tab. 2.2.

The other important features are the mass, the consumption, the lifetime (5-15 years under radiation environments), the cost, interface (1553 or RS422) and the rate range (± 20°/s).

The market for high performance gyros (class: 0.001 to 0.01 °/hr) is limited to the missions requiring very accurate pointing or stability requirements, e.g. Science, Earth Observation missions. About this class, the market is therefore expected to grow slowly to around 3 units per year. Future LEO missions are demanding continuous improvement of geolocation performance. Although the GNSS performance is expected to significantly improve with the introduction of new signals, the absolute localisation relies on GNSS receiver accuracy and star tracker accuracy. Relative navigation requires higher relative pointing performance which can be achieved by high precision gyros, but also by improvement of gyro defects estimation and by using image correlation techniques. In the worldwide market, the two very high-performance gyros available space qualified are the *SIRU* by Northrop-Grumman [28] (0.001 °/hr class of performance) based on the Hemispherical Resonator Gyroscopes (HRG), and the Airbus *Astrix-200* [29], based on a Fiber Optic Gyroscope (FOG). Honeywell has developed of a high performance IMU named *HG9900* [24], whose very high mass, power and price of the unit mean make it is suitable for only a small number of missions.

The market is wider for medium and low performance gyro (class: 0.1 to >5 °/hr), which can fulfil the functions of rate damping, Earth or Sun acquisition, slew manoeuvres, safe mode or coarse navigation. Most of the missions, i.e. Science, GEO Telecom, LEO and MEO satellites, rovers, widely use such a gyro, thanks its cost. As a result, it is expected that the trend for the coming years will be a slow reduction in the market for the medium accuracy class and an increase for the low accuracy (lower price) class.

Tab.2.2. Gyro classification, in terms of bias stability and angle random walk.

	Bias stability [°/hr]	**Angle random walk [°/√hr]**
Coarse	> 1	Don't care
Medium	> 0.01, < 1	> 0.001
High	< 0.01	< 0.001

The total annual market for European suppliers of the combined medium and low class is expected to be between 8 and 10 flight sets per year. As a flight set is typically 2 units, this means a total of between 16 and 20 units per year.

About the commercial products, Honeywell developed the *MIMU* [30] (0.01 °/hr class of performance), based on Ring Laser Gyroscope (RLG) technology. They captured a large market by selling this gyro in aeronautical applications. This large volume of sales proposes the *MIMU* at an attractive price for Space applications and have been selected for several ESA missions [9, 25-27]. The *Regys-20*, based on a HRG and developed by Sagem, is now flying and compares well on mass and lifetime to the *MIMU* but struggles with respect to performance (0.5 °/hr) [31]. Into the European Scenario, Thales Avionics proposed *Quasar 3000*, based on RLG, which is mounted on launchers *Ariane V* and *Vega* [32]. Airbus has also developed a medium accuracy version of its Astrix FOG product line, called the *Astrix 1000* series [33]. This series is intended to include an accelerometer equipped version for providing a complete European IMU solution.

In the low-class gyros, the MEMS solutions play an important role, proposing sensors and actuators optimized for microsats with significant improvement than more robust star trackers and higher performance gyro. The key of the MEMS success is the cost. As low-class gyroscope, within Europe there are development of low-cost MEMS gyros, which assemble a MEMS detector element with a front-end ASIC, as *STIM300* by Sensonor [34]. Northrop-Grumann developed the coarse *LN200S* gyro which was based on FOG technology [21]. This is a low performance, low cost product mainly targeted at the military market.

The comparison of the most performing commercial gyroscope is reported in Tab.2.3.

2.3 Gyroscope technologies

As previously described, the market sectors are dominated by RLGs and FOGs, both based on the Sagnac effect, whose operation is reported into the Appendix B, and the HRGs, based on the Coriolis force [12-13].

Tab.2.3. Comparison of gyroscope devices currently in the market [21, 24, 28-31, 34].

Name of item	Company	Country	Gyro features
SIRU [28]	Northrop-Grumann	USA	HRG-based Bias < 0.0015 °/hr ARW < 0.00015 °/√hr
Astrix-200 [29]	Airbus	Germany	FOG-based Bias < 0.0005 °/hr ARW < 0.0001 °/√hr
HG9900 [24]	Honeywell	USA	RLG-based Bias < 0.0035 °/hr ARW < 0.002 °/√hr
MIMU [30]	Honeywell	USA	RLG-based Bias < 0.005 °/hr ARW < 0.005 °/√hr
Regys-20 [31]	Sagem	France	HRG-based Bias < 0.5 °/hr ARW < 0.02 °/√hr
LN-200S [21]	Northrop-Grumann	USA	FOG-based Bias < 1 °/hr ARW < 0.07 °/√hr
STIM300 [34]	Sensonor	Norway	MEMS-based Bias < 0.3 °/hr ARW < 0.15 °/√hr

RLGs are robust devices, with no moving part, performing high insensitivity to vibrations and temperature gradients, a digital output, a wide dynamic range and a good reliability. These features allow high performance, i.e. resolution below 1°/hr and bias drift better than 0.1 °/hr. The RLG configuration includes either a triangular or a squared bulk optical cavity, with a high-quality mirror at each corner, where a gaseous gain medium, e.g. He-Ne mixture or Nd:YAG, sustains the excitation of two optical waves propagating in the two opposite directions and a high voltage is applied to ionize the gaseous medium. According to the Sagnac

effect, the rotation of the device involves a difference between resonance frequencies, proportional to the sensor angular rate Ω.

A portion of each wave is extracted by a partially reflective mirror and sent to the read-out system that includes a prism. Two extracted beams are combined at the prism and a photodetector array is used to produce a fringe pattern. Since the fringe pattern moves on the detector array surface in a direction depending on the sense of rotation, it is possible to determine the sign of the rotation rate and the angular velocity can be estimated by counting the intensity maxima in the fringe pattern.

The FOG is a fiber-based phase sensitive device where the phase shift between two counter-propagating waves is detected. Although its performance is similar to that of RLGs, i.e. bias drift ranging from 0.001 °/hr to 1 °/hr and resolution from 0.01 °/hr to 10 °/hr, FOGs cannot be extensively used for aircraft inertial navigation, caused by its high sensitivity to external perturbations, i.e. vibration transients, thermal and stress perturbations. The basic FOG configuration consists of a beam splitter, used to split the light from a light source into two different counter propagating beams, a long fiber coil, where the propagating beams are coupled, an external beam splitter, where the beams are recombined, and a photodetector, that receive the optical signal resulting from the beams interference. The phase shift between two counter-propagating waves is proportional to the sensor angular rate Ω. The minimum detectable angular rate $\delta\Omega$ is equal to:

$$\delta\Omega = \frac{c \cdot \lambda}{4 \cdot R \cdot L} \sqrt{\frac{BW \cdot h \cdot c}{\eta \cdot \lambda \cdot P_{pd}}} \times \frac{3600 \times 180}{\pi} \qquad [°/\text{hr}] \qquad (2.1)$$

where R is the outer fiber radius [m], L is the coil length [m], λ is the operating wavelength [m], P_{pd} is the average optical power at the input of the photodetector [W], η is the photodetector efficiency [a.u.], BW is the sensor bandwidth [Hz], h is the Planck constant [J · s] and c is the light velocity in vacuum [m/s].

Another kind of high-class gyroscope is the HRG. The sensing element is a quartz hemispherical resonator with extremely high-quality factor (< 26 million). Without rotation, the driving electrodes are used to excite a standing wave in the rim of the hemispherical resonator. In presence of rotation around the axis of the rim, nodes of the standing wave rotate of an angle proportional to the rotation rate.

Although its performance is excellent, the main drawbacks of this device are the large volume (thousands of cm^3) and the high cost.

RLGs, FOGs, and HRGs are expensive very powerful bulk sensors, having weight, size, and power consumption incompatible with some emerging applications as micro/nano satellites. The development of high-performance, small, low-cost miniaturized gyroscope is motivating an increasing research effort. In particular, the main approaches reported in literature regard the improvement of MEMS gyro performance, the development of micro-gyros based on Nuclear Magnetic Resonance (NMRG), and the miniaturization of photonic gyros by using integrated optical technologies, forming the so-called gyroscope on chip. While the improvement of MEMS gyro is still open, the NMRG, which exploits the shift of the Larmor precession frequency of nuclear spins to sense rotation, require a complex fabrication technique, showing also high sensitivity to magnetic fields. An integrated approach-based gyro performs high immunity to electromagnetic interference, with good hardness to harsh environment, and it is considered as the most promising gyroscope for the future Space missions [35].

2.3.1 Gyro-on-chip: Semiconductor Ring Laser

Among the gyro-on-chip, an active optoelectronic gyroscope, using a Semiconductor Ring Laser (SRL) as the source and the sensing element, was first proposed in [36] in the middle of 1980s.The architecture of active integrated optical gyros includes a SRL and some read-out optoelectronic components. When the gyro rotates, counter-propagating beams, generated within the laser, exhibit a frequency difference, which is proportional to the angular rate. This shift can be measured by the read-out optical circuit.

The basic requirements for SRL to be used in medium-high performance (resolution < 5 °/h, ARW < 0.02°/√hr) optical gyroscope are: laser radius at least in the range of millimetres, narrow linewidth of lasing emission and single longitudinal mode operation. A fully integrated active optical gyroscope based on a Multi Quantum Well (MQW) SRL operating at 845 nm has been proposed, designed and accurately modelled in [37-38] (Fig. 3.1 (a)).

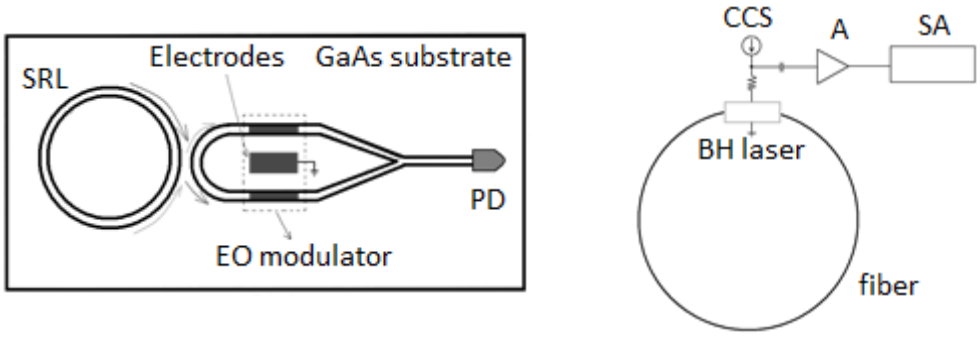

(a) (b)

Fig. 2.1. SRL-based gyroscope ([38] for (a), [39] for (b)), (*EO*: electro-optic; *PD*: photodiode; *BH*: buried heterostructure; *CCS:* constant current source; *A*: amplifier; *SA*: spectrum analyzer).

The gyro, designed to be integrated on a 15 mm wide and 3 mm long GaAs substrate, includes a GaAs/AlGaAs MQW circular SRL, with a radius of 1.5 mm; a curved directional coupler, with bending radius of 150 μm and coupling efficiency around 0.2 %, which extracts the optical beams from the SRL; an electro-optic phase modulator inducing a π/2 phase shift between the two optical signals coming out from the laser; a Y-junction enabling the interference of the two optical signals coming out from the laser; a photodetector (PD) located at the output of the Y-junction. When the sensor rotates with respect to the axis perpendicular to the substrate, the two beams with different frequencies interfere in the Y-junction so the optical signal at the output of the Y-junction has an amplitude oscillating with a frequency which is equal to the rotation-induced frequency shift. Device angular rate can be estimated by measuring the frequency of the output electrical signal generated by the photodiode. Critical aspects of this fully integrated optoelectronic sensor are the mode competition and the lock-in effect: for low angular rate values, the frequency difference between counter-propagating optical waves vanishes because of the coupling between the beams due to waveguide sidewalls roughness.

The detection of the frequency shift due to Sagnac effect by measuring the spectral components of the voltage signal between the terminals of an SRL has been explored in [39] (Fig. 2.1(b)). The experimental setup consists of an InGaAsP/InP Fabry-Perot laser, a single mode fiber, that form, with the laser, a 3.6 m long active ring resonator, and the laser driving circuit has been used. When the system rotates, a peak in correspondence of the beat frequency appears in the spectrum of the voltage signal.

Unfortunately, the minimum detectable angular rate of this angular rate sensor is around 100 °/h, limited by the lock-in effect.

A photonic integrated circuit (PIC) for rotation sensing based on two SRLs has been proposed and fabricated in [40]. The integrated device includes two unidirectionally operating racetrack-shaped SRLs, having a MQW and a quantum dots active region; two directional couplers with a reduced efficiency (~1%) which extract the optical beams from the SRLs; a Y-junction which combines CW and CCW waves; seven photodetectors used to monitor device performance. The spectrum of the photocurrent at the output of the Y-junction exhibits a peak at 12.2 GHz, with a linewidth of about 4 MHz) generated by the two optical signals with different frequencies that come into the Y-junction. In the last few years, the research effort on the SRL-based gyro was quickly decreasing due to the its aforementioned critical aspects, as the lock-in and the mode competition.

2.3.2 Gyro-on-chip: Resonant Micro Optical Gyroscope

The configuration of a Resonant Micro Optical Gyroscope (RMOG) consists of a narrow linewidth laser source, a high-Q Ring Resonator (RR), an optoelectronic processing unit, two photodetectors and an electronic read-out unit, as shown in Fig. 2.2. The OE processing unit generates two beams, that travels into the RR as clockwise and counter clockwise [13].

The rotation rate is measured by the difference between the resonance frequencies of the two counterpropagating beams injected into the high Q ring resonator. Thus, the resolution of the rotation rate $\delta\Omega$ strictly depends by the shot noise of the photodetectors and could be expressed as:

$$\delta\Omega = \frac{1}{d \cdot Q \cdot \sqrt{P_{pd}}} \sqrt{\frac{2 \cdot h \cdot c^3}{\tau_{int} \cdot \eta \cdot \lambda}} \times \frac{3600 \times 180}{\pi} \qquad [°/\text{hr}] \qquad (2.2)$$

where d is the diameter of the ring resonator [m], Q its quality factor [a.u.], λ is the sensor operating wavelength [m], τ_{int} is the sensor integration time [s] ($=1/BW$).

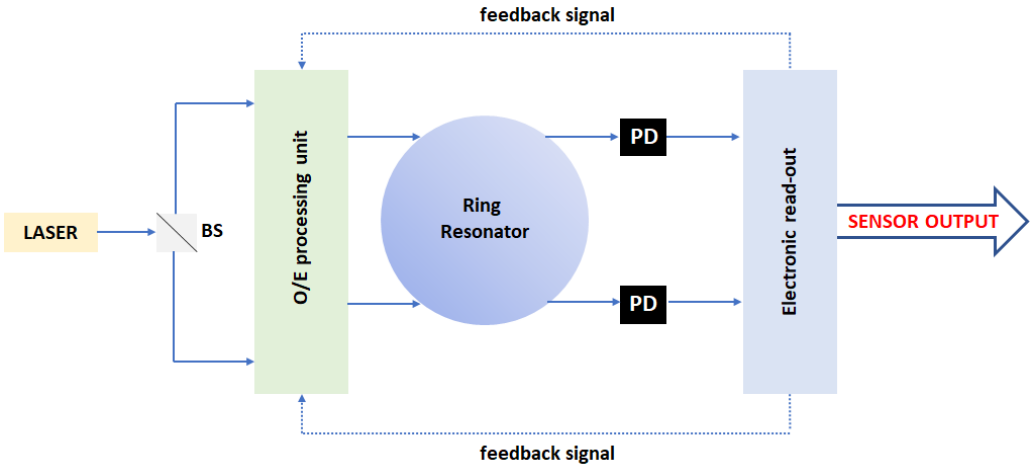

Fig. 2.2. Resonant Micro Optical Gyroscope (RMOG) architecture, (*BS:* beam splitter, *PD:* photodetector).

In addition to the unavoidable shot noise limit, the RMOG operation is affected by the polarization fluctuations of the two modes propagating in the resonator, the backscattering effect, and the Kerr effect [35].

The key element of the RMOG system is the ring resonator that strongly influences the gyro sensitivity. High resolution could be obtained by using ultra-high Q-factor ($> 10^7$). Very high Q-factor ring resonator could be implemented by using a discrete, i.e. fibers or crystals [41-47], or integrated approach, i.e. planar ring resonator [48-51].

In the fiber-based RMOGs, called as Resonant Fiber Optic Gyroscope (RFOG), the sensing element is a high-Q ring resonator that can be made by either a convectional fiber, typically a polarization maintaining fiber [41] or a hollow-core photonic crystal fiber [42-44]. The resonator, when properly excited, supports two counter-propagating resonant modes, which have the same resonance frequency when the sensor does not rotate. When the rotation rate $\Omega \neq 0$, the resonance frequencies are different and, according to the Sagnac effect, their resonance frequency difference is proportional to Ω. The resonator configuration including the ring coupled to just one fiber, is reported in Fig. 2.3. Since the RFOG operation requires the simultaneous excitation of two resonant modes within the cavity, the exciting beams are launched at the two ends of the fiber coupled to the resonator.

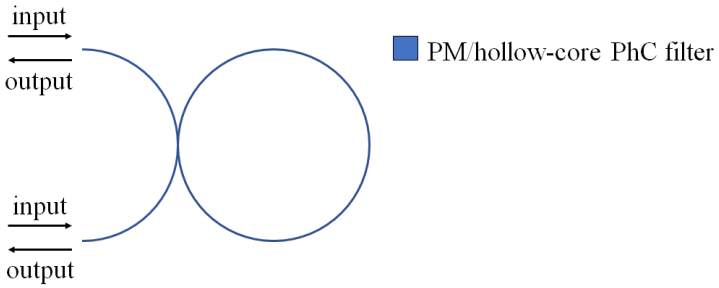

Fig. 2.3. Resonant Fiber Optic Gyroscope (RFOG).

In 2014, T. Qiu *et al.* proposed a gyroscope based on a ring resonator made by a PM fiber, having a length of 19 m and a coil diameter of 11.5 cm [41]. The device shows a bias drift of 0.1 °/h and an ARW of 0.008 °/√hr.

In 2016, I. Fsaifes, *et al.,* proposed the use of hollow-core photonic crystal fiber for the ring resonator [44]. It consists of a hollow-core photonic crystal fiber -based ring resonator having a length of 25 m and a coil diameter of 7 cm. A *Q*-factor of $4x10^8$ has been measured, and then, a theoretical value of the the shot-noise limited resolution of a gyro based on that RR is < 1 °/h has been calculated.

The main drawback of the gyro based on a fiber RR regards the volume. The volume of a 1-axis gyro based on a fiber RR is > 100 cm^3 and a further reduction of the gyro size is difficult because the resolution depends on the area enclosed by the resonant path and, therefore, cannot be strongly reduced and sub-centimetric coils would increase the bending losses, reducing the resonator quality factor and so worsening the resolution.

A packaged gyro based on crystalline Whispering Gallery Mode (WGM) resonator is commercialized by OEwaves [45]. The device shows a bias drift of 3°/hr and a resolution of 5 °/hr, taking into account a bandwidth *BW* of 20 Hz, in a very small volume (> 10 cm^3). A photograph of the device is reported in Fig. 2.4. The light is coupled to the resonator by a prism thus the gyroscope includes several microphotonic components assembled on a board. The high *Q* resonator is made by a CaF_2 crystal and it is an oblate spheroid with a diameter of 4.5 mm, a thickness of 0.5 mm and a diameter of sidewall curvature of 32 µm.

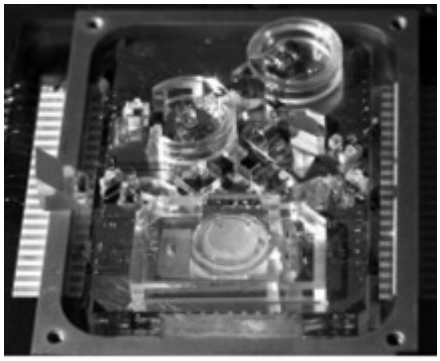

Fig. 2.4. Photograph of CaF_2 WGM resonator -based gyroscope [45].

In contrast to silica-based microsphere [46-47], the optical loss of fluorite-based device is limited only by the material attenuation, not by the surface scattering. A quality factor of the order of 10^{11} has been demonstrated for this WGM optical cavity [45].

In order to realize a volume and cost-effective gyroscope, planar ring resonator as sensitive element has been investigated both theoretically and by benchtop demonstrators including a packaged/fiber pigtailed resonator designed for gyro applications and other packaged/fiber pigtailed Commercial Off-The-Shelf (COTS) optoelectronic/photonic components [48]. In this approach, all gyro optoelectronic/photonic components can potentially be integrated on a single chip and the volume of a 1-axis gyro can be of the order of 1 cm^3.

High Q values can be achieved by reducing ring resonator loss, mainly propagation loss and scattering loss due to roughness in waveguide sidewalls. This motion sensor can be manufactured by using different technologies for each component: hybrid or monolithic integration.

In the hybrid integration, it is possible to choose, for each component, the technology that assures the best performance, but the alignment of all components is difficulty and the loss is larger. The best technology platforms for the fabrication of low loss resonators are silica-on-insulator [49] and silicon nitride technology [50-52]. In [49], measured propagation loss of a phosphorous doped silica-on-silicon ring resonator having a diameter of 6 cm, is equal to 0.85 dB/cm and the resulting Q-factor is equal to 2.3×10^7. Benchtop gyro demonstrator based on a silica-on-silicon ring resonator with a diameter of 6 cm and a Q-factor of 1.4 x 10^7 has been deployed by the Feng's group [53-54]. The gyro performs a bias drift of 0.013 °/hr

with a resolution = 200 °/hr (*BW* = 20 Hz). High-*Q* Si_3N_4 ring resonators on silicon substrate have been reported in [52]. For a ring resonator with 7 μm core width, 45 nm core thickness, and 9.8 mm ring radius, a loaded *Q*-factor of 3.5×10^7 at 1550 nm has been measured, and the intrinsic *Q*-factor resulted to be 5.5×10^7 [52]. The theoretical value of the shot-noise limited resolution of a gyro based on this planar ring resonator is less than 1 °/hr. Recently, a very innovative CMOS-compatible technological platform allows the hybrid integration on a silicon substrate of III-V optoelectronics components, e.g. lasers and photodiodes, and passive photonic devices, e.g. ring resonators or arrayed waveguide gratings (AWGs), based on an ultra-low loss Si_3N_4 waveguide [55].

Moreover, also microtoroids and wedge resonators have demonstrated very high *Q*-factor. In particular, Lee *et al.* [56], have experimentally demonstrated an ultra-high *Q*-factor equal to 8.75 x 10^8, for a wedge resonator with a diameter of 7.5 mm, with a fiber used as bus. A monolithically integration demonstration of a wedge resonator and a bus straight waveguide on a silicon is reported in [57] (Fig. 2.5).

A thermal silica-based wedge resonator, with a diameter of 4.3 mm, coupled to SiN waveguide as bus, has been demonstrated to have $Q = 1.20\times10^8$ and 2.05×10^8, for the TE and TM mode, respectively.

Monolithically integrated gyroscopes are surely more robust, compact, less power consuming and immune to external disturbances, as vibrations. The technology platform to pursue this approach is represented by the indium phosphide (InP), compliant to the technology platforms available for the other RMOG devices, as laser and photodiodes [58].

Fig. 2.5. SiO_2 wedge resonator and a SiN waveguide as bus [57].

Although ring resonators have been demonstrated both in $In_{1-x}Ga_xAs_yP_{1-y}$/InP and in GaAs/$Al_xGa_{1-x}As$ system, the research effort has been focused on the InP based material since it exhibits lower loss.

In 2013, C. Ciminelli *et al.* [59] demonstrated for a Fe-doped InGaAsP rib waveguide on an InP substrate a propagation loss value of 0.45 dB/cm. The ring resonator based on this technology with a radius of 13 mm performs a *Q*-factor in the order of 10^6. A radiation test of this device is reported into the Paragraph 3. The propagation loss and, then the *Q*-factor, has been improved by using a shallow InGaAsP/InP waveguide with Zn-diffusion. A propagation loss equal to 0.3 dB/cm and to 0.4 dB/cm have been measured, for TE and TM polarization, respectively [60-61].

For gyro applications, a benchtop gyro demonstrator, based on the InP ring resonator reported in [59], has been proposed in [62]. The demonstrator consists of a RMOG with an open loop configuration based on the phase modulation. For the system test, the sensor rotation has been simulated using two properly driven acousto-optic modulators, with a theoretical value of the shot-noise limited resolution of 10 °/hr, taking into account BW=1 Hz, η=0.9 and P_{pd}=10 mW. The integration of active and passive devices on a single chip is currently a very hot R&D topic, and some demonstrators have been proposed in the last few years.

In order to improve the *Q*-factor of the planar ring resonator, to fulfill the requirements of high-class gyroscope, an innovative configuration of RR, for RMOG gyro configuration, will be discussed into the Paragraph 3. It exploits the slow-light effect by integrating a one-dimensional photonic crystal along the whole ring resonator optical path. An improvement of the *Q*-factor more than 3 order of magnitude respect to a simple ring resonator with same footprint has been demonstrated in [63], theoretically performing a gyro resolution of about 0.01 °/hr.

2.3.3 Gyro-on-chip: emerging technologies

Optical gyroscopes based on the Sagnac effect suffer from a low signal-to-noise ratio, generally limited by thermal fluctuations, component drift and fabrication mismatch. Furthermore, their sensitivity is limited by the Kerr effect,

unequal thermal fluctuations between clockwise and anticlockwise propagating light, and Rayleigh scattering [13]. To improve the sensitivity, reducing the aforementioned harmful effects, in the last decades, several gyro configurations have been proposed in literature, based on the reciprocal sensitivity enhancement [64], integrated interferometry [65-66], Brillouin effect [67-68] and non-Hermitian degeneracies (parity-time symmetry) [69-70].

A gyroscope with reciprocal sensitivity enhancement architecture is shown in Fig. 2.6 [64]. The key sensing elements consist of two silicon-based ring resonators with radius of 500 μm. Unlike the standard approach, the light signal from a low-linewidth distributed feedback laser (DFB) is switched alternatively between the clockwise and anticlockwise propagation. Each ring sustains only one propagation direction. The switching allows to avoid the power exchange between the two counterpropagating beams. Furthermore, since the temperature fluctuations only manifest significantly above the microsecond timescale, temperature fluctuations can be filtered out, by switching the feed direction of the beams at a frequency on the order of MHz.

To switch the direction in which the rings are fed, a Mach–Zehnder interferometer (MZI), formed by two p–i–n diodes and a 50/50 directional coupler, is used. Two phase detectors, which consists of a Y junction and a photodiode, are connected to the ring resonators outputs. Each current is converted to voltage and amplified, by using a transimpedence amplifier (TIA) and a variable gain amplifier (VGA), respectively. The signals are then added together and multiplied by a reference frequency through a passive mixer, extracting the rotational rate information.

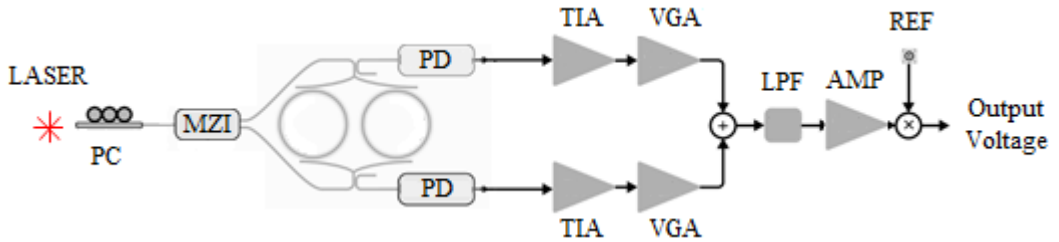

Fig. 2.6. Schematic of the nanophotonic optical gyroscope based on reciprocal sensitivity enhancement [64], (*PC*: Polarization Controller, *MZI:* Mach-Zehnder Interferometer, *PD*: photodiode, *TIA:* TransImpedence Amplifier; *VGA:* Variable Gain Amplifier, *LPF*: Low-Pass Filter, *AMP:* amplifier, *REF*: voltage reference).

The device has been experimentally characterized by using a switching speed of 20 kHz and 10 MHz. At a switching frequency of 20 kHz, a bias instability of 2,268,000 °/hr and an ARW of 97,800 °/√hr has been measured; instead, 10 MHz switching frequency resulted in a bias of instability 21,600 °/hr and ARW = 650 °/√hr.

Another trend of research is based on the interferometric optical gyroscopes with an integrated approach. This research boost is motivated by the high versatility of use of FOG, that can be used for low cost, smaller area industrial rate grade sensors and expensive large area strategic or precision grade devices to be used in IMU systems. The main goal regard the reduction of the sensitive element while maintain high sensitivity. While the cost and the complexity of assembling high quality fiber requires a high precision alignment and the assembly of discrete components, Gundavarapu *et al.* [66] proposed, for the first time, a large on-chip coil lengths based on Si_3N_4 based ultra-low loss waveguide, with the capability to integrate all the devices of the gyro architecture on the same chip. The architecture of the proposed gyro is reported in Fig.2.7, using a broadband source in order to minimize the loss of scattering and reflections.

The sensitive element consists of a long coil with a length of 3 m, an outer radius of 20 mm, an inner radius of 17.25 mm and a total area of 278 cm^2. An ARW, a resolution and a bias drift of 8.5 °/√hr, 66 °/hr and 59 °/hr, have been measured, respectively.

A new class of micro-optical gyroscope that uses counterpropagating Brillouin laser cavity, to measure the rotation as a frequency shift, has been demonstrated in [67].

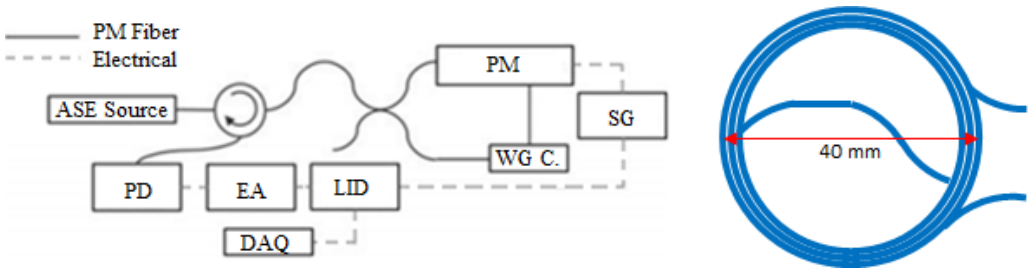

(a) (b)

Fig. 2.7. Interferometric Optical Gyroscope architecture (a), based on a Si_3N_4-based coil (b) [66], (*PD*: photodiode, *EA*: electrical amplifier, *LID*: lock-in amplifier, *WG:* waveguide, *WG C*: waveguide coil, *DAQ:* Data AcQuisition, *SG*: signal generator).

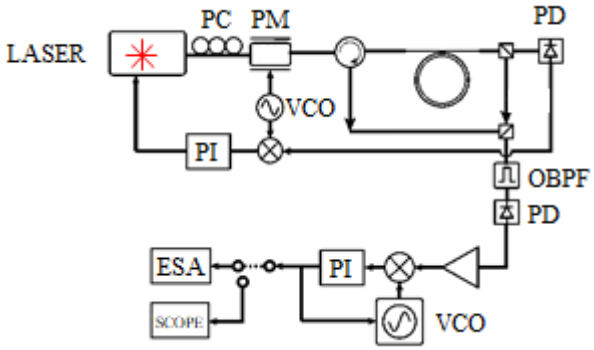

Fig. 2.8. Brillouin-based gyroscope architecture [67], (*PC*: polarization controller, *PM:* phase-modulator, *PI:* proportional integral servo, *OBPF*: optical band-pass filter, *ESA:* electrical spectrum analyzer, *VCO:* voltage-controlled oscillator, *PD*: photodiode).

The laser cavity consists of an ultra-high Q resonator in silicon on silicon technology platform. A detailed scheme is reported in Fig. 2.8. The optical pumping in the clockwise direction induces Brillouin laser action, which results in cascaded odd counter-clockwise and even clockwise order Stokes lasers. The laser pump is locked to a microcavity resonance using a Pound-Drever-Hall lock. These lasing modes experience opposing Sagnac frequency shifts. The second order and third order co-lasing Stokes frequency experience opposite Sagnac frequency shifts. They are coupled onto a photodetector using a circulator and a bidirectional coupler. As shown into the blue box of Fig.2.8, after filtering, the detection of the beat frequency of these co-lasing signals, followed by a frequency-to-voltage readout, provides the rotation sensing.

In 2017, Vahala's group demonstrates a resolution of 22°/hr by using a microdisk resonator with a diameter of 18 mm and an intrinsic Q-factor of 1.26×10^8 [67]. The resolution value has been furtherly improved by the same group, by using a wedge resonator with an intrinsic Q-factor of 8.75×10^8 and a diameter of 36 mm [56]. In particular, the Earth rotation rate (≈15°/h) has been measured with a bias drift < 4°/h [68].

2.3.4 Gyro-on-chip: summary

A comparison of the most performing micro photonic-based gyroscope is reported in Tab.2.4. For the theoretical shot-noise limited resolution, the bandwidth

Tab. 2.4. Comparison of the most promising RMOG technologies [41, 45, 62, 64, 66-68].

Microphotonic gyros based on …	Volume [cm^3]	Theoretical shot-noise limited resolution [°/hr]**	Experimentally measured performance
Fiber RR [41]	> 100*	< 0.4	ARW = 0.008°/√hr Bias drift = 0.1°/hr
Crystalline WGM resonator [45]	> 10	< 0.004	Bias drift = 3°/hr Resolution = 5°/hr
InP-based RR [62]	≈ 4*	< 60	-
Double Si-based ring resonator [64]	> 0.01*	-	ARW = 650°/√hr Bias drift = 21,600°/hr
Si_3N_4-based coil [66]	≈ 10*	< 7	ARW = 8.5°/√hr Bias drift = 59°/hr Resolution = 66°/hr
SiO_2-based microdisk resonator [67]	≈ 3*	< 0.7	Resolution = 22°/hr
SiO_2-based wedge resonator [68]	≈ 8*	< 0.05	Bias drift < 4°/hr Resolution = 15°/hr

* estimated; ** BW=20 Hz, η=0.9, P_{pd}=10 mW in Eqs. (2.1) - (2.2).

BW of the signal has been supposed equal to 20 Hz, according to the typical system level specification of AOCS [62].

2.4. Space qualification

Before the flight, any electronic devices or systems must be "Space qualified", reaching a Technology Readiness Level (TRL) at least equal to 8. Qualification tests are conducted on flight-quality components, subsystems, and

systems to demonstrate that structural design requirements have been achieved. In these tests, the device should properly operate in the hostile operational environment, as the Space. In particular, the device should be radiation hard, and resistant to thermal shock and vibrations.

The Space radiation environment affects the operation of the spacecraft instruments and it represents a hazard for the success of a Space mission. The radiation dangerousness is strictly related to its intrinsic nature [71-72]. In particular, it is made by electrons, protons and heavy ions. Radiation can be either non-ionizing or ionizing, with low (< ~ 10 eV) or high (> ~ 10 eV) energy, respectively [73]. The ionizing radiation is substantially harder to shield out rather than the non-ionizing one. Several causes of the ionizing radiations in Space could be identified, including protons and nuclei of Galactic origin, called Galactic Cosmic Radiation (CGR), protons and nuclei emitted by Solar flares and Coronal Mass Ejections, also known as Solar Energetic Particles (SEPs), trapped protons in the Van Allen Belts [74]. According to the experimental results of the satellite-borne space mission in the *PAMELA* experiment [75] over three years, the measured total final ionizing radiation dose is equal to about 1 krad, resulting by a total dose related to the SEPs and CGRs equal to 0.5 krad and 0.4 krad, respectively [76].

The ionizing rays are classified in α, β and γ rays, in terms of penetration capability and related energy. In particular, although the ionising ability of gamma rays is less than other ionizing rays, they could undermine even permanently the correct operation of a device, thanks their large capability of penetrating into the shield. A gamma radiation is a ionizing radiation, made by photons with an energy from a few keV to ~8 MeV. When a gamma ray passes through matter, the probability for absorption is proportional to the thickness of the layer, the density of the material, and the absorption cross section of the material. As it passes through matter, gamma radiation ionizes via three processes: the photoelectric effect, Compton scattering, and pair production [77-78]. The photoelectric effect happens when gamma photon interacts with and transfers its energy to an atomic electron, causing the ejection of that electron from the atom. The photoelectric effect is the dominant energy transfer mechanism for gamma ray photons with energies below 50 keV. The Compton scattering shows the interaction between an incident gamma

photon and an atomic electron, causing its ejection, with the remainder of the original photon's energy emitted as a new, lower energy gamma photon. Compton scattering and the pair production are the principal absorption mechanisms for gamma rays in the intermediate energy range 100 keV to 10 MeV and for energy over 5 MeV, respectively. By interaction with the electric field of a nucleus, the energy of the incident photon is converted into the mass of an electron-positron pair. The annihilation of positron-electron produces two gamma photons of at least 0.51 MeV energy each (or higher according to the kinetic energy of the annihilated particles) [79].

The operation of on-board electronics could be degraded or permanently damaged by each physical radiation process or the combination of some of them. In literature, several papers have demonstrated the performance degradation of the electronic devices [74, 80-81]. As example, the degradation of a transistor performance when exposed to gamma radiation is caused by the damaging ionizing effect, resulting in a change of the carrier's concentration and then a change of the device features, as the voltage threshold for the transistor [81].

The improvement of the radiation hardness of the on-board instruments is a hot R&D topic, because no replacement is possible once the instruments are in orbit. A photonic approach could help in achieving higher radiation resistance, together with the well-known advantages with respect to the electronics, as small size, robustness, high degree of integration and costs potentially lower [82].

The effect of ionizing radiation in Space on discrete optics (as LEDs, laser sources) [83-89] and on fiber optics [90-92] has been widely investigated. The performance are mainly affected by a non-ionizing damage, resulting by the Compton scattering, while, the operation of optical fibers and fiber-based components, e.g. fiber Bragg gratings, under ionizing radiation is affected by radiation-induced densification/compaction that causes refractive index changes [91, 93], involving an increase of the losses and to a shift of the operating wavelength [94].

Since the ring resonators have been widely used as fundamental components of integrated photonic circuits, such as for optical filtering, frequency comb generation and sensing, the radiation impact on their performance in Space

applications is of strong interest [85-88]. As reported into the Paragraph 2.3.2, the gyroscope performance of ring resonator-based RMOG is strictly related to the *Q*-factor of the ring, which depends on the intrinsic optical loss due to the absorption as well as the operating wavelength that could be affected by the gamma radiation. The radiation involves a Compton scattering and, in turn, the change of the refractive index and of the optical losses [87]. The effect of radiation has been investigated in ring resonators based on silicon [86-88] and silicon nitride [85]. The silicon hardness to radiation has been evaluated for Si ring resonator with *Q*-factor ranging from 5 x 10^3 to 3 x 10^4. In 2005, Dumon *et al.* [87] have experimentally demonstrated a linear blue shift of the resonance of a Si-based ring resonator ($Q \approx$ 5 x 10^3) with a slope of 0.33 pm/krad, and a decrease of the optical power of about 8 dBm, with a total absorbed dose of 300 krad. Moreover, recently, Ahmed *et al.* [88] have demonstrated that for ring resonators with *Q*-factor > 5 x 10^3, the free spectral range, the *Q*-factor and the peak position not show a dose-dependent change. Immunity to radiation has been also explored for silicon nitride-based ring resonators, demonstrating a negligible shift of the operation wavelength and the variation of the resonance *Q*-factor (from 10^6 to 0.5 x 10^5), after a proton radiation up to about 100 MeV [89].

For the first time, in order to confirm the suitability of InP technology for Space applications, radiation test on an InGaAsP/InP ring resonator, used as sensitive element into a *RMOG*, has been carried out at the *Co60* facility at ESTEC [95].

2.4.1 Optical characterization of the InGaAsP/InP ring resonator

The device under test consists of an InGaAsP/InP-based ring resonator with radius R = 13 mm, as shown in Fig. 2.9(a). The InGaAsP/InP waveguide has a rib profile, with a thickness $t_{wg,}$ = 0.3 μm and a width, w_{wg} = 2 μm, formed on a 0.7 μm thick slab layer. According to [96], the quasi-*TE* mode supported by the waveguide exhibits a confinement factor of about 80 % and propagation loss values in the range 0.5 ÷ 0.8 dB/cm.

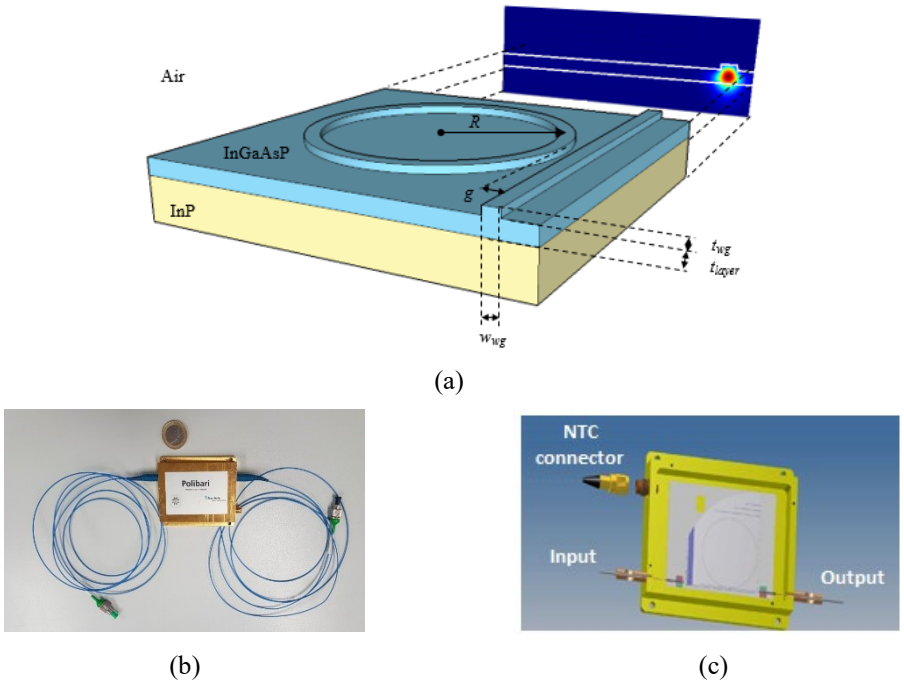

Fig. 2.9. (a) Schematic of the InGaAsP/InP ring resonator under test, with the map of the electric field of the TE_0 inside the bus waveguide; (b) packaged device under test; (c) schematic of the packaged device (R: radius, w_{wg}: waveguide width, g:gap, t_{wg}: waveguide thickness; t_{upper}: slab layer thickness). Reprinted with permission from [95] © The Optical Society.

The gap g between bus and ring resonator has been designed equal to 1.444 μm, aiming to obtain a coupling efficiency of about 52 %, then, a resonance depth of about 8 dB [97].

The details of the fabrication process of the InGaAsP/InP ring resonator can be found in [59]. In short, the ring resonator was manufactured by using a single standard lithography process. First, an InGaAsP layer was grown on the top of an InP substrate by using the metal-organic vapour-phase-epitaxy (MOVPE). The waveguide etching was realized using a thin Si_3N_4-based layer mask.

The brass packaged device, with single-mode fiber pigtails connected to the end tapered section of the bus waveguide, is shown in Fig. 2.9(b). A temperature transducer AD590 and a thermo-electric cooler (TEC) were placed above and beneath the resonator chip, respectively, to avoid resonance instability due to temperature changes. The packaged ring resonator is sketched in Fig. 2.9(c), where the two input and output Corning™ SMF-28 singlemode fibers (2 m long), and a NTC connector, as the TEC output, are shown.

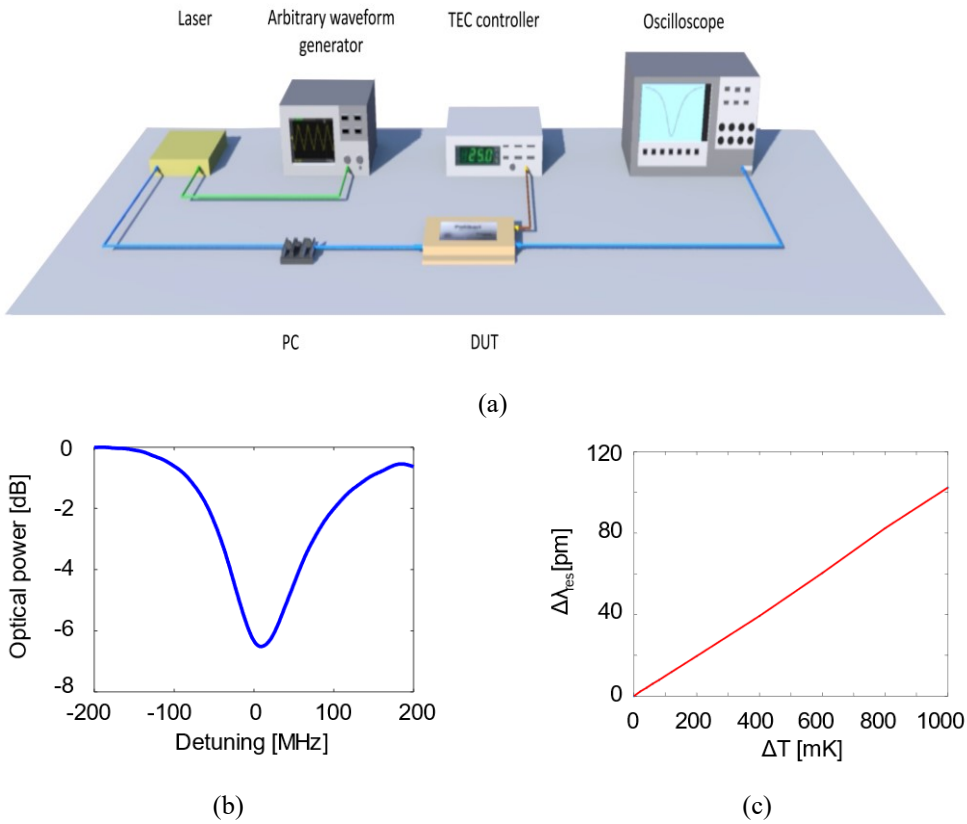

Fig. 2.10. (a) Overview of the measurement setup; (b) TE mode resonance spectrum; (c) Resonance detuning $\Delta\lambda_{res}$ when changing the chip temperature, (*TEC*: thermo-electric cooler, ΔT: temperature change, $\Delta\lambda_{res}$: resonance detuning). Reprinted with permission from [95] © The Optical Society.

The device under test has been experimentally characterized by using the measurement setup reported in Fig. 2.10(a). A single-frequency fiber laser (operating wavelength 1.55 μm), with a linewidth < 700 Hz and maximum output power of 30 mW, has been used as optical source. The laser wavelength has been tuned by using an external piezo-actuator, over a range of 400 MHz across the operating wavelength, to detect the resonance, by driving the laser through a triangle waveform with peak-to-peak amplitude and frequency equal to 20 V and 100 Hz, respectively. A polarization controller (PC) has been used to excite only the TE polarization state into the bus waveguide.

Figure 2.10(b) shows the TE measured transmission spectrum of the ring resonator (with a resolution of about 1.6 kHz), at temperature equal to 25.03 °C, with a typical Lorentzian shape and Fano behaviour [98], due to the ring backscattering. The resonance shows a $Q = 1.36 \times 10^6$ and $ER = 6.24$ dB for the TE mode at about 1550 nm, while, for the TM mode, $Q = 1.35 \times 10^6$ and $ER = 5.75$ dB

have been measured. This performance represents an improvement with respect the one reported in [96], having used more accurate instruments, i.e. in the experimental activity, the laser linewidth is about 2 orders of magnitude narrower than the one used in [96]. The achieved experimental results confirmed the capabilities to use the device as sensitive element in a RMOG configuration. In particular, by using the Eq. (2.2), a theoretical gyro resolution $\delta\Omega$ equal to about 42 °/hr has been estimated (with P_{PD} = 10 mW, η = 0.9, τ_{int} = 0.05 s).

Moreover, the temperature stability of the resonance has been simulated and measured, tuning the chip temperature in the range 25.03 °C – 26.03 °C, via the thermo-electric controller. The temperature change entails the effective refractive index change Δn_{eff}, and then, a shift of the resonance $\Delta\lambda_{res}$, according to:

$$\Delta\lambda_{res} = \frac{\Delta n_{eff} L}{m},\ m = 1, 2, 3, \ldots.. \qquad (2.3)$$

where L is the length of the ring resonator optical path [m] and m is the resonance order [a.u.] [99].

Performed measurements show a linear trend of the resonance shift $\Delta\lambda_{res,}$ changing the chip temperature, with a slope of 12 MHz/mK, as shown in Fig. 2.10(c), in good agreement with the simulated results (slope of about 13 MHz/mK) achieved by using the numerical approach reported in [100], taking into account the InGaAsP refractive index dependence by the temperature (InGaAsP thermo-optic coefficient equal to 2.3 x 10^{-4} [101]).

2.4.2 Experimental evaluation of the radiation impact on the InGaAsP/InP ring resonator

Since the γ-radiations are more dangerous than the other ionizing radiation, as described into the Paragraph 2.4.1, the evaluation of the radiation impact under γ- radiations represents a conservative approach in Space qualification of an optoelectronics component. The experimental activity was conducted following the steps provided by the European Cooperation for Space Standardization (ECSS) [102]. It represents a guide for testing electronic and optoelectronic devices under ionizing radiation. The radiation hardness evaluation of a device requires three steps: (a) irradiation step, to estimate the impact of the radiation on the device

performance; (b) annealing step, to estimate how the device responds to an absence of radiation, shutting down the radiation source; (c) overheating step, to clean the device from any charges present inside, especially in the oxide. Since the last step requires to insert the device under test in an oven at temperatures higher than 100° C, the overheating step has not been carried out, wanting to preserve the packaged device under test for future measurements.

In the framework of the NPI project of the European Space Agency, that sponsor the PhD activities, the radiation hardness evaluation of the InGaAsP/InP ring resonator has been conducted in the *Co60* facility at *ESTEC* [103]. The facility provides a *Co60* γ source that can radiate photons with energy of the order of 1 MeV. It consists of multiple small rods about 50 mm long placed around the periphery of a 30mm diameter cylindrical steel container. The γ beam produced by the *Co60* source is focused on the device under test through a collimator window. The experimental activity has been carried out with a dose rate of 99 rad/min of the collimated beam that irradiates the packaged ring resonator, placed at a distance of 52 mm from the irradiator. Only the device, sketched in Fig. 2.9(b), was placed in front of the collimator window, while the other instruments, reported in Fig. 2.10(a) were placed in the control room, shielded by the radiation, in order to avoid that the instruments sensitivity to the radiation could undermine the experimental measurements. A dosimeter has been used to measure the total absorbed dose, and its nominal value corresponds to the dose adsorbed into the water. The absorbed dose both in InGaAsP and brass results from the product of the dosimeter value and the conversion coefficients (0.793 for InGaAsP and 0.9 for brass). The source – device distance (52 mm) and the dose rate (99 rad/min) have been set taking into account the aforementioned conversion coefficients of InGaAsP and brass, the thickness of the brass layer placed over the ring resonator (≈ 4.5 mm), and the targeted total absorbed dose for the ring resonator (≈ 300 krad). The irradiation operation lasted about 68 hours with a total adsorbed radiation dose of ≈320 krad. According to [102], the irradiation activity is followed by an annealing activity lasted about 24 hours. It gives qualitative and quantitative indications of damage, in terms of performance, of the device under test.

A closed-loop measurement technique has been used, to measure the radiation effects on the resonance frequency, *Q* and *ER*. During the irradiation activity, the resonator resonance wavelength is kept-locked to the laser central wavelength, counteracting the radiation-induced shift with temperature one. The temperature change, imposed by the Peltier effect, driven by the TEC controller, counteracts the radiation shift. The resonance wavelength is real-time measured, and the temperature of the TEC controller is controlled to set to zero the resonance wavelength detuning. An indirect measurement of the radiation-induced shift has been carried out. In particular, since the resonance is shifted by changing the chip temperature (T_{chip}) and a linear relation λ_{res} vs. T_{chip} has been experimentally observed with a coefficient of about 12 MHz/mK (≈ 0.1 pm/mK), the resonance shift has been calculated by the chip temperature variation, controlled by the TEC controller (Thorlabs TED200) and useful to lock the resonance to the laser central wavelength.

The main error source in the measurements is the radiation-induced output current drift of the temperature sensor AD590, placed on top of the ring resonator in the package. The output current of the sensor AD590 decreases as the radiation dose increases, with a slope *S* of -0.04 μA/krad (± 7.5 %) for T_{chip} = 25 °C and a supply voltage of 5 V, as shown in Fig. 2.11. The dependence of *S* on the chip temperature is shown in Fig. 2.12. It shows that S increases as the sensor temperature increase, with a second order trend:

$$S[\mu A/krad] = -1.87 \cdot 10^{-6}\ T_{chip}^2 + 4.08 \cdot 10^{-4}\ T_{chip} + 3.097 \cdot 10^{-2} \qquad (2.4)$$

This systematic error has been compensated by a post-processing procedure, based on the assumptions that keeping constant the temperature of the sensor (green line in Fig. 2.11), the AD590 output current linearly decreases up to a dose equal to 3.25 kGy(Si), as experimentally demonstrated up to 0.35 kGy(Si).

The linear trend of AD590 vs. total adsorbed dose is compliant to data available in literature, where a linear trend over 0.35 kGy (Si) has been demonstrated [104]. The compensation of this error source allows a significant reduction of the measurement uncertainty. The measurements are affected also by the accuracy of the TEC controller. It has an accuracy of ± 0.1 °C, within the –

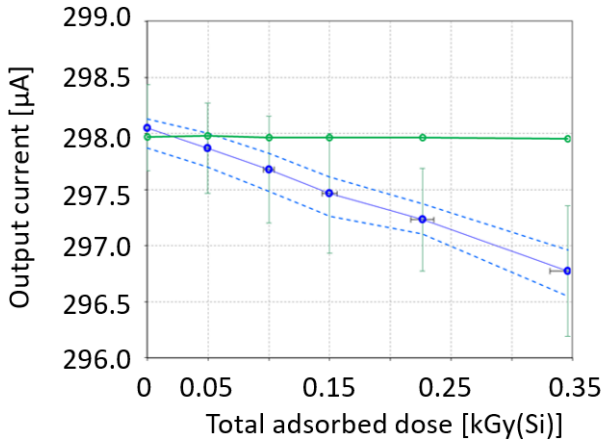

Fig. 2.11. AD590 output current (blue line) *vs* total absorbed dose. An output current = 298 µA guarantees a chip temperature equal to 25.0 °C, used as reference (supply voltage = 5 V). The dotted blue lines are referred to the maximum and minimum measured value. The green line is referred to the constant temperature of the chamber, where the measurements are carried out. Reprinted with permission from [95] © The Optical Society.

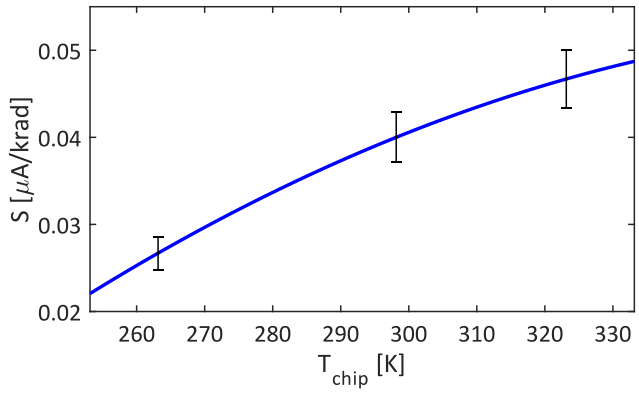

Fig. 2.12. *S* [µA/krad] vs T_{chip} [K]. Reprinted with permission from [95] © The Optical Society.

the temperature range of - 45°C – 145°C. This accuracy involves an error of about 0.02 %. Furthermore, since the radiation activity required long time, another error source could be related to the instability of the laser or the polarization controller.

A resonance shift of about 1 pm in 16 hours have been measured for the device without radiation. It involves an error on the resonance position of about 4.25 pm at the end of radiation activity.

In order to neglect the radiation impact on the Peltier cell, due to the change of the internal charges, and then, the temperature increase, when the cell is invested by the radiation, a closed-loop control has been used to set the chip temperature.

The temperature closed-loop control is reported in Fig. 2.13.

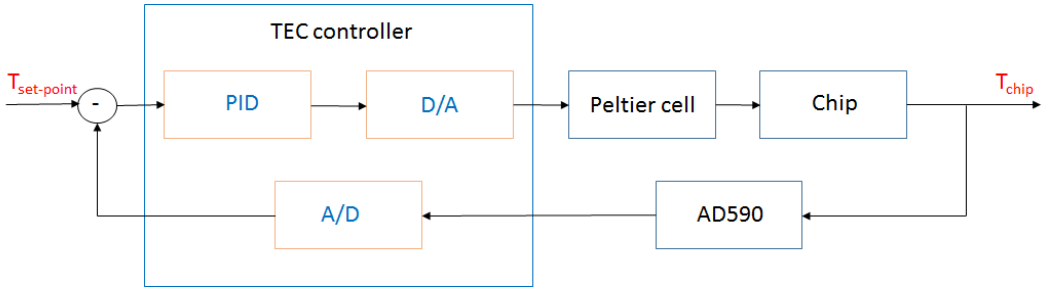

Fig. 2.13. Temperature closed-loop control (*PID*: Proportional-Integral-Derivative; *A/D*: analog-to-digital; *D/A*: digital-to-analog).

After selecting the temperature $T_{set\text{-}point}$ by using the TEC controller interface, the Proportional-Integral-Derivative (PID) controller feeds the Peltier Cell in order to match $T_{set\text{-}point}$ with the temperature of the chip T_{chip}, by comparing this last temperature to the temperature detected by the sensor AD590.

The single mode fibers into the package does not affect the wavelength shift measurement, because they act as bus waveguide extension. Although the refractive index of the fiber changes due to the gamma radiation absorption or the compaction/densification effect [90], the resonance peak does not depend on the bus refractive index, according to the theory of ring resonator [99]. Using high-performance measurements instruments, other sources errors, such as those due to oscilloscope, could be considered negligible.

The γ radiation impact on the TE resonance position, the related Q-factor, and the *ER* is shown in Figs. 2.14(a)-2.14(c), respectively. 100 measurements of the resonance were performed during the irradiation activity. The total error on the wavelength shift, sum of the aforementioned contributes, has been indicated by the black error bars in Fig. 2.14(a). In particular, at 3.2 Gy(InGaAsP), in the worst case, the error on the wavelength shift is equal to about 11%, mainly caused by the impact of radiation on the AD590 operation. The dominant ionization process in irradiated materials at *Co60* γ radiation energy is the Compton scattering: the structural deep point defects, typical of Compton scattering, involve the crystallographic damage, with a consequent change of the refractive index, and then the resonance positions, according to Eq. (2.3). From Fig. 2.14 (a), a fitted linear trend over the radiation time has been derived, with a maximum red-detuning $\Delta\lambda_{res}$ of about 810 pm at the end of irradiation activity. During the annealing step, the relaxation effect on the resonance leads a blue-shift of the resonance with a second order trend has been

observed, with a maximum offset of 60 pm with respect to the resonance position at 3.2 kGy(InGaAsP).

Figures 2.14(b)-2.14(c) show a stochastic distribution of *Q*-factor and *ER*. At about 320 krad, *Q* and *ER* detected mean variations (*ΔQ* and *ΔER*) are equal to about 13 % and 4 %, respectively. The slight change of the optical and coupling losses justifies these variations, although the radiation does not influence the spectrum of a ring resonator, confirmed by the same resonance shape before and after radiation, as shown in Fig. 2.15.

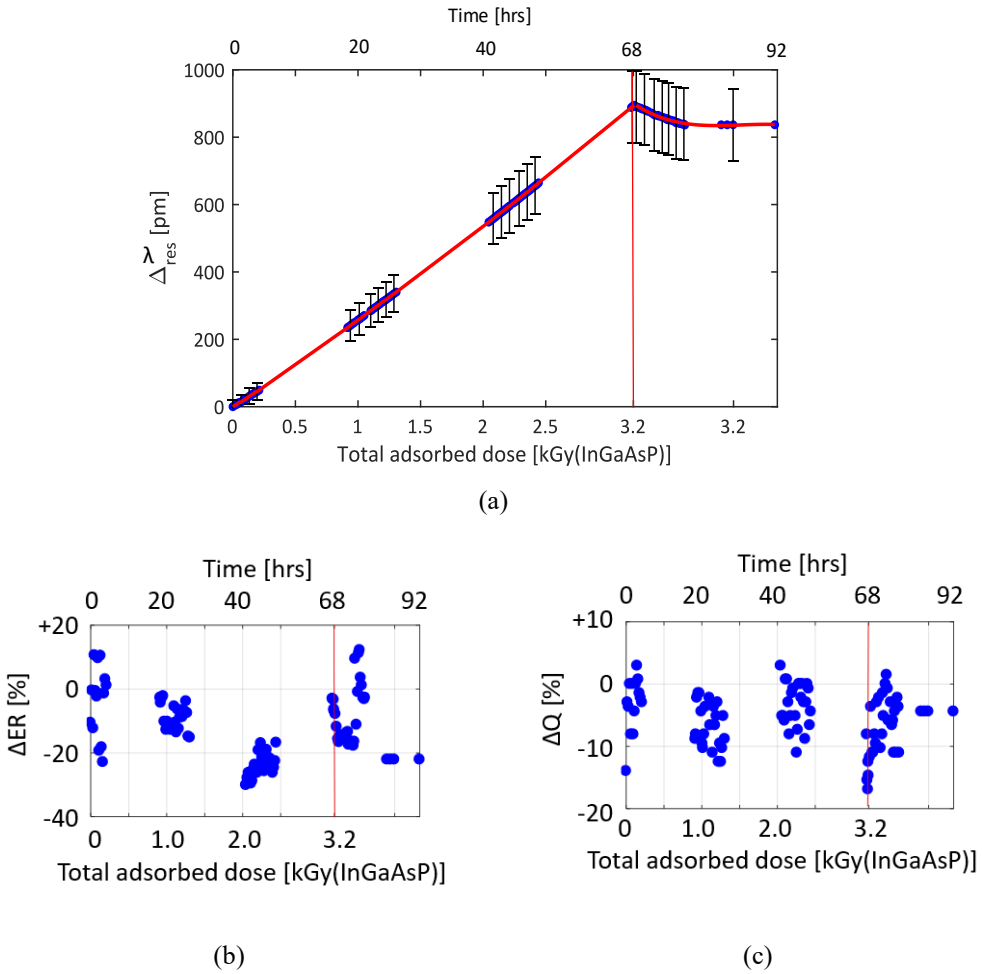

Fig. 2.14. (a) Red-shift of ring resonator resonance $\Delta\lambda_{res}$ vs total adsorbed dose. The bold red line is related to a linear fitting of the measured blue markers. (b) *ER* variation (*ΔER*) vs total adsorbed dose; (c) *Q*-factor variation (*ΔQ*) vs total adsorbed dose. The radiation and annealing activities are defined to the left and to the right of red line, respectively. Reprinted with permission from [95] © The Optical Society.

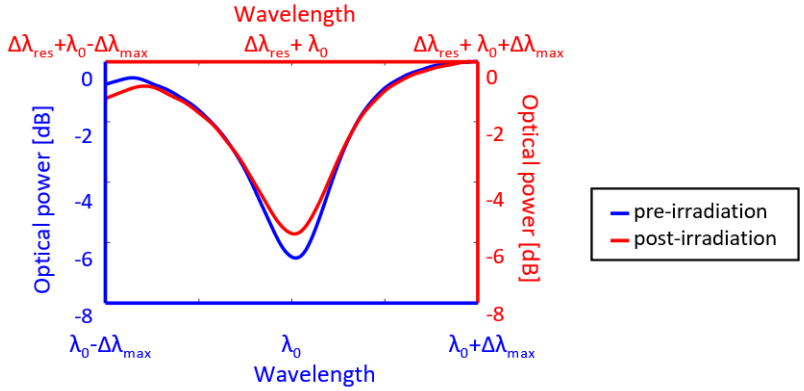

Fig. 2.15. TE resonance spectra pre- and after- irradiation ($\lambda_0 \approx 1.55$ μm; $\Delta\lambda_{max}$ is the maximum value of the laser scan across the operating wavelength λ_0 (200 MHz); $\Delta\lambda_{res}$ is the resonance detuning, caused by the radiation effect). Reprinted with permission from [95] © The Optical Society.

Since $Q = \lambda_{res}/FWHM$, the measurement error affects only the position of the wavelength peak, being negligible the errors on the FWHM because it is obtained with a differential measurement. Thus, the error on the *Q*-factor estimation could be considered negligible, being equal to ± 0.001%.

According to my knowledge, the proposed activity is the first evaluation of the radiation hardness of the InGaAsP/InP ring resonator and a comparison of the proposed results on devices based on other technology platforms as reported in literature is not easy to carry out, because of different radiation types, energies and dose rates that have been used. The most appropriate comparison is with radiation experiments on silicon ring resonators carried out at the *Co60* facility. A very linear resonance wavelength shift during irradiation was detected, with a slope of 0.33 pm/krad, investing the Si-based ring resonator with a dose rate of 83 rad/min and a total absorbed dose of about 320 krad [88]. A maximum shift of about 0.1 nm at 300 krad has been measured. Moreover, the extinction ratio of the resonance decreases of about 18 % with respect to the pre-irradiation value.

Using the device under test as sensing element in an RMOG, since the two waves, that travel through the ring resonator, experience the same resonance red-shift induced by γ radiation, according to the Sagnac effect, the angular velocity measurement results insensitive to radiations. Moreover, the slight change of *Q*-factor involves a negligible variation of the gyro resolution (in the worst case, a theoretical resolution of about 48 °/h has been calculated).

2.5 1D Photonic Crystal Ring Resonator

In the research field, microring resonators emerged as a fundamental component of integrated photonic circuits [105]. The operation of RR is based on the strong interaction between the electromagnetic fields and the surrounding material, then, confining the electromagnetic wave into the core of the waveguide-based RR. Also, for Space applications, as mentioned in the Paragraph 2.3.2, RR acting as sensitive element of RMOG configuration, provides high versatility, small size with high performance, the capability of monolithic/hybrid integration for the constitution of the entire system on chip.

Since the RMOG resolution is strictly correlated to the *Q*-factor of the sensitive element, it can be improved, for example, designing the ring resonator such as to exploit the slow light phenomenon. Slow light is a phenomenon which has found a great interest in the last decades [106-107]. Coupled ring resonators, as Coupled-Resonator Optical Waveguides (CROWs) and Side-Coupled Integrated Spaced-Sequence of Resonator (SCISSORs), as example, have been widely employed to the slow light [108-110].

The slow light effect is an interference phenomenon like Bragg scattering, with standing wave as a result. The main advantages of slow-light effect are the possibility to control the optical signals in the time domain and to comprise optical signal into the space, enhancing the light-matter interactions [107]. The enhancement of linear and non-linear effects, such as gain, thermo-optic, electro-optic, can be used to increase the performance of switching systems and amplifiers.

The most important parameter to identify the slow light regime is the group velocity v_g of the propagating wave signal. It represents the velocity, with which the overall envelope shape of the wave's amplitude propagates through space. The group velocity v_g could be expressed as:

$$v_g = \frac{\partial \omega}{\partial k} \tag{2.5}$$

where k is the wavenumber [rad/m] and ω is the wave's angular frequency [rad/s]. Since the wavenumber k is strictly correlated to the refractive index of the structure, the group velocity can be reduced by a large first order dispersion of the structure. The performance of dielectric slow light devices scales with the refractive index contrast [111]. Thus, since PhCs show a high index contrast, they appear promising

to engineer and to maximize the slow light effect. The operating wavenumber is typically near the edge of the Brillouin zone on the dispersion curve of the PhCs [112].

PhC slabs are the most used structures to generate the slow light effect, as a result of their intrinsic lossless optical confinement and simple fabrication process. A PhC slab consists of a 2D PhC with a 1D line defect into a two-dimensional PhC, as shown in Fig. 2.16 (a) [106]. The PhC slab operation is based on the light confinement in the vertical and lateral directions by Total Internal Reflection (TIR) and Bragg reflection, respectively. As shown in Fig. 2.16(b), the PhC dispersion generates the slow light effect near the photonic bandgap edge, with a remarkable increase of the group index n_g, that is inversely proportional to the v_g (see Fig. 2.16(c)).

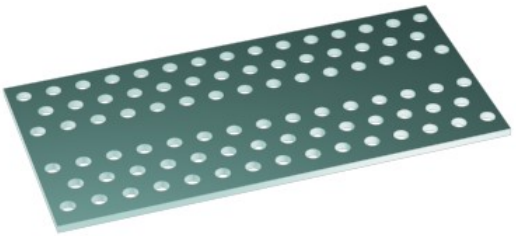

(a)

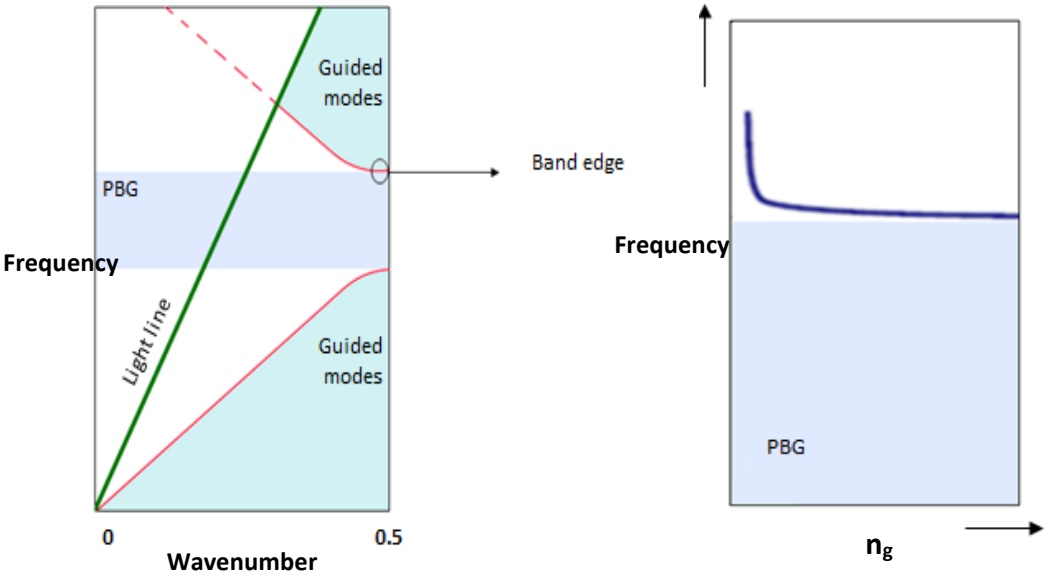

(b) (c)

Fig.2.16. PhC slab waveguide (a), relative band diagram (b) and n_g *vs* frequency at the band edge (c).

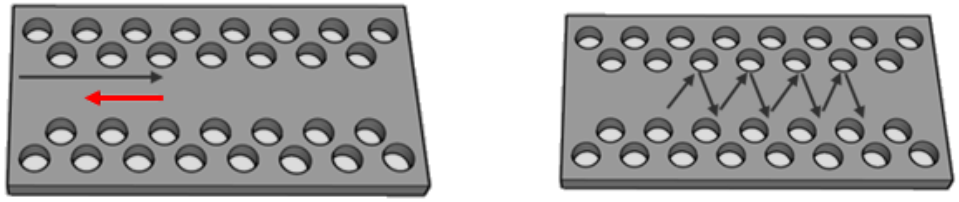

(a) (b)

Fig. 2.17. Mechanisms to obtain slow light in photonic crystals: Backscattering (a), omnidirectional reflection (b).

Two possible mechanisms of light propagation can be exploited to achieve the slow light phenomenon in PhC waveguides [107].

According to the so-called coherent backscattering mechanism (see Fig. 2.17(a)), when the light flows through the defect, it encounters multiple dielectric interfaces, producing the conversion of forward propagating wave (black arrow in Fig. 2.17(a)) into a backward propagating wave (red arrow in Fig. 2.17(a)).

When k is near the photonic band edge, a standing wave results by the constructive interference of the backward/forward propagating waves. The standing wave shows a zero - group velocity's wave, then to the slow light resonance in the photonic crystal waveguide. Moving away from band edge, the forward and backward waves are out of phase, and, then, the propagation of light waves is dominated by the TIR mechanism without the formation of standing wave.

The omnidirectional mechanism is another mechanism that control the slow light in PhCs, shown in Fig. 2.17(b). Since a defect is placed into the PhC, the light propagates into the PhC with a zig-zag behavior, forming a standing wave.

As previously mentioned, the most important feature of the slow light effect is the enhancement of light-matter interaction, due to a low group velocity. It ensures to increase the time of interaction between the propagating field with the material. Furthermore, the low group velocity leads an increase of the optical energy density, due to a group velocity difference between the front and the back of the light pulse.

The main effect of an increase of the light matter-interaction is the improvement of the Q-factor in slow light-based resonators. The improvement of

the Q-factor results by the transmission comparison between a non-dispersive (Eq. (2.6)) and a dispersive resonator (Eq. (2.7)) [113]:

$$T_{non\text{-}disp}(\omega)=\frac{\Gamma_{IO}^2}{(\omega-\omega_{res})^2+(\Gamma_{rad}+\Gamma_{abs}+\Gamma_{IO})^2} \tag{2.6}$$

$$T_{disp}(\omega)=\frac{\dfrac{\Gamma_{IO}^2}{\left[1+\dfrac{\sigma}{n(\omega_{res})}\left(\dfrac{c}{v_g}-n(\omega_{res})\right)\right]^2}}{(\omega-\omega_{res})^2+\dfrac{(\Gamma_{rad}+\Gamma_{abs}+\Gamma_{IO})^2}{\left[1+\dfrac{\sigma}{n(\omega_{res})}\left(\dfrac{c}{v_g}-n(\omega_{res})\right)\right]^2}} \tag{2.7}$$

where Γ_{rad}, Γ_{abs}, Γ_{IO} represent the radiation, absorption and input/output FWHMs [Hz], respectively, ω_{res} is the resonant frequency of the microresonator [rad/s], σ is the fraction of the electric displacement field energy in the highly dispersive material [a.u.] $\left(\sigma\equiv\dfrac{\left[\int_{V\partial n}\varepsilon(r)|E(r)|^2d^3x\right]}{\left[\int_{V_{mode}}\varepsilon(r)|E(r)|^2d^3x\right]}\right)$. From the comparison between the two equations, the FWHM factor is reduced by a factor of $\left[1+\dfrac{\sigma}{n(\omega_{res})}\left(\dfrac{c}{v_g}-n(\omega_{res})\right)\right]^2$, then an enhancement of the Q-factor is obtained.

In order to exploit the slow light effect in a ring resonator, then, improving the Q-factor, a one-dimensional photonic crystal structure could be comprised onto a standard ring resonator, forming the so-called 1D Photonic Crystal Ring Resonator (1D-PhCRR) [63]. The basic structure is shown in Fig. 2.18, where the PhC is sketched as a repetition of blue and red sections. The light input and output sections of the bus waveguide are connected to a light source and a light detector, respectively.

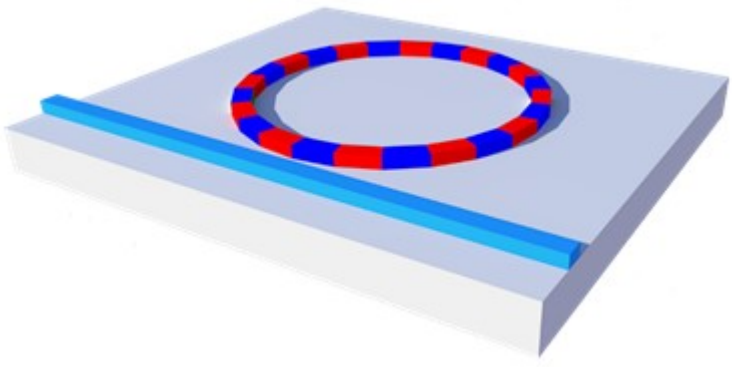

Fig. 2.18. 1D-Photonic Crystal Ring Resonator.

The PhCRR shows several differences respect to a conventional ring resonator, where the operation at the resonance frequencies strictly depends by the physical and geometrical features. These features guarantee a reduction of the wave's group velocity not enough to operate in the slow light regime.
Instead, the periodic dielectric structure inserts a "structural dispersion" into the PhCRR, leading an accurate control of the group velocity at the resonance.
Generally, to maximize the *Q*-factor improvement in a PhCRR, the following conditions must be fulfilled simultaneously in the PhCRR design:

- small index contrast between the elements of the 1D periodic structure;
- high number of periods;
- weakly coupling between the ring resonator and the bus waveguide.

The first condition can be satisfied by PhC with low-kappa values ($< 10^{-3}$ μm^{-1}), such as sidewall gratings [114], post gratings [115], direct write gratings [116, 117], and other PhC shapes [118].

Since in an isotropic material, the linewidth is proportional to the square number of the periods, the second condition is required to improve the *Q*-factor of the band edge resonance [119]. Thus, the linewidth decreases by increasing the number of periods, and then, the *Q*-factor increases, resulting in a trade-off between the *Q*-factor and the resonator footprint.

From the ring resonator theory [99], a trade-off between the resonance extinction ratio and the *Q*-factor exists. Thus, the third condition allows to improve the *Q*-factor, at the expense of *ER*. To allow a proper resonance detection, a minimum value of *ER* equal to 8 dB has been taken into account in PhCRRs design.

In order to demonstrate the *Q*-factor improvement between a 1D PhCRR and a RR with same footprint, the transmission spectra of the devices reported in Figs. 2.19 (a) - 2.20(a) have been compared. A 2D Finite Difference Time Domain (FDTD) approach has been used for the electromagnetic simulations.

Both the ring resonator and the 1D PhCRR are based on the Silicon on Insulator (SOI) technology, with a radius R = 2.52 μm, a waveguide width w = 0.3973 μm, a gap between ring and bus waveguide g = 100 nm, and a period of the holes Λ = 0.3973 μm with a hole diameter d = 238.4 nm [120]. The simulated

transmission spectra of the simple ring resonator and photonic crystal ring resonator are shown in Figs. 2.19(b)- 2.20(b), respectively.

For the simple ring resonator (Fig.2.19), a FWHM of the resonance labelled with a red star of 0.6 nm, then, a *Q*-factor of about 2580, and a Free Spectral Range (FSR) of 50.2 nm have been calculated.

For the PhCRR (Fig.2.20), the FWHM of the resonance labelled with a red star is equal to 0.3 nm, then, the *Q*-factor is about 5200, and the FSR between the first and the second peak is about 9.3 nm. From the comparison between the two transmission spectra, several features of photonic crystal ring resonator arise. At first, the *Q*-factor of the first band-edge PhCRR resonance is about the twice respect to the RR one. In addition, the FSR increases with increasing distance from the photonic band edge. This effect is due to non-linear PhCRR's dispersion relation, differently to the linear simple ring resonator's dispersion relation, that allows a constant FSR.

Furthermore, the resonances, away from the band edge, show a lower *Q*-factor respect to the first resonance, not being in the slow-light regime.

As will be widely described in the following Paragraphs, the *Q*-factor improvement in 1D-PhCRR respect to a simple RR could be maximized by a proper design of the 1D-PhCRR, as example by reducing the waveguide propagation loss and/or increasing the RR radius.

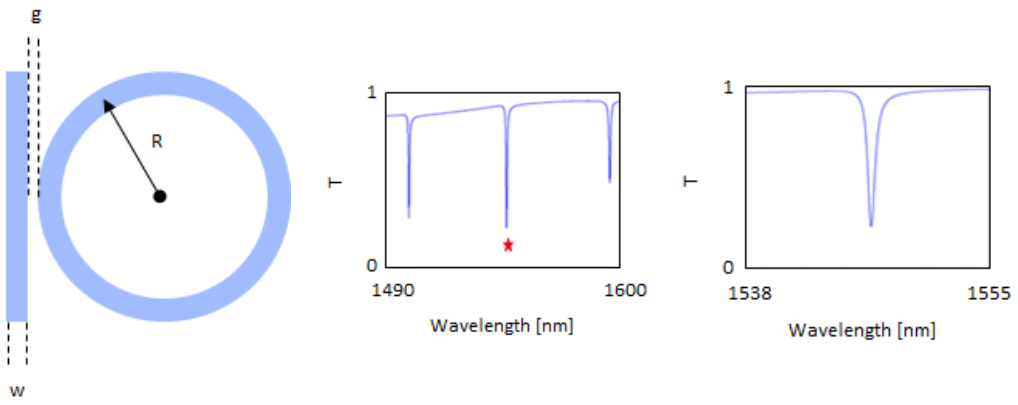

(a) (b) (c)

Fig. 2.19. a) Simple ring resonator, b) transmission spectrum, c) peak of resonance at λ= 1547 nm (*R*: radius, *w*: waveguide width, *g*: bus-ring gap).

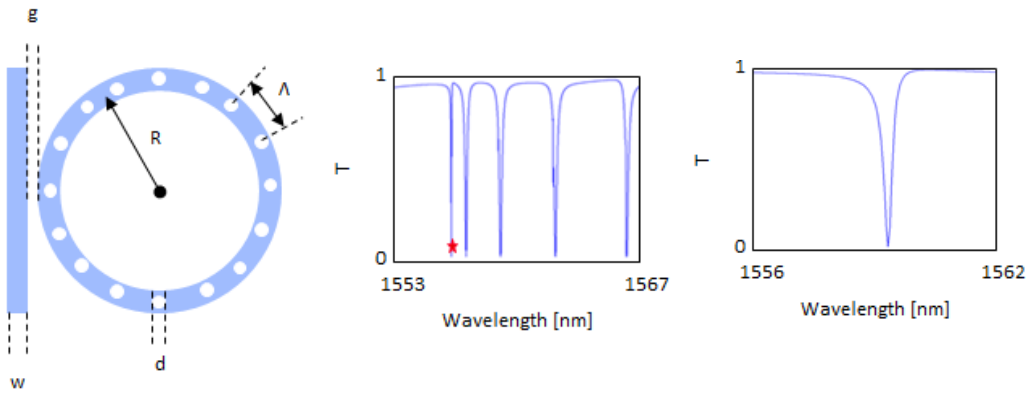

(a) (b) (c)

Fig. 2.20. a) PhCRR with air holes, b) transmission spectrum, c) band-edge peak at λ= 1559 nm (*R*: radius, *w*: waveguide width, *g*: bus-ring gap, *d*: holes diameter, *Λ*:period).

2.5.1 State of the art of PhCRRs

In the last years, several configurations of PhCRR have been proposed in literature [121-140], with different target applications, such as lasing [123-126], filters for WDM telecommunication [127, 137], sensing [135] or exploiting resonance splitting effect [140].

Ring resonators including a partial reflector, called ring-based in-line reflectors, have been proposed in [121], to reduce the ripple of sample grating Bragg reflectors. The ring-based in-line reflectors show a narrower FWHM compared to sample grating Bragg reflectors. Furthermore, the FWHM is strictly correlated to the coupling coefficient. In a weakly coupling regime, the resonance peak could degenerate into two symmetric peaks. These devices are mainly used for filtering and sensing.

In 1998, B. E. Little *et al.* [131] proposed a simple configuration of PhCRR to realize a Wavelength Division Multiplexing (WDM) filter (Fig.2.21(a)). The configuration presents a small perturbation, called notch, into the microring coupled to a bus waveguide. The reflection spectrum shows periodic peaks as result of a proper design of the notch. The response exhibits ripple in each peak when the perturbation is large.

In 2010, Y. M. Kang *et al.* [121-130] have proposed several configurations of PhCRR with a generic reflective element. The device consists of an integrated Bragg grating, distributed on a single section or along the whole optical path of the ring, acting as a planar reflective element. Forward and backward propagating

waves are generated by the Bragg reflector. A coupling between the counterpropagating waves leads the resonance splitting, with a maximum value of *Q*-factor equal to 10^3 [123-126]. A *Q*-factor of about 10^5 has been measured by using two concentric rings, with a width modulation of the inner one [130]. The PhCRR could be used as a comb mirror, a single peak mirror, an ultra-narrow band transmission filter, and a sharp transition mirror, by engineering the Bragg grating element.

For laser application, several configurations of PhCRR have been proposed in literature [123-126]. The introduction of periodic structure, acting as mirror, allows the reduction of the linewidth and the threshold voltage in single mode laser. A PhCRR in SiN_x technology, based on a half - Distributed Bragg Reflector (DBR), with a radius of 3.92 μm, is reported in [123] (Fig. 2.21(b)). A *Q*-factor in the order of 10^3 has been simulated by using a 2D Finite Element Method (FEM) approach. In order to improve the *Q*-factor, a PhCRR with full DBR along the whole ring optical path has been proposed in [126]. The ring resonator is based on the $GaAs/Al_{0.8}Ga_{0.2}As$ technology with quantum well in InGaAs. The PhCRR shows the modulation of the waveguide width, as shown in Fig. 2.21 (c). This device provides a threshold current density of 8 kA/cm^2 and it is able also to emit at multiple wavelengths.

The resonance splitting effect has been exploited for refractive index sensing applications [132, 140]. Wang *et al.* [132] analytically studied the effect of quasi-grating sidewall corrugation, resulting from fabrication issues of a microring resonator (Fig. 2.21(d)). The mode splitting results by the mode coupling between the forward- and backward- propagating modes in the ring, and it can be tailored by engineering the period and the length of the grating.

In the last years, periodically patterned ring resonators, evanescently coupled with a waveguide coupler on a silicon-on-insulator platform, have been demonstrated [132-138], demonstrating a *Q*-factor improvement by a factor 8 compared to a simple ring resonator with a ring radius less than 10 μm, and by a factor 70 for a ring radius of 30 μm (Fig. 2.21(e))[133]. MRRs with air holes along the whole ring optical path have been reported in [134], where a maximum loaded quality factor higher than 14,600, for a group index of about 27.3, has been

measured. Due to the strong optical confinement in the PhC holes, this configuration could be used for refractive index sensing [135-136]. The insertion of gold into the holes [136] (Fig. 2.21(f)), makes the device sensitive to the external environment, resulting in the shift of the resonance wavelength. This device has an improved sensitivity of more than a factor 2 compared to a simple ring resonator.

For biosensing, Donzella *et al.* [140] proposed a PhCRR with standard silicon photonic strip waveguides and a sub-wavelength grating. Sub-wavelength gratings are periodic structures not operating at the Bragg wavelength. The combination of strip waveguides and sub-wavelength grating offers a decrease of the light confinement in the waveguide core, and then, the improvement of the resonator sensitivity to changes of the refractive index in the surrounding medium. The fabricated rings show Q-factors of about 10^3 with sensitivity of 383 nm/RIU in water and 270 nm/RIU in air.

Other technologies and other configuration have been explored to achieve very high performance in several fields. For example, Teraoka *et al.* [141] presented a hybrid ring-Bragg grating resonator for band-stop filtering, made by a periodic refractive index variation of grating elements, coupled to a plain linear waveguide. This device shows a Q-factor of about 10^6 in the weakly coupling regime.

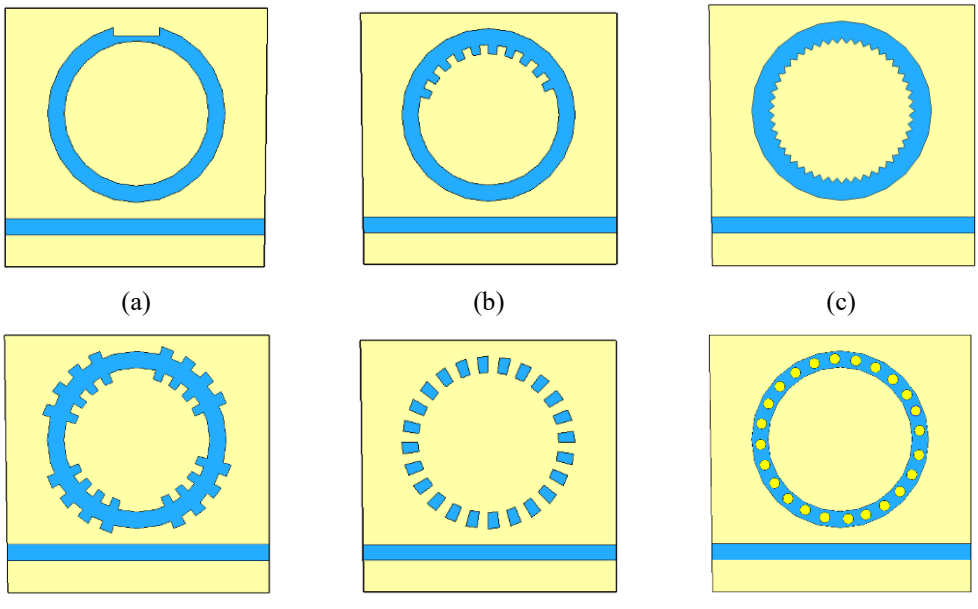

Fig. 2.21. Sketch of some configurations of PhCRR proposed in literature [131, 123, 126, 132, 133, 136].

Although the aforementioned devices are very promising, the performance is not suitable for the high-class gyro. Furthermore, the improvement of the PhCRR's *Q*-factor respect to the RR one is quite small. This effect is strictly correlated to the physical, i.e. high-index contrast and quite high propagation loss technology platform (silicon - [132, 134] or GaAs -based [126]), and geometrical features, i.e. radii in the order of μm, of the devices proposed in literature.

2.5.2 Mathematical modelling

The rigorous modelling of such ultra-high *Q* resonant cavities based on PhCRRs is very challenging, due to the insertion of the 1D PhC along the whole ring resonator optical path. Well known numerical approaches, e.g. 3D Finite Element Method (FEM), Finite Difference Time Domain (FDTD), Scattering Matrix Theory (SMT), Time Domain Equations, require large memory and huge computing resources, to obtain a PhCRRs' spectra with very high resolution. Furthermore, the above aspects result critically in case of devices with a large footprint, that are necessary in some applications to achieve high values of the *Q*-factor, also when the simulations are carried out by assuming a 2D approximation of the structure. In literature, both analytical and semi-analytical methods have been proposed for studying ring resonators including a periodic structure of variable length [121, 137]. Both mathematical methods show several intrinsic limitations, as the absence of the waveguide dispersion [121, 137], and the lossless assumption [121]. Furthermore, both models assume a point-like coupling region, not taking into account the effects of the periodic structure in the coupling region, when it is extended to the whole ring resonant path.

Goddard *et al.* [121] proposed a travelling-wave approach, based on scattering matrix theory. The coupler region and the periodic element are described by the coupling matrix and by a scattering matrix, respectively, with some physical approximations, such as lossless and neglected dispersion relations. By imposing the continuity conditions of the tangential components of the e.m. field at the edges of the coupling region, the reflection and the transmission response of the ring resonator can be derived as a function of the characteristics of the periodic element.

However, this approach assumes that the periodic structure does not extend to the coupling region.

Goldring *et al.* [137] proposed a numerical model, based on the time domain equations, which does not account for the effects of the grating in the coupling region, when the periodic structure is extended to the whole resonant path.

From the above reasons, a rigorous mathematical model, based on the Coupled Mode Theory (CMT), has been developed [142]. The model can evaluate the spectrum of a PhCRR based on any dielectric material systems, with any shape of a slowly varying and weakness grating, according to the hypotheses of the CMT approach [143]. Furthermore, the model can consider 1D-PhC extended, either on a portion or full optical path (namely Full-PhCRR) and extended also in the coupling region, to tailor the resonator spectrum. Since the electromagnetic behaviour of the PhCRR is affected by the coupling between the forward mode and the backward mode propagating in the photonic crystal, simulations on the PhCRR operation should take into account all contributions of forward and backward fields generated into the PhC. The transfer function of the 1D-PhCRR, reported in Fig. 2.17, has been derived by combining the transfer functions of the two dotted ring portions in the Figs. 2.22(a) - 2.22(b). A comprehensive analysis of both sections is described in the following Paragraphs, where a comparative analysis of the model and 2D-FDTD spectra have been carried out in terms of computing time and performance. As an example, while the 2D FDTD simulation of the coupler assisted grating requires about 45 hours, accurate results are obtained using our mathematical model in about 2 hours, by using a quad-core computer with 64 Gb RAM.

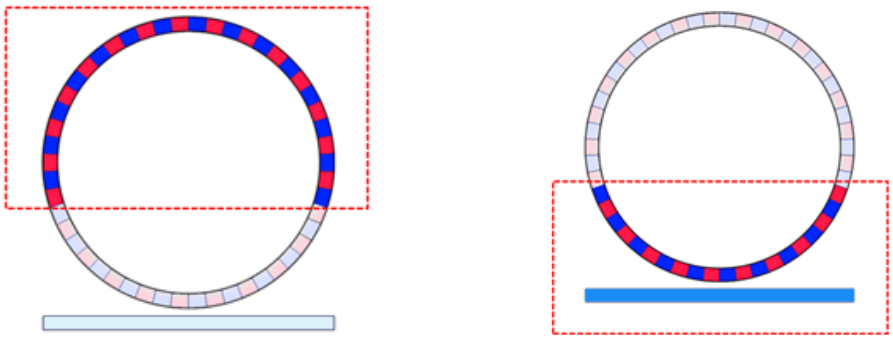

(a) (b)

Fig. 2.22. (a) 1D-Photonic Crystal, (b) grating-assisted coupling region.

2.5.2.1 CMT model of a bent 1D PhC

In Photonic Integrated Circuits, bent waveguides play very important role. They are used to connect input-output ports of different devices, reducing the device insertion loss and the footprint allowing a high packaging density of components. Unfortunately, when an optical waveguide is bent, radiation loss occurs. This phenomenon is due to boundedness of speed of the electromagnetic wave, and then, straight wave fronts in a curved waveguide cannot occur.

The curvature of the wave front causes the radiation of the mode away from the waveguide. This effect involves that the mode propagation constant is a complex value, where the imaginary contribute is related to the radiation effect due to the bend. The approach followed for the e.m. study of a bent waveguide is reported in Ref. [144]. For the e.m. analysis, both the Cartesian (x,y,z) and cylindrical (r,y,θ) coordinate systems have been considered (Fig.2.23).

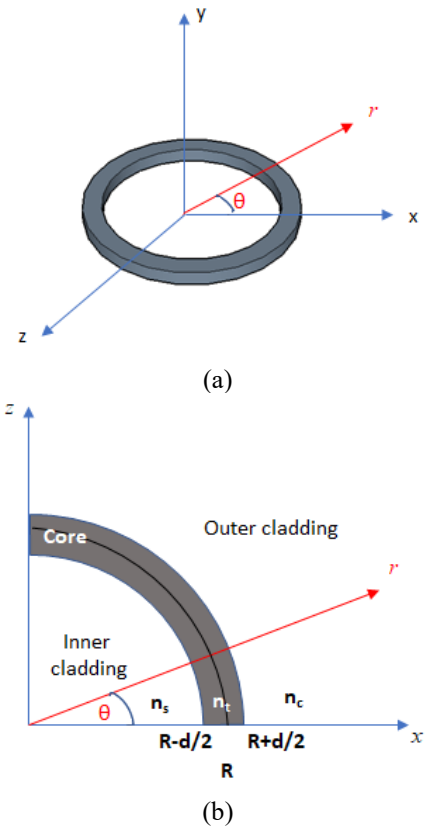

Fig. 2.23. (a) 3D waveguiding ring in Cartesian (blue lines) and Cylindrical (red lines) coordinates. (b) 2D focus on a ring resonator section, (n_s = refractive index of inner cladding, n_t = refractive index of core, n_c = refractive index of outer cladding, R = radius of curvature, d = waveguide width).

The three-dimensional electromagnetic analysis of channel waveguides can be simplified in a two-dimensional domain (r,θ) by using the effective-index approach, according to the effective-index method (EIM) proposed by Knox and Toulios [145]. It allows to carry out the e.m. study of quasi-TE/TM modes in a 2D domain, identifing an equivalent refractive index dependent by the geometrical waveguide features and by the refractive indices of the waveguide.

The dispersion equations for both quasi-TE and quasi-TM have been derived, by using the cylindrical coordinates and assuming a complex propagation constant $\gamma=\beta+i\alpha$, with β the phase constant and α the attenuation constant. The field components and the propagation constant result by solving the second order partial differential equation for each wave and by imposing the continuity conditions of the tangential field components at the waveguide interfaces. As example, a SiN ($n_{core} \approx 1.99$@1550 nm) -based single mode waveguide, embedded in SiO_2 cladding ($n_s \equiv n_c$=1.445@1550 nm), with a thickness of 100 nm and a width of 2.8 μm [146] has been taken into account. The trend of the $n_{eff,b}$ (=β/k0) and losses α_{loss} (=α/k_0) for the quasi-TM mode, for several radius of curvature, is shown in Fig. 2.24. The $n_{eff,b}$ shows a logarithmic behaviour as a function of the curvature radius: increasing the radius, $n_{eff,b}$ approaches the horizontal asymptote, represented by $n_{eff,s}$ of the straight waveguide, equal to about 1.464 (dotted line in Fig.2.24(a)). The difference between $n_{eff,s}$ and $n_{eff,b}$ is < 10^{-3} for radius values > 2 mm, and the curvature losses can be negligible, as shown in the inset of Fig. 2.24(b), in good agreement with Ref. [146]. The loss increase for small radii is due to a shift of the peak of the mode profile, with respect to the symmetry position R, towards the waveguide sidewalls, with consequent increase of optical losses. A shift of 162 nm, 120 nm and 63 nm along the positive direction of the x-axis have been calculated for R = 800 μm, R = 1 mm, R = 2 mm, respectively.

A schematic diagram of the bent 1D-PhC is shown in Fig. 2.25, where F_g denotes E or H fields propagating forward or backwards (subscripts + or -, respectively). Under Bragg conditions, the grating generates a back-propagating mode, (fields F_g^-) that couples to the forward-propagating one (fields F_g^+). Their phase contributions depend on the PhC shape with the assumption that any additional scattering source is negligible.

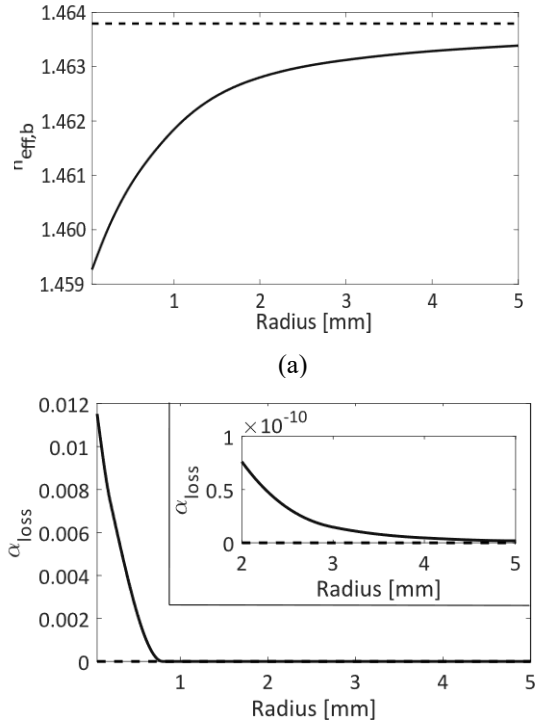

Fig. 2.24. n_{eff} *vs* curvature radius (a), α_{loss} [a.u.] *vs* curvature radius (b).

Since the coupling between forward and backward mode is responsible for the typical spectral behaviour of a PhC structure with a photonic band gap and sharp band edge resonances, the grating features result critical parameters for the tailoring of the resonance shape. To obtain an exact solution for the propagation modes in a generic periodic structure, a CMT based approach has been used [147]. The solutions of the e.m. equation is a combination of the solution relevant to the structure without any perturbation. In particular, the permittivity function $\varepsilon(r,\theta)$ of the waveguide under study results by the sum of an unperturbed and perturbed terms, $\varepsilon^{(0)}(r)$ and $\Delta\varepsilon(r,\theta)$, respectively:

$$\varepsilon(r,\theta)=\varepsilon^{(0)}(r)+\Delta\varepsilon(r,\theta) \tag{2.8}$$

The perturbed term $\Delta\varepsilon(r,\theta)$ along the θ direction can be expressed, in the most general form, as a Fourier series expansion [148]:

$$\Delta\varepsilon(r,\theta)=\sum_{n=-\infty,n\neq 0}^{n=\infty}\Delta\varepsilon^{(n)}(r)e^{i\frac{2\pi}{\Lambda}nR\theta} \tag{2.9}$$

where Λ is the grating period and $\Delta\varepsilon^{(n)}(r)$ are the coefficients of the Fourier series.

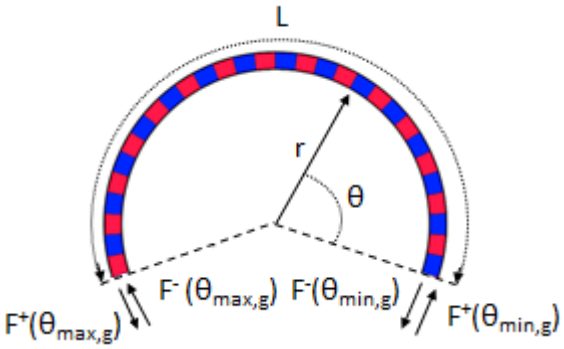

Fig. 2.25. Schematic of a bent 1D-PhC.

In a real case, the value of n ranges between 0 to ∞ taking into account the odd or even perturbation symmetry. The zero-th order coefficient depends on the unperturbed structure while higher order coefficients describe the grating shape along the propagation direction. For the first order grating, the first order of $\Delta\varepsilon^{(n)}(r)$ has been considered [149]. The coefficient $\varepsilon^{(0)}(r)$ is equal to the weighted average by the duty cycle of the coefficients ε in the perturbation, according to the effective medium theory [150].

From Maxwell equations, neglecting the time dependence and for the quasi-TM mode, H_y could be expressed, in terms of the unperturbed waveguide modes, as:

$$H_y = \sum_{m=-\infty}^{\infty} A_m(\theta) H_y^{(m)}(r) e^{i\gamma_m R\theta} \tag{2.10}$$

where m refers to the mode number (as TM_0, TM_1, TM_2, and so on), and $H_y^{(m)}(r)$ is the transverse modal distribution with a corresponding propagation constant γ_m. Focusing on the coupling between the forward propagating γ_{fw} mode to the backward propagating γ_{bw} mode, where bw=-fw, and assuming assuming $A_m(\theta)$ as slowly varying functions, the coupled mode equations in cylindrical coordinates have been derived:

$$\frac{\partial A_{fw}(\theta)}{\partial\theta} = iK_{ab} A_{bw}(\theta) e^{-i2(\beta_{bw}-\pi/\Lambda)R\theta} \tag{2.11}$$

$$\frac{\partial A_{bw}(\theta)}{\partial\theta} = iK_{ba} A_{fw}(\theta) e^{i2(\beta_{fw}-\pi/\Lambda)R\theta} \tag{2.12}$$

$$K_{ab} = \frac{\omega}{2}\int_{-\infty}^{\infty} \Delta\varepsilon^{(1)}(r) \frac{(\gamma_{bw}+\gamma_{bw}^{*}) i\mu r^3}{\gamma_{fw}\gamma_{bw}\varepsilon_0\varepsilon} \left|H_y^{(fw)}\right|^2 \partial r \tag{2.13}$$

$$K_{ba}=-\frac{\omega}{2}\int_{-\infty}^{\infty}\Delta\varepsilon^{(1)}(r)\frac{\left(\gamma_{fw}+\gamma_{fw}^{*}\right)i\mu r^{3}}{\gamma_{fw}\gamma_{bw}\varepsilon_{0}\varepsilon}\left|H_{y}^{(fw)}\right|^{2}\partial r \tag{2.14}$$

where $\gamma_{bw}=-\gamma_{fw}^{*}$, taking into account the propagation losses, and K_{ab} and K_{ba} are the coupling coefficients between the forward/backward and backward/forward modes, respectively. The following normalization equation of the e.m. fields have been used in Eqs.(2.11-2.14):

$$\int E^{(m)}\times H^{(s)*}\cdot a_{\theta}\,\partial r+\int E^{(m)*}\times H^{(s)}\cdot a_{\theta}\,\partial r=\frac{\left(\gamma_{s}+\gamma_{s}^{*}\right)iR\mu r}{\gamma_{s}\varepsilon_{0}\varepsilon}\int\left|H_{y}^{(s)}(r)\right|^{2}\partial r \tag{2.15}$$

where the apexes *m* and *s* are referred to forward or backward propagating modes. From Eqs.(2.11-2.14), a matrix form is obtained:

$$\frac{\partial}{\partial\theta}\begin{bmatrix}A(\theta)\\B(\theta)\end{bmatrix}=\mathrm{i}\begin{bmatrix}\Delta\beta & K_{ab}\\K_{ba} & \Delta\beta\end{bmatrix}\begin{bmatrix}A(\theta)\\B(\theta)\end{bmatrix} \tag{2.16}$$

where

$$\Delta\beta=R\cdot\left(\beta_{s}-\frac{\pi}{\Lambda}\right) \tag{2.17}$$

$$A(\theta)=A_{s}(\theta)e^{i\Delta\beta\theta} \tag{2.18}$$

$$B(\theta)=A_{-s}(\theta)e^{-i\Delta\beta\theta} \tag{2.19}$$

The general solution of Eq. (2.16) can be written as:

$$\begin{bmatrix}A(\theta)\\B(\theta)\end{bmatrix}=c_{1}\begin{bmatrix}-K_{ab}\\\Delta\beta-iS\end{bmatrix}e^{-Sz}+c_{2}\begin{bmatrix}-K_{ab}\\\Delta\beta+iS\end{bmatrix}e^{Sz} \tag{2.20}$$

where the constants c_1 and c_2 have been derived applying the boundary conditions. The fields $A(\theta_{max,g})$ and $B(\theta_{min,g})$ result from the Eq. (2.20), by imposing the boundary conditions $A(\theta_{min,g})\equiv 1$ - $B(\theta_{max,g})\equiv 0$, and $A(\theta_{min,g})\equiv 0$ - $B(\theta_{max,g})\equiv 1$, according to the superposition principle. Finally, the magnitude of the magnetic field for the forward propagating mode is:

$$F_{g}^{+}(\theta)=A_{fw}(\theta)e^{i\gamma_{fw}R\theta}=A(\theta)e^{-i\Delta\beta\theta}e^{i\beta_{fw}R\theta}e^{-\alpha R\theta}=A(\theta)e^{i(l\pi/\Lambda)R\theta}e^{-\alpha R\theta} \tag{2.21}$$

For the backward propagating mode, the field derived is:

$$F_{g}^{-}(\theta)=B_{bw}(\theta)e^{i\gamma_{bw}R\theta}=B(\theta)e^{i\Delta\beta\theta}e^{-i\beta_{fw}R\theta}e^{-\alpha R\theta}=B(\theta)e^{-i(l\pi/\Lambda)R\theta}e^{-\alpha R\theta} \tag{2.22}$$

The structure has been assumed as symmetrical: it starts and finishes with the same semi-period so that $F_{g}^{-}(\theta_{min,g})=-F_{g}^{+}(\theta_{max,g})$, for both aforementioned boundary conditions.

As an example, a Si_3N_4 top grating has been investigated (see Fig. 2.26(a)). The grating is based on a Si_3N_4 waveguide (thickness t_H = 100 nm and a width w = 2.8 μm), embedded in SiO_2 [146]. It results as single-mode, as confirmed by FEM simulations. A curvature radius R equal to about 2 mm has been considered, with $\theta_{min,g}$ and $\theta_{max,g}$ equal to 0 and 11°, respectively. The top grating shows a thickness modulation, with maximum t_H and minimum t_L values equal to 100 nm and 60 nm, respectively, with a duty cycle equal to 50%. A period Λ = 526 nm has been designed to operate at the Bragg wavelength at about 1540 nm. For the grating propagation loss, a value of propagation loss equal to 15 dB/m has been taken into account, with a conservative approach. Moreover, the aforementioned propagation loss value has been added to the bending losses α_{loss} (Fig.2.24(b)), in order to take into account, the bending of the grating. The propagation constant γ has been calculated by using the aforementioned model: for λ≈1.54 μm, n_{eff} = 1.4633 (for straight waveguide, n_{eff} = 1.4760) and α_{loss}=6.4886 x 10^{-10} dB/m. The transmission power of the quasi - TE mode is reported in Fig. 2.26(b), calculated by solving Eq. (2.20), placing the boundary conditions $A(\theta_{min,g})\equiv 1$ **-** $B(\theta_{max,g})\equiv 0$. A photonic bandwidth PBG_w equal to 14.83 nm, an ER of the bandgap region equal to 93 dB, and a central wavelength λ_B at about 1.54 μm, have been calculated.

To confirm the model general validity, a comparison between the results obtained using the 2D FDTD approach and those of our mathematical model has been carried out for the structure reported in Fig. 2.27(a). It consists of a sidewall grating, showing a width modulation with $R\rightarrow\infty$. The grating is based on the same waveguide of the aforementioned top grating. The features of the grating, shown in Fig. 2.27(a) are: h = 100 nm, w = 2.8 μm, Λ = 525.5 nm, w_H = 3.4 μm, w_L = 2.2 μm, and L = 200 μm. Results of the comparison for the quasi-TE mode are shown in Fig. 2.27(b). Red line refers to the results from the 2D FDTD algorithm, while the blue line has been derived from the mathematical model. The performance parameters are summarized in Tab. 2.5. A very good matching between the results of the model and the 2D-FDTD ones can be observed in Fig. 2.27(a), for the quasi-TE mode. The quasi-TM mode was also investigated. Results for quasi-TE and quasi-TM modes show a slight frequency shift of the output spectrum due to a different value of the effective index.

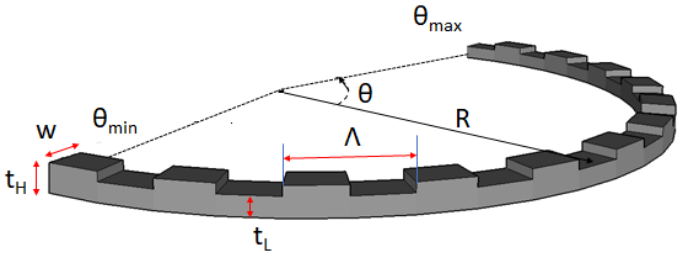

(a)

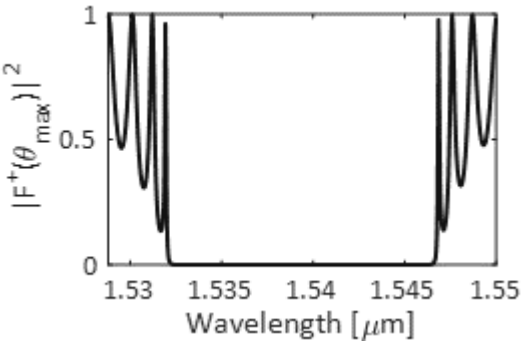

(b)

Fig. 2.26. Schematic of a bent Si_3N_4 top grating (a) and its transmission power ($|F_g^+(\theta_{max})|^2$) spectrum.

For some applications, such as optical gyroscope, the waveguide must be engineered so that the birefringence is very low to get a negligible modal interference between TE and TM modes [151].

Fig. 2.27(b) shows that the spectrum shape obtained with both techniques, i.e. 2D-FDTD and our model, is the same. The shift of the Bragg wavelength (about 0.4 nm) is related to the mismatch between the double precision of the code based on our model and the single precision of the 2D-FDTD code. In addition, the calculation time of the mathematical model is much less than that of the FDTD simulations using a quadcore computer with 64 Gb RAM at 3.6 GHz. The FDTD simulation requires 1.65 days, while only 239 seconds are required by the mathematical model, with the same wavelength step.

The model vs 2D FDTD approach comparison was carried out, because 3D FDTD simulations are much more time consuming and require a huge amount of memory.

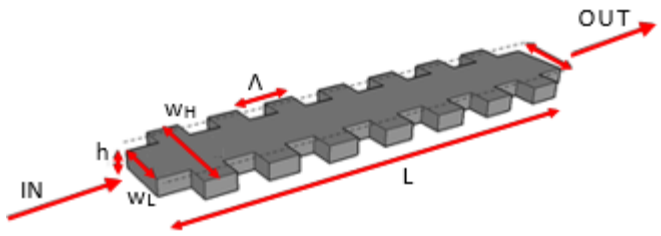

(a)

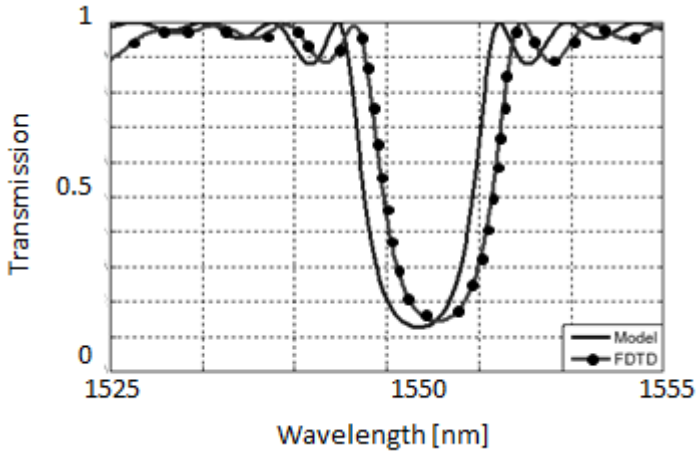

(b)

Fig. 2.27. Schematic of a Si_3N_4 sidewall grating (h = 100 nm, w = 2.8 µm, Λ = 525.5 nm, w_H = 3.4 µm, w_L = 2.2 µm, L = 200 µm) (a) and the comparison of the transmission power calculated by using CMT (blue line) or 2D-FDTD (red line) approach (b).

Tab.2.5. Sidewall grating performance comparison between our model and 2D-FDTD for the quasi TE-mode.

Performance	This model	2D-FDTD
λ_B [nm]	1549.70	1551.10
PBG_w [nm]	6.30`	6.18
ER [dB]	19.77	19.10
Simulation time	239 s	1.65 days

2.5.2.2 Coupler model

The features of the coupling region are the key elements to control the spectral behaviour of the grating assisted coupler. As previously discussed into the Paragraph 2.5, a point-like coupling region represents a strong approximation in the

theoretical study of the PhCRR, because it neglects the presence of counter-propagating fields that could facilitate the bus-ring coupling.

The coupling region can be considered as a grating assisted coupler (see Fig. 2.28), *gap(x,z)* is the centre-to-centre gap between the two waveguides and gap_0 is the minimum gap. The grating assisted coupler consists of two slab waveguides, w_b and w_g wide, with core refractive indices n_b and $n_{g,1}$, respectively, and perturbation $n_{g,2}$ in the top waveguide. Both waveguides are assumed as single-mode with propagation constant β_b and γ_g for bus and bent grating, respectively.

The coupler shows a length of $2L_{max,}$ where L_{max} is the semi-coupler length at whose ends the power coupling between the two waveguides in negligible, as will be widely described in the following. The z-dependent amplitudes of the guided modes in the waveguide q (q is referred to the waveguide b or g), defined as $F_{c,q}^{\pm}(z)$ (the superscripts + and – are related to the forward and backward propagating fields, respectively), are denoted in Fig. 2.28.

Being the transverse mode profiles of the waveguides g and b direct along r and x axis, respectively, both bus and grating waveguide has been analysed in Cartesian co-ordinate system (x,y,z). For the g waveguide, a conversion from Cylindrical to Cartesian system is needful, according to the following relationship between the cylindrical components (A_r, A_y, A_θ) and the Cartesian components (A_x, A_y, A_z):

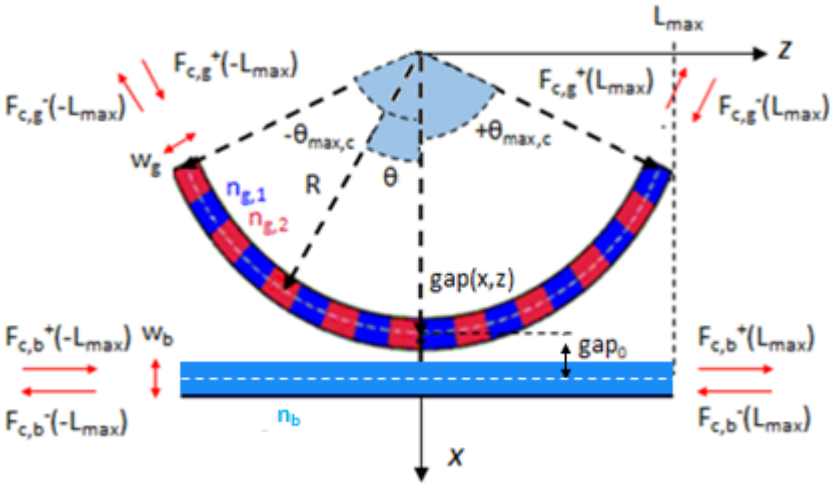

Fig. 2.28. Schematic of the grating assisted-coupling region (b = bus waveguide, g = grating waveguide, n_b = refractive index of b, $n_{g1,2}$ = refractive indices of the two grating region, w_b = bus width, w_g, = grating width, g_0 = minimum gap).

$$\begin{bmatrix} A_x \\ A_y \\ A_z \end{bmatrix} = \begin{bmatrix} cos\theta & 0 & -sin\theta \\ 0 & 1 & 0 \\ sin\theta & 0 & cos\theta \end{bmatrix} \begin{bmatrix} A_r \\ A_y \\ A_\theta \end{bmatrix} \tag{2.23}$$

The components of a TM bend mode ($E_{g,y}^{\,0} = 0$, $H_{g,x}^{\,0} = 0$, $H_{g,z}^{\,0} = 0$) for the g waveguide in the cartesian system will be:

$$E_{g,x}^{0}(x,z) = cos\theta \cdot \left[-\frac{\gamma R}{\varepsilon_0 \varepsilon \omega r} H_{g,y}^{0}(r) \right] - sin\theta \cdot \left[\frac{i}{\varepsilon_0 \varepsilon \omega} \frac{dH_{g,y}^{0}(r)}{dr} \right] \tag{2.24}$$

$$E_{g,z}^{0}(x,z) = sin\theta \cdot \left[-\frac{\gamma R}{\varepsilon_0 \varepsilon \omega r} H_{g,y}^{0}(r) \right] + cos\theta \cdot \left[\frac{i}{\varepsilon_0 \varepsilon \omega} \frac{dH_{g,y}^{0}(r)}{dr} \right] \tag{2.25}$$

$$H_{g,y}^{0}(x,z) = H_{g,y}^{0}(r) e^{i\gamma_b R\theta} \tag{2.26}$$

where $r = \sqrt{x^2 + z^2}$ and $\theta = arctan\, z/x$. The electromagnetic field components for the TM mode in the straight waveguide b ($E_{b,y}^{\,0} = 0$, $H_{b,x}^{\,0} = 0$, $H_{b,z}^{\,0} = 0$) are given by:

$$E_{b,x}^{0}(x,z) = \frac{\beta_b}{\omega \varepsilon_0 \varepsilon} H_{b,y}^{0}(x) \tag{2.27}$$

$$E_{b,x}^{0}(x,z) = \frac{i}{\omega \varepsilon_0 \varepsilon} \frac{dH_{b,y}^{0}(x)}{dx} \tag{2.28}$$

$$H_{b,x}^{0}(x,z) = H_{b,y}^{0}(x) e^{i\beta_b z} \tag{2.29}$$

where the superscript *0* is referred to the mode profile. $\theta_{max,c,}$ is defined as the angle at whose ends the power coupling between the two waveguides is negligible (approximately of the order of 10^{-10} with respect to the maximum value of the forward coupling coefficient, where + is referred to the forward field, $|K_{bg}^{+}(z)|^2$). The forward coupling coefficient $|K_{bg}^{+}(z)|^2$ shows a Gaussian shape, as shown in Fig. 2.29, symmetrical with respect to the z point where the gap between the two waveguides is minimum ($z = 0$). Then, the semi-length of the coupler L_{max} could be defined as $R \cdot sin(\theta_{max,c})$, where R is the radius of the resonator.

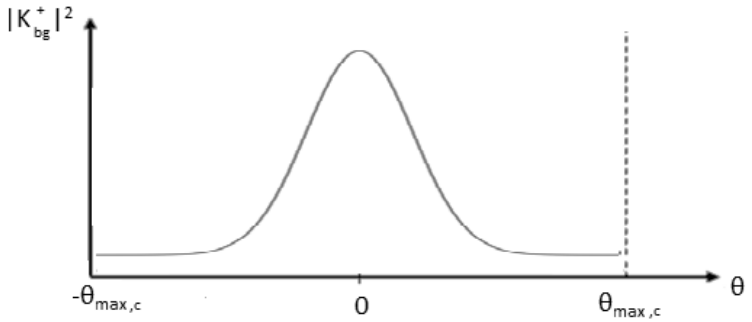

Fig. 2.29. Calculated Gaussian trend of $|K_{bg}^{+}(z)|^2$ in the grating assisted coupling region.

In order to implement a general and rigorous mathematical model, it is valid for any shape, material, location and perturbation of the grating, as index modulation or shape variation, compliant to the hypothesis of the CMT as weak coupling between two modes.

According to the mode expansion technique [152], the transverse e.m. field components of a single-mode waveguide could be expressed as the superposition of four guided modes:

$$E_{c,t}(x,y,z)=[u_b^+(z)+u_b^-(z)]E_{b,t}(x,y)+\left[u_g^+(z)+u_g^-(z)\right]E_{g,t}(x,y) \tag{2.30}$$

$$H_{c,t}(x,y,z)=[u_b^+(z)-u_b^-(z)]H_{b,t}(x,y)+\left[u_g^+(z)-u_g^-(z)\right]H_{g,t}(x,y) \tag{2.31}$$

where $E_{b,t}(x,y) - H_{b,t}(x,y)$, and $E_{g,t}(x,y) - H_{g,t}(x,y)$ are the lowest-order normalized modes in the waveguide *b* and *g*, respectively. The CMT based analysis of the grating assisted gives-a set of four coupled-mode equations [149]:

$$\frac{\partial \mathbf{F_c}(z)}{\partial z}=i\mathbf{M}\mathbf{F_c}(z) \tag{2.32}$$

where $\mathbf{F_c}(z)$ is the transposed matrix of the amplitude fields:

$$\mathbf{F_c}(z)=\left[f_{c,b}^+(z),f_{c,g}^+(z),f_{c,b}^-(z),f_{c,g}^-(z)\right]^T \tag{2.33}$$

and **M**(z) is a 4x4 matrix given by:

$$\mathbf{M}(z)=\mathbf{C}^{-1}[\mathbf{B}\mathbf{C}+\mathbf{K}(z)] \tag{2.34}$$

with **B** defined by

$$\mathbf{B}=\mathrm{diag}(\beta_b,\gamma_g,-\beta_b,-\gamma_g) \tag{2.35}$$

C is the matrix of coefficients:

$$\mathbf{C}=\begin{bmatrix} 1 & C_{bg}^+ & 0 & C_{bg}^- \\ C_{gb}^+ & 1 & C_{gb}^- & C_{gg}^- \\ 0 & -C_{bg}^- & 1 & C_{bg}^+ \\ -C_{gb}^- & -C_{gg}^- & C_{gb}^+ & 1 \end{bmatrix} \tag{2.36}$$

where:

$$C_{bg}^{\pm}=z\cdot\iint E_{b,x}^*\times H_{g,y}\pm H_{b,y}^*\times E_{g,x}\,\partial x\partial y \tag{2.37}$$

$$C_{gb}^{\pm}=z\cdot\iint E_{g,x}^*\times H_{b,y}\pm H_{g,y}^*\times E_{b,x}\,\partial x\partial y \tag{2.38}$$

$$C_{gg}^{-}=z\cdot\iint E_{b,x}^*\times H_{g,y}-H_{b,y}^*\times E_{g,x}\,\partial x\partial y \tag{2.39}$$

with a normalization condition:

$$z\cdot \iint E^{*}_{q,x}\times H_{q,y}+H^{*}_{q,y}\times E_{q,x}\,\partial x\partial y=1 \tag{2.40}$$

where $q=b,g$.

The coupling coefficient matrix **K**(z) is given by:

$$\mathbf{K}(z)=\begin{bmatrix} K^{-}_{bb} & K^{-}_{bg} & K^{+}_{bb} & K^{+}_{bg} \\ K^{-}_{gb} & K^{-}_{gg} & K^{+}_{gb} & K^{+}_{gg} \\ -K^{+}_{bb} & -K^{+}_{bg} & -K^{-}_{bb} & -K^{-}_{bg} \\ -K^{+}_{gb} & -K^{+}_{gg} & -K^{-}_{gb} & -K^{-}_{gg} \end{bmatrix} \tag{2.41}$$

The elements of **K**(z) matrix are expressed as:

$$K^{\pm}_{pq}=K^{t}_{pq}\pm K^{z}_{pq} \tag{2.42}$$

$$K^{t}_{pq}=\omega \iint \Delta\varepsilon_{p}(x,y,z)E_{p,t}(x,y)E_{q,t}(x,y)\partial x\partial y \tag{2.43}$$

$$K^{z}_{pq}=\omega \iint \frac{\varepsilon_{p}(x,y)\Delta\varepsilon_{p}(x,y,z)}{\varepsilon(x,y,z)}E_{q,z}(x,y)E_{p,z}(x,y)\,\partial x\partial y \tag{2.44}$$

where $\Delta\varepsilon_p$ ($p,q = b$ or g) is the permittivity perturbation of ε_b or ε_g due to the otter waveguide. In the grating region, the perturbation is assumed as in Eq. (2.8). Finally, from Eq. (2.32), the expression of the fields amplitude $F_{c,q}$(z) are:

$$F^{+}_{c,b}(z)=f^{+}_{c,b}(z)e^{i\beta_b z} \tag{2.45}$$

$$F^{+}_{c,g}(z)=f^{+}_{c,g}(z)e^{i\gamma_g R\,asin(z/R)} \tag{2.46}$$

$$F^{-}_{c,b}(z)=f_{c,b}(z)e^{-i\beta_b z} \tag{2.47}$$

$$F^{-}_{c,g}(z)=f_{c,g}(z)e^{-i\gamma_g R\,asin(z/R)} \tag{2.48}$$

In order to validate the aforementioned model, the performance of the coupler based on sidewall grating, that show a waveguide width modulation, (see Fig. 2.30(a)), has been calculated both using our model and 2D FDTD algorithm. The spectra have been derived, considering a specific set of boundary conditions: at $z = -L_{max}$ of the waveguide b, $u^{+}_{b}(-L_{max})=1$ and $u^{-}_{g}(L_{max})=0$. The sidewall grating shows the same features reported into the Paragraph 2.5.2.1. The bus waveguide 300 μm long is coupled to a Si_3N_4 based - bus waveguide, 2.8 μm wide and 100 nm thick, with gap_0 equal to 5.5 μm. In order to speed up the 2D FDTD simulation a large enough value of the radius has been considered. Furthermore, an asymmetrical spatial grid size has been used for the simulation of the structure in Fig.2.30 using our mathematical model, reducing the residual errors related to the solutions of the coupled mode equations system. Fig. 2.30(b) reports the spectrum of the grating

assisted coupler, shown in Fig. 2.30(a), calculated by 2D FDTD and by our model. The black line indicates the transmission power $|F_{cg}(L)|^2$ of quasi TE mode in the grating waveguide evaluated using our mathematical model, while the dotted black line shows the 2D-FDTD result. The summary of the comparison between the two approaches is reported in Tab. 2.6, where the different numerical precision between the two different solver techniques causes, a small deviation of the center bandgap position λ_B (5.5 nm) and a difference in the transmission value at both band edges, although with same shape of transmission spectrum and photonic bandgap width (PBG_w). The simulation time of the mathematical model is about 3.5% of the FDTD simulations.

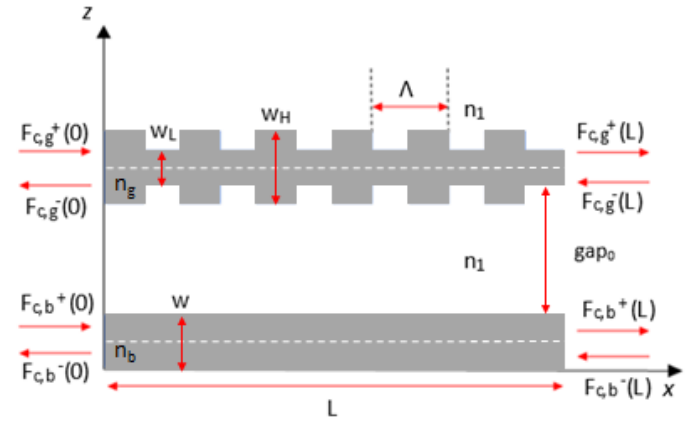

(a)

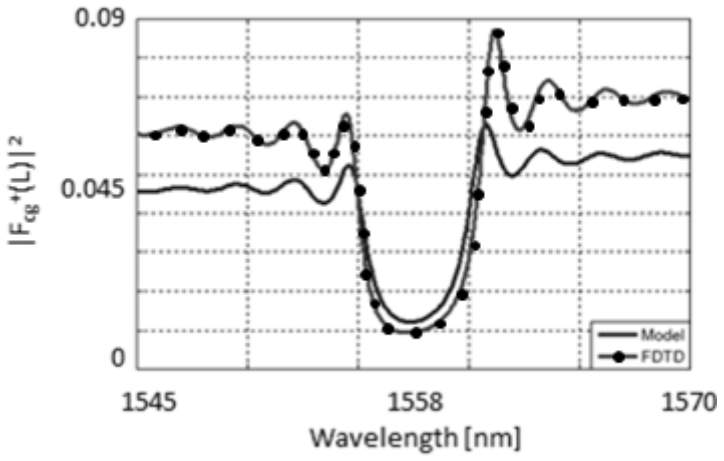

(b)

Fig. 2.30. Top view of a schematic diagram of the coupling region (w = 2.8 µm, Λ = 525.5 nm, w_H = 3.4 µm, w_L = 2.2 µm, gap_0 = 5.5 µm, L = 300 µm) (a) and the comparison of the transmission grating output power calculated by using CMT (blue line) or 2D-FDTD (red line) approach (b).

Tab. 2.6. Coupling region performance comparison between the model and 2D-FDTD approach.

Performance	This model	2D-FDTD
λ_B [nm]	1548.49	1554.14
PBG_w [nm]	5.95	5.24
Max ER [dB]	24.28	24.28
Simulation time	~ 1.58 hours	1.88 days

2.5.2.3 Transmission function of the 1D-PhCRR

The transmission function of the 1D-PhCRR has been derived by integrating the sections related to the grating-assisted coupler and the ring resonator portion with grating. The 1D-PhC and the grating assisted-coupler have been represented in a matrix form to solve the e.m. problem [153] and facilitate the integration between the two sections. Furthermore, both sections have been designed in order to avoid PhC defects related to a periodicity mismatch. The grating assisted coupling region has been represented by the matrix **M**, whose elements M_{Cij} are calculated by solving the differential equations system of Eq. (2.32):

$$\begin{bmatrix} F^{+}_{c,g}(L_{max}) \\ F^{+}_{c,b}(L_{max}) \\ F^{-}_{c,g}(-L_{max}) \\ F^{-}_{c,b}(-L_{max}) \end{bmatrix} = \begin{bmatrix} M_{C11} & M_{C12} & M_{C13} & M_{C14} \\ M_{C21} & M_{C22} & M_{C23} & M_{C24} \\ M_{C31} & M_{C32} & M_{C33} & M_{C34} \\ M_{C41} & M_{C42} & M_{C43} & M_{C44} \end{bmatrix} \begin{bmatrix} F^{+}_{c,b}(-L_{max}) \\ F^{-}_{c,b}(L_{max}) \\ F^{+}_{c,g}(-L_{max}) \\ F^{-}_{c,g}(L_{max}) \end{bmatrix} \tag{2.49}$$

Considering a symmetric coupling region (it starts and ends with the same semi-period), note that

$$M_{C(i+2)(j+1)} = -M_{Cij} \text{ for } i = 1,2 \text{ and } j = 1,3 \tag{2.50}$$

$$M_{C(i-2)(j+1)} = -M_{Cij} \text{ for } i = 3,4 \text{ and } j = 1,3 \tag{2.51}$$

The grating in the remaining part of the ring can be described by the 2x2 scattering matrix **S**, according to the CMT-based model reported in Paragraph 2.5.2.2. Thus:

$$\begin{bmatrix} F^{-}_{g}(\theta_{min,g}) \\ F^{+}_{g}(\theta_{max,g}) \end{bmatrix} = \begin{bmatrix} S_{11} & S_{12} \\ S_{21} & S_{22} \end{bmatrix} \begin{bmatrix} F^{+}_{g}(\theta_{min,g}) \\ F^{-}_{g}(\theta_{max,g}) \end{bmatrix} \tag{2.52}$$

where, according to the Paragraph 2.5.2.1, for a symmetric grating: $S_{22}=-iS_{11}$ and $S_{21}=-iS_{12}$.

The tangential field continuity conditions should be imposed at the boundary of each region, to derive the transfer function of the 1D-PhCRR: $F^{+}_{c,g}(L_{max})\equiv F^{+}_{g}(\theta_{min})$, $F^{-}_{c,g}(L_{max})\equiv F^{-}_{g}(\theta_{min})$, $F^{+}_{c,g}(-L_{max})\equiv F^{+}_{g}(\theta_{max})$ and $F^{-}_{c,g}(-L_{max})\equiv F^{-}_{g}(\theta_{max})$. Then, the transmission function of the 1D-PhCRR bus has been evaluated at the output of the bus waveguide *b*, imposing $F^{+}_{c,b}(-L_{max})\equiv 1$ and $F^{-}_{c,b}(L_{max})\equiv 0$.

2.5.3 Design

The main idea of the novel mathematical model proposed is to handle a set of features, as waveguide thickness/width, coupling gap or the ring radius, as to be able to tailor the structure according to the performance requirements, in terms of *Q*-factor and *ER*.

The physical and geometrical features of PhCRR have to be designed to operate into the slow light regime. In particular, the mode at the band edge should have a wave number equal to π/Λ, where Λ is the PhC period. Thus, due to the scale invariance of Maxwell's equations, the absolute frequency values v_d at the band edge strongly depend by the period Λ. Since v_d could be expressed as $v_d = v_0\Lambda = c$ and $\lambda_0 v_0 = c$, the condition $\Lambda = v_d\lambda_0$ ensures the operation into the slow-light regime at the target wavelength. Furthermore, the phase matching and periodicity conditions must be satisfied, to ensure the proper operation of the PhCRR.

The phase matching requirement is satisfied by imposing the length of the ring as a multiple of the normalized wavelength. This condition is given by:

$$2\cdot\pi\cdot R\cdot k = 2\cdot m\cdot\pi \tag{2.53}$$

where *R* is the ring radius, *k* is the mode wave vector and *m* is an integer number. The second condition can be expressed as:

$$2\cdot\pi\cdot R = N\cdot\Lambda \tag{2.54}$$

where *N* is an integer number [120].

The main design steps are summarized as follows:

1. technology platform selection, in order to ensure low-propagation loss that strongly affect the PhCRR *Q*-factor;
2. PhC selection, compliant to technology platform chosen;

3. period Λ definition, satisfying Eq.(2.54) at the operating wavelength;
4. choosing the gap gap_0 and the radius R, compliant to Eqs.(2.53 - 2.54), to satisfy the requirements of ER and Q-factor.

The fulfil of the design constraints and Eqs. (2.53 -2.54) guarantee an optimal design of the 1D-PhCRR with excellent performance, taking advantage by the slow light effect.

2.5.3.1 Technology platform selection

The design of a high Q-factor RR requires a technology platform with ultra-low propagation loss: quality factor value in the order of 10^9 can be obtained [52], by reducing the optical losses. In a planar waveguide, the sources of the propagation losses are similar to those of optical fiber: the total loss is the sum of many contributions, including material absorption, Rayleigh scattering, interfacial scattering, substrate leakage, bend radiation, and crosstalk loss.

The material absorption, mainly due to the OH- ions, could be strongly reduced by annealing, as example, resulting in values < 0.01 dB/m for silicon nitride-based waveguide. The interface scattering losses are larger than the bulk scattering ones, caused by the high index contrast and the waveguide sidewall roughness. The crosstalk loss can be reduced including a wide spacer between the waveguide cores, while, the substrate leakage can be minimized through the deposition of the thick bottom cladding layer. As example, a value of substrate loss of about 0.001 dB/m has been measured for Si_3N_4-based waveguides [154]. The interfacial loss can be reduced with slow fabrication steps, such as photoresist reflow, aiming at reducing the roughness of the core edges. The Rayleigh scattering, with propagation loss in the order of 0.1 dB/km, could be considered negligible respect to the higher contributions of the total propagation loss, as the interfacial scattering and bend radiation loss. The reduction of the scattering loss is the goal for all foundries. According to the scattering loss theory, the propagation losses could be reduced by decreasing the index contrast or the modal core confinement. The modal core confinement decreases in waveguides with high aspect ratio (waveguide width >> thickness), while, the index contrast could be reduced by

using stoichiometric materials. However, an ultra-small index contrast or modal core confinement involves an increase of the macro-bend radiation loss, then, affecting the total propagation losses.

Several technology platforms have been investigated, including silicon nitride [52, 155], silicon-on-insulator (SOI) [156-158], P- [49] and Ge-doped [159-160] silica and polymer [161]. The main features of the ultra-low loss waveguides (ULLWs) are summarized in Tab.2.7, focusing on the waveguide description, index contrast and the propagation loss.

Although the technology of UV written Ge-doped silica on silicon is a modern technique that allows low values of propagation losses, and a small footprint with low index contrast, it is not able to realize curvilinear waveguides. The silicon nitride technology represents the best compromise to realize a PhCRR with low propagation losses, small index contrast and small footprint.

Tab.2.7. Comparison between ULLWs, proposed in literature [49, 52, 155-161].

Technology platform	Silicon nitride	SOI	Polymer	P-doped silica	Ge-doped silica
Waveguide	LPCVD/ PECVD Si_3N_4 core with SiO_2 upper/bottom cladding	SOI wire or rib	Dopant-free core PBVE on plastic	P- doped core on SiO_2 with B- and P-doped glass as top cladding layer	Ge-doped core on SiO_2
Index contrast [%]	25	58	0.5	0.6 – 0.7	0.75
Propagation loss [dB/m]	0.7* [155] 0.045** [52]	40*,[1] [156] 12**,[1] [157] 2.7**,[2] [158]	3-4** [161]	0.85* [49]	4* [159] 0.3*** [160]

*single-mode; ** multi-mode; *** quasi single-mode; [1] wire; [2] rib.

As clearly shown in Tab. 2.7, silicon nitride ensures the lowest loss at the state-of-the-art, to my knowledge, in the order of 10^{-2} dB/m, about three orders of magnitude less than the silicon and polymer and one order of magnitude less than the P-doped silica on silicon, with the capability of hybrid integration of the all RMOG devices into a single chip.

For RMOG application, a single mode waveguide occurs to avoid the modal coupling inside the ring resonator, which could affect the correct operation of the device. Several silicon nitride-based single mode waveguides have been proposed in literature [146, 155, 162-163], and have been compared in Tab. 2.8, in terms of geometrical features, propagation losses and modal confinement TE (Γ_{TE}) and TM (Γ_{TM}).

The chosen waveguide shows a thickness of 100 nm and a width of 2.8 μm, ensuring a high TE power confinement and low value of replicable propagation loss, as reported into the Tab.2.8. The waveguide cross section is shown in Fig. 2.31.

Tab. 2.8. Comparison between single-mode Si_3N_4 ULLWs, proposed in literature at about 1550 nm [146, 155, 162-163].

Ref.	Core width [μm]	Core thickness [nm]	α [dB/m]	Top cladding thickness [μm]	Bottom cladding thickness [μm]	Γ_{TE} [%]	Γ_{TM} [%]
[162]	2.8	60	1.01	6	15	3.83	0.63
[146]	2.8	80	2.91	7.5	8	7.5	1.57
[146]	2.8	90	4.22	7.5	8	9.63	2.26
[146]	2.8	100	3.5	7.5	8	11.91	3.07
[163]	2.8	100	3.63	18.1	15	11.92	3.07
[155]	5.3	50	0.7	15	15	3.31	0.72

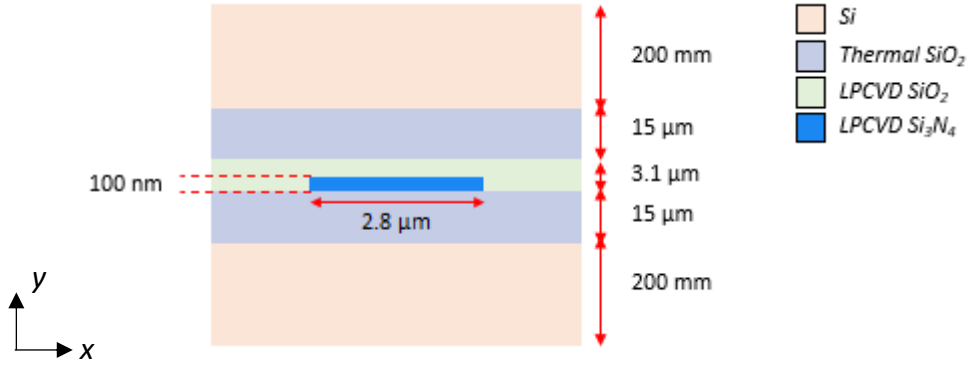

Fig. 2.31. Si_3N_4 – based waveguide 100 nm thick and 2.8 µm wide *(LPCVD*: Low Pressure Chemical Vapour Deposition).

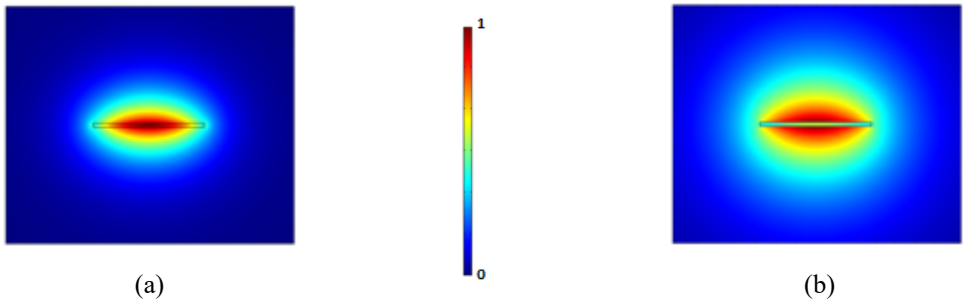

(a) (b)

Fig. 2.32. Electric field normalized distribution of the TE (a) and TM (b) mode into the waveguide in Fig.2.31.

The waveguide is fabricated on 200 mm Si substrate with 15 µm of thermal oxide as the lower cladding (n=1.45), with a core waveguide thickness of 100 nm of stoichiometric Si_3N_4 (n=1.98) deposited by low-pressure chemical vapor deposition (LPCVD) and patterned by contact lithography. The upper cladding shows 3.1 µm of SiO_2 deposited by LPCVD. Then, the waveguide cross-section is finished by the wafer bonding.

The waveguide has been proposed for sidewall grating manufacturing [114] and the TE waveguide propagation loss, measured over the range 1540 - 1570 nm, shows a monotonic behaviour from 5.5 to 2.7 dB/m.

The distributions of the electric field for the TE and TM modes, are reported in Figs. 2.32 (a) – 2.32(b), respectively. At 1550 nm, the TE and TM effective refractive index are 1.47869 and 1.45569, respectively.

The thinner upper cladding, respect to other waveguides [155, 163], ensures a small confinement of the TM mode, and the, the waveguide could be considered as strictly single-mode. The simulations have been carried out by using the FEM

approach, assuming all SiO_2 layers with same refractive index (n=1.45). The confinement of the fundamental TM mode (Fig. 2.32(b)) in Si_3N_4 core, is much lower than that of the fundamental TE mode (Fig. 2.32(a)) ($\Gamma_{TE}/\Gamma_{TM}\approx6.8$), in such high-aspect-ratio designs (waveguide width : thickness > 100 : 1). The TE confinement factor Γ_{TE} of the waveguide is about 11.5%: a low value of the confinement ensures low loss and the capability to use such waveguide for sensing applications, eliminating the upper cladding, intercepting any externally molecules.

2.5.3.2 Photonic crystal selection

Several topologies of Si_3N_4-based 1D photonic crystal have been investigated, as post, sidewall and top grating [114-115,118]. Although the post grating is easily manufacturable, it shows a very low coupling factor value (≈ 1 cm^{-1}), and then, a large number of PhC periods is required to obtain high performance. The sidewall grating as building block of 1D-PhCRR has been investigated in the last years [164-166]. It ensures the highest value of the coupling factor (> 10 cm^{-1}), but it could be manufactured by using the in-line stepper lithography, whose typical resolution (in the order of 450 nm) involves the grating operation at wavelength not of interest ($\lambda\approx2.6$ μm). Then, the top grating has been preferred for the PhCRR design, showing a quite high coupling factor (≈ 10 cm^{-1}). Furthermore, the fabrication of the top grating along a long and bent optical path is feasible by using the standard e-beam lithography with a resolution of about 10 nm. The schematic of the top grating is reported in Fig. 2.33. It consists of a 1D PhC made by a thickness modulation, with a square profile, along the propagation direction. For a proper operation, the two sections of the PhC should be single-mode. Thus, the modulation depth d is defined by the modal analysis of the waveguide thickness, fixing the waveguide width = 2.8 μm. The TE_0 and TE_1 effective refractive index trends ($n_{eff,TE}$), varying the waveguide thickness, are reported into the Fig.2.34, where the single-mode and multi-mode regions are highlighted. The waveguide could be considered single mode up to a waveguide thickness of 105 nm.

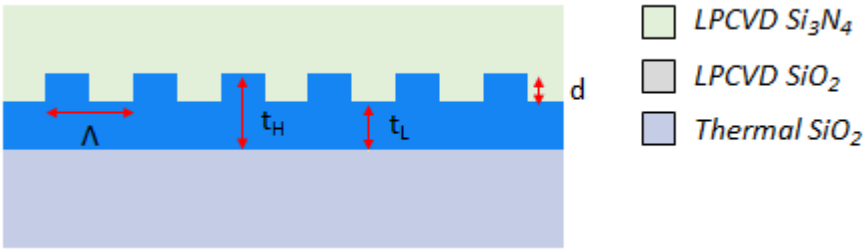

Fig.2.33. Si_3N_4-based top grating, (Λ: period; t_H: maximum thickness; t_L: minimum thickness; d: modulation depth).

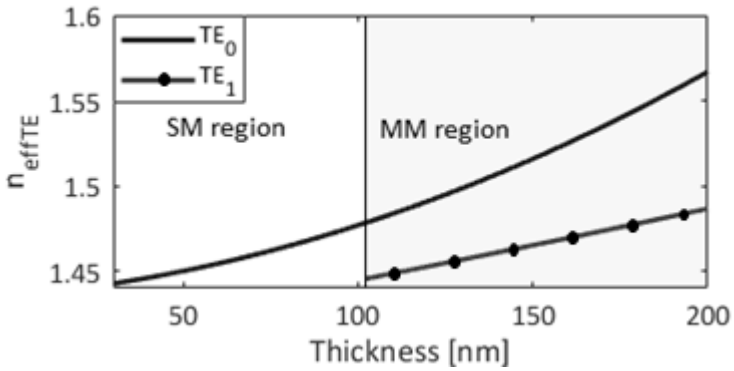

Fig. 2.34. n_{effTE} *vs* waveguide thickness.

In order to prevent that some manufacturing issues could excited higher modes and to ensure a fabrication feasibility, a t_H and t_L equal of 100 nm and 60 nm, respectively, has been considered. To ensure the operation at about 1550 nm, a period Λ = 526 nm has been designed.

2.5.4 PhCRR simulated performance

Several radii of the 1D-PhCRR have been investigated. As example, a PhCRR with a radius R of about 2 mm is shown in Fig. 2.35 (the top cladding is not shown). The waveguide and grating features have been reported in Paragraphs 2.5.3.1 and 2.5.3.2, respectively. The propagation loss of the grating has been assumed equal to 15 dB/m, about 5 times greater than the propagation loss of the bare straight waveguide (see Tab. 2.8), with a conservative approach. This assumption is due to a lack of losses value of Si_3N_4 grating in literature. It represents a conservative approach, in order to consider the large losses due to sidewall

roughness of the grating. For the bent grating, the propagation losses have been added to the curvature one.

As example, a centre-to-centre gap gap_0 of 4.8 µm has been considered. The TE mode transmission spectrum of the device is reported in Fig. 2.36, focusing on the right band-edge. The magnification of the first band edge peak is shown in Fig. 2.37 and shows a *Q*-factor equal to 2 x 10^{10} with an *ER* of 6.26 dB, while, the other resonances in the spectrum show a *Q*-factor of the order of 10^9.

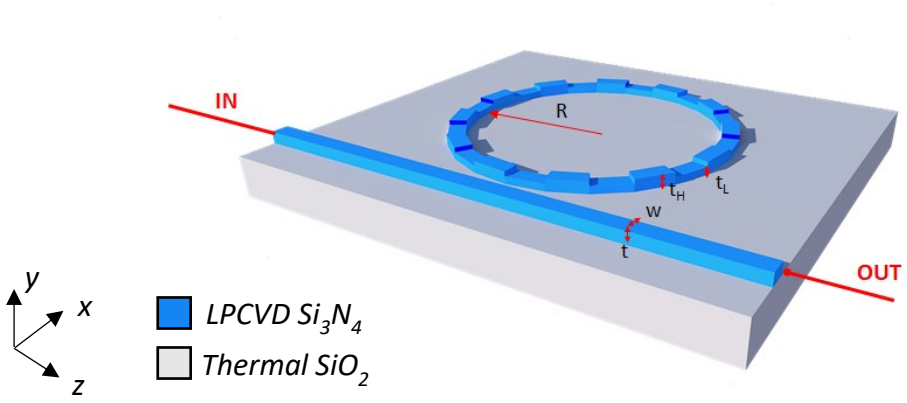

Fig. 2.35. 1D PhCRR based on top grating, (*w*: waveguide width; *t*: waveguide thickness; t_H: grating maximum thickness; t_L: grating minimum thickness; *R*: radius).

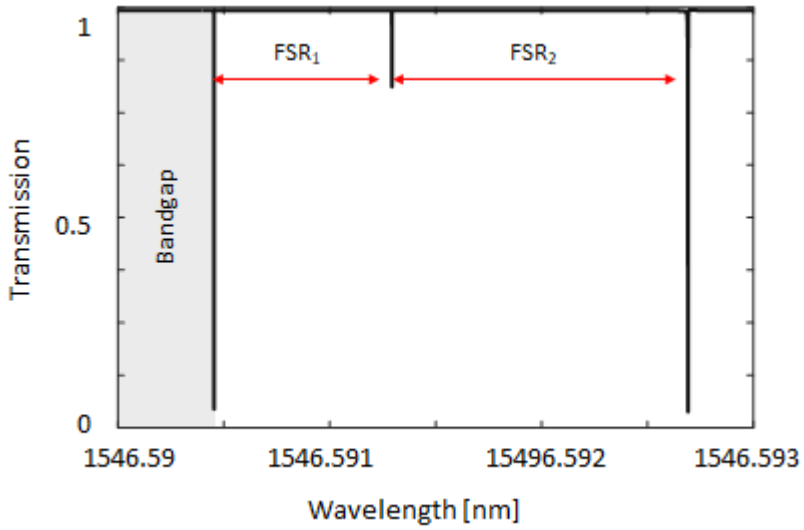

Fig. 2.36. Simulated TE-polarized transmission spectrum of 1D-PhCRR based on top grating (*FSR:* Free Spectral Range).

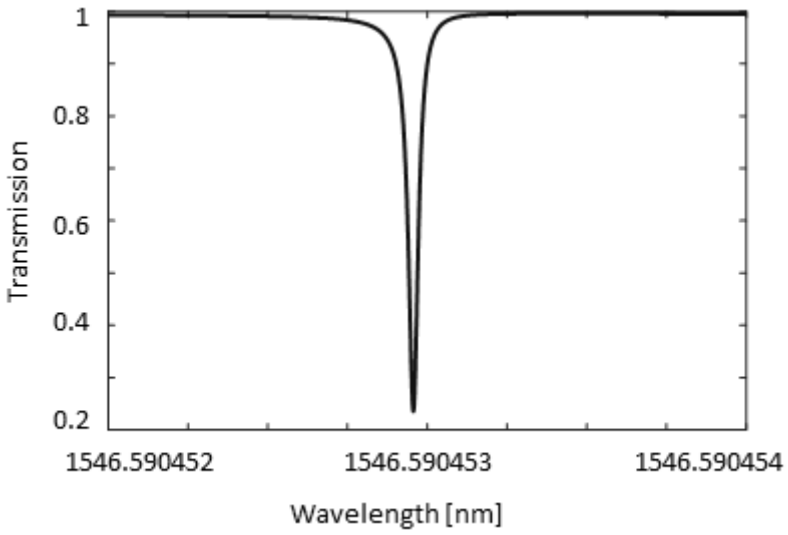

Fig. 2.37.1st band edge transmission peak of Full-PhCRR based on top grating.

The 1D-PhCRR performs an improvement of 3 order of magnitude, with respect to a ring resonator with R = 2 mm, based on the selected waveguide: a Q-factor in the order of 10^6, with ER of about 6 dB, has been simulated. Furthermore, the peak shows a typical Fano resonance, with an asymmetric behaviour, due to a self-consistent process.

Since the PhC generates two backpropagating modes, the interference between them generates the Fano resonance peak into the PhCRR response, in contrast to the Lorentzian behaviour generated by a simple ring resonator, where the reflection of the structure is null. The Fano response results by a different phase variation of the forward and backward waves, around the resonance frequency [167]. Then, the constructive and destructive interferences lead the generation of spikes, on the right or left side of the resonance peak for even or odd orders of resonance, respectively, with a transmission excursion of about 0.1%.

Another feature of the PhCRR transmission spectrum is the non-constant FSR, due to the strong dispersion of the PhC at the band-edge. In particular, it increases with the frequency: the FSR between the first and the second resonance, called FSR_1, is equal to about 0.8 pm, instead the FSR between the second and the third resonance, called FSR_2, is equal to about 1 pm.

Changing some features of the PhCRR (length of PhC, gap between bus and ring waveguides), the targeted resonance ER can be obtained to satisfy specific application requirements, as reported in Tab.2.9.

Tab. 2.9. Simulated PhCRR features to obtain ER of 8 and 10 dB, and the performance of the RMOG based on the designed PhCRRs.

R [mm]	gap_0 [µm]	Q	ER [dB]	δΩ [°/hr]
2	4.09	1.18×10^{10}	7.99	0.03130
	3.95	8.14×10^{9}	10.08	0.04544
4	4.27	9.34×10^{10}	8.03	0.00198
	4.19	8.15×10^{10}	10.12	0.00227
6	4.32	1.80×10^{11}	7.95	0.00068
	4.26	1.59×10^{11}	9.81	0.00077
8	4.36	2.67×10^{11}	7.87	0.00034
	4.30	2.53×10^{11}	9.86	0.00036

A minimum radius R of 2 mm has been considered in order to neglect the propagation losses associated to the waveguide curvature, as demonstrated in the Paragraph 2.5.2.1.

Finally, according to the Eq. (2.2), taking into account BW=20 Hz, η=0.9, P_{PD}=10 mW, a shot-noise limited resolution < 0.05 °/hr could be obtained by using a Si_3N_4 -based PhCRR, with a radius more than 2 mm, as sensitive element of a RMOG configuration (see Tab.2.9). The resolution could be furtherly improved by using a wider bandwidth BW. Furthermore, the proposed PhCRR is suitable for a hybrid integration of the RMOG architecture on a single chip, with an estimated footprint of 0.2 mm^2. This performance makes the RMOG based on the designed device suitable for high-class gyro applications.

2.6 Conclusions

The main operation of the attitude and orbit control sub-systems is briefly described in this Chapter, reviewing the commercial inertial measurement unit. Aiming at the development of an optoelectronic ultra-compact gyro having performance and reliability compliant with the requirement of high-class missions, well-established, i.e. SRL and RMOG, and emerging, i.e. exploiting the Brillouin effect, approaches have been explored. All those devices have been critically

discussed, reporting advantages, critical aspects and theoretical/experimental performance of each technology.

In this context, a compact and high performing RMOG configuration, based on an ultra-high *Q* ring resonator, called as PhCRR, has been proposed. It consists in a simple ring resonator, that include a 1D PhC along the whole optical path. The electromagnetic simulations of this device have been carried out by using a self-made mathematical model based on the CMT. A *Q*-factor > 10^9 has been calculated, for a Si_3N_4 based PhCRR with top grating and a radius more than 2 mm. This performance ensures a shot-noise limited resolution less than 0.05 °/hr, compliant to the high-class requirements, using the designed PhCRR as sensitive element of a RMOG configuration. Furthermore, the choice of a Si_3N_4 technology platform offers the capability of hybrid integration of all RMOG devices on a single chip, with an estimated volume < 1 cm^3. Besides the Space applications, the proposed PhCRR could be considered promising for medical diagnostic and drink water monitoring.

2.7 References

[1] W. A. Imbriale, S. S. Gao, and L. Boccia, *Space antenna handbook*, John Wiley & Sons, 2012.

[2] K. H. Glassmeier, H. Boehnhardt, D. Koschny, E. Kührt, and I. Richter, "The Rosetta mission: flying towards the origin of the solar system. Space Science Reviews," **128**, 1-4, pp. 1-21, 2007.

[3] M. S. Lefebvre, "New Satellite Missions for Solid Earth Studies-Status and Preparations," CSTG Bulletin, **11**, pp. 25-32, 1989.

[4] C. Donlon, B. Berruti, A Buongiorno, M-H Ferreira, P. Femenias, J. Frerick, P. Goryl, U. Klein, H. Laur, C. Mavrocordatos, J. Nieke, H. Rebhan, B. Seitz, J. Stroede, and R. Sciarra, "The Global Monitoring for Environment and Security (GMES) Sentinel-3 Mission," Remote Sensing of the Environment, **120**, pp. 37–57, 2012.

[5] L. Perret, E. Boussarie, J. M. Lachiver, and P. Damilano, "The Pléiades System high resolution optical satellite and its performances," Proc. of the

53rd IAC/World Space Congress, Houston, Texas, USA, October 10-19, 2002.

[6] J. M. Dow, R. E. Neilan, and C. Rizos, "The international GNSS service in a changing landscape of global navigation satellite systems," Journal of geodesy, **83**, 3-4, pp.191-198, 2009.

[7] A. El-Rabbany, *Introduction to GPS: the global positioning system*, Artech house, 2002.

[8] A. Leick, "GLONASS satellite surveying," Journal of surveying engineering, **124**, 2, pp, 91-99, 1998.

[9] J. Benedicto, S. Dinwiddy, G. Gatti, R. Lucas, and M. Lugert, "GALILEO: Satellite system design," European Space Agency. Int. Business, 2000.

[10] C. Shi, Q. Zhao, M. Li, W. Tang, Z. Hu, Y. Lou, H. Zhang, X. Niu, and J. Liu, "Precise orbit determination of Beidou Satellites with precise positioning," Science China Earth Sciences, **55**, 7, pp. 1079-1086, 2012.

[11] W. J. Feller, M. L. Whitehead, and J. A. McClure, Combined GNSS gyroscope control system and method, U.S. Patent No. 8,265,826, Washington, DC: U.S. Patent and Trademark Office, 2012.

[12] C. Ciminelli, F. Dell'Olio, and M. N. Armenise, *Photonics in Space: Advanced Photonic Devices and Systems*, World Scientific, 2016.

[13] M. N. Armenise, C. Ciminelli, F. Dell'Olio, and V. M. Passaro, *Advances in gyroscope technologies*, Springer Science & Business Media, 2010.

[14] C. C. Liebe, E. W. Dennison, B. Hancock, R. C. Stirbl, and B. Pain, "Active pixel sensor (APS) based star tracker," Proc. of 1998 IEEE Aerospace Conference Proceedings, IEEE, **1**, pp. 119-127, Aspen, Colorado, USA, March 28, 1998.

[15] B. N. Agrawal, and W. J. Palermo, "Angular Rate Estimation for Gyroless Satellite Attitude Control," Proc. of AIAA Guidance, Navigation, and Control Conference, pp. 4463, Monterey, California, USA, August 5–8, 2002.

[16] Platino Project, https://indico.esa.int/event/252/contributions/3837/attachments/3003/3607/PLATiNO_Project.pdf

[17] E. J. Lefferts, F. L. Markley, and M. D. Shuster, "Kalman filtering for spacecraft attitude estimation," Journal of Guidance, Control, and Dynamics, **5**, 5, pp. 417-429, 1982.

[18] Colibrys MS1000 series, https://www.colibrys.com/wp-content/uploads/2016/12/30s-ms1000-e-04-18-datasheet.pdf

[19] Colibrys MS9000 series, https://www.colibrys.com/wp-content/uploads/2015/03/30S-MS9000.M.03.15-nod1.pdf

[20] Honeywell HG9030, https://aerospace.honeywell.com/en/~/media/aerospace/files/brochures/n61-1523-000-010-hg4930-mems-inertial-measurement-unit-bro.pdf

[21] Northrop Grumann LN200S, https://www.northropgrumman.com/Capabilities/LN200FOG/Documents/ln200s.pdf

[22] Honeywell QA2000, https://aerospace.honeywell.com/en/~/media/aerospace/files/brochures/accelerometers/q-flexqa-2000accelerometer_bro.pdf

[23] Honeywell QA3000, https://asc-sensors.de/datenblatt/honeywell/beschleunigungssensor/q-flex/qa-3000.pdf

[24] Honeywell HG9900, https://aerospace.honeywell.com/en/~/media/aerospace/files/brochures/n61-1638-000-000-hg9900inertialmeasurementunit-bro.pdf

[25] R. Schmidt, "Mars Express-ESA's first mission to planet Mars," Acta Astronautica, **52**, 2-6, pp. 197-202, 2003.

[26] P. McNamara, S. Vitale, and K. Danzmann, "LISA pathfinder," Classical and Quantum Gravity, **25**, 11, 114034, 2008.

[27] H. Svedhem, *et al.,* "Venus Express—the first European mission to Venus," Planetary and Space Science, **55**, 12, pp. 1636-1652, 2007.

[28] Northrop Grumman SIRU,

https://www.northropgrumman.com/MediaResources/MediaKits/Satellite/Documents/SIRU_Family.pdf

[29] Airbus Astrix-200, https://spaceequipment.airbusdefenceandspace.com/avionics/fiber-optic-gyroscopes/astrix-200/

[30] Honeywell MIMU, https://aerospace.honeywell.com/en/products/space/satellite-products-and-systems/satellite-bus-equipment/miniature-inertial-measurement-unit-mimu

[31] A. Jeanroy, G. Grosset, J. C. Goudon, and F. Delhaye, "HRG by Sagem from laboratory to mass production," Proc. of 2016 IEEE International Symposium on Inertial Sensors and Systems, IEEE, pp. 1-4, March 23-26 , 2016.

[32] Thales Avionics, "*QUASAR 3000: Manuel d'utilisation et de maintenance*." A5E-MU-1432100B-101259 J14109AA, pp. 110-117.

[33] Airbus Astrix 1000, https://spaceequipment.airbusdefenceandspace.com/avionics/fiber-optic-gyroscopes/astrix-1000/

[34] Sensonor STIM300, https://www.sensonor.com/media/1132/ts1524r9-datasheet-stim300.pdf

[35] F. Dell'Olio, T. Tatoli, C. Ciminelli, and M. N. Armenise, "Recent advances in miniaturized optical gyroscopes," Journal of the European optical society-Rapid publications, **9**, 2014.

[36] S. Liao, and S. Wang, "Semiconductor injection lasers with a circular resonator," Applies Physics Letters, **36**, 10, pp. 801-803, 1980.

[37] M. N. Armenise, V. M. N. Passaro, F. De Leonardis, and M. Armenise, "Modeling and design of a novel miniaturized integrated optical sensor for gyroscope applications," Journal of Lightwave Technologies, **19**, 10, pp. 1476–1494, 2001.

[38] M. N. Armenise, M. Armenise, V. M. N. Passaro, and F. De Leonardis, Integrated optical angular velocity sensor, European Patent # 1219926, 2000.

[39] K. Taguchi, K. Fukushima, A. Ishitani, and M. Ikeda, "Self-detection characteristics of the Sagnac frequency shift in a mechanically rotated semiconductor ring laser," Measurement, **27**, 4, pp. 251-256, 2000.

[40] M. Osiński, H. Cao, C. Liu, and P. G. Eliseev, "Monolithically integrated twin ring diode lasers for rotation sensing applications," Journal of Crystal Growth, **288**, 1, pp. 144-147, 2006.

[41] T. Qiu, J. Wu, L. K. Strandjord, and G. A. Sanders, "Performance of resonator fiber optic gyroscope using external-cavity laser stabilization and optical filtering ", Proc. of 23rd International Conference on Optical Fibre Sensors, International Society for Optics and Photonics, **9157**, p. 91570B, Santander, Spain, June 2-6, 2014.

[42] G. A. Sanders, L. K. Strandjord, and T. Qiu, "Hollow core fiber optic ring resonator for rotation sensing," Proc. of Optical Fiber Sensors, p. ME6, Cancún, Mexico, October 23–27, 2006.

[43] M. A. Terrel, M. J. F. Digonnet, and S. Fan, "Resonant fiber optic gyroscope using an air-core fiber," Journal of Lightwave Technology, **30**, 7, pp. 931–937, 2012.

[44] I. Fsaifes, G. Feugnet, A. Baz, A. Ravaille, B. Debord, F. Gérome, G. Humbert, S. Schwartz, F. Benabid, and F. Bretenaker, "Hollow-Core Photonic-Bandgap Fiber Resonator for Rotation Sensing," Proc. of CLEO: Science and Innovations, Optical Society of America, pp. SM2P-4, June 5-10, 2016.

[45] W. Liang, V. S. Ilchenko, A. A. Savchenkov, E. Dale, D. Eliyahu, A. B. Matsko, and L. Maleki, "Resonant microphotonic gyroscope," Optica, **4**, 1, pp. 114-117, 2017.

[46] A. A. Savchenkov, V. S. Ilchenko, A. B. Matsko, and L. Maleki, "Kilohertz optical resonances in dieletric crystal cavities," Physical Review A, 70, 5, 051804, 2004.

[47] A. A. Savchenkov, A. B. Matsko, V. S. Ilchenko, and L. Maleki, "Optical resonators with ten million finesse," Optics Express. 15, 11, pp. 6768-6773, 2007.

[48] F. Dell'Olio, G. Brunetti, D. Conteduca, N. Sasanelli, C. Ciminelli, and M. N. Armenise, "Planar Photonic Gyroscopes for Satellite Attitude Control," Proc. of 7th International Workshop on Advances in Sensors and Interfaces (IWASI), pp. 167-169, Vieste, Italy, June 15-16, 2017.

[49] R. Adar, M. R. Serbin, and V. Mizrahi, "Less than 1 dB per meter propagation loss of silica waveguides measured using a ring resonator," Journal of Lightwave Technology, **12**, 8, pp. 1369–1372, 1994.

[50] D. T. Spencer, Y. Tang, J. F. Bauters, M. J. R. Heck, and J. E. Bowers, "Integrated Si_3N_4/SiO_2 ultra high Q ring resonators," Proc. of IEEE Photonics Conference 2012, pp. 141–142, Burlingame, California, USA, September 23-27, 2012.

[51] M.-C. Tien, J. F. Bauters, M. J. R. Heck, D. T. Spencer, D. J. Blumenthal, and J. E. Bowers, "Ultra-high quality factor planar Si_3N_4 ring resonators on Si substrate," Optics Express, **19**, 14, pp. 13551-13554, 2011.

[52] D.T. Spencer, J.F. Bauters, M. J. Heck, and J. E. Bowers, "Integrated waveguide coupled Si_3N_4 resonators in the ultrahigh-Q regime," Optica, **1**, 3, pp. 153-157, 2014.

[53] J. Wang, L. Feng, Q. Wang, X. Wang, and H. Jiao, "Reduction of angle random walk by in-phase triangular phase modulation technique for resonator integrated optic gyro," Optics Express, **24**, 5, pp. 5463-5468, 2016.

[54] J. Wang, L. Feng, Q. Wang, H. Jiao, and X. Wang, "Suppression of backreflection error in resonator integrated optic gyro by the phase difference traversal method," Optics Letters, **41**, 7, pp. 1586-1589, 2016.

[55] J. T. Bovington, M. J. R. Heckand, and J. E. Bowers, "Heterogeneous lasers and coupling to Si_3N_4 near 1060 nm," Optics Letters, **39**, 20, pp. 6017-6020, 2014.

[56] H. Lee, T. Chen, J. Li, K. Y. Yang, S. Jeon, O. Painter, and K. J. Vahala, "Chemically etched ultrahigh-Q wedge-resonator on a silicon chip," Nature Photonics, **6**, 6, 369, 2012.

[57] K. Y. Yang, D. Y. Oh, S. H. Lee, Q. F., Yang, X. Yi, B. Shen, H. Wang, and K. Vahala, "Bridging ultrahigh-Q devices and photonic circuits," Nature Photonics, **12**, 5, 297, 2018.

[58] M. Smit, *et al.*, "An introduction to InP-based generic integration technology," Semiconductor Science and Technology, **29**, 8, 083001, 2014.

[59] C. Ciminelli, F. Dell'Olio, M. N. Armenise, F. M. Soares, and W. Passenberg, "High performance InP ring resonator for new generation monolithically integrated optical gyroscopes," Optics Express, **21**, 1, pp. 556–564, 2013.

[60] D. D'Agostino, G. Carnicella, C. Ciminelli, P. Thijs, P. J. Veldhoven, H. Ambrosius, and M. Smit, "Low-loss passive waveguides in a generic InP foundry process via local diffusion of zinc," Optics Express, **23**, 19, pp. 25143-25157, 2015.

[61] C. Ciminelli, D. D'Agostino, G. Carnicella, F. Dell'Olio, D. Conteduca, H. P. Ambrosius, M. K. Smit, and M. N. Armenise, "A high-Q InP resonant angular velocity sensor for a monolithically integrated optical gyroscope," IEEE Photonics Journal, **8**, 1, pp. 1-19, 2015.

[62] F. Dell'Olio, F. Indiveri, F. Innone, P. Dello Russo, C. Ciminelli, and M. N. Armenise, "System test of an optoelectronic gyroscope based on a high Q-factor InP ring resonator," Optical Engineering, **53**, 12, 127104, 2014.

[63] C. Ciminelli, C. E. Campanella, and M. N. Armenise, Optical rotation sensor as well as method of manufacturing an optical rotation sensor, European Patent # EP 056933, 2013.

[64] P. P. Khial, A. D. White, and A. Hajimiri, "Nanophotonic optical gyroscope with reciprocal sensitivity enhancement," Nature Photonics, **12**, 11, pp. 671-676, 2018.

[65] S. Srinivasan, R. Moreira, D. Blumenthal, and J. E. Bowers "Design of integrated hybrid silicon waveguide optical gyroscope," Optics Express, **22**, 21, pp. 24988-24993, 2014.

[66] S. Gundavarapu, M. Belt, T. A. Huffman, M. A. Tran, T. Komljenovic, J. E. Bowers, and D. J. Blumenthal, "Interferometric optical gyroscope based on

an integrated Si_3N_4 low-loss waveguide coil," Journal of Lightwave Technology, **36**, 4, pp. 1185-1191, 2018.

[67] J. Li, M. G. Suh, and K. Vahala, "Microresonator Brillouin gyroscope," Optica, **4**, 3, pp. 346-348, 2017.

[68] K. Vahala, Y. H. Lai, and M. G. Suh, "An On-chip Optical Brillouin Gyroscope with Earth-Rotation-Rate Sensitivity," Proc. of CLEO:QELS_Fundamental Science, Optical Society of America, pp. FTu3B-1, San Jose, California, USA, May 5-10, 2019.

[69] J. Ren, H. Hodaei, G. Harari, A. U. Hassan, W. Chow, M. Soltani, D. Christodoulides, and M. Khajavikhan, "Ultrasensitive micro-scale parity-time-symmetric ring laser gyroscope," Optics letters, **42**, 8, pp. 1556-1559, 2017.

[70] W. Chen, J. Zhang, B. Peng, Ş. K. Özdemir, X. Fan, and L. Yang, "Parity-time-symmetric whispering-gallery mode nanoparticle sensor," Photonics Research, **6**, 5, pp. A23-A30, 2018.

[71] "Basic mechanisms of radiation effects in the natural space radiation environment", (No. SAND-94- 1580C; CONF-940726-12). Sandia National Labs., Albuquerque, NM (United States), 1994.

[72] E. R. Benton**,** and E. V. Benton, "Space radiation dosimetry in low-Earth orbit and beyond," Nuclear Instruments and Methods in Physics Research, Sect. B, **184**, 1-2, pp. 255–294, 2001.

[73] IARC Working Group on the Evaluation of Carcinogenic Risks to Humans, World Health Organization, & International Agency for Research on Cancer, Non-ionizing Radiation: Static and extremely low-frequency (ELF) electric and magnetic fields, **80**, World Health Organization, 2002.

[74] E. G. Stassinopoulos**,** and J. P. Raymond, "The space radiation environment for electronics," Proc. of IEEE, **76**, 11, pp. 1423–1442, 1988.

[75] O. Adriani, *et al.*, "The PAMELA experiment on satellite and its capability in cosmic rays measurements," Nuclear Instruments and Methods in Physics Research, Sect. A, **478**, 1-2, pp. 114–118, 2002.

[76] M. Boscherini, O. Adriani, M. Bongi, L. Bonechi, G. Castellini, R. D'Alessandro,A. Gabbanini, M. Grandi, W. Menn, P. Papini, S. B. Ricciarini, M. Simon, P. Splillantini, S. Straulino, F. Taccetti, M. Tesi**,** and W. Vannuccini, "Radiation damage of electronic components in space environment," Nuclear Instruments and Methods in Physics Research, Sect. A, **514**, 1-3, pp. 112 – 116, 2003.

[77] J. L. Barth**,** and E. Stassinopoulos, "Space, Atmospheric, and Terrestrial Radiation Environments," IEEE Transactions Nuclear Science, 50, 3, pp. 466–482, 2003.

[78] S. Bourdarie**,** and M. Xapsos, "The Near-Earth Space Radiation Environment," IEEE Transactions Nuclear Science, **55**, 4, pp. 1810–1832, 2008.

[79] W. Heitler, *The quantum theory of radiation*, Courier Corporation, 1984.

[80] T. P. Ma**,** and P. V. Dressendorfer, *Ionizing radiation effects in MOS devices and circuits*, John Wiley & Sons, 1989.

[81] F. Larin, *Radiation Effects in Semiconductor Devices*, Wiley, 1968.

[82] C. E. Barnes**,** and J. J. Wiczer, "Radiation Effects in Optoelectronics Devices," (No. SAND-84-0771), Sandia National Labs., Albuquerque, NM (United States), 1984.

[83] H. Lischka, H. Henschel, W. Lennartz**,** and K. U. Schmidt, "Radiation sensitivity of light emitting diodes (LED), laser diodes (LD) and photodiodes (PD)," IEEE Transactions Nuclear Science, **39**, 3, pp. 423–427, 1992.

[84] K. A. Gill, G. Cervelli, R. Grabit, F. B. Jensen**,** and F. Vasey, "Radiation damage and annealing in 1310-nm InGaAsP/InP lasers for the CMS tracker," Proc. of Photonics for Space Environments VII, International Society for Optics and Photonics, **4134**, pp. 176–185, San Diego, California, USA, July 31 – August 1, 2000.

[85] V. Brasch, Q. F. Chen, S. Schiller**,** and T. J. Kippenberg, "Radiation hardness of high-Q silicon nitride microresonators for space compatible integrated optics," Optics Express, **22**, 25, pp. 30786–30794, 2014.

[86] S. Bhandaru, S. Hu, D. M. Fleetwood, and S. M. Weiss, "Total Ionizing Dose Effects on Silicon Ring Resonators," IEEE Transactions Nuclear Science, **62**, 1, pp. 323–328, 2015.

[87] P. Dumon, R. Kappeler, D. Barros, I. Mc Kenzie, D. Doyle, and R. Baets, "Measured radiation sensitivity of Silica-on-Silicon and Silicon-on-insulator micro-photonic devices for potential space application," Proc. of Photonics for Space Environments X, International Society for Optics and Photonics, 5897, p. 58970D, San Diego, California, USA, August 1-2, 2005.

[88] Z. Ahmed, L. T. Cumberland, N. N. Klimov, I. M. Pazos, R. E. Tosh, and R. Fitzgerald, "Assessing Radiation Hardness of Silicon Photonic Sensors," Scientific Reports, **8**, 1, 13007, 2018.

[89] A. H. Johnston, "Radiation Effects in Light-Emitting and Laser Diodes," IEEE Transactions Nuclear Science, **50**, 3, pp. 689–703, 2003.

[90] A. F. Fernandez, B. Brichard, and F. Berghmans, "In situ measurement of refractive index changes induced by gamma radiation in germanosilicate fibers," IEEE Photonics Technology Letters, **15**, 10, pp. 1428–1430, 2003.

[91] S. Girard, A. Morana, A. Ladaci, T. Robin, L. Mescia, J. J. Bonnefois, M. Boutillier, J. Mekki, A. Paveau, B. Cadier, E. Marin, Y. Ouerdane, and A. Boukenter, "Recent advances in radiation-hardened fiber-based technologies for Space applications," Journal of Optics, **20**, 9, 093001, 2018.

[92] R. S. Evenblij, T. van Leest, and M. B. Haverdings, "Integrated photonics for fiber optic based temperature sensing," Proc. of International Conference on Space Optics—ICSO 2016, International Society for Optics and Photonics, **10562**, p. 1056210, Biarritz, France, October 16-21, 2016.

[93] W. Primak, "Fast-Neutron-Induced Changes in Quartz and Vitreous Silica," Physical Review, **110**, 6, pp. 1240–1254, 1958.

[94] A. H. Johnston, "Radiation effects in optoelectronic devices," IEEE Transactions Nuclear Science, **60**, 3, pp. 2054–2073, 2013.

[95] G. Brunetti, I. McKenzie, F. Dell'Olio, M. N. Armenise, and C. Ciminelli, "Measured radiation effects on InGaAsP/InP ring resonators for space applications", Optics Express, **27**, 17, pp. 24434-24444, 2019.

[96] F. Dell'Olio, C. Ciminelli, M. N. Armenise, F. M. Soares, and W. Rehbein, "Design, fabrication, and preliminary test results of a new InGaAsP/InP high-Q ring resonator for gyro applications," Proc. of 2012 International Conference on Indium Phosphide and Related Materials (IPRM), IEEE, pp. 124–127, Santa Barbara, California, USA, August 27-30, 2012.

[97] C. Ciminelli, and M. N. Armenise, "Final report", ESA-founded project MiOS (Micro Optical Angular Velocity Sensor), November, 2014.

[98] U. Fano, "Effects of configuration interaction on intensities and phase shifts," Physical Review, **124**, 6, pp. 1866–1878, 1961.

[99] W. Bogaerts, P. De Heyn, T. Van Vaerenbergh, K. De Vos, S. K. Selvaraja, T. Claes, P. Dumon, P. Bienstman, D. Van Thourhout, and R. Baets, "Silicon microring resonators," Laser Photonics Review, **6**, 1, pp. 47–73, 2012.

[100] A. Yariv, "Critical coupling and its control in optical waveguide-ring resonator systems," IEEE Photonics Technology Letters, **14**, 4, pp. 483–485, 2002.

[101] A. Waqas, A. Alippi, D. Melati, and A. Melloni, "An improved model to predict thermo-optic coefficient in InGaAsP waveguides," Proc. of 2016 18th International Conference on Transparent Optical Networks (ICTON), IEEE, pp. 1-4, Trento, Italy, July 10-14, 2016.

[102] Total Dose Steady-State Irradiation Test Method, ECSS European Space Components Coordination, 5, June 2016, http://escies.org/escc- specs/published/22900.pdf.

[103] Co-60 source at ESA-ESTEC, https://escies.org/webdocument/showArticle?id=251.

[104] R. L. Pease, G. W. Dunham, J. E. Seiler, D. G. Platteter, and S. S. McClure, "Total dose and dose rate response of an AD590 temperature transducer," IEEE Transactions Nuclear Science, **54**, 4, pp. 1049–1054, 2007.

[105] C. Ciminelli, G. Brunetti, F. Dell'Olio, F. Innone, D. Conteduca, and M. N. Armenise, "Emerging applications of Whispering Gallery Mode photonic resonators," Lecture Notes in Electrical Engineering, **429**, pp. 185-191, 2017.

[106] T. Baba, "Slow light in photonic crystals," Nature photonics, **2**, 8, pp. 465-473, 2008.

[107] T. F. Krauss, "Slow light in photonic crystal waveguides," Journal of Physics D: Applied Physics, **40**, 9, pp. 2666-2670, 2007.

[108] A. Yariv, Y. Xu, R. K. Lee, and A. Scherer, "Coupled-resonator optical waveguide: a proposal and analysis," Optics Letters, **24**, 11, pp. 711-713, 1999.

[109] J. E. Heebner, R. W. Boyd, and Q.-H. Park, "SCISSOR solitons and other novel propagation effects in microresonator-modified waveguides," Journal of Optical Society of America B, **19**, 4, pp. 722-731, 2002.

[110] J. E. Heebner, P. Chak, S. Pereira, J. E. Sipe, and R. W. Boyd, "Distributed and localized feedback in microresonator sequences for linear and nonlinear optics," Journal of Optical Society of America B, **21**, 10, pp. 1818-1832 2004.

[111] A. Sakai, G. Hara, and T. Baba, "Propagation characteristics of ultrahigh-Δ optical waveguide on silicon-on-insulator substrate," Japanese Journal of Applied Physics, **40**, 4B, pp. 383-385, 2001.

[112] J. Joannopoulos, S.G. Johnson, J. N. Winn, and R.D. Meade, *Photonic Crystals Molding the Flow of Light*, Second Edition, Princeton University Press, 2008.

[113] M. Soljačić, E. Lidorikis, L. V. Hau, and J. D. Joannopoulos, "Enhancement of microcavity lifetimes using highly dispersive materials," Physical Review E, **71**, 2, 026602, 2005.

[114] M. Belt, J. Bovington, R. Moreira, J. F. Bauters, M. J. Heck, J. S. Barton, J. E. Bowers, and D. J. Blumenthal, "Sidewall gratings in ultra-low-loss Si_3N_4 planar waveguides," Optics Express, **21**, 1, pp. 1181-1188, 2013.

[115] D. T. Spencer, M. Davenport, S. Srinivasan, J. Khurgin, P. A. Morton, and J. E. Bowers, "Low kappa, narrow bandwidth Si3N4 Bragg gratings," Optics Express, **23**, 23, pp. 30329-30336, 2015.

[116] C. Sima, J. C. Gates, H. L. Rogers, P. L. Mennea, C. Holmes, M. N. Zervas, and P. G. R. Smith, "Ultra-wide detuning planar Bragg grating fabrication technique based on direct UV grating writing with electro-optic phase modulation", Optics Express, **21**, 13, pp. 15747-15754, 2013.

[117] G. Lepert, M. Trupke, E. A. Hinds, H. Rogers, J. C. Gates, and P. G. R. Smith, "Demonstration of UV-written waveguides, Bragg gratings and cavities at 780 nm, and an original experiment measurement of group delay", Optics Express, **19**, 25, pp. 24933-24943, 2011.

[118] D. Taillaert, P. Bienstman, and R. Baets, "Compact efficient broadband grating coupler for silicon-on-insulator waveguides," Optics letters, **29**, 23, pp. 2749-2751, 2004.

[119] G. Alagappan, and P. Wu, "Design of sharp transmission filters using band-edge resonances in one-dimensional photonic crystal hetero-structures," Applied Physics B, **96**, 4, pp. 709-713, 2009.

[120] K. McGarvey-Lechable, and P. Bianucci, "Maximizing slow-light enhancement in one-dimensional photonic crystal ring resonators," Optics Express, **22**, 21, pp. 26032-26041, 2014.

[121] Y. M. Kang, A. Arbabi, and L. L. Goddard, "Engineering the spectral reflectance of microring resonators with integrated reflective elements", Optics Express, **18**, 16, pp. 16813-16825, 2010.

[122] Y. M. Kang, M. Xue, A. Arbabi, J. M. Jin, and L. L. Goddard, "Modal expansion approach for accurately computing resonant modes in a high-Q optical resonator," Microwave and Optical Technology Letters, **56**, 2, pp. 278-284, 2014.

[123] A. Arbabi, Y. M. Kang, and L. L Goddard, "Analysis and design of a microring inline single wavelength reflector" Proc. of Frontiers in Optics, Optical Society of America, FThQ3, Rochester, New York, USA, October 24-28, 2010.

[124] A. Arbabi, Y. M. Kang, C.-Y. Lu, E. Chow, and L. L. Goddard, "Realization of a narrowband single wavelength microring mirror," Applied Physics Letters **99**, 9, 091105, 2011.

[125] A. Arbabi, S. M. Kamali, E. Arbabi, B. G. Griffin, and L. L. Goddard, "Grating integrated single mode microring laser," Optics Express, **23**, 4, pp. 5335-5347, 2015.

[126] A. Arbabi, and L. L. Goddard, "Single wavelength microring laser," Proc. of CLEO: Science and Innovations, Optical Society of America, CM3F-2, San Jose, California, USA, June 9-14, 2013.

[127] A. Arbabi, and L. L. Goddard, "Grating Assisted Mode Coupling in Microring Resonators", Proc. of IEEE Photonics Conference (IPC 2013), IEEE, pp. 434-435, Belleve, Washington, USA, September 8-12, 2013.

[128] Y. M. Kang, A. Arbabi, and L. L. Goddard, "A microring resonator with an integrated Bragg grating: a compact replacement for a sampled grating distributed Bragg reflector," Optical and quantum electronics, **41**, 9, pp. 689-697, 2009.

[129] L. L. Goddard, and Y. M. Kang, Distributed reflector in a microring resonator, Patent US 0063484 A1, 2012.

[130] Y. M. Kang, "In-line microring reflector for photonic applications," Ph.D Thesis in Electrical and Computer Engineering, University of Illinois at Urbana-Champaign, 2013.

[131] B. E. Little, S. T. Chu, and H. A. Haus, "Second-order filtering and sensing with partially coupled traveling waves in a single resonator," Optics letters, **23**, 20, pp. 1570-1572, 1998.

[132] T. Wang, Z. Zhang, F. Liu, Y. Tong, J. Wang, Y. Tian, M. Qiu, and Y. Su, "Modeling of quasi-grating sidewall corrugation in SOI microring add-drop filters," Optics Communications, **282**, 17, pp. 3464-3467, 2009.

[133] J. Y. Lee, and P. M. Fauchet, "Slow-light dispersion in periodically patterned silicon microring resonators," Optics letters, **37**, 1, pp. 58-60, 2012.

[134] G. Gao, Y. Zhang, H. Zhang, Y. Wang, Q. Huang, and J. Xia, "Air-mode photonic crystal ring resonator on silicon-on-insulator," Scientific reports, **6**, 19999, 2016.

[135] M. Gabalis, D. Urbonas, and R. Petruskevicius, "A perforated microring resonator for optical sensing applications," Journal of Optics, **16**, 10, 105003, 2014.

[136] D. Urbonas, A. Balčytis, M. Gabalis, K. Vaškevičius, G. Naujokaitė, S. Juodkazis, and R. Petruškevičius, "Ultra-wide free spectral range, enhanced sensitivity, and removed mode splitting SOI optical ring resonator with dispersive metal nanodisks," Optics Letters, **40**, 13, pp. 2977-2980, 2015.

[137] D. Goldring, U. Levy, and D. Mendlovic, "Highly dispersive micro-ring resonator based on one dimensional photonic crystal waveguide design and analysis," Optics Express, **15**, 6, pp. 3156-3168, 2007.

[138] Q. Li, T. Wang, Y. Su, M. Yan, and M. Qiu, "Coupled mode theory analysis of mode splitting in coupled cavity system," Optics Express, **18**, 8, pp. 8367-8382, 2010.

[139] F. - L. Hsiao, and Y.-T. Ren, "Computational study of slot photonic crystal ring-resonator for refractive index sensing," Sensors and Actuators A: Physical, **205**, pp. 53-57, 2014.

[140] V. Donzella, A. Sherwali, J. Flueckiger, S. M. Grist, S. Talebi Fard, and L. Chrotowski, "Design and fabrication of SOI micro-ring resonators based on sub-wavelength grating waveguides," Optics Express, **23**, 4, pp. 47391 -4803, 2015.

[141] I. Teraoka, "A hybrid filter of Bragg grating and ring resonator", Optics Communications, **339**, pp. 108-114, 2015.

[142] G. Brunetti, D. Conteduca, F. Dell' Olio, M. N. Armenise, and C. Ciminelli, "Comprehensive Mathematical Modelling of Ultra-high *Q* Grating-Assisted Ring Resonators," Journal of Optics, 2020, https://doi.org/10.1088/2040-8986/ab71eb.

[143] H. Kogelnik, and C. V. Shank, "Coupled wave theory of distributed feedback lasers," Journal of Applied Physics, **43**, 5, pp. 2327-2335, 1972.

[144] K. R. Hiremath, M. Hammer, R. Stoffer, L. Prkna, and J. Čtyroký, "Analytic approach to dielectric optical bent slab waveguides," Optical and quantum electronics, **37**, 1-3, pp. 37-61, 2005.

[145] R. M. Knox and P. P. Toulios, "Integrated circuits for the millimeter through optical frequency range," Proc. of MRI Symposium Submillimeter Waves, **20**, pp. 497-515, Brooklyn, NY , USA, 1970.

[146] J .F. Bauters, M. J. Heck, D. John, D. Dai, M. C. Tien, J. S., Barton, A. Leinse, R. G. Heideman, D. J. Blumenthal and J. E. Bowers, "Ultra-low-loss high-aspect-ratio Si_3N_4 waveguides," Optics Express, **19**, 4, pp. 3163-3174, 2011.

[147] H. Kogelnik, "Theory of Optical Waveguides" in Guided-wave optoelectronics, T. Tamir Ed., Berlin Heidelberg, D: Springer Series in Electronics and Photonics, **26**, pp. 7-87, 1998.

[148] S. M. Kamali, E. Arbabi and L. L. Goddard, "A Zeroth-Order Modification of Coupled Mode Theory for Waveguide Gratings," IEEE Photonics Technology Letters, **27**, 7, pp. 790-793, 2015.

[149] A. A. Hardy, "A unified approach to coupled-mode phenomena," IEEE Journal of Quantum Electronics, **34**, 7, pp. 1109-1116, 1998.

[150] T. C. Choy, *Effective medium theory: principles and applications*, 2nd ed., 165, Croydon, UK: Oxford University Press, 2015.

[151] J. F. Bauters, M. J. R. Heck, D. Dai, J. S. Barton, D. J. Blumenthal and J. E. Bowers, "Ultralow-Loss Planar Si_3N_4 Waveguide Polarizers," IEEE Photonics Journal, **5**, 1, 660207, 2013.

[152] N. Izhaky and A. Hardy, "Analysis of grating-assisted backward coupling employing the unified coupled-mode formalism," Journal of the Optical Society of America A, **16**, 6, pp. 1303-1311, 1999.

[153] J. Čtyroky, I. Richter, and M. Šiňor, "Dual resonance in a waveguide-coupled ring microresonator," Optical and quantum electronics, **38**, 9, pp. 781-797, 2006.

[154] M. J. Heck, J. F. Bauters, M. L. Davenport, D. T. Spencer, and J. E. Bowers, "Ultra-low loss waveguide platform and its integration with silicon photonics," Laser & Photonics Reviews, **8**, 5, pp. 667-686, 2014.

[155] J. F. Bauters, M.J.R.Heck, D.John, M.-C.Tien, W.Li, J.S.Barton, D. J. Blumenthal, J. E. Bowers, A.Leinse, and R.G.Heideman, "Ultra-low-loss single- mode Si_3N_4 waveguides with 0.7 dB/m propagation loss," Proc. of European Conference and Exposition on Optical Communications (ECOC), Optical Society of America, Th-12, Geneva, Switzerland, September 18-22, 2011.

[156] T. Horikawa, D. Shimura, and T. Mogami, "Low-loss silicon wire waveguides for optical integrated circuits," MRS Communications, **6**, 1, pp. 9-15, 2016.

[157] S.K.Selvaraja, G.Murdoch, A.Milenin, C.Delvaux, P.Ong, S.Pathak, D.Vermeulen, G.Sterckx, G.Winroth, P.Verheyen, G.Lepage, W.Bogaerts, R. Baets, J. Van Campenhout, and P.Absil, "Advanced 300-mm waferscale patterning for silicon photonics devices with record low loss and phase errors," Proc. of 17th Opto-Electronics and Communications Conference (OECC-2012), IEEE, pp. 15-16, Busan, Korea, July 2-6, 2012.

[158] A. Biberman, M. J. Shaw, E. Timurdogan, J. B. Wright, and M. R. Watts, "Ultralow-loss silicon ring resonators," Optics letters, **37**, 20, pp. 4236-4238, 2012.

[159] C. Sima, J. C. Gates, H. L. Rogers, P. L. Mennea, C. Holmes, M. N. Zervas, and P. G. R. Smith, "Ultra-wide detuning planar Bragg grating fabrication technique based on direct UV grating writing with electro-optic phase modulation," Optics Express, **21**, 13, pp. 15747-15754, 2013.

[160] T. Kominato, Y. Hida, M. Itoh, H. Takahashi, S. Sohma, T. Kitoh, and Y. Hibino, "Extremely low-loss (0.3 dB/m) and long silica-based waveguides with large width and clothoid curve connection," Proc. of European Conference and Exposition on Optical Communications (ECOC), Optical Society of America, pp. 5-9, Stockholm, Sweden, September 5-9, 2004.

[161] Y. Kuwana, S. Takenobu, K. Takayama, S. Yokotsuka, and S. Kodama, "Low loss and highly reliable polymer optical waveguides with perfluorinated dopant-free core," Proc. of Optical Fiber Communication Conference, Optical Society of America, OWF2, Anaheim, California, USA, March 5-10, 2006.

[162] R. L. Moreira, J, Garcia, W. Li, J. Bauters, J. S. Barton, M. J. Heck, J. E. Bowers, and D. J. Blumenthal, "Integrated ultra-low-loss 4-bit tunable delay for broadband phased array antenna applications," IEEE Photonics Technology Letters, **25**, 12, pp. 1165-1168, 2013.

[163] J. F. Bauters, M. J. Heck, D. D. John, J. S. Barton, C. M. Bruinink, A. Leinse, R. H. Heideman, D. J. Blumenthal, and J. E. Bowers, "Planar waveguides with less than 0.1 dB/m propagation loss fabricated with wafer bonding," Optics Express, **19**, 24, pp. 24090–24101, 2011.

[164] C. Ciminelli, G. Brunetti, F. Dell'Olio, F. Innone, D. Conteduca, and M.N. Armenise, "Emerging applications of Whispering Gallery Mode photonic resonators," Lecture Notes in Electrical Engineering, **429**, pp. 185-191, 2017.

[165] F. Dell'Olio, G. Brunetti, D. Conteduca, N. Sasanelli, C. Ciminelli, and M. N. Armenise, "Planar Photonic Gyroscopes for Satellite Attitude Control," Proc. of 7th International Workshop on Advances in Sensors and Interfaces (IWASI), pp. 167-169, Vieste, Italy, June 15-16, 2017.

[166] F. Dell'Olio, G. Brunetti, D. Conteduca, N. Giovinazzi, N. Sasanelli, C. Ciminelli, and M.N. Armenise, "Integrated Microwave Photonics: Overview and Promising Space Applications," Proc. of ApplePies International Conference (Applications in Electronics Pervading Industry, Environment and Society), Rome, Italy, September 21-22, 2017.

[167] S. Fan, W. Suh, and J. D. Joannopoulos, "Temporal coupled-mode theory for the Fano resonance in optical resonators," Journal of the Optical Society of America A, **20**, 3, pp. 569-572, 2003.

Chapter 3

Telecommunication payloads

Telecom satellites are the most mature Space applications. Starting 1960s, with the launch of *Telstar* [1] and *Syncom* [2], the development of satcoms has continued to grow. Satellite communications offer features that are not available with other communication approach, such as seamless coverage of remote and sparsely populated areas, capabilities of multicasting and broadcasting, and high hardness to extreme conditions, e.g. earthquakes and hostile weather conditions.

In the last decades, the massive growth in mobile multimedia applications and Space exploration activity has created new opportunities for satellite communication. According to the report provided by Satellite Industry Association in September 2018 [3], telecom satellites represent more than 44 % of total operational satellites, as shown in Fig. 3.1, with an estimation revenue of about US $ 189.2 billion in 2013 [4]. The most famous commercial companies into the world, as Apple, Google, Amazon, Facebook, are currently interested to improve the satellite communication systems to increase their revenue in this context.

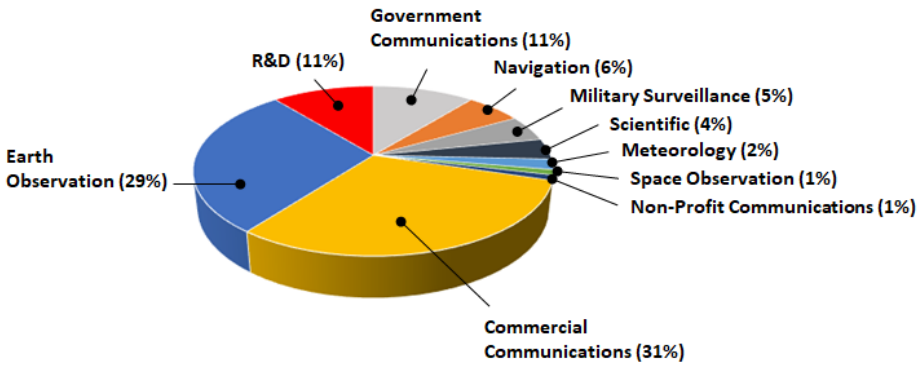

Fig. 3.1. Classification of satellite currently in orbit according to their functions.

In the 1990s, the satcoms operated for the telephone telecommunications and broadband TV. Currently, they are mainly focused on the internet connectivity. In particular, new European targets have been set to ensure a connectivity of 100 Mbps by 2025. The communication systems must be adapted to support the advent of the Internet of Things and the 5G concept [5], which combines various access technologies, such as cellular, wireless, wireline and satellite, for improving the area connectivity with reliable performance. To facilitate the rapid growth of satellite communications, responding to the evolutions of the satellite communication services, innovations are urgently required, in particular very high throughput satellite payloads.

The most common types of communications satellites payloads include the transparent "bent-pipe" payload, the regenerative payload, or a hybrid solution [6]. The "bent-pipe" payload acts as a relay to send whatever is received back to Earth solely by amplification and a shift from uplink to downlink frequency. Although its capacity is limited by the bandwidth-utilization inefficiency and relatively poor bit-error-rate performance, the "bent-pipe" payload is able to support multiple-access schemes, protocols and waveform and flexible, because its operation is not strictly related to its physical features.

The regenerative payload overcomes the "bent-pipe" payload issues, by using an onboard resource allocation and signal remodulation for the transmission back to the Earth. Although it shows a large capacity, the main problem regards the flexibility, because its operation strictly depends by the physical characteristics.

Most satellites operators require flexible telecom payload that can be adapted and optimized after the launch according to the varying user demands in terms of bandwidth, coverage, and frequency allocation. This choice is caused by the rapid evolution of the telecommunication market, that could be faster than the life of a satellite (15 years or more). To obtain both high capacity and high flexibility, a new class of payload called "software-defined payload" has been designed [7-8]. This payload consists of a baseband digital signal processor, reconfigurable via software, and a broadband analog RF platform that perform full in-orbit reconfigurability of functionalities. This demands that the payload RF components, analog-to-digital converters (ADCs), and digital-to-analog converters

(DACs) have a large bandwidth, to cover all frequencies of the designed communication tasks. Furthermore, in order to ensure an increase of the bandwidth and the reduction of the antenna footprint, the operation frequency of satellite must move from low-frequency C/Ku bands (4–8/12–18 GHz) to high-frequency Ka (26.5– 40 GHz) or Q/V bands (40–50/50–75 GHz) [9]. Traditional electronic device cannot be used to implement the software defined payload, suffering from electromagnetic interference (EMI), mass, volume, complexity, RF isolation, and high-power consumption.

The so-called MicroWave Photonic (MWP) may take a significant place in telecom payloads with broader bandwidth, wider connectivity, and enhanced routing flexibility at ever lower mass and smaller size [10-16]. The migration to higher frequency increases the attractiveness of optical processing, performing also small footprint and low power dissipation. Beginning in the early 1990s, the European Space Agency (ESA) has supported research on novel communication satellite payloads based on microwave photonics, e.g. the *Artes* programmes [17].

The "software-defined payload" performance fits well the requirements of the widely used multi-beam broadband mission scenario. As shown in Fig. 3.2, the network shows a star topology, where the terminal users are connected to the global network by a gateway. The necessity of a coverage with a large bandwidth require small spot, 0.4° -0.7 ° in Ka-band, that allows to reuse several times the allocated bandwidth. This is satisfied by using a scheme with four colours, where the colour results by the combination of a frequency with a polarization state. The user beams are connected to the gateway through the satellite in both directions: from gateway to users (known as forward direction), and from user to gateway (known as return direction). The number of users connected to the same gateway is strictly limited by the bandwidth and regulatory constraints.

In the following Paragraph, a configuration of Opto-Microwave Analogue Repeater for the forward and return direction is reported. Furthermore, the design of innovative architectures of the RF optical-based repeaters' building blocks, is reported, as optoelectronic oscillator, and pass-band optical filter.

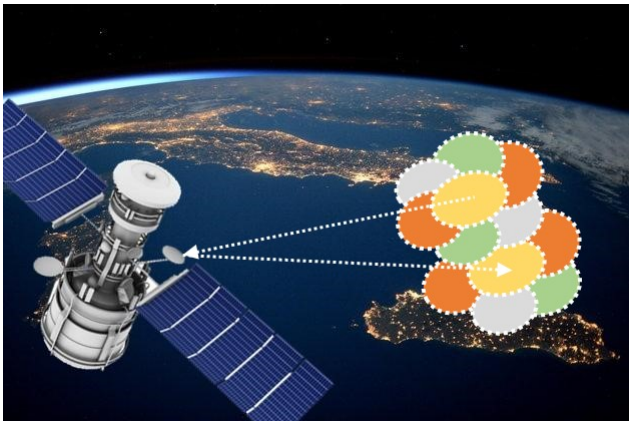

Fig. 3.2. Multi-beam network approach.

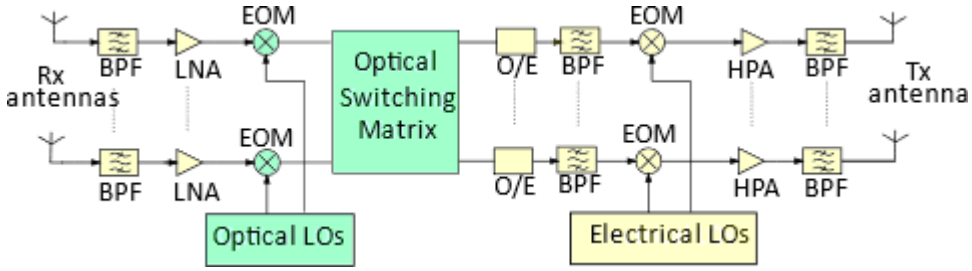

Fig. 3.3. Simplified scheme of a photonic-based RF repeater, (*Rx*: reception; *BPF*: pass-band filter; *LNA*: low-noise amplifier; *EOM*: electro-optical modulator; *O/E*: optical-electro converter; *HPA*: high power amplifier; *Tx*: transmission). The green building blocks are based on a photonic approach. The yellow building blocks are based on a standard RF approach.

3.1 Photonic RF payload architecture

Broadband operation, transparency to RF frequency bands and flexible reconfiguration of the payload after the launch are essential features into the future payload.

A schematic of the new payload generation is shown in Fig. 3.3. It is based on microwave photonic repeater able to route any microwave signal from any input access port to any output access port, in the receiver section. Instead, the transmit section consists of conventional microwave low-noise receive front ends and high-power amplification chains. In particular, microwave telecom signals received from up-link antenna accesses are filtered, low-noise amplified and transferred at the electro-optical mixers (EOMs), down-converted to an intermediate frequency (IF). All the generated local oscillating signals fed up the EOMs. Oscillating signal generation, distribution and switching are performed in the optical domain, by using an optical oscillator (LO) and a switching matrix [18], respectively. The electro-

optical (E/O) units receivers convert the optical signals back into microwave ones at IF. Downstream of the E/O unit, a pass-band RF filter (BPF) is used [10]. It also could be implemented by using a photonic approach, as well as the standard RF technologies.

Key functionalities of the proposed photonic repeater are the optical distribution of high frequency microwave local oscillator (LO) signals, the photonic frequency conversion of RF signals, the routing of the signals by means of photonic switching, designed with the features of large scalability and RF frequency independence.

In the specific context of a multi-beam broadband access mission, this optical reconfiguration concept based on optical multi-frequency conversion and optical sections can support flexible allocation of gateway to user beams. Thus, this approach could offer the possibility for an operator to improve progressively the distribution of services, reducing the risks of a large initial investments. In contrast to the RF approach that require unaffordable complexity and amount of software, the MWP architecture can provide the in-orbit reconfiguration capability, reducing the initial investments and then, increasing the potential revenues.

3.2 Chip-scaled optoelectronic oscillator

In the scenario of the new generation telecom repeaters, miniaturized Ka-band oscillators with very low phase noise (< -120 dBc/Hz at 10 kHz offset from the carrier) are strongly demanded being key building blocks of the above-mentioned systems. Their implementation by the common microwave technology is very challenging. A phase noise @10kHz offset from the carrier in the range form -80 dBc/Hz to -100 dBc/Hz has been demonstrated for a microwave oscillator in the Ka-band, based on dielectric resonator oscillator [19-22].

According to the well-known advantages of the photonics, as the performance independence by the operating frequency, it represents the most promising approach to develop a miniaturized RF oscillator. Starting from 1990s, a great research effort by several groups [23-27] has been focused on the photonic solution, implementing the so-called optoelectronic oscillator (OEO). A bulk OEO

with a phase noise equal to -163 dBc/Hz at 10 kHz offset from the carrier (10 GHz) has been reported in [28]. The main drawback of this high performing system, based on a very long (> 10 Km) fiber delay line, is its size, which is greater than 10,000 cm^3. To overcome the large footprint and high-performance compromise, in literature, several architectures have been investigated to implement a miniaturized OEO [29], including coupled [30-31], multi-loop [32-34] and injection-locked [35-37] architectures or system based on whispering gallery mode (WGM) resonator [38-44].

The coupled OEOs are based on coupled oscillators, that consist of an optical and optoelectronic feedback loop. A phase noise of -140 dBc/Hz @10 kHz in the X band has been demonstrated by a coupled OEO, made by 550 m long fiber and a semiconductor optical amplifier into the optical loop and an optical fiber delay line, a fast photodiode and RF filter into the optoelectronic feedback loop. The two loops are coupled together by using a Mach-Zehnder modulator, and, a phase shifter, ensure the resonance matching between the two loops [30]. Although a very large phase noise has been demonstrated, this configuration suffers of low rejection ratio of the undesired mode (for the configuration reported in [30], the first spur shows a phase noise of -137 dBc/Hz @10kHz).

The multi-loop OEO is based on the Vernier effect, reducing the amplitude of the undesired modes. These systems are based on multiple loops, based on fibers with different lengths. Since the performance in terms of *Q*-factor depends by the average of the loops individually, a phase noise (< -70 dB/Hz @10 kHz in K band [32]) higher than the coupled approach is achieved. Furthermore, the tunability of these systems is challenging.

The injection locked dual OEO represents a promising solution to suppress the undesired modes maintaining a high-*Q* factor from the optical loop. As reported in [35], the system consists of two loops with different lengths, master and slave. The RF signal from the master is injected into the slave that lock the oscillating frequency, filtering the spurious modes. A phase noise of -130 dBc/Hz @ 1 kHz from the carrier into the X band has been reported in [35]. The main drawback regards a complex manufacturing of the two loops.

In order to implement a chip-scale OEO, with large rejection ratio of the spurious modes and phase noise, WGM [38-40] or fiber ring resonator [41-44] – based OEOs have been proposed in literature.

A miniaturized OEO, based on a WGM resonator, operating in the Ka-band, currently into the market, performs a phase noise equal to -108 dBc/Hz at 10 kHz offset from the carrier, with a very small volume (≈ 1 cm^3) [38, 45]. It is based on a discrete architecture, with a spheroid, that acts as WGM resonator, co-packaged with other optoelectronic and RF devices. In the Space field, the vibrations during the satellite launch phase could lead a failure of the co-packaged device. In order to overcome this critical aspect, Tang *et al.* [46] have been proposed a fully integrated OEO on the InP technology platform. Although the device shows a phase noise of -92 dBc/Hz @ 1 MHz from the carrier (9 GHz) with a chip volume of 5 x 6 cm^2, the device is an important step for the monolithic integration of the photonic device into the TLC field.

In order to improve the sine-wave Ka-band phase noise, a new way to implement a miniaturized Ka-band OEO has been explored. In particular, the OEO is based on the very innovative technological platform, reported in [47], allowing the integration of photonic components based on an ultra-low loss silicon nitride waveguide-based high-Q ring resonator (1D-PhCRR, widely discussed into the Chapter 2) with InP-based high-performance optoelectronic devices.

The configuration of the proposed OEO [48] is reported in Fig. 3.4, based on the architecture reported in [38, 42]. A continuous wave is generated by a distributed feedback laser and modulated by a Mach-Zehnder interferometer (MZI). The optical beam is filtered, and time delayed by the 1D-PhCRR, locked at the same frequency of the DFB laser. Then, is O/E converted by using a fast photodiode (PD). The electrical RF signal is amplified, filtered, phase shifted and then fed back to the MZ modulator. The RF 3 dB coupler splits the RF signal, generating the output oscillating signal. The oscillating signal starts when the gain of the feedback loop compensates the losses. The laser frequency is stabilized by using the Pound-Drever-Hall technique [49], and then, by an additional electronic feedback loop between the photodiode and the laser source (not shown in the block diagram in Fig. 3.4).

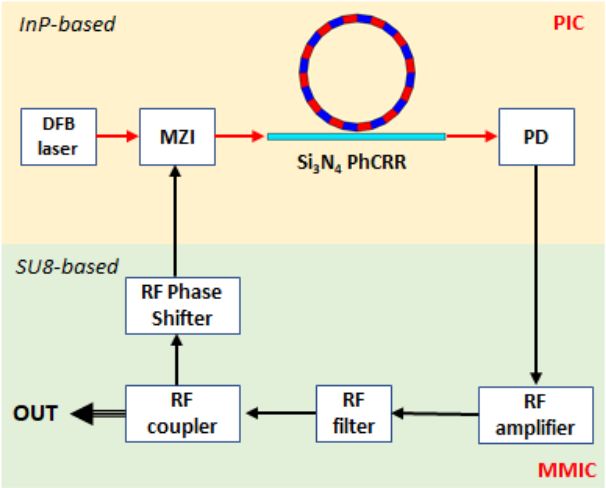

Fig. 3.4. Configuration of the Ka-band OEO, (*DFB laser*: distributed-feedback laser; *MZI*: Mach-Zehnder Interferometer; *PhC*: photonic crystal; *PIC*: Photonic Integrated Circuit; *MMIC*: Monolithic Microwave Integrated Circuit).

All the optoelectronic devices, such as the DFB laser, the MZ modulator, and the PhCRR, could be integrated in a chip scale solution. Two InP-based dies, one including the DFB laser and the MZI and the other including the PD, should be bounded on the same chip by using the technique reported in [47]. The operating wavelength of the optoelectronic section of the OEO is about 1.55 μm, due to the availability of high-performance DFB lasers, MZ modulators, and fast photodiodes in the C-band. The RF components, as the amplifier, the filter, the coupler and the phase shifter, can be integrated on a monolithic microwave integrated circuit (MMIC), which should be co-packaged with the photonic integrated circuit (PIC) including all the optoelectronic section.

3.2.1 Resonator design

The requirement of a very low phase noise, less than -120 dBc/Hz at 10 kHz offset from the carrier into the Ka-band, can be fulfil by an optical cavity with a *Q*-factor > 10^9, then, the 1D-PhCRR results suitable as the OEO heart.

A parametric analysis has been carried out to define a relationship between the *Q*-factor of the first band edge resonance and the PhCRR radius. For the 1D-PhCRR electromagnetic simulations, by using the mathematical model reported into the Chapter 2, the bare waveguide and grating propagation losses have been assumed equal to 3.5 dB/cm and 35 dB/m, respectively.

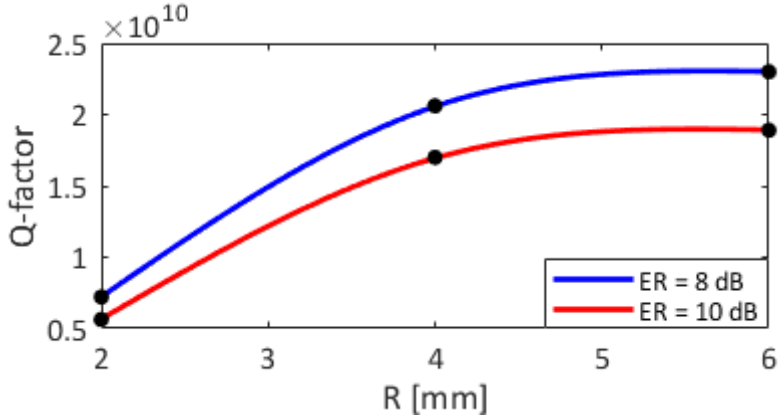

Fig. 3.5. *Q*-factor of the first band edge resonance *vs* ring radius, for different values of ER.

The choice to assume the grating losses one order of magnitude larger than the waveguide one is conservative approach, considering any additional losses due to the grating fabrication. The design of the PhCRRs has been carried out to achieve two values of the spectral response extinction ratio (ER), i.e. ER = 8 dB, and 10 dB. The result of this analysis (see Fig. 3.5) shows that, for all values of ER, the Q-factor increases as the radius increases with a logarithmic behaviour. For $R > 4$ mm, the enhancement of the Q-factor, due to an increase of the radius, is counteracted by an increase of the propagation losses, resulting in a quasi-flat trend. Since high Q-factor and large ER are conflicting requirements, the Q-factor decreases as ER increases. Q-factor values > 10^9 have been predicted for ring radius larger than 2 mm.

3.2.2 OEO performance

In order to rank the OEOs, the single side-band phase noise is widely used as figure of merit. The single side-band phase noise $L(f_m)$ is the ratio of the power density at an offset frequency f_m from the carrier to the total power of the carrier signal. The phase noise provides the spectral purity of the oscillator and the short-term stability of the frequency of the generated sine-wave signal.

The common phase noise spectrum ($L(f_m)$ vs f_m) of the OEOs includes three sections (Fig. 3.6): flicker noise section (trend of -30 dBc/Hz), a white frequency noise section (trend of -20 dBc/Hz) and phase noise floor section (flat trend) [50]. For radar and telecom system applications, the phase noise is usually evaluated at

10 kHz offset from the carrier, that is located in the white frequency noise section, according to the literature [51].

Therefore, to evaluate the OEO phase noise model, the well-known Leeson's approach has been used [50]. The OEO phase noise at f_m offset from the carrier is given by:

$$L(f_m)=20\log\left(\frac{f_{opt}}{2\cdot\sqrt{2}\cdot Q_{opt}\cdot f_m}\right)+10\log\left(\frac{2\cdot\left[RIN\cdot P^2\cdot R_{PD}^2+(4k_BT/R)+2\cdot q\cdot R_{PD}\cdot P\right]}{P^2\cdot R_{PD}^2\cdot m^2}\right) \quad (3.1)$$

where k_B is the Boltzmann's constant, q is the electron charge, Q_{opt} is the Q-factor of the optical cavity, and the other parameters are defined in Tab. 3.1.

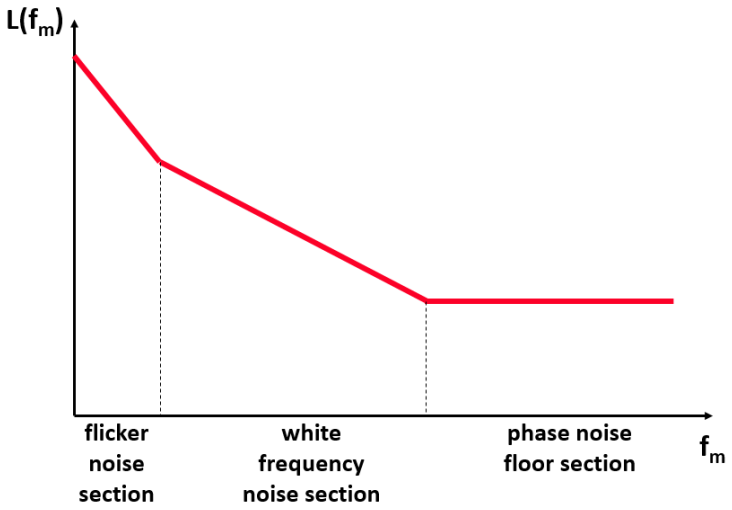

Fig. 3.6. Typical phase noise spectrum of an OEO.

Tab. 3.1. Assumed values for the OEO key parameters.

Parameter	Symbol	Value
Operating frequency of the OEO	f_{opt}	193 THz
Extinction ratio of the optical cavity spectral response	ER	8 dB
Laser relative intensity noise	RIN	-160 dB/Hz
Photodiode responsivity	R_{PD}	0.8 A/W
Optical power at the photodiode input	P	1 mW
Modulation index of the MZ modulator	m	0.8
Photodiode load resistance	R	50 Ω
OEO operating temperature	T	300 K

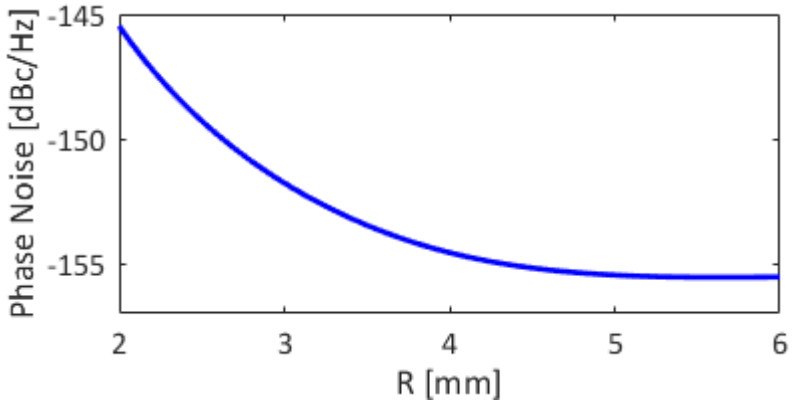

Fig. 3.7. Oscillator phase noise at 10 kHz offset from the carrier *vs* the ring radius.

As shown in Tab.3.1, a common InP-based DFB laser relative intensity noise (*RIN*) of -160 dB/Hz has been assumed [52]. Moreover, an InP-based p-i-n photodiode responsivity R_{PD} of 0.8 A/W and a load resistance R of 50 Ω [53] have been assumed. For the MZ modulator, a modulation index m = 0.8 has been assumed [54]. Taking into account the trade-off between the minimization of the cavity insertion loss at the resonance, requiring low values of ER, and the maximization of the filtering function, requiring high values of ER, an ER of 8 dB represents a good comprise.

The phase noise trend @10kHz from the carrier, calculated by Eq. (3.1), varying the PhCRR radius, is reported in Fig. 3.7. The phase noise has been derived by assuming a laser power, the sum of the insertion losses of the modulator, the optical cavity, and the photodiode, and the optical power at the input of the photodiode equal to 13 dBm (= 20 mW), 13 dB, and 0 dBm (= 1 mW), respectively.

As shown in Fig. 3.7, the oscillator phase noise decreases as the ring radius increases, according to Fig. 3.6 and Eq. (3.1), with an inverse logarithmic trend. Although, large ring radii ensure low values of phase noise, at the expense of a large footprint. Furthermore, a too large ring radius makes critical the uniformity of the fabrication process. The radius value of 4 mm has been chosen as good compromise. Thus, the proposed Ka-band OEO shows a phase noise @10 kHz from the carrier (40 GHz) of about -155 dBc/Hz with a footprint of about 1 cm^3. Although the proposed device shows a footprint similar to the state-of-the-art [45], an improvement of 47 dBc/Hz has been theoretically demonstrated.

Furthermore, in terms of generated electric power, since the power at the RF input of the MZ modulator is 19.5 dBm [55], a value of -3.95 dBm (= 0.4 mW) has been calculated at the PD input. In order to sustain the oscillation, the gain of the RF amplifier should be 40 dB, because of the electric power of the RF signal at the photodiode output is -19 dBm (= 0.0125 mW) and the power at the output of the RF amplifier should be 21 dBm. Thus, since the insertion loss of the phase shifter, the coupler, and the filter is 3.5 dB [56], 0.45 dB [57], and 7 dB [58], the RF output power is about 11 dBm. The gain required is compliant to the state-of-the-art of the Ka-band amplifiers [59].

As already mentioned, the proposed OEO, sketched in Fig. 3.4, could be manufactured by using a very innovative CMOS-compatible technological platform allowing the hybrid integration on a silicon substrate of III-V optoelectronics components, e.g. lasers and photodiodes, and passive Si_3N_4 – based photonic devices, e.g. ring resonators or arrayed waveguide gratings (AWGs) [47, 60]. In [47], the integration of an 8-channel Si_3N_4 – based AWG with InGaAs photodiodes has been experimentally demonstrated. The main technological steps are: the fabrication of the Si_3N_4 - based AWG on an oxidized silicon substrate, the bonding of the patterned silicon layer on the passive low loss component (the silicon and the Si_3N_4 layers are interleaved by a SiO_2 600 nm thick), the bonding of the III/V wafer on the silicon layer, and, finally, the patterning of the photodetectors with the deposition of the metal contacts and the plasma-enhanced chemical vapor deposition of a passivation SiO_2 layer.

Instead, the integration of an ultra-low loss Si_3N_4 waveguide with a continuous-wave Fabry-Perot InGaAs/GaAs multiple quantum well laser operating at 1.06 μm has been demonstrated in [60].

The optoelectronic section of the proposed OEO can be hybridly integrated on a silicon substrate by the CMOS-compatible technological platform reported in [47]. The fabrication process includes the manufacturing on the oxidized silicon substrate of the Si_3N_4 1D-PhCRR, the bonding of the patterned silicon layer with taper structures, the bonding on the silicon layer of two different III-V wafers, and finally the patterning of the photodetector and MZ modulator on two different

wafers [61]. The estimated overall footprint of the PIC including all the optoelectronic section of the proposed Ka-band OEO is about 200 mm^2 (= 2 cm^2).

3.3 Microwave Photonic Filter

The future generations of wireless communications are expected to provide new services and applications, requiring a dynamic and adaptive filtering operation, according to the user demands. A tuneable and reconfigurable multiband RF filter is needed, very challenging with RF electronics. Microwave Photonic Filters (MPFs) have attracted considerable interests in the past few years, thanks to their intrinsic features of large frequency coverage, flexible tunability (over multi-GHz bandwidths), light weight, immunity to electromagnetic interferences, re-configurability, and low energy consumption [62]. Furthermore, in the new radio-over-fiber systems, their use fits the requirements of payload adjustment and optimization after the launch, in terms of bandwidth, coverage and frequency allocation [63-64]. In particular, the future telecommunications networks demand for optical bandwidths of the order of GHz with high rejection, large tunability of both bandwidth and central frequency (more than 10 GHz), flat band shape of the filter frequency response (pass-band ripple less than 0.5 dB), ultra-fast (< 1 μs) and easy spectral response reconfigurability, device compactness with the idea to integrate all filter components in a single chip.

As reported in [62, 65], MPFs can be implemented in an incoherent operational regime or in a coherent one.

An incoherent microwave filter is usually realized by using a delay line - based configuration, as shown in Fig. 3.8(a). It consists in fiber Bragg gratings (FBGs) [66], chirped FBGs [67-68], PhC waveguides [69] or dispersive fibers [70], inducing a wavelength-dependent delay. In an incoherent MPF, the RF signal to be filtered feeds an electro-optic modulator, which modulates the light beam generated by a laser source. A splitter at the modulator output produces several optical signal replicas that are weighted and delayed in the optical domain. Finally, the replicas are combined, and the resulting beam is transduced into the RF domain by a photodiode (PD). The output signal is the result of the interference between all

optical signals modulated to which specific delays and weights have been applied. The operation of the incoherent MPF could be affected by the optical interference between the replicas, avoided by using a broadband incoherent light source. In order to ensure a wideband tunability, the tuning of the spectral response of the filter requires complex weights to keep the same spectral shape during the tuning, and this requires a more complex configurations, such as the ones involving the use of high-power erbium-doped fiber amplifiers (EDFAs) [71] and Mach-Zehnders [72].

In the coherent regime, a single wavelength source is needed, and the spectral response of the MPF depends directly on the spectral response of the optical filter. The building block scheme of a coherent MPF is shown in Fig. 3.8 (b). A narrow-linewidth light wave from a laser source is sent to a phase modulator. Assuming small signal modulation, at the output of the PM, an optical carrier and two sidebands are generated. The optical filter partially removes one of the sidebands, producing a single-sideband intensity-modulated signal. This is detected by a PD that generates the RF signal at the filtered frequency.

The key building block of a coherent microwave filter is an optical filter with a spectral response tightly controlled, that can be implemented by different approaches, e.g. Bragg gratings [73-75], FBGs [76], planar ring resonators [77], or integrated ring-assisted Mach-Zehnder interferometers [78]. The frequency of the microwave bandpass filter in a coherent configuration can be tuned by shifting the central frequency of the notch optical filter, keeping its spectral shape unchanged.

Comparing the two aforementioned configurations, in a coherent MPF configuration the optical interference does not affect the stable operation of the filter, in contrast to the incoherent configuration. Furthermore, the design of a coherent MPF is much simpler than an incoherent one and the tuning of the spectral response does not involve any change in the filtering shape or any increase of the design complexity. In addition to the above mentioned MPF configurations, recently new approaches for RF filtering have been reported in the literature. They are based on slow and fast light effects in semiconductor optical amplifiers added to fiber Bragg gratings [79] or stimulated Brillouin scattering in As_2S_3 optical planar waveguides [80], with good performance in terms of bandwidth and tunability at the expense of a complex design.

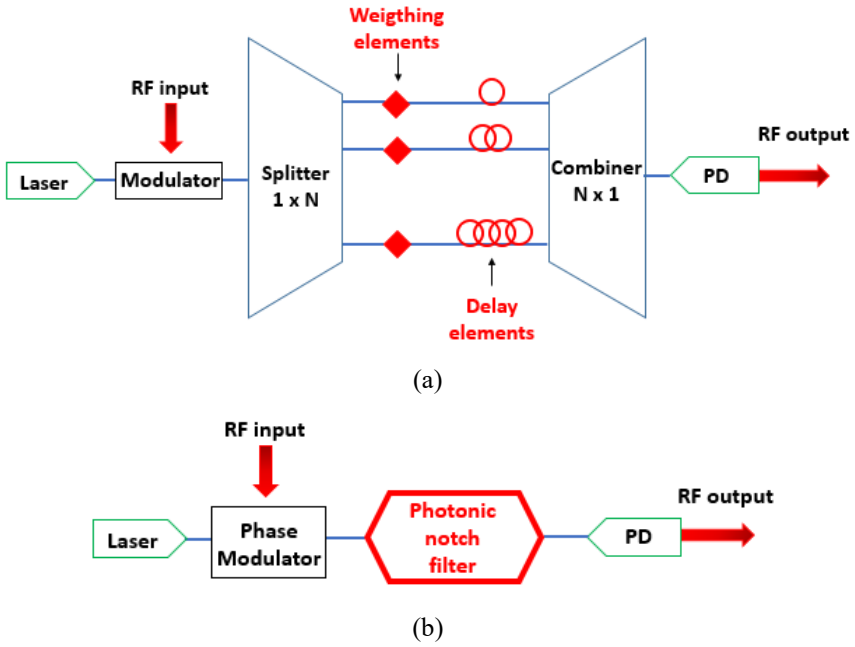

Fig. 3.8: Microwave photonic filter in an incoherent (a) and coherent (b) regime.

An integrated approach has a supplementary benefit on wideband frequency tunability. In 2016, Fandiño *et al.* [81] firstly demonstrated an integrated MPF (IMPF) with a coherent configuration, monolithically integrated on the InGaAsP/InP platform. The reported MPF filter with a reconfigurable RF response is based on a thermo-optic tuneable optical filter that consists in a ring assisted Mach Zehnder interferometer (RAMZI). The filter has demonstrated a tuneable bandwidth from a maximum of 5.5 GHz to a minimum of 2.5 GHz, with a maximum central frequency shifting of 4 GHz. In order to fit the requirements of small footprint, low cost and good tunability, an integrated approach on silicon platform could be a promising solution. In fact, more recently, Zhang *et al.* [82] demonstrated an integrated bandpass MPF on a silicon-on-insulator (SOI) wafer, including a PM, a high-Q microdisk resonator, and a PD. The filter has shown a bandwidth of 2.3 GHz, with a wide tuneable range of the central frequency (7 GHz – 25 GHz). Disadvantages of this configuration are a lack of chip planarity, a hard manufacturing of the microdisk resonator and a large chip footprint.

As already mentioned, the performance of a RF filter is strongly influenced by the frequency response of the notch optical filter that is the key component of the MWF configuration. The notch filter has to be engineered to satisfy the demands

of the specific application. According to the aforementioned advantages of SOI technology platform, several notch filters, based on silicon resonators, have been proposed in literature [83-84], even if with the issue of low filter selectivity, being the bandwidth larger than 20 GHz, limited by the *Q*-factor of the resonators. An ultra-narrowband bandpass notch filter, using an ultra-high *Q* racetrack resonator, has been proposed in [85]. The high *Q*-factor of the resonator (of the order of 10^6) ensures a bandwidth of 170 MHz, with a thermal tunability in 16.4 GHz, in a footprint of 0.05 mm^2.

The major limitation of the mostly performing MPFs is the poor flatness of the passband due to the Lorentz-shaped notch spectral response. The flat band is required in order to emulate the ideal filter response, filtering all spectral components in the bandwidth with the same attenuation coefficient. To increase the band-flatness, a reasonable result has been achieved in [86], where a specially designed superstructured fiber Bragg grating acts as notch filter. The superstructure is a FBG that is spatially modulated by a periodic sampling function. The notch filter is designed with two closely spaced notches, achieved by two phase shifters into the structure. The combination of the two closely spaced Lorentz-shaped notches results in a notch with a flat band. The filter performs a bandwidth of 143 MHz, with a band ripple less than 0.25 dB, at the expense of a length of 13.2 mm and the incompatibility with an integrated approach.

Although suitable for telecom purposes, several integrated solutions have been proposed in literature to increase the band-flatness of the notch and/or pass-band response, mostly by using microring resonators (MRRs) [87-92], BGs [93-96] or MZIs [97].

A Gaussian shaped resonance with a pass band ripple less than 0.5 dB has been demonstrated by using five series coupled MRRs [88] and 40 cascaded MRRs [90], with a bandwidth of 1.9 GHz and 20-100 GHz, respectively. Thus, the design of coupler MRRs enables a quasi-flat bandwidth, at expense of a large footprint, higher insertion loss, and a challenging device manufacturing. Recently, Huang *et al.* [91] proposed a solution based on a single MRR. It consists of an electrically tuned single microring and a reflector, able to provide a flat notch or pass-band response. Its operation is based on the exploitation of the fast and slow light effect

for notch or pass-band behaviour, respectively. The device shows a 0.5 dB flatness response with a -3 dB bandwidth of 7.5 GHz in a footprint of 0.47 mm^2, not compliant with the requirements of large bandwidth and compactness.

In order to overcome such limitations, BG solutions have been proposed in literature [93-94]. A notch filter based a SOI Bragg grating 800 μm long has been proposed [93], measuring a notch response with a bandwidth of about 100 GHz, a ripple of about 1 dB and an insertion loss of 0.5 dB [93].

Complex Bragg gratings-based devices have been proposed to obtain simultaneous pass-band and notch filtering response [95-96]. As example, a 2x2 Mach-Zehnder interferometer, with Bragg gratings on the two arms, has been reported in [95], measuring a notch/passband filtering shape at through/drop port with high rejection ratio (about 15 dB), high flatness (ripple < 0.5 dB for the pass-band shape, ripple ≈ 10 dB for the notch shape) and bandwidth of about 50 GHz. Recently, Jiang *et al.* [96] have proposed a broadband tuneable filter based on a multimode anti-symmetric waveguide SOI Bragg grating, acting as pass-band and notch filter simultaneously. The device provides a wide filtering bandwidth (in the order of THz), with a ripple of the passband and notch shape less than 0.5 dB and 5 dB, respectively.

Besides the wide and flat bandwidth, the tuning of the filter central frequency is a crucial requirement for the optical filtering in the next generation networks. A thermo-optical [83-88] and electromechanical [92] tuning have been investigated in literature. The electromechanical tuning is strictly related to the deflection of a cantilever. Although it provides a power consumption in the order of hundreds of nW, a frequency shift is limited to few GHz [92]. Furthermore, the slow switching time and the manufacturing complexity limit its use.

To overcome these bottlenecks, the thermo-optic tuning mechanism of a filter ensures a wavelength shift of the order of tens GHz, low optical loss [88], at the expense of a power consumption of a few mW for simple configurations [87] and tens of mW (≈ 70 mW) for complex geometries [88]. Although the thermo-optic mechanism is characterized by ease of manufacturing, this approach presents some issues related to the thermal crosstalk between multiple resonators and to the slow switching time (tens of μs) [87].

The electro-optic tuning mechanism, based on the free-carrier-plasma-dispersion, has been proposed to mitigate the issues related to the electromechanical and the thermal tuning. It provides a switching time less than 1 ns [98-100], together with his aptitude for integration into CMOS circuit.

An ultra-compact and electro-optical tuneable 1st order Butterworth notch filter with a narrow and flat-bottom passband, based on a photonic crystal ring resonator (PhCRR), has been designed as building block for a MW coherent filter [101].

3.3.1 Photonic notch filter

The designed optical notch filter consists of a silicon-based PhCRR, with radius R (see Fig. 3.9(a)), where the photonic crystal is superimposed only on a ring resonator section, in contrast to the device reported in Chapter 2. The based waveguide consists of a SOI rib structure with a thickness $t_{wg,}$ = 200 nm and a width w_{wg} = 500 nm, on a 50 nm thick slab layer. The rib waveguide is embedded in silicon dioxide with top and bottom cladding 1 μm and 3 μm thick, respectively. (Fig. 3.9(b)). Among several SOI waveguides, a rib structure has been chosen according to its suitability for the electro-optical tuning mechanism [98], enabling low loss values for the tuning [99].

The PhC section is made by a width modulation of the waveguide, forming the so-called sidewall grating (Fig. 3.9(c)), having a maximum w_{max} and minimum w_{min} width, with a duty-cycle DC. The ring section without the PhC has a length L_1.

Since the TE polarization ensures fewer scattering losses than the TM one, the fundamental TE_0 mode has been considered, whose normalized Poynting vector is shown in Fig. 3.9(d). A grating period Λ = 304 nm has been designed to ensure the operation around 1550 nm. w_{max} and w_{min} equal to 500 nm and 400 nm, respectively, have been chosen to avoid the excitation of higher order modes that could affect the filter operation. In order to tailor the PhCRR frequency response, the PhC section includes a number of defects w_{def} wide ($w_{def} = w_{max}$) and L'_{def} long, as shown in Fig.3.9(c).

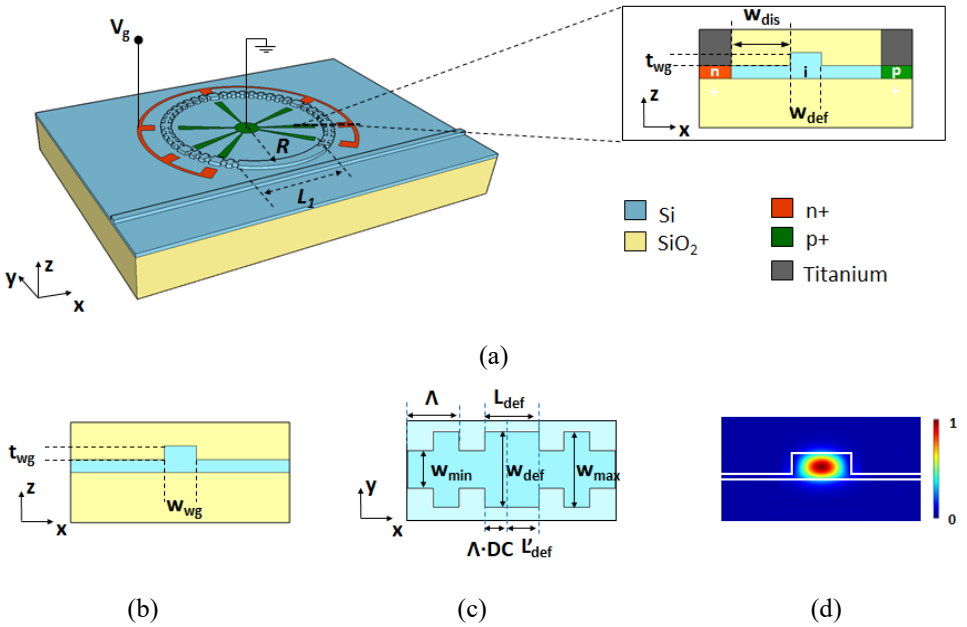

Fig. 3.9. (a) Schematic of the photonic crystal ring resonator with Newton distribution of the defects. Inset: Cross-section of the defect region into the PhC section. (b) Cross-section of the waveguide without PhC. (c) Top-view of the sidewall grating superimposed along a section of the ring resonator. (d) Normalized Poynting vector of TE_0 mode into the unperturbed waveguide cross-section, (t_{wg}: waveguide thickness, w_{wg}: waveguide width, L_1: ring resonator section without PhC, R: radius, w_{min}: PhC minimum width, w_{def}: PhC defect width, w_{max}: PhC maximum width, DC: duty-cycle, Λ: period, L_{def}: defect length, w_{dis}: core-doping regions distance, V_g: applied voltage) [101] © 2019 IEEE.

The electro-optical tuning mechanism has been chosen, according to the considerations reported in Section 3.3. Since the introduction of a defect into the PhC generates a resonance into the photonic bandgap, the frequency response is tuned by changing the effective index in correspondence of the defect regions by varying the applied voltage at the p-i-n junctions. A p-i-n junction has been considered in the regions of defects, with n+ and p+ doped regions (inset of Fig. 3.9(a)). The distance w_{dis} larger than 1 µm, between the doped regions and the rib allows to neglect the losses due to the ion implantation [100].

The propagation loss of the bare waveguide at $\lambda = 1550$ nm is assumed equal to 5.1 dB/cm [102], one order of magnitude higher than the state-of-the-art [103], in order to consider additional losses due to the grating manufacture. Furthermore, the tuning loss has been added to this value in correspondence of the defects.

3.3.2 Modelling and design of the PhCRR

The tailoring of the notch filter response can be achieved by inserting

defects inside the PhC sections. A single defect inside the PhC involves the creation of localized photonic states into the photonic bandgap. By including several defects inside a ring resonator and designing the ring resonator to match the resonance condition into the PBG, a notch pass-band behaviour of the reflected frequency response could be obtained, due to the presence of a Lorentzian-shaped peak inside the ring resonator spectrum [104]. This approach requires a circulator before the resonator [105], at expense of a large footprint and high chip complexity.

By engineering the position of the defects into the PhC, a notch filtering response with Gaussian shape could be achieved. The insertion of multiple defects into the PhC leads a number of ridges and valleys equal to the number of defects, according to [106]. By placing the defects according to the Newton binomial series, the PhC transmission response could be equalized. It results by the envelope of resonances binomial distributed and centred at the Bragg wavelength. This approach derives from the well-known antenna theory [107], where the ripple in the radiation pattern could be suppressed choosing the feeding currents of a binomial antenna array, according to the Newton binomial series coefficients.

The insertion of N_d defects inside the PhC with a total number of semi-periods N_t, involve the creation of $N_{sections}$ ($N_{sections} = N_d + 1$). The length of the n^{th} grating section, where n is an integer number ($n \in [0{:}N_d]$), is correlated to the product of the coefficients B_n, corresponding to the coefficients of a generic binomial $(a+b)^{N_d}$, reported in the Pascal triangle (Tab. 3.2), and the ratio $N_t/\sum_{n=1}^{N_d} B_n$ [108]. As example, the sketch of a sidewall grating, with $N_d = 6$ and $N_t = 128$, based on the silicon rib waveguide above described is shown in Fig. 3.10(a), reporting the length of each section.

As shown in Fig. 3.9(c), the length of all defects L'_{def} results by the sum of the grating semi-period length ($\Lambda \cdot DC$) and the length L_{def} of a waveguide portion, w_{max} wide, that acts as discontinuity of the grating periodicity:

$$L'_{def} = DC \cdot \Lambda + L_{def} \tag{3.2}$$

$$L_{def} = \frac{4m+1}{4} \frac{\lambda_B}{n_{eff\text{-}def}} \quad m = 1, 2, \ldots \tag{3.3}$$

where λ_B is the Bragg wavelength (≈ 1550 nm) and $n_{eff\text{-}def}$ is the effective refractive index of the defect region.

A single resonance inside the PBG can be observed for $5 < m < 50$ for $N_t = 128$. By increasing the m value ($m > 50$), multiple resonances appear into the PBG. Then, $L_{def} = 3.11$ µm for $m = 5$ and DC = 50%, which corresponds to a total grating length $L_g \approx 38.27$ µm ($N_d = 6$ and $N_t = 128$).

Tab.3.2. Pascal Triangle of Binomial Coefficients B_n Related to the Number of Defects N_d [101].

N_d	B_n													
0							1							
1						1		1						
2					1		2		1					
3				1		3		3		1				
4			1		4		6		4		1			
5		1		5		10		10		5		1		
6	1		6		15		20		15		6		1	
7	1	7		21		35		35		21		7		1

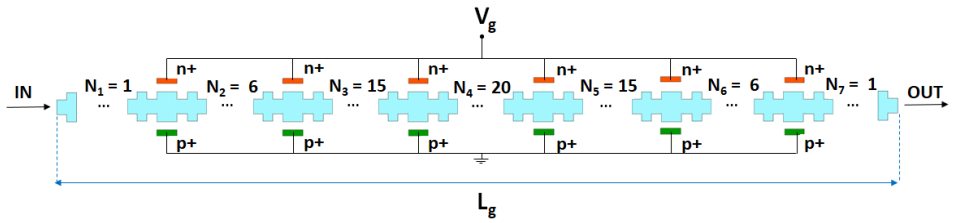

(a)

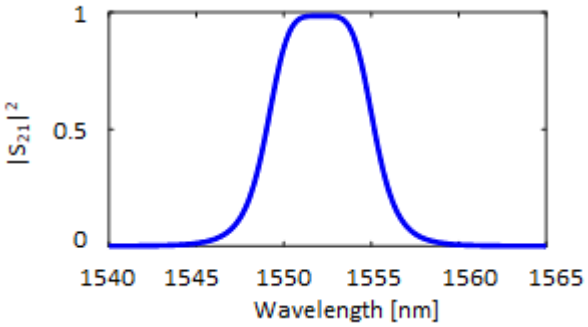

(b)

Fig. 3.10. (a) Silicon-based sidewall grating with defects placed according to the Newton rule; (b) Transmission spectrum of the PhC section with $L_{def} = 3.11$ µm, $N_d = 6$ and $N_t = 128$ [101] © 2019 IEEE.

The device electromagnetic behaviour has been calculated by using the Effective Index Method (EIM) [109], for the propagating modes definition, and the Transfer Matrix Method (TMM) [110] to estimate the grating reflection/transmission through the *S*-parameters. Each defect and semi-period of the grating have been modelled as a 4x4 transmission matrix. Thus, the final expression of the transmission matrix is obtained by multiplying the transmission matrix of each single element (semi-periods and defects). The grating has been assumed symmetric ($S_{21} = S_{12}$), simplifying the analytical approach. The grating simulated transmission spectrum ($|S_{21}|^2$) is reported in Fig. 3.10(b), where the Gaussian flat top behaviour results by the overlap between the Lorentzian-like resonances caused by each defect.

By injecting carriers using a p-i-n structure embedded into the defects, the PhC response can be frequency tuned. The spectral response is affected by the effective index change of the defects section, where a voltage V_g is applied to the junction. The carrier density into the cross-section of the p-i-n junction has been calculated (inset in Fig. 3.9(a)), by using the drift diffusion equations [111], when the applied voltage changes. Finally, a FEM-based approach and the Soref-Bennet equations [112] have been used to calculate the index change and the complex effective index, respectively. The effective index change (blue curve) and related losses (red curve), varying the applied voltage V_g, have been reported in Fig. 3.11.

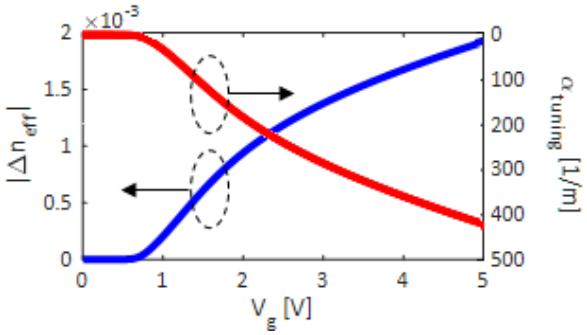

Fig. 3.11. Silicon-based rib waveguide: (Blue curve) trends of effective index change Δn_{eff}, and (Red curve) tuning loss α_{tuning} [1/m], as function of the applied voltage V_g [101] © 2019 IEEE.

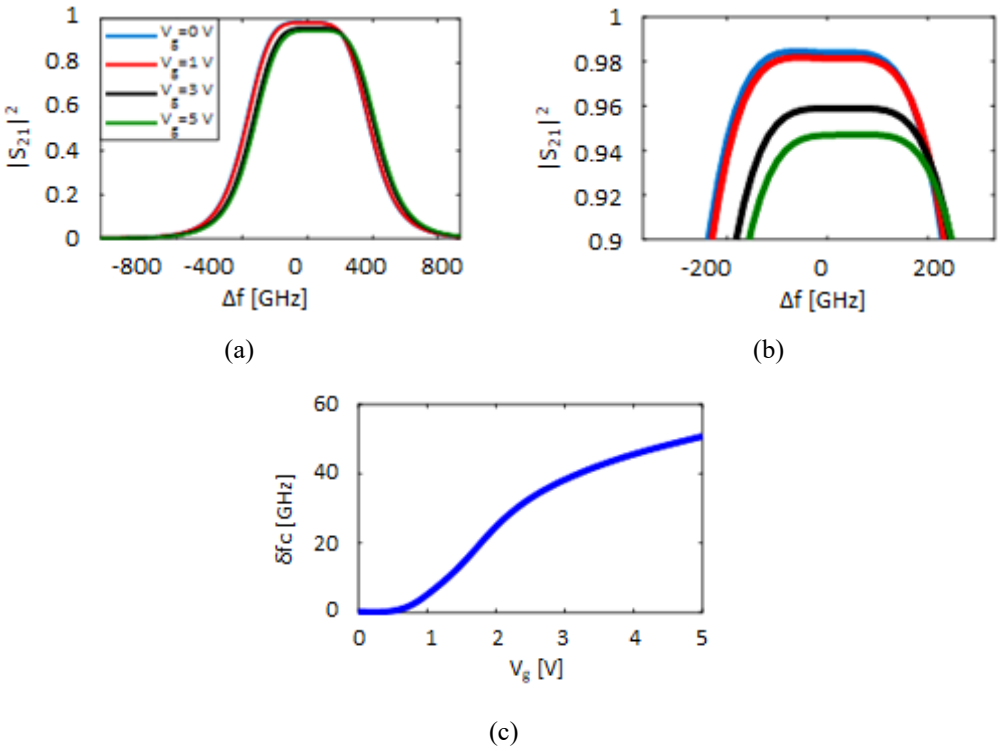

Fig. 3.12. Silicon-based sidewall grating with defects placed according to the Newton rule: (a) transmission spectra vs Δf, which is the frequency shift from the operating frequency ($f_0 \approx 193$ THz); (b) inset of transmissions spectra vs Δf, (c) central frequency detuning, δf_c, as a function of V_g [101] © 2019 IEEE.

The effective index change $|\Delta n_{eff}|$ increases as V_g increases, but at the expenses of higher value of losses, that should be added to the waveguide loss, in correspondence to the defects. The effect of the electro-optical tuning on the spectrum of the PhC under study is reported in Fig. 3.12(a)-(b).

As shown in Fig. 3.12, the central frequency f_c blue shifts with respect to its value at $V_g = 0$ V, $f_0 \approx 193.223$ THz. Thus, the frequency detuning $\delta f_c = f_c - f_0$ shows a similar trend of $|\Delta n_{eff}|$ (Fig. 3.11), varying the applied voltage V_g.

By integrating the PhC with defects, placed according the binomial rules, into a simple ring resonator, forming a PhCRR, a 2nd order Gaussian shape of the transmission response can be achieved. In order to simulate the PhCRR behaviour, a self-made e.m. model of the PhCRR has been implemented. The transfer function T has been derived by imposing the continuity conditions of the fields at the interfaces between the coupling region and the PhC section:

$$T = \frac{S_{21} k^2 e^{\varphi} e^{i\theta} + \tau \cdot (k^2 \det \boldsymbol{S}_{\boldsymbol{PhC}} e^{2i\theta} + 1)}{\tau (S_{12} + S_{21}) e^{\varphi} e^{i\theta} + \tau^2 e^{2i\theta} \det \boldsymbol{S}_{\boldsymbol{PhC}} - e^{2\varphi}} \tag{3.4}$$

where k is the coupling coefficient (no loss into the coupling region has been assumed), $\tau=\sqrt{1-k^2}$, $\theta=\beta_{portion}\cdot L_1$, $\varphi=\alpha\cdot L_1$; $\beta_{portion}$ is the real part of the propagation constant related to L_1, α is the waveguide propagation loss [dB/cm].

The PhC region L_g long is described by a scattering matrix, S_{PhC}, numerically calculated by using the aforementioned S matrix – based approach. The PhCRR section unperturbed has been designed in order to satisfy the following equations at the operation wavelength:

$$\angle S_{21}+\theta=2m\pi \qquad m = 1, 2, \ldots \tag{3.5}$$

$$L_1 \geq 0.2 \cdot (L_1+L_g) \tag{3.6}$$

The fulfilment of Eq. (3.6) is required to increase the coupling efficiency, assuming L_1 longer than the coupling length, according to a conservative approach. Since the length L_1 also depends on the ring radius, a minimum PhCRR radius R = 5 µm has been assumed, to neglect the bending losses [113]. As example, by integrating the PhC section, sketched in Fig. 3.10(a), in a ring resonator with R > 5 µm, a length L_1 = 10.066 µm and a ring radius R = 7.7 µm have been obtained by satisfying the Eqs. (3.5-3.6).

For a proper operation of the notch filter, the value k is a crucial parameter. Its squared value represents the coupling efficiency inside the coupling region. The critical value of the power efficiency $K_{critical,}$ that is about 15.3 % for the configuration under investigation, has been estimated [114].

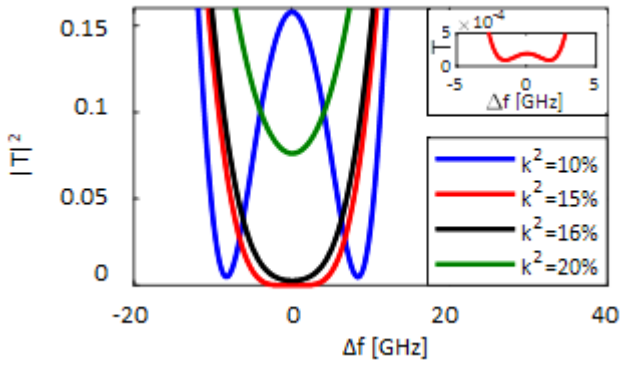

Fig. 3.13. Bottom band of the PhCRR transmission response, for several values of coupling efficiency k^2 [101] © 2019 IEEE.

The magnification on the bottom band of the notch response has been reported in Fig. 3.13, for several integer k^2 values. $k^2 \approx K_{critical}$ (k^2 = 15 % - 16 %) leads a Gaussian profile of the notch response (very small ripple values for k^2 = 15 % (inset of Fig. 3.13) and null ripple for k^2 = 16 %), while high ripple values and a Lorentzian-like shape with no-flat bottom band are observed into the band for $k^2 << K_{critical}$ (k^2 = 10 %) and $k^2 >> K_{critical}$ (k^2 = 20 %), respectively.

Interesting results have been achieved observing the phase transmission response. In particular, for $k^2 \approx K_{critical,}$ the phase response shows a linear trend at the operating frequency, at $\angle T = 0$ for $k^2 \leq K_{critical}$ (Fig. 3.14(a)) and at $\angle T = \pi$ for $k^2 \geq K_{critical}$ (Fig. 3.14(c)), as highlighted into the magnification in the red boxes. This phase trend justifies the transmission behaviour reported in Fig. 3.13. To exploit the phase linearization, a proper design of the PhC region is required. By imposing $\angle S_{12} \equiv \angle S_{21} = 0$, the contour plots of the phase of T, depending on the phase of S_{11} and S_{22}, have been reported in Fig. 3.14.

The phase of S_{11} and S_{22}, and, then, the PhC section, should be designed in order to obtain $\angle T = 0$ for $k^2 \leq K_{critical}$ (Fig. 3.14(b)) and $\angle T = \pi$ for $k^2 \geq K_{critical}$ (Fig. 3.14(d)). The satisfice of these requirements ensure a linear phase response of T, and then, a flat Gaussian shape of the frequency response.

The condition $\angle S_{11}=\angle S_{22}$ (described by the central diagonal white line in Fig. 3.14(b)-(d)) ensures to satisfy only the requirement $\angle T = \pi$ for $k^2 \geq K_{critical}$.

Instead, both requirements ($\angle T = 0$ for $k^2 \leq K_{critical}$ and $\angle T = \pi$ for $k^2 \geq K_{critical}$) are satisfied by the condition $|\angle S_{11}-\angle S_{22}|=\pi$ (described by the symmetrical blue and white lines with respect to the diagonal in Fig. 3.14(b) and Fig. 3.14(d), respectively). In summary, the PhC section must satisfy both the following conditions:

$$\angle S_{12}=\angle S_{21}=0 \tag{3.7}$$

$$|\angle S_{11}-\angle S_{22}|=\pi \tag{3.8}$$

In order to fulfil the Eqs. (3.7)-(3.8), the PhC must be symmetric: if the number of defects is odd, the PhC must end with a semiperiod, while if the number of defects is even, additional grating periods must be added.

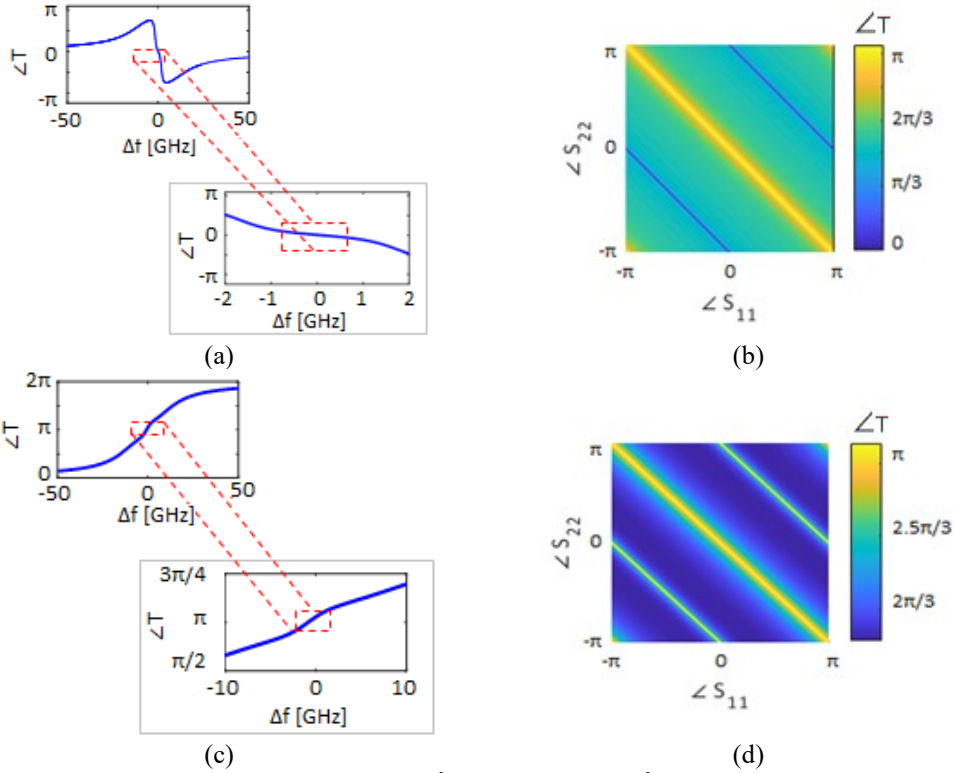

Fig. 3.14. Phase response of PhCRR for (a) $k^2 \leq K_{critical}$ and (c) $k^2 \geq K_{critical}$, and phase transmission $\angle T$ contour map depending on S_{11} and S_{22} to achieve a phase linear response null at 0 (b) or π (d) [101] © 2019 IEEE.

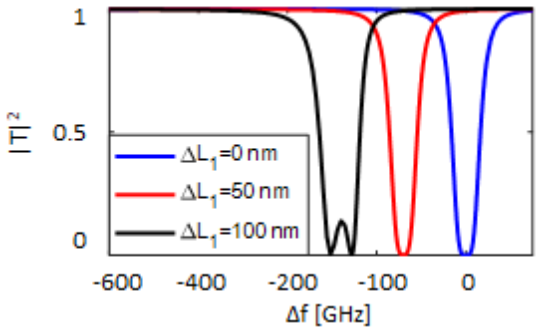

Fig. 3.15. PhCRR transmission as function of Δf at three different values of ΔL_1 [101] © 2019 IEEE.

Furthermore, the impact of some manufacturing issues on the PhCRR frequency response has been evaluated. As example, if the length L_1 is not compliant with the Eq. (3.5), a shift of the filter central frequency occurs, resulting in a Lorentzian-shape with a high ripple into the stopband, as shown in Fig. 3.15.

The PhCRR under investigation has been designed to satisfy the Eqs. (3.7)-(3.8) and the related transmission spectrum is reported in Fig. 3.16(a).

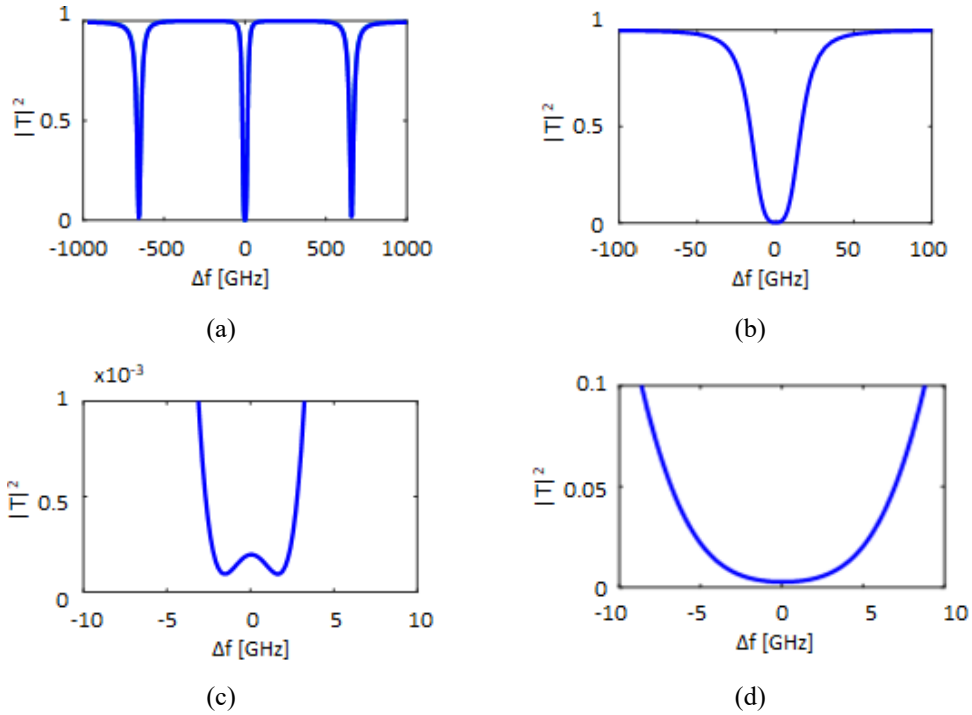

Fig. 3.16. Wide transmission spectrum of PhCRR under investigation (a), with a zoom on the Gaussian-like resonance (b). Magnification on the bottom band for k^2 = 15% (c) and k^2 = 16% (d) [101] © 2019 IEEE.

In particular, the resonance at the operating frequency (f_0 = 193.223 THz) shows a bandwidth BW = 32.82 GHz and a Gaussian profile, while, the other resonances show a Lorentzian profile with Fano behaviour. Furthermore, the Gaussian resonance has an extinction ratio more than 40 dB and a filter slope of about 2.62 dB/GHz, measured between 90% and 10% of the transmission spectrum. As shown in Fig. 3.16(c)-(d), a ripple equal to 0.33 dB can be observed for k^2 = 15 %, while an equalized stopband has been obtained with k^2 = 16 %.

The Gaussian behaviour has been confirmed by a root-mean-square error for the Gaussian fitting ($RMSE_{gauss}$) one order of magnitude lower than the error ($RMSE_{Lorentz}$), obtained by fitting with a Lorentzian profile.

For the PhCRR fabrication, the silicon-based device can be manufactured by using electron-beam lithography followed by reactive ion plasma etching. The p-i-n diode can be defined with lithography and phosphorous (for n+ region) and boron implantation (for p+ region). The silica top cladding can be deposited by plasma-enhanced chemical vapour deposition followed by an annealing process for the dopants activation.

3.3.3 Design results

The PhC portion of the PhCRR has been designed to obtain the best compromise in terms of *B*, *ER*, tuning range and band flatness of the PhCRR frequency response. Several parametric simulations have been carried out on the semi-periods number N_t, defects number N_d and defects lengths L_{def} of the Newton-based sidewall gratings. According to the PhC design procedure, reported into the Paragraph 3.3.2, the transmission spectra of the gratings with $N_t = 128$ and $N_t = 256$, for several values of N_d, and $L_{def} = 3.11$ µm, are reported, in Fig. 3.17(a) and Fig. 3.17(b), respectively. The maximum number of defects, that could be inserted into the grating, strictly depends on the fulfilment of the Newton rule (see Tab. 3.2). The number of binomially distributed defects N_d affects the ripple into the PhC response, the *ER*, and the bandwidth.

Furthermore, by comparing the spectra with the same N_d, the configuration with $N_t = 256$ provides an enhancement of the bandwidth with respect to the configuration with $N_t = 128$. According to the condition of N_t equal to a power of 2, a minimum value of $N_t = 128$ has been considered for the PhC design, in order to avoid PhCRR radii < 5 µm, so preventing a remarkable increase of the optical losses [113]. Moreover, the transmission of a PhC with a number of semiperiods N_t larger than 256, i.e. $N_t = 512 - 1024$, shows a maximum value of about 0.1, making difficult the Gaussian trend estimation.

The performance of the most promising PhC, and PhCRR configurations have been summarized in Tab. 3.3, in terms of maximum transmission amplitude, the ratio $R_{lorentz/gauss}$ between $RMSE_{lorentz}$ and $RMSE_{gauss}$ (for $R_{lorentz/gauss} > 10$, the resonance fits perfectly with a Gaussian shape).

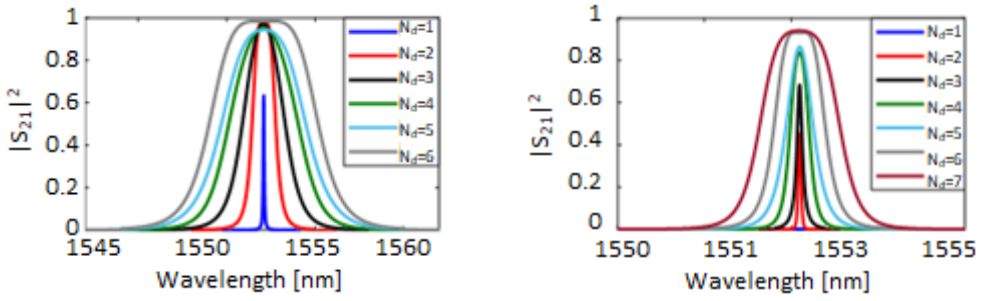

(a) (b)

Fig. 3.17. Transmission spectra of silicon-based sidewall gratings with $N_t = 128$ (a) and $N_t = 256$ (b) and for several values of N_d ($L_{def} = 3.11$ µm), designed according to Tab. 3.2 [101] © 2019 IEEE.

The comparison between PhC and related PhCRR performance highlights the influence of the PhC section on the PhCRR spectrum. The PhCRRs, reported in Tab. 3.3, have been designed according to the Eqs. (3.5) – (3.8), with a Newtonian distribution of the PhC defects (Tab.3.2) and L_{def} = 3.11 µm.

As shown in Table 3.3, the power coupling coefficient $K_{critical}$ strictly depends on the value of the transmission of the PhC at the operating frequency, on the PhC geometrical parameters, such as N_t and N_d, and on the PhCRR radius R.

Tab.3.3. Design parameters of several PhC configurations and related PhCRRs (L_{def} = 3.11 µm) [101].

N_t	N_d	PhC			PhCRR				
		BW **[GHz]**	$\|S_{12}\|^2$ **(@** f_0**)**	$R_{lorentz/gauss}$	$K_{critical}$ **[%]**	***R*** **[µm]**	***B*** **[GHz]**	***ER*** **[dB]**	$R_{lorentz/gauss}$
128	2	171.20	0.970	2.46×10^2	~16	5.18	14.48	28.36	2.55×10^1
128	3	311.45	0.973	9.43×10^1	~20	5.84	35.21	38.82	2.16×10^1
128	4	507.62	0.953	5.24×10^1	~32	6.50	69.08	57.13	2.25×10^1
128	5	621.92	0.943	2.60×10^1	~36	7.06	82.57	37.56	2.95×10^1
128	6	774.64	0.984	2.50×10^2	~16	7.70	32.94	25.68	2.23×10^1
256	4	30.45	0.837	1.32×10^2	~31	10.35	8.29	23.41	1.22×10^1
256	5	43.92	0.864	1.19×10^2	~36	11.01	15.04	49.33	3.59×10^1
256	6	75.87	0.932	2.22×10^2	~14	11.57	6.40	18.48	1.15×10^1
256	7	117.79	0.940	2.92×10^2	~20	12.14	10.43	41.25	1.41×10^1

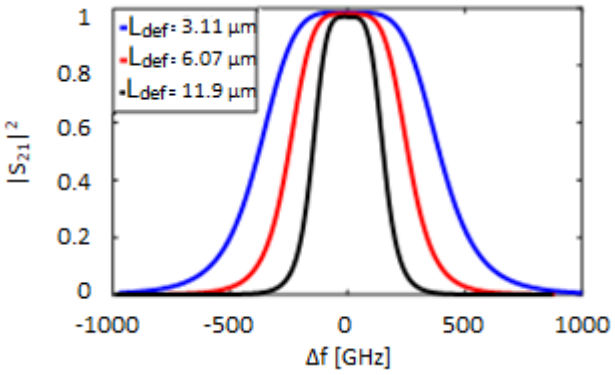

Fig. 3.18. Transmission spectra S_{21} of sidewall grating with N_t = 128 and N_d = 6 for several values of the L_{def}, compliant to Eq. (3.3) [101] © 2019 IEEE.

Low values of $K_{critical}$ ensure an enhancement of the bandwidth, at the expense of *ER* [84]. Moreover, the bandwidth is furtherly enhanced, of about one order of magnitude, when the performance of the PhC and PhCRR are quite similar, at the expense of a decrease of $R_{lorentz/gauss}$.

Although the PhCRR configuration with N_t = 256, and N_d = 6 shows the most promising results of the PhCRR performance, in terms of bandwidth *B* and *ER*, i.e. *BW* = 6.4 GHz and *ER* = 18.48 dB, a deviation ΔL_1 = 10 nm, as example due to some manufacturing issues, involves an asymmetric-Lorentzian shape of the resonance. Thus, this configuration results very sensitive to possible technological issues (as the configuration with N_t = 256, and N_d = 4). These configurations have been not considered in the final design of the PhCRR.

The defect length L_{def} is another degree of freedom of the PhC design that could be engineered to obtain a narrow bandwidth. The increase of the defect length, designed according to Eq. (3.3), provides a bandwidth improvement. For instance, the transmission response of a PhC section with N_t = 128 and N_d = 6 as function of L_{def}, is shown in Fig. 3.18.

The defect lenghts L_{def} equal to 3.11 μm, 6.07 μm and 11.99 μm, (corresponding to *m* = 5, *m* = 10 and *m* = 20, respectively, in Eq. (3.3)), have been designed to ensure the operation at about 1550 nm. Doubling the *m* value, a *B* enhancement by a factor 1.5 is achieved, keeping the Gaussian profile of the resonance.

In order to evaluate the impact of L_{def} on the PhCRR performance, a parametric analysis has been carried out, aiming at satisfying the requirements of narrow bandwidth and high extinction ratio, also, maximizing the figure of merit (*FOM*), expressed as *FOM* = *ER/BW* (expressed in dB/GHz). The investigated configurations are N_t = 256 with N_d = 5 and N_d = 7, according to the aforementioned considerations. The behaviour of the *FOM* and *R* as a function of L_{def} has been reported in Fig. 3.19(a) and Fig. 3.19(b), respectively. The blue and red curves result from the interpolating fitting of the blue and red dots, referred to the L_{def} values compliant to Eq. (3.3).

A maximum value of *FOM* has been obtained with L_{def} = 3.11 µm for both configurations. A worsening of *ER* could be observed by increasing the L_{def} value, that counteract the associated bandwidth improvement.

Therefore, the value L_{def} = 3.11 µm represents the best solution to perform a narrow bandwidth, high *ER*, and then, high *FOM* value, with a small footprint. In particular, the PhCRR with N_t = 256, N_d = 5 and L_{def} = 3.11 µm provides *BW* = 15.04 GHz, *ER* = 49.33 dB with *R* = 11.01 µm, while PhCRR with N_t = 256, N_d = 7 and L_{def} = 3.11 µm leads *BW* = 10.43 GHz, *ER* = 41.25 dB with *R* = 12.14 µm.

According to the electro-optical effect, a resonance blue-shift can be obtained, by applying a voltage V_g to the p-i-n junction. Although a large applied voltage leads a wide resonance blue shift (δf_c), a worsening of the bandwidth *BW* and *ER* is observed. Therefore, the maximum voltage V_{max} has been estimated in order to keep a Gaussian-like response with a maximum worsening of the bandwidth equal to 10 %, with respect to the value at V_g = 0 V. The summary of the tuning performance for the configurations under study is reported in Tab. 3.4.

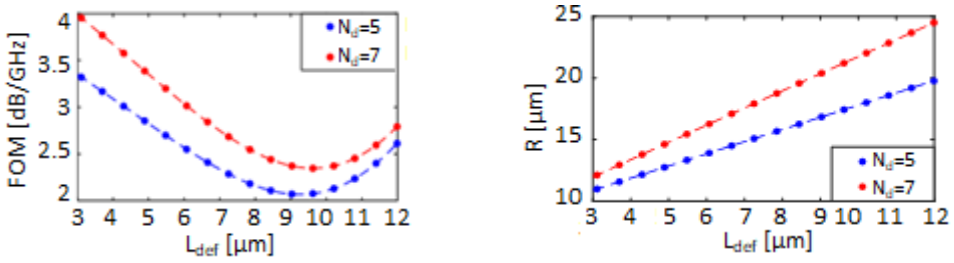

(a) (b)

Fig. 3.19. (a) Figure-of-merit *FOM* (*ER*/*BW*); (b) PhCRR radius R as a function of L_{def}, for PhCRRs with N_t = 256 and N_d = 5 (blue curve), and N_d = 7 (red curve). The dotted points refer to defects lengths L_{def} that are compliant to Eq. (3.3) [101] © 2019 IEEE.

Tab. 3.4. Tuning performance comparison (ER_{MAX} = ER @ V_g = 0 V, ER_{MAX} = ER @ V_g = V_{MAX}) [101].

N_t	N_d	L_{def} [µm]	$K_{critical}$ [%]	*BW* [GHz]	V_{max} [V]	δf_c [GHz]	ER_{max} [dB]	ER_{min} [dB]
256	5	3.11	36	15.04	1.69	18.65	49.98	26.72
256	7	3.11	20	10.43	1.50	15.18	41.25	25.46

In particular, the configuration with $N_d = 5$ ensures δf_c of about 18 GHz with a minimum ER value $ER_{min} > 26$ dB, while, the PhCRR with $N_d = 7$ performs δf_c of about 15 GHz with $ER_{min} > 25$ dB. According to the behaviour of Fig. 3.11(b), the resonance shift with $V_g \leq 0.6$ V could be considered negligible (Fig. 3.20). Thus, assuming an initial condition $V_g = 0.6$ V, a fine tuning of the central frequency is achieved, with a higher curve slope, and then a higher tuning efficiency, for the configuration with $N_d = 7$ with respect to $N_d = 5$. The PhCRR with $N_t = 256$, $N_d = 7$ and $L_{def} = 3.11$ µm represents the best compromise to achieve a performing Gaussian notch filter with flat band. The power coupling efficiency $K_{critical}$ between the bus waveguide and the ring portion without grating with length L_1 has to be 20% for the selected configuration, according to Tab. 3.3, to avoid ripple into the pass-band. The coupling efficiency k^2 as a function of the gap g between the bus and the ring has been estimated by using a 2D Finite Difference Time Domain (FDTD) approach (Fig. 3.21), considering $R = 12.14$ µm, and $L_1 = 15.392$ µm, that is about 20% of the PhCRR perimeter. In particular, a gap $g = 116$ nm ensures a coupling efficiency k^2 equal to 20%.

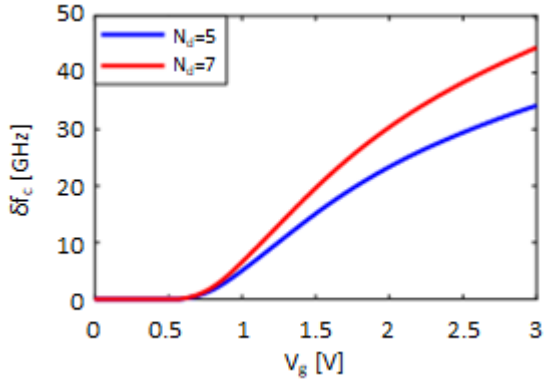

Fig. 3.20. Detuning, δf_c, of the central frequency of the notch filter *vs* applied voltage V_g [101] © 2019 IEEE.

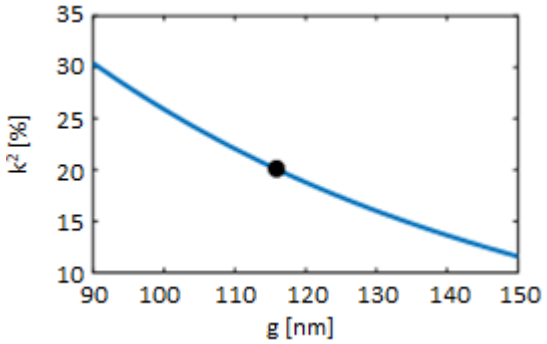

Fig. 3.21. Coupling efficiency k^2 [%] vs gap bus-ring g [nm] [101] © 2019 IEEE.

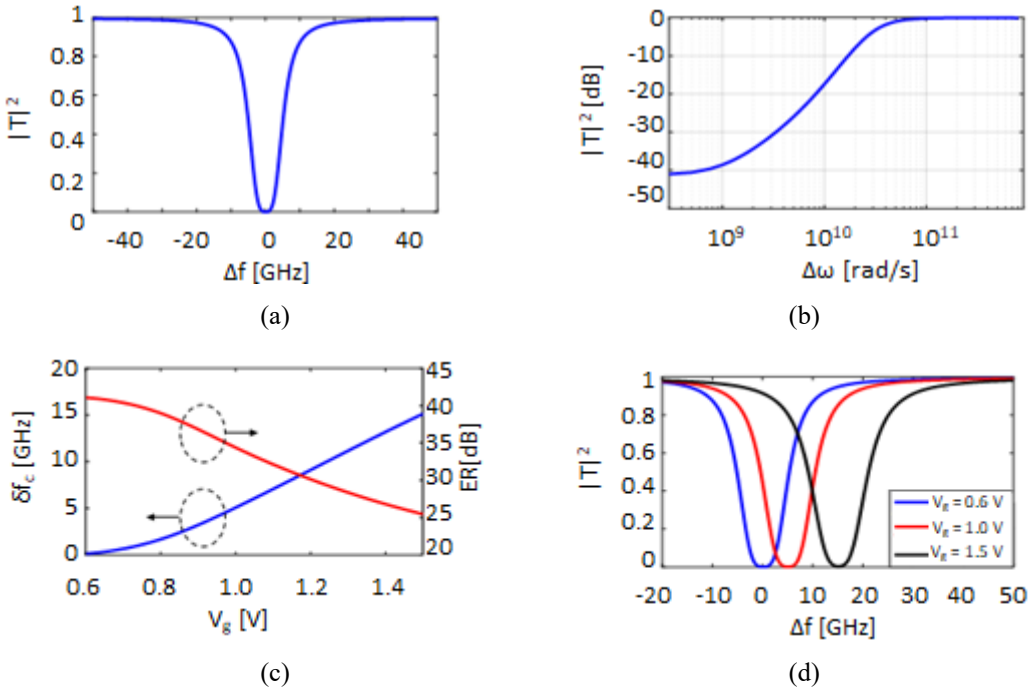

Fig. 3.22. (a) Transmission spectrum of the PhCRR with $N_t = 256$, $N_d = 7$, $L_{def} = 3.11$ µm ($k^2 = 20\%$) and Bode plot (b) of the 1st order Butteworth low pass filter (ω is the angular frequency [rad/s] and $\Delta\omega$ is the angular frequency shift from the operating angular frequency). (c) Shifting of the central frequency and ER trends as a function of the applied voltage V_g, with some examples of the transmission spectra after voltage tuning (d) ($f_0 \approx 193.2877$ THz) [101] © 2019 IEEE.

A maximum ripple of about 0.2 dB could be obtained if the value of the coupling efficiency slightly moves from the nominal value ($k^2 = 19$ %).

The transmission spectrum of the tuneable Newton-based PhCRR with $N_t = 256$, $N_d = 7$ and $L_{def} = 3.11$ µm is reported in Fig. 3.22. The related Gaussian profile with a flat bandwidth ($BW = 10.43$ GHz), high ER (41 dB) and high slope of the sidewalls of the spectrum (2.62 dB/GHz), is shown in Fig. 3.22(a). In particular, as shown in Fig. 3.22(b), the frequency response shows a behaviour of a 1st order Butterworth notch filter, with a slope of 20 dB per decade and maximally flat stopband. Furthermore, a fine, continuous and quasi-linear tuning of the central frequency has been obtained by applying a voltage from 0.6 V to 1.5 V, with a maximum detuning of the central frequency of about 15 GHz. The electro-optical effect ensures a reconfigurability time of about 1 ns, with a tuning efficiency of 20.17 GHz/V, and a minimum $ER = 25$ dB, as shown in Fig. 3.22 (c)-(d).

3.4 Conclusions

Innovative telecom payload concepts making full use of photonic technologies have been reported into this Chapter. By introducing microwave photonic components plus subsystems, which realize multi- LO generation and distribution, frequency conversion, analog-to-digital conversion, digital-to-analog conversion, multi-beamforming, and switching, software-defined satellite payloads operating in the high-frequency band satisfy the requirements of the telecom operators, as flexibility, in-orbit reconfigurability with significant reduction of mass, volume, and power consumption. Innovative architectures of software-defined payload building blocks, as microwave photonic filter and oscillator signal generator, have been presented.

In particular, the theoretical feasibility of a miniaturized Ka-band optoelectronic oscillator with a phase noise at 10 kHz offset from the carrier of about -155 dBc/Hz (more than 47 dBc/Hz better than the state-of-the-art) and an output electric power > 10 dBm (more than three times better than the state-of-the-art) has been demonstrated. The optoelectronic section of the OEO is a PIC to be fabricated by a new technological platform allowing the hybrid integration of ultra-low loss passive photonic devices with active III-V active ones, such as laser and photodiodes. The RF components of the OEO can be monolithically integrated on a properly designed MMIC to be co-packaged with the PIC. The proposed OEO having a volume of about 1 cm^3, a power consumption of a few Watts, and the above-mentioned performance in terms of spectral purity have a wide range of applications in the field aerospace & defence industry.

Furthermore, the design of a novel ultra-compact photonic-crystal ring resonator with a bandwidth BW = 10.43 GHz and ER > 40 dB, acts as notch filter, has been reported. The Newton distribution of the defects inside the photonic crystal section provides a Gaussian-shaped frequency response, with very steep sidewalls (2.62 dB/GHz). The integration of a p-i-n junction, in correspondence to the PhC defects, enables a continuous tuning of the central frequency (15 GHz), fast switching time (≈ 1 ns) with a power consumption equal to about 47 mW. It represents a clear improvement of the state-of-the-art, in terms of stopband

equalization, monolithic integration capability, wide band tunability, low power consumption, very short switching time, and ultra- small footprint.

3.5 References

[1] A. C. Dickieson, "The Telstar experiment," The Bell System Technical Journal, **42**, 4, pp. 739-746, 1963.

[2] R. M. Bentley, and A. T. Owens, "Syncom satellite program," Journal of Spacecraft and Rockets, **1**, 4, pp. 395-399, 1964.

[3] Satellite Industry Association, Report "State of the Satellite Industry Report", September 2018.

[4] Satellite Industry Association, Report "State of the Satellite Industry Report", September 2014.

[5] T. Janevski, "5G mobile phone concept," Proc. of. 2009 6th IEEE Consumer Communications and Networking Conference, IEEE, Las Vegas, Nevada, USA, January 10-13, 2009.

[6] S. Pan, D. Zhu, S. Liu, K. Xu, Y. Dai, T. Wang, J. Liu, N. Zhu, Y. Xue and N. Liu, "Satellite payloads pay off," IEEE Microwave Magazine, **16**, 8, pp. 61-73, 2015.

[7] P. Angeletti, R. de Gaudenzi, and M. Lisi, "From 'Bent pipes' to 'software defined payloads': Evolution and trends of satellite communications systems," Proc. of 26th AIAA Int. Communications Satellite Systems Conference, pp. 1–10, Florence, Italy, October 15-17, 2008.

[8] C. Morlet, M.-L. Boucheret, V. Calmettes, B. Paillassa, and T. Pérennou, "Towards generic satellite payloads: Software radio," Proc. of 17th International Symposium Parallel Distributed Processing, pp. 1–7, Geneva, Switzerland, June 25-28, 2003.

[9] M. Aloisio, P. Angeletti, F. Coromina, and R. de Gaudenzi, "Exploitation of Q/V-band for future broadband telecommunication satellites," Proc. of IEEE 13th International Vacuum Electronics Conference, pp. 351–352, Monterey, California, USA, April 24-26, 2012.

[10] M. Sotom, M. Aveline, R. Barbaste, B. Benazet, A. Le Kernec, J. Magnaval, and M. Picq, "Flexible photonic payload for broadband telecom satellites: from concepts to system demonstrators," Proc. International Conference on Space Optics—ICSO 2016, International Society for Optics and Photonics, **10562**, p. 105621Y, Biarritz, France, October 18-21, 2017.

[11] N. Karafolas, J. M. P. Armengol, and I. Mckenzie, "Introducing photonics in spacecraft engineering: ESA's strategic approach," Proc. of 2009 IEEE Aerospace conference, IEEE, pp. 1-15, Big Sky, Montana, March 7-14, 2009.

[12] D. Poudereux, J. Barbero, J. Tijero, I. Esquivias and I. McKenzie, "Evaluation of optical switches for Space applications," Proc. of International Conference on Space Optics—ICSO 2018, International Society for Optics and Photonics, **11180**, p. 111807H, Chania, Greece, October 9-12, 2019.

[13] J. Capmany, and D. Novak, "Microwave photonics combines two worlds," Nature Photonics, **1**, 6, p. 319, 2007.

[14] F. Dell'Olio, G. Brunetti, D. Conteduca, N. Giovinazzi, C. Ciminelli, and M. N. Armenise, "Integrated microwave photonic devices and circuits in space," Proc. of 49th Annual Meeting of the Associazione Società Italiana di Elettronica (SIE), Palermo, Italy, June 21-23, 2017.

[15] F. Dell'Olio, G. Brunetti, D. Conteduca, N. Giovinazzi, N. Sasanelli, C. Ciminelli, and M. N. Armenise, "Integrated microwave photonics: overview and promising space applications," Lecture Notes in Electrical Engineering, **512**, pp. 107-112, 2018.

[16] C. Ciminelli, F. Dell'Olio, G. Brunetti, and M. N. Armenise, "Microwave Photonics: An Opportunity for Space Systems and 5G Networks," Proc. of 1st International Conference on Dieletric Photonic Devices and Systems Beyond Visible (D-PHOTON 2018), Bari, Italy, October 1-2, 2018. (INVITED).

[17] M. Aveline, M. Sotom, R. Barbaste, B. Benazet, A. Le Kernec, J. Magnaval, and M. A. Piqueras, "Reconfigurable microwave photonic repeater for broadband telecom missions: Concepts and technologies," Proc. of

International Conference on Space Optics—ICSO 2014, International Society for Optics and Photonics, **10563**, p. 105633M, Tenerife, Spain, October 6-10, 2014.

[18] C. Ciminelli, F. Dell' Olio, G. Brunetti, A. Di Benedetto, and M. N. Armenise, "Integrated Microphotonic Switching Matrices for Flexible and Broadband Telecom Satellite Payloads," Proc. of 21st International Conference on Transparent Optical Networks (ICTON 2019), Angers, France, July 9-13, 2019. (INVITED).

[19] R. Sorrentino, and G. Bianchi, *Microwave and RF Engineering*, John Wiley & Sons., 2010.

[20] K / Ka -Band, Programmable Frequency Synthesizer, http://www.emresearch.com/

[21] Agilent E8257D PSG Microwave Analog Signal Generator, http://www.agilent.com/

[22] BOVI45 Ka-band Phase Locked Oscillator, BHE, http://www.bhe-mw.eu/

[23] X. S. Yao, and L. Maleki, "High frequency optical subcarrier generator," Electronics Letters, **30**, 18, pp. 1525-1526, 1994.

[24] X. S. Yao, and L. Maleki, "Optoelectronic microwave oscillator," Journal of the Optical Society of America B, **13**, 8, pp. 1725-1735, 1996.

[25] K. Saleh, P.-H. Merrer, A. Ali-Slimane, O. Llopis, and G. Cibiel, "Study of the Noise Processes in Microwave Oscillators Based on Passive Optical Resonators," International Journal of microwave and wireless technologies, **5**, 3, pp. 371-380, 2013.

[26] J. Xiong, R. Wang, T. Fang, T. Pu, D. Chen, L. Lu, P. Xiang, J. Zheng, and J. Zhao, "Low-cost and wideband frequency tuneable optoelectronic oscillator based on a directly modulated distributed feedback semiconductor laser," Optics Letters, **38**, 20, pp. 4128-4130, 2013.

[27] X. Xie, C. Zhang, T. Sun, P. Guo, X. Zhu, L. Zhu, W. Hu, and Z. Chen, "Wideband tuneable optoelectronic oscillator based on a phase modulator and a tuneable optical filter," Optics Letters, **38**, 5, pp. 655-657, 2013.

[28] D. Eliyahu, D. Seidel, and L. Maleki, "Phase Noise of a High Performance OEO and an Ultra Low Noise Floor Cross-Correlation Microwave Photonic

Homodyne System," Proc. of IEEE International Frequency Control Symposium, pp. 811-814, Honolulu, HI, USA, May 19-21, 2008.

[29] H. Hao, J. Tang, D. Domenech, W. Li, N. Zhu, J. Capmany, and M. Li, "Toward monolithic integration of OEOs: From systems to chips," Journal of Lightwave Technology, **36**, 19, pp. 4565-4582, 2018.

[30] O. Lelièvre, V. Crozatier, G. Baili, P. Nouchi, D. Dolfi, L. Morvan, F. Goldfarb, F. Bretenaker, and O. Llopis, "Low phase noise 10 GHz coupled optoelectronic oscillator," Proc. of 2017 Joint Conference of the European Frequency and Time Forum and IEEE International Frequency Control Symposium (EFTF/IFCS), pp. 493-494, Besancon, France, July 9-13, 2017.

[31] X. S. Yao, and L. Maleki, "Dual microwave and optical oscillator," Optics Letter, **22**, 24, pp. 1867-1869, 1997.

[32] T. Bànky, B. Horvath, and T. Berceli, "Optimum configuration of multiloop optoelectronic oscillators," Journal of Optical Society of America B, **23**, 7, pp. 1371-1380, 2006.

[33] X. S. Yao, L. Maleki, Y. Gi, G. Lutes, and M. Tu, "Dual-loop optoelectronic oscillator," Proc. IEEE Int. Freq. Control Symposium, 545-549, May 1998.

[34] S. Jia, J. Yu, J. Wang, W. Wang, Q. Wu, G. Huang, and E. Yang, "A novel optoelectronic oscillator based on wavelength multiplexing," IEEE Photonics Technology Letters, **27**, 2, pp. 213-216, 2014.

[35] K. H. Lee, J. Y. Kim, and W. Y. Choi, "Injection-locked hybrid optoelectronic oscillators for single-mode oscillations," IEEE Photonics Technology Letters, **20**, 19, pp. 1645-1647, 2008.

[36] W. Zhou, and G. Blasche, "Injection-locked dual opto-electronic oscillator with ultra-low phase noise and ultra-low spurious level," IEEE Transactions on Microwave Theory and Techniques, **53**, 3, pp. 929–933, 2005.

[37] G. Serafino, P. Ghelfi, P. Pérez-Millán, G. E. Villanueva, J. Palací, J. L. Cruz, and A. Bogoni, "Phase and Amplitude Stability of EHF Band Radar Carriers Generated From an Active Mode-Locked Laser," Journal of Lightwave Technology, **29**, 23, pp. 3551-3559, 2011.

[38] V. S. Ilchenko, J. Byrd, A. A. Savchenkov, A. B. Matsko, D. Seidel, and L. Maleki, "Miniature Oscillators Based on Optical Whispering Gallery Mode

Resonators," Proc. of 2008 IEEE International Frequency Control Symposium, Honolulu, USA, pp. 305-308, May 19-21, 2008.

[39] K. Volyanskiy, P. Salzenstein, H. Tavernier, M. Pogurmirskiy, Y. K. Chembo, and L. Larger, "Compact optoelectronic microwave oscillators using ultra-high Q whispering gallery mode disk-resonators and phase modulation," Optics Express **18**, 21, pp. 22358-22363, 2010.

[40] Y. Yu, H. Tang, W. Liu, X. Hu, Y. Zhang, X. Xiao, Y. Yu, and X. Zhang, "Frequency Stabilization of the Tunable Optoelectronic Oscillator based on an ultra-High-Q Microring resonator," IEEE Journal of Selected Topics in Quantum Electronics, **26**, 2, pp. 1-9, 2020.

[41] K. Saleh, O. Llopis, and G. Cibiel, "Optical Scattering Induced Noise in Fiber Ring Resonators and Optoelectronic Oscillators," Journal of Lightwave Technology, **31**, 9, pp. 1433-1446, 2013.

[42] K. Saleh, R. Henriet, S. Diallo, G. Lin, R. Martinenghi, I. V. Balakireva, P. Salzenstein, A. Coillet, and Y. K. Chembo, "Phase noise performance comparison between optoelectronic oscillators based on optical delay lines and whispering gallery mode resonators," Optics Express, **22**, 26, pp. 32158-32173, 2014.

[43] L. Pierno, A. M. Fiorello, A. Secchi, and M. Dispenza, "Fibre Optics in Radar Systems: advantages and achievement," Proc. of 2015 IEEE Radar Conference (RadarCon), pp. 1627-1633, Arlington, USA, May 10-15, 2015.

[44] A. Bluestone, D. T. Spencer, S. Srinivasan, D. Guerra, J.E. Bowers, and L. Theogarajan, "An Ultra-Low Phase-Noise 20-GHz PLL Utilizing an Optoelectronic Voltage-Controlled Oscillator," IEEE Transactions on Microwave Theory and Techniques, **63**, 3, pp. 1046-1052, 2015.

[45] Preliminary product brief of the Micro-Opto-Electronic Oscillator (uOEO), http://www.oewaves.com/

[46] J. Tang, T. Hao, W. Li, D. Domenech, R. Banos, P. Munoz, N. Zhu, J. Capmany, and M. Li, "An integrated optoelectronic oscillator," Optics Express, **26**, 9, pp. 12257-12265, 2018.

[47] M. Piels, J. F. Bauters, M. L. Davenport, M. J. R. Heck, and J. E. Bowers, "Low-Loss Silicon Nitride AWG Demultiplexer Heterogeneously

Integrated With Hybrid III–V/Silicon Photodetectors," Journal of Lightwave Technology, **32**, 4, pp. 817-823, 2014.

[48] F. Dell' Olio, G. Brunetti, M. N. Armenise, and C. Ciminelli, "Ka-band optoelectronic oscillator based on ultra-high *Q* ring resonator," accepted by European Frequency and Time Forum (EFTF 2020), Noordwijk, The Netherlands, April 21-23, 2020.

[49] K. Saleh, L. Guoping, and Y. K. Chembo, "Effect of Laser Coupling and Active Stabilization on the Phase Noise Performance of Optoelectronic Microwave Oscillators Based on Whispering-Gallery-Mode Resonators," IEEE Photonics Journal, **7**, 1, pp. 1-11, 2015.

[50] B. Schiek, H.-J. Siweris, and I. Rolfes, *Noise in High-Frequency Circuits and Oscillator*, John Wiley & Sons., 2006.

[51] A. Bouchier, K. Saleh, P.-H. Merrer, O. Llopis, and G. Cibiel, "Theoretical and Experimental Study of the Phase Noise of Opto-Electronic Oscillators based on High Quality Factor Optical Resonators," Proc. of IEEE International Frequency Control Symposium, pp. 544-548, Newport Beach, USA, June 2-4, 2010.

[52] .J. M. Senior, and M. Y. Jamro, *Optical Fiber Communications: Principles and Practice*, Prentice Hall, 2009.

[53] A. Beling, and J. C. Campbell, "Advances in Photodetectors and Optical Receivers," in I. Kaminow, T. Li, A. E Willner, Eds., *Optical Fiber Telecommunications Volume VIA: Components and Subsystems*, Academic Press, 2013.

[54] K. Saleh, "High spectral purity microwave sources based on optical resonators," Université Paul Sabatier - Toulouse III, PhD Thesis, 2012.

[55] P.-H. Merrer, K. Saleh, O. Llopis, S. Berneschi, F. Cosi, and G. Nunzi Conti, "Characterization technique of optical whispering gallery mode resonators in the microwave frequency domain for optoelectronic oscillators," Applied Optics, **51**, 20, pp. 4742-4748, 2012.

[56] TGP2104, TriQuint Semiconductor, http://www.triquint.com/

[57] TGB4002, TriQuint Semiconductor, http://www.triquint.com/

[58] HMC899LP4E, Hittite Microwave Corporation, https://www.hittite.com/

[59] AMF-6F-27003100-22-13P Ka-band amplifier, https://miteq.com/

[60] J. T. Bovington, M. J. R. Heck, and J. E. Bowers, "Heterogeneous lasers and coupling to Si_3N_4 near 1060 nm," Optics Letters, **39**, 20, pp. 6017-6020, 2014.

[61] J. D. M. Adams, C. Rolland, N. Puetz, R. S. Moore, F. R. Shepherd, H. B. Kim, and S. Bradshaw, "Mach–Zehnder modulator integrated with a gain-coupled DFB laser for 10 Gbit/s, 100 km NDSF transmission at 1.55 μm," Electronics Letters, **32**, 5, pp. 485-486, 1996.

[62] J. Yao, "Photonics to the rescue: A fresh look at microwave photonic filters," IEEE Microwave Magazine, **16**, 8, pp. 46–60, 2015.

[63] C. Ciminelli, F. Dell'Olio, and M. N. Armenise, *Photonics in Space: Advanced Photonic Devices and Systems*, World Scientific, 2016.

[64] M. Sotom, B. Benazet, A. Le Kernec, and M. Maignan, "Microwave photonic technologies for flexible satellite telecom payloads," Proc. of 45th European Conference on Optical Communication (ECOC 2019), pp. 20-24, Dublin, Ireland, September 22-26, 2009.

[65] J. Capmany, B. Ortega, and D. Pastor, "A tutorial on microwave photonic filters," Journal of Lightwave Technology, **24**, 1, pp. 201-229, 2006.

[66] N. Shi, T. Hao, W. Li, N. Zhu, and M. Li, "A reconfigurable microwave photonic filter with flexible tunability using a multi-wavelength laser and a multi-channel phase-shifted fiber Bragg grating," Optics Communications, **407**, pp. 27-32, 2018.

[67] D. B. Hunter, and R. A. Minasian, "Tuneable microwave fiber-optic bandpass filters," IEEE Photonics technology letters, **11**, 7, pp. 874-876, 1999.

[68] W. Shi, V. Veerasubramanian, D. Patel, and D. V. Plant, "Tuneable nanophotonic delay lines using linearly chirped contradirectional couplers with uniform Bragg gratings," Optics Letters, **39**, 3, pp. 701-703, 2014.

[69] J. Sancho, J. Bourderionnet, J. Lloret, S. Combrié, I. Gasulla, S. Xavier, S. Sales, P. Colman, G. Lehoucq, D. Dolfi, J. Capmany, and A. de Rossi,

"Integrable microwave filter based on a photonic crystal delay line," Nature Communications, **3**, 1075, pp. 1–9, Sept. 2012.

[70] K. Wilner, and A. P. Van Den Heuvel, "Fiber-optic delay lines for microwave signal processing," Proceedings of the IEEE, **64**, 5, pp. 805-807, 1976.

[71] A. Loayssa, J. Capmany, M. Sagues, and J. Mora, "Demonstration of incoherent microwave photonic filters with all-optical complex coefficients", IEEE Photonics Technology Letters, **18**, 16, pp. 1744-1746, 2006.

[72] Y. Yan, and J. Yao, "A tuneable photonic microwave filter with a complex coefficient using an optical RF phase shifter," IEEE Photonics Technology Letters, **19**, 19, pp. 1472-1474, 2007.

[73] E. C. Heyde, and R. A. Minasian, "A solution to the synthesis problem of recirculating optical delay line filters," IEEE Photonics Technology Letters, **6**, 7, pp. 833-835, 1994.

[74] A. D. Simard, and S. LaRochelle, "High performance narrow bandpass filters based on integrated Bragg gratings in silicon-on-insulator," Proc. of Optical Fiber Communications Conference and Exhibition (OFC), IEEE, pp. 1-3, Los Angeles, California, USA, March 22-26, 2015.

[75] M. Burla, X. Wang, M. Li, L. Chrostowski, and J. Azaña, "Wideband dynamic microwave frequency identification system using a low-power ultracompact silicon photonic chip," Nature communications, **7**, 13004, 2016.

[76] X. Yi, and R. A. Minasian, "Microwave photonic filter with single bandpass response," Electronics letters, **45**, 7, pp. 362-363, 2009.

[77] J. Palací, G. E. Villanueva, J. V. Galán, J. Martí, and B. Vidal, "Single bandpass photonic microwave filter based on a notch ring resonator," IEEE Photonics Technology Letters, **22**, 17, pp. 1276-1278, 2010.

[78] F. Horst, W. M. Green, S. Assefa, S. M. Shank, Y. A. Vlasov, and B. J. Offrein, "Cascaded Mach-Zehnder wavelength filters in silicon

photonics for low loss and flat pass-band WDM (de-) multiplexing", Optics Express, **21**, 10, pp. 11652-11658, 2013.

[79] W. Xue, S. Sales, J. Mork, and J. Capmany, "Widely tuneable microwave photonic notch filter based on slow and fast light effects," IEEE Photonics Technology Letters, **21**, 3, pp. 167-169, 2009.

[80] D. Marpaung, B. Morrison, M. Pagani, R. Pant, D.-Y. Choi, B. Luther-Davies, S. J. Madden, and B. J. Eggleton, "Low-power, chip-based stimulated Brillouin scattering microwave photonic filter with ultrahigh selectivity," Optica, **2**, 2, pp. 76-83, 2015.

[81] J. S. Fandiño, P. Muñoz, D. Doménech, and J. Capmany, "A monolithic integrated photonic microwave filter," Nature Photonics, **11**, 2, pp. 124-129, 2017.

[82] W. Zhang, and J. Yao, "A silicon photonic integrated frequency-tuneable microwave photonic bandpass filter," Proc. of 2017 International Topical Meeting on Microwave Photonics (MWP), IEEE, pp. 1-4, Beijing, China, October 23-26, 2017.

[83] B. Jalali, and S. Fathpour, "Silicon photonics," Journal of Lightwave Technology, **24**, 12, pp. 4600-4615, 2006.

[84] W. Bogaerts, P. De Heyn, T. Van Vaerenbergh, K. De Vos, S. Kumar Selvaraja, T. Claes, P. Dumon, P. Bienstman, D. Van Thourhout, and R. Baets, "Silicon microring resonators," Laser & Photonics Reviews, **6**, 1, pp. 47-73, 2012.

[85] H. Qiu, F. Zhou, J. Qie, Y. Yao, X. Hu, Y. Zhang, X. Xiao, Y. Yu, J. Dong, and X. Zhang, "A Continuously Tuneable Sub-gigahertz Microwave Photonic Bandpass Filter Based on An Ultra-high-Q Silicon Microring Resonator," Journal of Lightwave Technology, **36**, 19, pp. 4312-4318, 2018.

[86] L. Gao, X. Chen, and J. Yao, "Tuneable microwave photonic filter with a narrow and flat-top passband," IEEE Microwave and Wireless Components Letters, **23**, 7, pp. 362-364, 2013.

[87] P. Dong, W. Qian, H. Liang, R. Shafiiha, D. Feng, G. Li, J. E. Cunningham, A. V. Krishnamoorthy, and M. Asghari, "Thermally

tuneable silicon racetrack resonators with ultralow tuning power," Optics Express, **18**, 19, pp. 20298-20304, 2010.

[88] P. Dong, N. N. Feng, D. Feng, W. Qian, H. Liang, D. C. Lee, B. J. Luff, T. Banwell, A. Agarwal, P. Toliver, R. Menendez, T. K. Woodward, and M. Asghari, "GHz-bandwidth optical filters based on high-order silicon ring resonators," Optics Express, **18**, 23, pp. 23784-23789, 2010.

[89] F. Xia, M. Rooks, L. Sekaric, and Y. Vlasov, "Ultra-compact high order ring resonator filters using submicron silicon photonic wires for on-chip optical interconnects," Optics Express, **15**, 19, pp. 11934-11941, 2007.

[90] P. A. Morton, J. B. Khurgin, Z. Mizrahi and S. J. Morton, "Commercially packaged optical true-time-delay devices with record delays of wide bandwidth signals," Proc. of 2014 Conference on Lasers and Electro-Optics (CLEO), pp. 1-2, San Jose, CA, USA, June 8-13, 2014.

[91] M. Huang, S. Li, M. Xue, L. Zhao, and S. Pan, "Flat-top optical resonance in a single-ring resonator based on manipulation of fast-and slow-light effects," Optics Express, **26**, 18, pp. 23215-23220, 2018.

[92] C. Errando-Herranz, F. Niklaus, G. Stemme, and K. B. Gylfason, "Low-power microelectromechanically tuneable silicon photonic ring resonator add-drop filter," Optics Letters, **40**, 15, pp. 3556-3559, 2015.

[93] I. Giuntoni, A. Gajda, M. Krause, R. Steingrüber, J. Bruns, and K. Petermann, "Tuneable Bragg reflectors on silicon-on-insulator rib waveguides", Optics Express, **17**, 21, pp. 18518-18524, 2009.

[94] K. Chen, F. Duan, and Y. Yu, "High-performance thermo-optic tuneable grating filters based on laterally supported suspended silicon ridge waveguide," Optics Express, **126**, 15, pp. 19479-19488, 2018.

[95] A. D. Simard, and S. LaRochelle, "Complex apodized Bragg grating filters without circulators in silicon-on-insulator," Optics Express, **23**, 13, pp. 16662-16675, 2015.

[96] J. Jiang, H. Qiu, G. Wang, Y. Li, T. Dai, X. Wang, H. Yu, J. Yang, and X. Jiang, "Broadband tuneable filter based on the loop of multimode Bragg grating," Optics Express, **26**, 1, pp. 559-566, 2018.

[97] M. G. Saber, Y. Wang, E. El-Fiky, D. Patel, K. A. Shahriar, M. S. Alam, M. Jacques, Z. Xing, L. Xu, N. Abadìa, and D. V. Plant, "Transversely coupled Fabry–Perot resonators with Bragg grating reflectors," Optics Letters, **43**, 1, pp. 13-16, 2018.

[98] Q. Xu, B. Schmidt, S. Pradhan, and M. Lipson, "Micrometre-scale silicon electro-optic modulator," Nature, **435**, pp. 325-327, 2005.

[99] G. T. Reed, G. Z. Mashanovich, F. Y. Gardes, M. Nedeljkovic, Y. Hu, D. J. Thomson, L. Ke, P. Wilson, S.-W- Chen, and S. S. Hsu, "Recent breakthroughs in carrier depletion based silicon optical modulators," Nanophotonics, **3**, 4-5, pp. 229-245, 2014.

[100] C. A. Barrios, V. R. Almeida, R. Panepucci, and M. Lipson, "Electrooptic modulation of silicon-on-insulator submicrometer-size waveguide devices," Journal of Lightwave Technology, **21**, 10, pp. 2332-2339, 2003.

[101] G. Brunetti, F. Dell' Olio, D. Conteduca, M. N. Armenise, and C. Ciminelli, "Ultra-compact tuneable notch filter using silicon photonic ring resonator," Journal of Lightwave Technology, **37**, 13, pp. 2970-2980, 2019.

[102] Q. Xu, and M. Lipson, "Carrier-induced optical bistability in silicon ring resonators," Optics Letters, **31**, 3, pp. 341-343, 2006.

[103] S. K. Selvaraja, P. De Heyn, G. Winroth, P. Ong, G. Lepage, C. Cailler, A. Rigny, K. K. Bourdelle, W. Bogaerts, D. Van Thourhout, J. Van Campenhout, and P. Absil, "Highly uniform and low-loss passive silicon photonics devices using a 300mm CMOS platform," Proc. of Optical Fiber Communications Conference and Exhibition (OFC),pp. Th2A-33, San Francisco, CA, USA, March 9-14, 2014.

[104] Y. M. Kang, A. Arbabi, and L. L. Goddard, "Engineering the spectral reflectance of microring resonators with integrated reflective elements," Optics Express, **18**, 16, pp. 16813-16825, 2010.

[105] C. Ciminelli, F. Dell'Olio, G. Brunetti, D. Conteduca, and M. N. Armenise, "New microwave photonic filter based on a ring resonator including a photonic crystal structure," Proc. of 2017 19th International

Conference on Transparent Optical Networks (ICTON), pp. 1-4, Girona, Spain, July 2-6, 2017.

[106] A. Yariv, Y. Xu, R. K. Lee, and A. Scherer, "Coupled-resonator optical waveguide: a proposal and analysis," Optics Letters, **24**, 11, pp. 711-713, 1999.

[107] S. Ramo, and J. R. Whinnery, *Fields and waves in modern radio*, John Wiley & Sons, 1953.

[108] J. L. Coolidge, "The story of the binomial theorem," The American Mathematical Monthly, **56**, 3, pp. 147-157, 1949.

[109] R. M. Knox, and P. P. Toulios, "Integrated Circuits for the Millimeter Through Optical Frequency Range," Proc. of MRI Symposium on Submillimeter Waves, Polytechnic Press, New York, 1970.

[110] M. Born, and E. Wolf, *Principles of optics: electromagnetic theory of propagation, interference and diffraction of light*, Elsevier, 1980.

[111] D. Vasileska, S. M. Goodnick, and G. Klimeck, *Computational Electronics: semiclassical and quantum device modeling and simulation*, CRC press, 2016.

[112] R. Soref, and B. Bennett, "Electrooptical effects in silicon," IEEE Journal of Quantum Electronics, **23**, 1, pp. 123-129, 1987.

[113] Y. A. Vlasov, and S. J. McNab, "Losses in single-mode silicon-on-insulator strip waveguides and bends," Optics Express, **12**, 8, pp.1622-1631, 2004.

[114] A. Yariv, "Critical coupling and its control in optical waveguide-ring resonator systems," IEEE Photonic Technology Letters, **14**, 4, pp. 483-485, 2002.

Chapter 4

Photonic-based Synthetic Aperture Radar system

Payloads currently used in Earth Observation (EO) missions can be classified into two main classes, depending on the operating wavelength, including optical payloads, that measure reflective light in a wavelength range from ultraviolet to infrared, and microwave sensors, that operate at wavelengths longer than infrared rays (300 MHz - 300 GHz).

The main advantage of the microwave sensors, such as Radars and Synthetic Aperture Radars (SARs), regard their observation capability that typically is not affected by the weather conditions [1]. SARs are unanimously considered very powerful tools for the EO, exhibiting a spatial resolution of the order of 1 m and operation in several RF bands, i.e. S-, C-, X- and Ka- bands (see Table 4.1).

Synthetic Aperture Radars were developed to overcome the limitations of real aperture radars, in terms of resolution, compactness and sensitivity by the weather conditions. For real aperture radars, a narrow beam is directed perpendicularly to the flight path of the carrier platform.

Tab.4.1. Frequency bands for SAR systems.

Frequency Band	P	L	S	C	X	Ku	Ka
Frequency [GHz]	0.25-0.5	1-2	2-3.75	3.75-7.5	7.5-12	12-17.6	25-40
Wavelength [cm]	60-120	15-30	8-15	4-8	2.5-4	1.7-2.5	0.75-1.2

A pulse of energy is transmitted from the radar antenna, and the relative intensity of the reflections is used to produce the image of the illuminated land. When the next pulse is transmitted, the radar will have moved forward a small distance and a slightly different strip of land will be illuminated. The image consists of the two-dimensional data array, formed by the sequential strips.

For such radars, azimuth resolution can be improved only by longer antenna or shorter wavelength, and then, a large antenna is required to obtain high-resolution image [2-3]. Furthermore, the use of shorter wavelength generally involves a higher cloud and atmospheric attenuation, reducing the capabilities of imaging radars.

SAR systems provides high-resolution 2D images independent from daylight, cloud coverage and weather conditions, using, also, a small antenna and relatively long wavelengths. They are sophisticated imaging systems that emit electromagnetic radiation at microwave frequencies. As opposed to optical imaging systems, which measure the visible spectrum return of solar electromagnetic radiation in a scene, SAR systems use their own transmit signal to cover the scene of interest. The side-looking imaging geometry and the pulsed radar installed on a platform with a forward movement ensures a large illumination range with a high resolution. The radar system transmits high power electromagnetic pulses receives the echoes of the backscattered signal. Its operation ensures a considerable penetration of the beam, so that the imaged objects can be modelled into the volume, useful for several applications, as topography, oceanography, glaciology, geology and forestry, including forest height, biomass, and deforestation [4].

Since the launch of *Seasat* in 1978 [5], the first civilian SAR satellite for the oceans observation, the Space agencies, as National Aeronautics and Space Administration (NASA), the European Space Agency (ESA) and the Japan Aerospace Exploration Agency (JAXA), have developed boosted SAR system for the Earth monitoring [5-13], as shown in Tab. 4.2, retrieving geo/bio-physical parameters from the Earth surface.

About the spacecraft, current SAR payloads are installed on board of satellites with masses of the order of a few tons, as *COSMO-Skymed* [14], and -

Tab.4.2. Examples of SAR sytems for civil applications launched into the Space [5-13].

SAR	First launch	Frequency band	Institution
Seasat	1978	L	NASA
ERS-1	1991	C	ESA
JERS-1	1992	L	JAXA
Radarsat-1	1995	C	CSA
TerraSAR-X	2007	X	DLR/Astrium
Cosmo-SkyMed	2007	X	ASI
Sentinel-1	2014	C	ESA
NovaSAR-S	2016	S	Astrium
PAZ	2018	X	CDTI

are characterized by large volume and high-power consumption. In the last decades, the interest has been focused on high-resolution remote sensing systems, that should be, at the same time, low cost solutions, with reduced size, weight and power consumption to be employable also on board of small satellites. In particular, the attention has been oriented on satellites with mass in the range 100-500 kg, and on satellite constellations that demand SAR payloads with a mass of some tens of kilos and average power consumption of the order of 100 W [15].

Several SAR payloads based on standard electronic components, are currently already available, such as the *NovaSAR-S*, launched in 2016. It is a multi-mode SAR with a spatial resolution of 6 m and a mass of approximately 140 kg [16]. Aiming at improving improve the performance of the SAR payloads, several functionalities of the system, such as the chirped waveform generation, the beamforming and the direct analog-to-digital conversion (without down-conversion) of the radar echo, can be realized in the photonic domain with potential improvements in terms of size and mass, integration of the antennas system and reduction of the risks related to its in-orbit deployment [17]. In this Chapter, the use of integrated micro-photonic devices and circuits in the context of advanced small SAR payloads will be discussed.

4.1 RADAR fundamentals

Typical RAdio Detection And Ranging (RADAR) systems consist of transmitter, switch, antenna, receiver and data recorder. At first, the transmitter generates a high-power RF electromagnetic wave, which is routed to antenna by using a switch. The antenna transmitted the EM pulse with a pulse rate τ towards the area to be imaged (swath) and collects returned echoes. The returned echo signal is digital converted by the receiver and stored by the data recorder for processing and display. A sketch of an operating radar antenna D wide and L long is reported in Fig. 4.1.

The radar platform flies along the satellite flight path direction, parallel to the nadir, at constant velocity v. For real aperture imaging radar, its large antenna emits a spread beam illuminating the ground below [3].

In SAR, forward motion of the antenna is used to emulate and, then, synthetizing a very long antenna. As a conventional radar, during the movement of the antenna along the satellite flight path, EM waves are transmitted at a pulse repetition rate τ and the backscattered echoes are collected by the radar antenna [18]. The lower bound of τ is determined by the Doppler bandwidth of the radar, which is the range of Doppler frequencies observed by the radar during the collection [19]. The pulse repetition rate likewise must be low enough to ensure that the echo from the far edge of the illuminating area is detected before arrival of the echo from the near edge of the next scene.

An appropriate coherent combination of the received signals at the receiver, matching the Doppler frequency variations and demodulating by adjusting the -

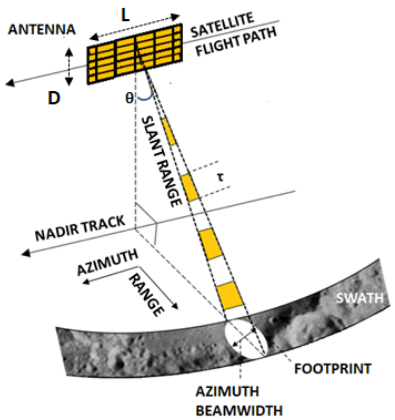

Fig. 4.1. Illustration of imaging radar geometry.

frequency variation in the return echoes from each point on the ground, allows the construction of a virtual aperture that is much longer than the physical antenna length. The radar image results from processing the collected raw data. This SAR feature is the origin of its name "synthetic aperture," giving it the property of being an imaging radar.

Besides the pulse duration and the antenna bandwidth, the spatial resolution can be considered as one of the most important classification criteria of the imaging radar systems. A range and azimuth resolution can be defined along the spatial direction of the illuminated terrain.

The range resolution is defined as the ability of the system to distinguish between two targets on the ground. For aperture radar systems, the range resolution res_{range} is expressed as:

$$res_{range} = \frac{c \cdot \tau}{2 \cdot sin\theta} \tag{4.1}$$

where τ is the pulse width, θ is the look angle and c is the speed of the light [4]. The range resolution strictly depends by the pulse width and the look angle, but it is independent by the platform height. Then, the look angle must be shorter, or the pulse duration must be narrower to improve the range resolution. On the other hand, it is very hard to put enough energy into a very narrow pulse because the energy of a signal is proportional to its duration. To improve the range resolution and maintain enough transmitted energy, radar systems generate a long pulse with a linear frequency modulation, called chirp. Then, res_{range} becomes:

$$res_{range} = \frac{c}{2 \cdot BW} \tag{4.2}$$

where BW is the bandwidth of the chirp [2].

Azimuth resolution is the minimum distance on the ground in the direction parallel to the flight path of the platform at which two targets can be separately resolved. Two targets located at same slant range can be distinguished only if they are not in the radar beam at the same time. For real aperture radar antenna, the azimuth resolution $res_{azimuth}$ is equal to:

$$res_{azimuth} = \frac{\lambda \cdot R}{L} \tag{4.3}$$

where λ is the operating wavelength, R is the length of the slant range and L is the antenna length (see Fig. 4.1). The azimuth resolution is dependent on aperture

length, and then, a larger antenna is required to improve the resolution. In several cases, an acceptable azimuth resolution, e.g. in the order of meters, requires an antenna size of several hundred of meters or even several kilometres, and then the practical implementation of the antenna size is not possible.

For SAR systems, the exploitment of the Doppler effect involves that the $res_{azimuth}$ can be calculated as:

$$res_{azimuth} = \frac{\lambda \cdot R}{2 \cdot v} \cdot \delta f \tag{4.4}$$

where δf is the Doppler frequency shift, approximately equal to the inverse of the time t_{span} during which the target is into the beam. The time t_{span} can be expressed as:

$$t_{span} = \frac{\theta \cdot R}{v} \approx \frac{\lambda \cdot R}{L \cdot v} \tag{4.5}$$

and then, the azimuth resolution for SAR systems is equal to:

$$res_{azimuth} \approx \frac{L}{2} \tag{4.6}$$

Then, a very high azimuth resolution is obtained with very small antenna, opposite to the behaviour of real image antenna. Although the smaller the antenna length, the better the resolution, the length of the antenna must be large enough to create the proper interference pattern between the dipoles of the antenna necessary for the desired beamspread at a frequency [2].

4.2 SAR operating modes

Three different imaging modes of SAR are typically used, including Stripmap, ScanSAR and Spotlight modes. The most fundamental mode is the Stripmap operation, where the antenna is in a fixed position and the pattern is fixed to one swath. A single continuous strip is generated by the forward or backward movement of the antenna, as shown in Fig. 4.2 (a). If a wider swath is required, the system can operate in the ScanSAR mode (Fig. 4.2 (b)).

The antenna elevation pattern is steered to different elevation angles, corresponding to multiple sub-swaths (SSWs). Each SSW is illuminated by multiple pulses for a shorter time than in the Stripmap case. After an appropriate

data processing, this mode generates a wide-swath SAR image, with, a worst azimuth resolution respect to the Stripmap mode.

The Spotlight mode is a proven technique used when a better azimuth resolution is required (Fig.4.2 (c)). The antenna pattern is steered in azimuth and a given region is illuminated for a long time, involving an increase of the synthetic aperture length and, then, an improvement of the azimuth resolution. The Spotlight mode is used to focus on individual patches along the radar flight path, not providing a continuous swath [2].

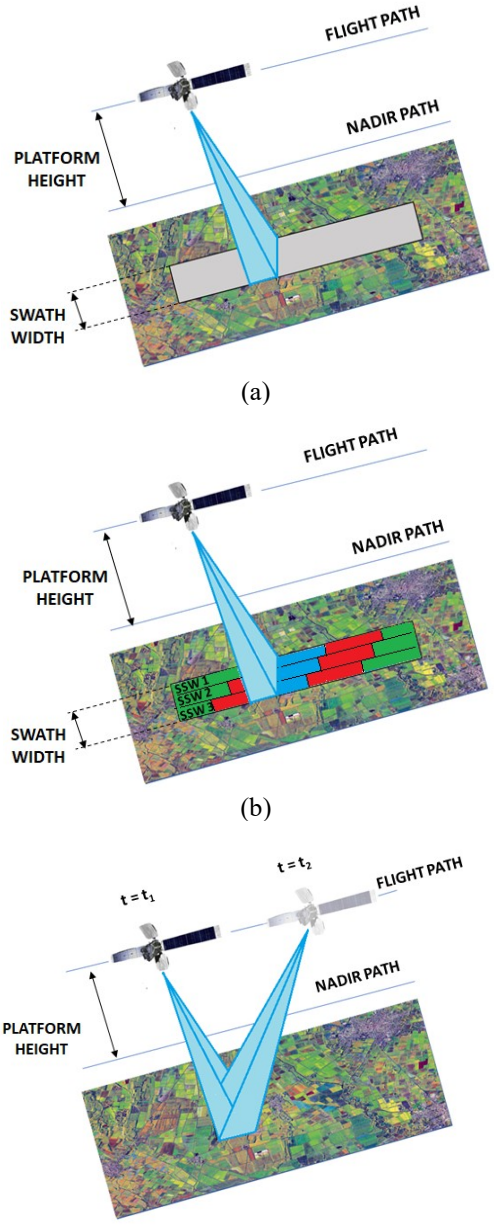

Fig. 4.2. SAR operating modes: Stripmap (a), ScanSAR (b) and Spotlight (c).

4.3 Photonic-based SAR payloads

As shown in Fig. 1, a SAR payload typically consists of a linearly chirped microwave waveform (LCMW) generator, frequency converters (FC), an analog-to-digital converter (ADC) and a phased array antenna (PAA), including hundreds of radiating elements [20-22]. After the In-phase/Quadrature (I/Q) modulation, the signal is multiplied and up converted. The amplitude of the signal is limited by a gain-controlled driver amplifier that feeds the antenna network. Several hundred T/R frontends amplify the RF signal and shift the respective phase according to the beamforming networks. The signal transmission and reception are realized by PAAs. At the receiver, the received echo signal is amplified and post-processed by down-conversion, I/Q demodulation and baseband filtering [23].

All functionalities can be implemented through integrated microphotonic devices and circuits. Over the ADC, beamforming, and chirped generation photonics-based functionalities, that are widely discussed into the following sections, the photonic approach could be used also for on board pre-processing and handling the SAR data [17], and transmitting the data towards a ground station or another satellite, aiming to improve the transmission data rate.

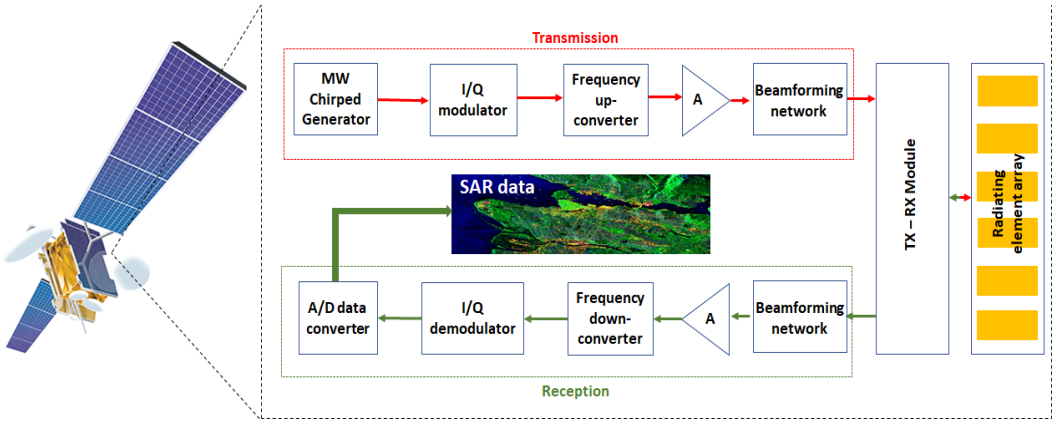

Fig. 4.3. Design scheme of a SAR payload (*MW*: microwave; *A/D*: analog-to-digital; *Tx*: transmission; *Rx*: reception; *A*: amplifier). Inset image source: RADARSAT-2 Data and Products © MacDonald Dettwiler and Associates Ltd (2009) – All Rights Reserved – RADARSAT is an official mark of the Canadian Space Agency [22].

4.3.1 Photonic ADCs

The analog-to-digital conversion is usually performed after the down-conversion of the RF beams received by the satellite, by providing data to the cascade sub-systems. When the number of the channels, exceeds few hundreds, the mass and the power consumption of the RF sub-systems are large, e.g. if the number of channels is equal to 200, a mass and a power consumption of 180 kg and 1.6 kW, respectively, are required. These issues could be mitigated by using a direct analog-to-digital conversion, without any down-conversion.

Although in the last decades, a great research effort has been focused on the direct analog-to-digital conversion, space-qualified electronic analog-to-digital converters (ADCs) allow the direct conversion of RF signals up to a few GHz [24], not compliant with the frequency band used for SAR.

A photonic ADC could be considered as a powerful solution to overcome the limitations of electronic ADCs. In addition, photonic ADCs support high values of carrier's frequency and related bandwidth, hence, enabling the use of smaller antennas and give higher resolution with respect to the state-of-the-art [25].

Photonic ADCs have been widely investigated in the last four decades, and they could be classified according to the mode of operation, including photonic assisted, photonic sampled or quantized, and photonic sampled and quantized ADCs. In photonic assisted ADCs, the photonics is used to improve the sampling or the quantization functionality. Instead, in photonic sampled or photonic quantized ADCs, the sampling or the quantization, respectively, are performed in the optical domain. Finally, ADCs with photonic-based sampling and quantization functionalities are called photonic sampled and quantized [26].

The photonic sampled ADCs are the most mature and promising photonic ADCs, able to overcome the limitations imposed to electronic ADCs by aperture jitter, i.e. the temporal variation of the exact sampling time instant. The aperture jitter limits the effective number of bits (ENOB), and it is directly proportional to the analog input frequency. Currently, the best electronic ADC exhibits a sampling jitter of about 100 fs, with an ENOB < 6 for the input frequency $\geq$10 GHz. As demonstrated in [27-28], the use of photonic technology allows jitter values in the

order of tens of fs, with an improvement of about one order of magnitude respect to the electronic counterparts.

Khilo *et al.* [28] have experimentally demonstrated a direct analog-to-digital conversion of RF signals, without down-conversion, by using sampled photonic ADCs, performing a time jitter of 15 fs, and an ENOB = 7 with 41 GHz signal. The fully integrated electronic-photonic ADC include dual-output silicon-modulator, two matched banks of microring resonator filters, balanced photoreceivers, electronic ADCs, and digital post-processing circuits. The entire chirp is sourced by an external mode locked laser.

For applications that required a larger value of ENOB, a decrease of the operating frequency is required. Integrated solutions have been proposed in literature to improve the ENOB value [29-31]. In 2016, DAS Photonics has proposed a photonic sampled ADC, based on mode-locked laser, a lithium niobate Mach-Zehnder Interferometer and a digital filter post-processor [31]. The experimental results show an ENOB equal to 10 at 2 GHz with high flexibility of the operating bandwidth, i.e. S- and Ka- band.

4.3.2 Photonic Beamformer

PAAs consist of arrays of stationary radiating elements that are closely spaced. The elements are spaced at a distance of the order of the wavelength of the RF signal to be transmitted. By controlling the phase of RF signals feeding each antenna element, the direction of the transmitted beam from each antenna can be electrically tuned, and then, the overall radiation pattern is the result of the combination, in amplitude and phase, of the waves radiated by the antenna elements. PAAs are extremely attractive in Space engineering, and they are already mounted in several Space Systems, such as telecom or radar payloads [32-34]. The main advantage of PAAs regards their ability to produce multiple simultaneous antenna beams, with an accurate control of the steering direction. The PAAs could be designed by using an active, passive or intermediate approach.

In passive PAAs (Fig. 4.4 (a)) the RF signal is generated by a high-power RF source. The power splitter generates several replicas, that feed the antenna

elements after their attenuation and phase shifting, labelled as a and ϕ in Fig. 4.4 (a), that are electronically controlled. The beam shaping results by the change of the shape of the radiated beam, that strictly depends by the amplitude of each signal, while, the beam steering consists of a change of the direction of the beam, correlated to the phase of each signal. Beam shaping and beam steering enable the so-called beamforming, while the entire circuit is called beamformer.

In active PAAs (Fig. 4.4 (b)), the high-power RF transmitter is replaced by solid-state RF amplifiers, each one connected directly to the antenna elements.

The phase shift provided by the phase shifters depends on the frequency of the input signal. For this reason, a wideband RF signal leads a non-uniform phase shift of the different spectral components, with a lack of the uniformity in beam pointing (beam squinting).

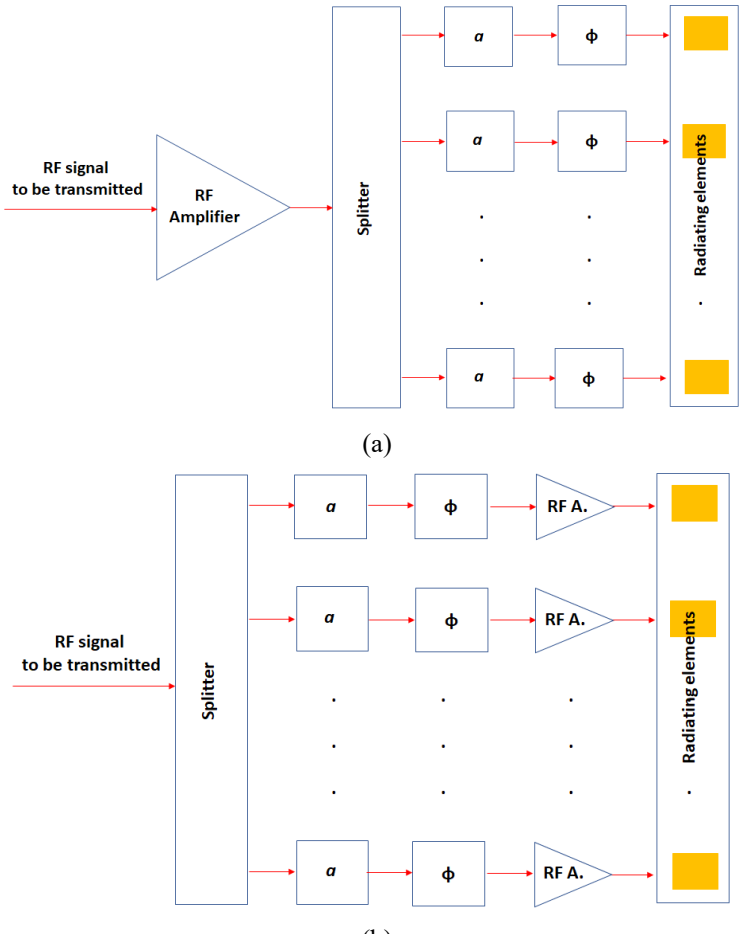

Fig.4.4. Passive (a) and active (b) phased-array antenna, (a: attenuation stage, *RF A.*: RF amplifier, ϕ: phase shifter).

To prevent this issue, true-time delay phase shifters are used, with a phase shift independent by the operating frequency. These components are the critical sub-systems in a phased array antenna. Typical requirements for optical delay lines used in SAR systems for EO applications are a broad bandwidth ($BW \geqslant 1$ GHz), wide and continuous delay tunability (delay range in the order of hundreds of picoseconds), fast reconfigurability, and low power consumption [35].

For the operation in the Ka- or Q-band, the phase shifters are bulky, leaky and heavy. Therefore, the use of photonics for true-time delay lines has been widely investigated into the last decades, aiming also to miniaturize the beamformers.

Since 1980s, beamformers based on fiber optic delay elements have been explored [36-37]. The phase shifts are performed by fiber links with slightly different dispersion. The lack of equality between the fiber links involves that the time delay imposed by each link is different for the beamforming channels. Thus, the time delay between the beams at the output of the fiber links are changed by tuning the frequency of the laser source. A prototype of an multi-band and multi-beam optically steered X-band 8-element PAA based on this approach has been recently proposed in [37], showing a beam steering speed of 15°/μs in a system volume of 7.6 cm × 20.3 cm × 43.2 cm.

In order to reduce the beamformer footprint and increase the accuracy of the time delay of the beams that feed the antenna elements, several configurations of integrated optical beamformers have been proposed in literature, mainly based on three concepts, as a long optical path (discrete [38-39] or integrated [40-41] configurations), non-linear-effects (exploiting third-order non-linear response of chalcogenide waveguides [42-43]), and the slow light effect.

The resonant true-time delay lines (TTDLs), based on the latter aforementioned effect, lead higher values of optical delay times and large bandwidth. The slow light effect allows the control of the group velocity, and then, ensures a fine control of the delay lines operating condition. Several configurations of TTDLs have been proposed in literature, as Bragg gratings [44], Photonic Crystal Waveguides (PhCWs) [45] and Ring Resonators (RRs) [46-48]. Although these devices show an intrinsic compromise between the maximum delay time, the

optical bandwidth and the footprint, they can ensure large bandwidth up to 100 GHz, with a maximum value of delay time lower than 100 ps [44, 48].

According to the aforementioned requirements, more complex structures have been investigated to increase the maximum delay time, without sacrificing the bandwidth, such as Coupled-Resonator Optical Waveguides (CROWs) [49], Side-Coupled Integrated Spaced Sequences Of Resonators (SCISSORs) [50], or delay lines obtained by the insertion of an element to compensate the ring resonator loss [51]. High values of delay times up to 800 ps for CROW [49] and 345 ps for SCISSOR [50] have been obtained, in a large footprint (7 mm^2 and 0.13 mm^2 for the CROW and SCISSOR, respectively). Novel configurations have been proposed to circumvent this critical aspect. An innovative configuration of tunable optical delay line, based on a ring resonator array and a Mach-Zehnder interferometer switch array has been proposed in [46]. The device performs a continuous delay range of few nanoseconds, wide bandwidth (~ 60GHz), but with slow reconfigurability time (>13μs).

The thermo-optic tuning ensures a wide and continuous delay range, although at the expense of a slow response time (> 6 μs) [44, 50, 52]. However, although the electro-optic method is affected by of absorption loss that could be limited only with optimized design and manufacturing technique, it shows a much faster response compared to the thermal approach.

Recently, graphene-based optical delay lines, that exploit the electro-optic tuning, have been proposed [35, 53-55]. During the last years, a great research interest has been focused on the graphene due to its unique optical properties. Several graphene-based optical devices have been designed for several applications, such as antennas [56], optical modulators [57-59], photodetectors [60-61] and optical sensors [62]. In particular, in the field of beamforming application, the main advantage of graphene is represented by the capability of tuning the Fermi levels by low values of the applied voltages, due to the low value of carrier density of states near the Dirac Point. Therefore, the applied voltages induce changes in the refractive index that are strong enough to affect the behaviour of the optical delay time [63-64]. A continuous time delay range of the order of 200 ps has been obtained in graphene-based CROWs and SCISSORs by using the electro-optic

tuning, with a footprint smaller than 0.1 mm^2 [53]. Furthermore, the graphene structures ensure a very fast reconfiguration time of about 0.12 ns, five orders of magnitude faster than the typical values obtained by the thermo-optic approach. In 2015, two vertically coupled ring resonators interleaved by a graphene capacitor has been proposed [54]. This device shows a fast and continuous delay tuning of approximately 230 ps, a bandwidth $BW > 1$ GHz, a very small footprint (1.6×10^{-3} μm^2) and an insertion loss value of 23 dB. Lower values of insertion loss are necessary to avoid an amplification stage at the output of the device.

4.3.2.1 Graphene-based optical delay line

An innovative optical delay line based on an ultra-compact silicon-based 1D-PhC has been designed [65-67]. The grating consists of a periodic pattern of a graphene capacitor placed on the top of a single-mode Si-wire. By changing the voltage applied to the graphene capacitor, the value of the delay time changes in a wide range ($\Delta\tau > 200$ ps) with a maximum delay time of 274.85 ps, in a very small footprint ($A = 1.35 \times 10^{-3}$ mm^2), so providing the highest value of the figure of merit $FOM = \Delta\tau/A = 1.54 \times 10^5$ ps/mm^2 obtained in literature, according to my knowledge.

4.3.2.1.1 Device configuration

The proposed optical delay line is based on a 1D periodic pattern of a graphene capacitor on a silicon nanowire, as shown in Fig.4.5.

The capacitor consists of two graphene monolayer electrodes, with a thickness $t_{gr} = 0.34$ nm, placed on the silicon nanowire, interleaved by a layer of Al_2O_3 ($n_{Al2O3} = 1.746$ at $\lambda = 1550$ nm), with a thickness $t_{Al} = 7$ nm [54]. The change of the electrical conductivity of the graphene layers, caused by the accumulation of the carriers, allows the effective index change in the nanowire. The silicon single-mode nanowire, placed on 2 μm SiO_2 substrate, shows a width, w_{si}, equal to 500 nm and a thickness, t_{Si}, equal to 220 nm [68].

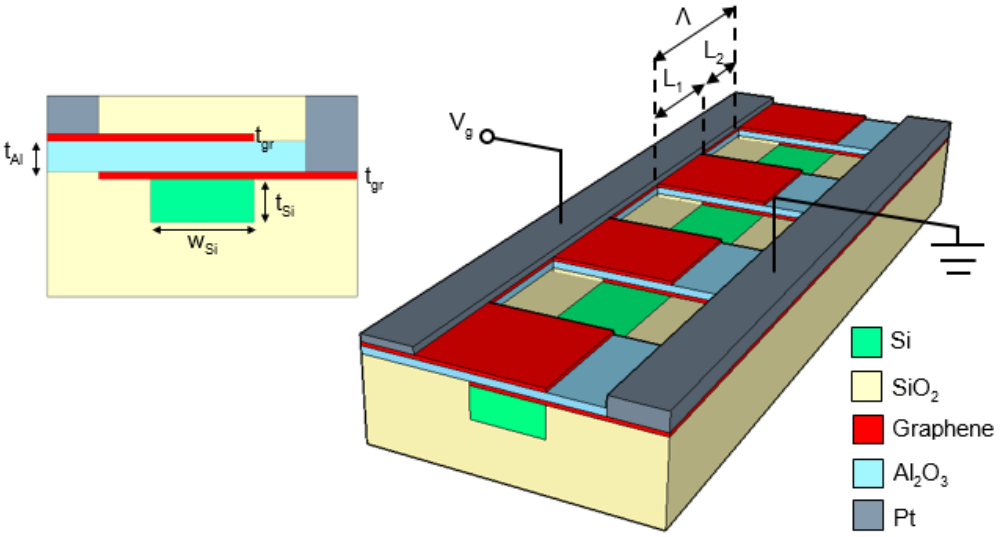

Fig. 4.5. Configuration of the graphene-based silicon Bragg grating, with the nanowire cross-section in the inset (t_{Si}: waveguide thickness, w_{Si}: waveguide width, t_{gr}: graphene thickness, t_{Al}: Al_2O_3 thickness; V_g: applied voltage; Λ: period, $L_1 - L_2$: PhC sections). Reprinted with permission from [65] © The Optical Society.

The whole structure is embedded in SiO_2, with $n_{SiO2} = 1.444$ at $\lambda = 1550$ nm, as shown in Fig. 4.5. The propagation losses of the bare waveguide at $\lambda = 1550$ nm are $\alpha_{TE} = 2.4$ dB/cm and $\alpha_{TM} = 0.59$ dB/cm for the TE mode and the TM mode, respectively. Although, the double layer graphene structure performs low values of the insertion loss [69-70], compared to a single layer configuration [71], the optical losses related to the graphene capacitor should be taken into account.

For the graphene-based photonic silicon Bragg grating, a mature manufacturing technique is available. The graphene monolayer can be fabricated by Chemical Vapour Deposition (CVD) [72] and transferred to the silicon nanowire. The platinum bottom electrode region [60] is directly placed on the graphene layer, followed by the deposition of the Al_2O_3 spacer by using the Atomic Layer Deposition (ALD). Finally, the second monolayer and the relative electrode are deposited on the stack structure by using the CVD and a second metal deposition, respectively. The grating pattern could be realized with several techniques, such as direct mechanical cleavage, scanning probe lithography, chemical etching or plasma etching [73].

4.3.2.1.2 Numerical results

The electromagnetic simulation of the proposed device has been carried out by using the Transmission Matrix Theory (TMT) approach [74]. It is based on the study of a single period of the grating, and, then, the transfer function results by the matrix product of the single period transmission matrices:

$$T=\begin{bmatrix} \frac{1}{t^2}\left(e^{j\phi_+}-r^2e^{-j\phi_-}\right) & \frac{r}{t^2}\left(e^{-j\phi_+}-e^{j\phi_-}\right) \\ \frac{r}{t^2}\left(e^{-j\phi_+}-e^{j\phi_-}\right) & \frac{1}{t^2}\left(e^{-j\phi_+}-r^2e^{j\phi_-}\right) \end{bmatrix}^N \tag{4.7}$$

where $r=\left(n_{eff1}-n_{eff2}\right)/\left(n_{eff1}+n_{eff2}\right)$ is the reflection coefficient, $t=\sqrt{1-r^2}$ is the transmission coefficient, N is the number of the periods and $\phi_\pm=\beta_1L_1\pm\beta_2L_2$ is the phase change, where the subscripts 1 and 2 are referred to the region with and without the graphene capacitor, respectively. The Eq. (8) allows to define the *S*-parameters, and then, the transmission at the output of the grating [74]. The *S* matrix could be expressed as:

$$S=\frac{1}{T_{11}}\begin{bmatrix} T_{21} & \det T \\ 1 & -T_{12} \end{bmatrix} \tag{4.8}$$

The matrix has been assumed symmetrical in case of linear reciprocal system, considering that the grating starts and finishes with the same semi-period. The delay time τ is evaluated as the derivative of the grating transmission phase ($\angle S_{12}$) with respect to the pulsation ω:

$$\tau=\frac{\partial(\angle S_{12})}{\partial\omega} \tag{4.9}$$

The e.m. study of the semi-periods has been carried out by using the Finite Element Method (FEM) approach. For the section with the graphene capacitor, a value of the effective refractive index equal of 2.448634 and 1.772773 have been obtained at λ = 1550 for the TE and TM mode, respectively.

As previously reported, the graphene has received great interest during the last years, and to study its optical properties, several theoretical models have been proposed [75-77]. For the e.m. study of the grating section with graphene capacitor, a closed form expression of the graphene optical conductivity has been assumed. It

considers the main physical effects and factors, such as interband and intraband transitions, temperature, chemical potential and hopping parameter, useful for wavelength from the visible to the infrared range [77]. A detailed mathematical model description is reported in [54]. The model accuracy is confirmed by an error matching < 1 % with numerical results obtained by using the Kubo formula. Furthermore, the model results are compliant with experimental one, avoiding the mathematical singularity obtained by that formulation for $hf = 2\mu_c$ (h is the Planck constant, f is the frequency and μ_c is the Fermi level). The equation $\varepsilon = 1 + i \cdot \frac{\sigma}{\omega \varepsilon_0 t_{gr}}$, where ε_0 is the vacuum permittivity, take into account the relationship between the anisotropic complex optical conductivity σ and the relative permittivity ε of the graphene. The real and imaginary part of TE and TM effective indices at 1550 nm vs the the electrochemical potential μ_c are reported in Fig. 4.6.

In the following of the delay line design, the TM mode has been chosen. It provides lower optical losses of the waveguide without graphene capacitor respect to the TE ones, while comparable losses between TE and TM modes for Bragg sections with graphene layers have been calculated, but much lower than the propagation losses in the bare waveguide for $\mu_c > 0.6$ eV. Moreover, the TM mode allows to reduce the device footprint A, providing an index contrast (Δn = 1.01 x 10^{-2}) almost one order of magnitude higher than the value of TE mode, corresponding to a stronger grating strength (κ).

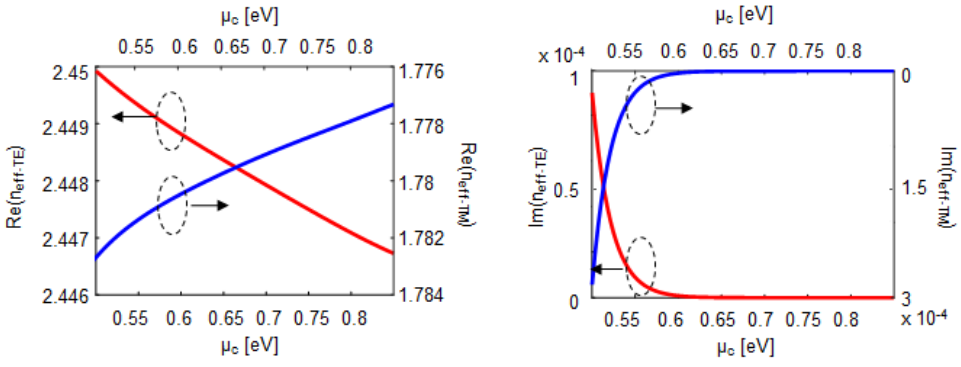

(a) (b)

Fig.4.6. Real (a) and imaginary (b) part of the effective indices in the sections with the graphene capacitor, for TE (red curve) and TM (blue curve) modes, as a function of the electrochemical potential μ_c. Reprinted with permission from [65] © The Optical Society.

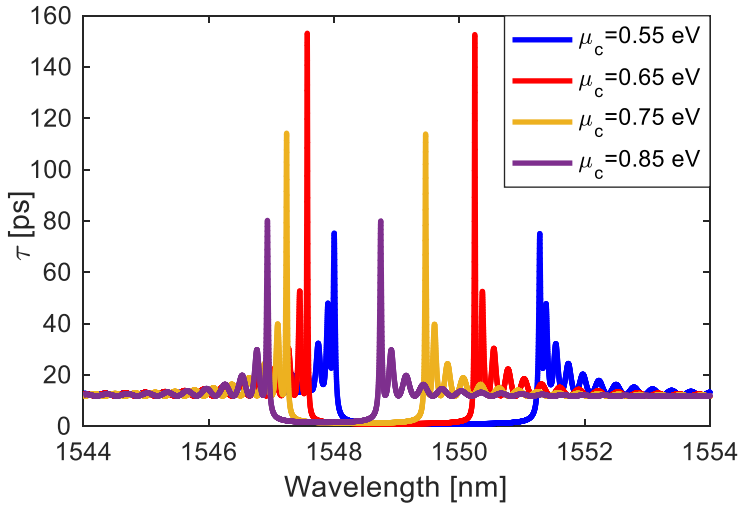

Fig. 4.7. Time delay spectra for several values of the electrochemical potential μ_c with L_g = 2 mm. Reprinted with permission from [65] © The Optical Society.

Therefore, a period Λ = 1.308 μm has designed to operate at around 1.55 μm. Firstly, the optical delay time spectra for several values of the chemical potential have been calculated for a grating length $L_g \approx 2$ mm, and then, for a number of grating periods N = 1988, as shown in Fig. 4.7. The slow light effect ensures the highest value of the optical delay time at the photonic bandgap band-edge.

Since V_g is the voltage applied across the electrodes, v_F is the Fermi velocity, C' ($= \varepsilon_{Al2O3} \cdot \varepsilon_0 / s$) is the effective capacitance per unit area with ε_{Al2O3} = 10, e is the electron charge, s is thickness of the alumina layer, and V_0 is the offset voltage referred to the natural doping, equal to 0.8 V, the relationship between the electrochemical potential and the applied voltage could be expressed as [69]:

$$\mu_c(V_g) = \hbar v_F \sqrt{\pi \frac{C'}{e} |V_g - V_0|} \tag{4.10}$$

The maximum values of the optical delay time $\tau_{max,}$ as a function of the chemical potential μ_c and the applied voltage $V_{g,}$ across the graphene electrodes, for an optical delay line 2 mm long, are shown in Fig. 4.8. Since lower values of Q-factor have been achieved for small values of μ_c, due to the high value of losses (see Fig. 4.6(a)), a decrease of τ_{max} has been calculated. Instead, a weaker refractive index for high value of μ_c involves a worsening of the Q-factor, and then, of $\tau_{max.}$

The value of electrochemical potential μ_c = 0.619 eV, and then, V_g = 4.363 V, corresponds to the peak in Fig. 4.8, providing a maximum value of the delay time τ_{max} = 161 ps, at λ = 1547.69 nm, as shown in Fig. 4.9(a). For such electrochemical potential, the delay time and group index spectra are reported in Figs. 4.9 (a)-(b). According to the slow light effect, the maximum value of τ_{max} is achieved at the band-edge of the proposed delay line, where the group index is maximum and then, the group velocity decrease, with a consequent enhancement of the light-matter interaction.

Considering the operation wavelength at the band-edge of Fig. 4.9, the tuning of the applied voltage provides a worsening of the *Q*-factor, and a minimum delay time τ_{min} = 13 ps has been calculated with V_g = 4.229 V.

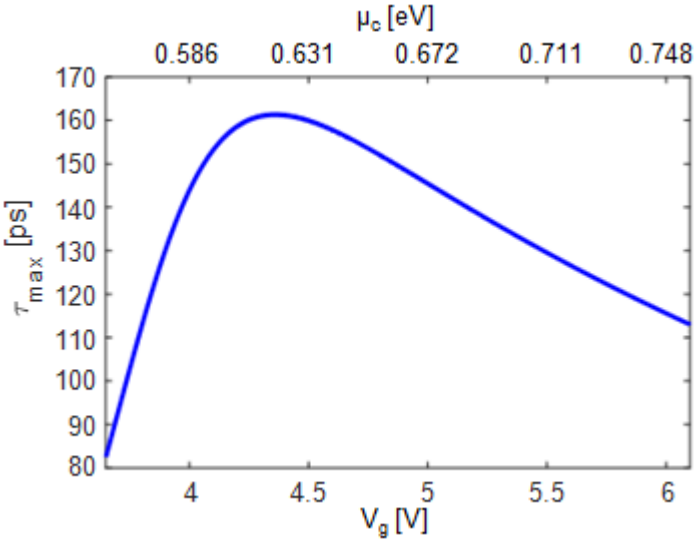

Fig.4.8. Maximum delay time τ_{max} vs voltage V_g and electrochemical potential μ_c with L_g = 2 mm Reprinted with permission from [65] © The Optical Society.

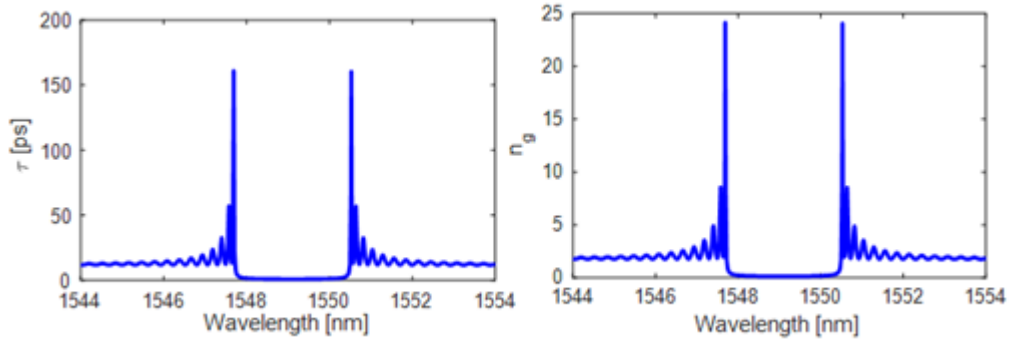

(a) (b)

Fig.4.9. (a) Delay time and (b) group index spectra of 2 mm Bragg grating, applying voltage V_g = 4.363 V. Reprinted with permission from [65] © The Optical Society.

Thus, a delay range $\Delta\tau = \tau_{max} - \tau_{min}$ =148 ps is obtained with a length of the Bragg grating of 2 mm. Furthermore, an average insertion loss (*IL*) value IL_{av} of 6.09 dB has been achieved (when $\tau = \tau_{max}$, *IL*=2.46 dB, while, when $\tau = \tau_{min}$ *IL* = 9.72 dB).

Since a tuning range of the delay time of 200 ps has been required for the X-band optical steering application [35], a parametric analysis on both the grating length and the operating voltage range has been carried out, also maximing both the ratio $IL_{av}/\Delta\tau$, defined as *Delay Loss* [dB/ps], and the figure of merit (*FOM*), defined as $FOM = \Delta\tau/A$ [ps/mm^2]. The applied voltages $V(\tau_{max})$ and $V(\tau_{min})$, corresponding to the condition of the maximum and minimum delay time, respectively, have been calculated for different values of L_g. As shown in Fig. 4.10(a), higher values of τ_{max} and τ_{min} can be obtained, while, the difference between $V(\tau_{max})$ and $V(\tau_{min})$ decreases as the length increases (Fig. 4.10(b)). To obtain $\Delta\tau$ = 200 ps, a minimum length L_g = 2.3 mm is required.

As previously mentioned, the design activity has been carried out also aiming at reducing the delay loss (blue curve) and the FOM (red curve), either reported in Fig. 4.11(a). As expected, the FOM decreases as L_g increases, due to an enlargement of the delay line footprint.

For low values of L_g, high values of $V(\tau_{max})$ - $V(\tau_{min})$ are required to ensure a delay range equal to 200 ps. As example, for L_g = 2.3 mm, $V(\tau_{max})$ - $V(\tau_{min})$ is equal to 98.2 mV and causes a wavelength detuning δ of about 30 pm (Fig. 4.11(b)) (operating wavelength $\lambda_0 = \lambda(\tau_{max})$ = 1547.67 nm), corresponding to high value of delay loss.

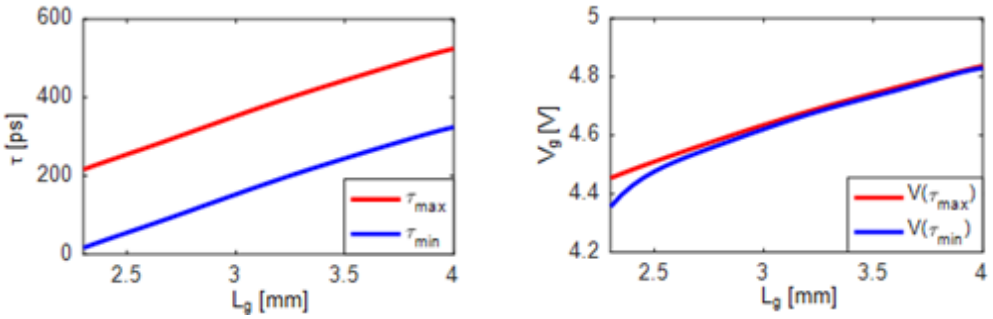

(a) (b)

Fig. 4.10. (a) Behaviour of τ_{max} and τ_{min} and (b) of $V(\tau_{max})$ and $V(\tau_{min})$ as a function of the grating length L_g Reprinted with permission from [65] © The Optical Society.

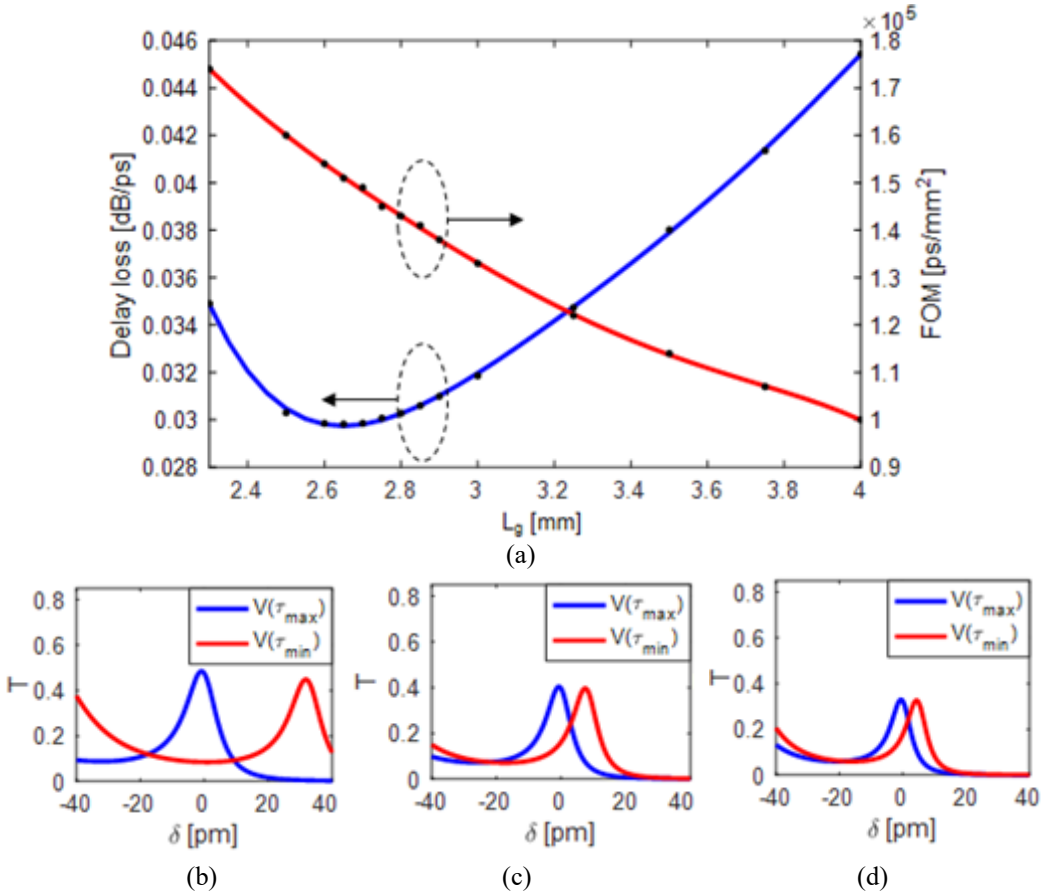

Fig. 4.11. (a) Delay loss (blue line) and FOM (red line) as a function of L_g. Transmission spectra at the band edge of the Bragg grating with (b) L_g = 2.3 mm ($\lambda_0 = \lambda(\tau_{max})$ = 1547.67 nm), (c) L_g = 2.6 mm ($\lambda_0 = \lambda(\tau_{max})$ = 1547.65 nm), and (d) L_g = 2.9 mm ($\lambda_0 = \lambda(\tau_{max})$ = 1547.63 nm), when $V(\tau_{max})$ and $V(\tau_{min})$ are applied to the graphene electrodes**.** Reprinted with permission from [65] © The Optical Society.

For large values of L_g, small values of $V(\tau_{max})$ - $V(\tau_{min})$ have been calculated, and, as shown in Fig. 4.11(d), a smaller wavelength detuning δ has been achieved (~ 5 pm) (operating wavelength $\lambda_0 = \lambda(\tau_{max})$ = 1547.63 nm). Although the difference in IL corresponding to τ_{max} and τ_{min} cases is less evident, higher optical losses have been obtained with a longer grating.

Therefore, L_g = 2.6 mm represents the best compromise, as explained by the valley into the Fig. 4.11(a). A less evident wavelength detuning is obtained respect to the shorter grating lengths case, but at the same time the intrinsic optical losses are also lower respect to the longer device case (Fig.4.11(c)). In particular, a low value of delay loss (= 2.9849 x 10^{-2} dB/ps) and a high value of FOM = 1.54 x 10^5 ps/mm^2, (see Fig. 4.11(a)) have been calculated for L_g = 2.6 mm.

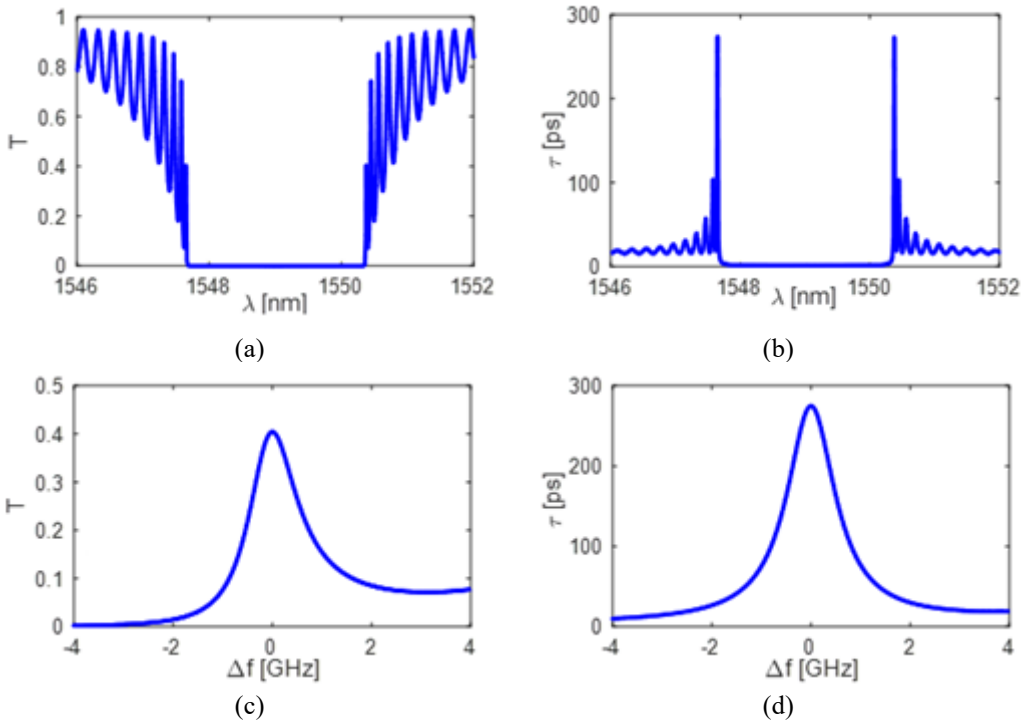

Fig. 4.12. (a) Transmission spectrum of the Bragg grating with L_g = 2.6 mm and (b) related delay time. (c) Zoom of the transmission spectrum and (d) delay time of the first resonance peak at the band edge. Δf is the frequency shift from resonant frequency ($f_0 \approx 193.824$ THz corresponding to $\lambda_0 \approx 1547.65$ nm). Reprinted with permission from [65] © The Optical Society.

In particular, its transmission spectrum and the related time delay are reported in Fig. 4.12, taking into account an applied voltage $V_g = V(\tau_{max}) = 4.5369$ V. A maximum value delay time $\tau_{max} = 274$ ps has been obtained with a flat and wide bandwidth BW of 1.19 GHz (Fig. 4.12(d)). By tuning V_g from 4.5113 V to 4.5369 V, corresponding to $V(\tau_{max})$ - $V(\tau_{min}) = 25.6$ mV, assuming the same operation wavelength at $\tau = \tau_{max}$, a delay range $\Delta\tau$ of 200 ps has been achieved (Fig.4.13). Moreover, an $IL = 7.91$ dB and $IL = 4.02$ dB at τ_{max} and τ_{min} have been obtained, respectively. A higher value of delay range (≈ 255.76 ps) can be performed, at the expense of higher value of insertion loss up to 11.45 dB.

The aforementioned performance of the proposed delay line with $L_g = 2.6$ mm has been summarized in Tab. 4.3. A fast switching time t_{switch} and low energy consumption P_{eff} have been obtained, by using the graphene-based electro-optical effect. Since the switching energy for the electro-optical effect is given by:

$$E_{switch} = \frac{1}{2} C\left(V(\tau_{max})^2 - V(\tau_{min})^2\right) \tag{4.11}$$

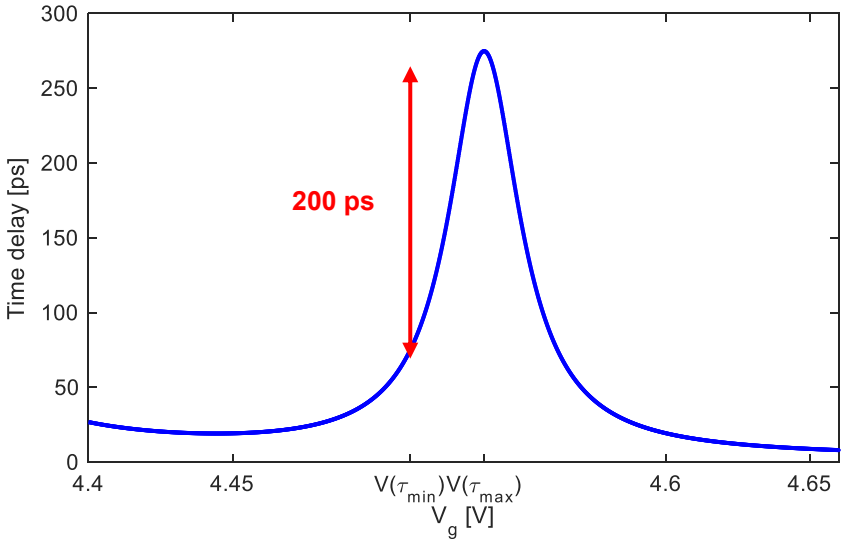

Fig.4.13. Tuning of the time delay as a function of the capacitor voltage**.** Reprinted with permission from [65] © The Optical Society.

where C is the capacitance of the graphene capacitor. An area of the electrodes has been assumed, corresponding to C = 8.22 pF.

A value of E_{switch} = 0.96 pJ and then a very high-power efficiency value P_{eff} = $P_{switch}/\Delta\tau$ = 6 x 10^{-4} mW/ps have been calculated by Eq. (4.11), assuming $A \sim (L_g/2)\cdot w_{Si}$ = 1.3 x 10^{-3} mm^2 (C = 8.22 pF), $V_{ON} = V(\tau_{max})$ = 4.5369 V and $V_{OFF} = V(\tau_{min})$ = 4.5113 V, and $P_{switch} = E_{switch}/t_{switch}$. A typical value of the switching time t_{switch} of about 8 ns has been calculated, being proportional to the time constant $R_{es}C$ (the system resistance R_{es} has been assumed equal to 1 kΩ [58]).

The proposed optical delay line shows the highest FOM compared to the state-of-the-art of integrated optical delay lines, reported in Tab. 4.4. Furthermore, the graphene electro-optic effect rises the attractiveness of this device for optical beamforming in Earth Observation optical payload, providing a very high power efficiency and a fast switching time (8 ns).

Tab.4.3: Performance of the graphene-based Si Bragg grating with L_g = 2.6 mm [65].

L_g [mm]	A [mm^2]	τ_{max} [ps]	$\Delta\tau$ [ps]	BW [GHz]	Delay loss [dB/ps]	FOM [ps/mm^2]
2.60	1.3 x 10^{-3}	274.85	200	1.19	2.98 x 10^{-2}	1.54 x 10^{5}

Tab.4.4. State-of-the-art of optical delay lines [65] with optical resonators [35, 45, 46, 49, 50, 53, 54].

	$\Delta\tau$ [ps]	τ_{max} [ps]	BW [GHz]	Delay loss [dB/ps]	t_{switch} [ns]	FOM [ps/mm^2]	Tuning
PhCW [45]	54	90	0.37	0.17	-	$9.00\text{x}10^2$	TO
RR+MZI [46]	1280	1280	59	0.01	$> 13\text{x}10^3$	44.5	TO
CROW [49]	800	800	6.25	0.01	-	$1.14\text{x}10^2$	TO
SCISSORS [50]	345	~380	10.5	0.06	$> 5.9\text{x}10^3$	$7.33\text{x}10^4$	TO
CROWs – SCISSORs [53]	~200	~250	-	-	0.12	$\sim 2.00\text{x}10^3$	EO
Stacked–RRs [54]	230	360	> 1	0.1	2	$1.44\text{x}10^5$	EO
Stacked-RRs+spirals [35]	690	920	> 1	0.03	< 2	$1.66\text{x}10^2$	EO
Proposed optical delay line	200	274	1.19	0.03	< 8	$1.54\text{x}10^5$	EO

4.3.3 Chirped waveform generator

In order to ensure a good range resolution of the SAR systems, as previously mentioned into the Paragraph 4.1, the microwave pulse compression is a commonly used approach. A linearly chirped microwave waveform generator with a time-bandwidth product (TBWP) in the order of 10^2 or 10^3 ensure the enhancement of the res_{range} according to Eq. (4.2).

In satellites currently in orbit, the chirped signal is generated by a Voltage-Controlled Oscillator (VCO) or a Digital signal Processing (DSP), based on digital synthesizers or field programmable gate arrays (FPGAs). A DSP system consists of a digital section with an Analog to Digital Converter (ADC), that generate the chirped signal into the base-band, and an up-converter, that shifts the signal to the desired frequencies. Digital synthesizer uses the DSP to make the chirped signal,

with low noise and high accuracy, while, the FPGA exploits algorithms of digital processing for the chirped signal generation, allowing also to realize chip-scaled system with digital generators and filters placed on the same chip.

Chirped generator based on DSP shows a TBWP in the order of 1000, with a resolution more than 12 bit [78]. Although, recently a great research effort has been focused on the development of DSP – based generator without up-converter, the limited speed and bandwidth of the electronics limit the achieved central frequency and the generator bandwidth of the electronic chirped generator at few gigahertz, not compliant to the requirements for SAR applications [79]. The photonic-assisted chirped generation, on the other hand, has demonstrated a wide range frequency tunability and low phase noise, in addition to large values of TBWP.

During the last decades, several techniques of photonic-based chirped generation have been reported in literature, including the spectral shaping and frequency-to-time mapping (SS-FTT), self-heterodyne, optically injected semiconductor laser or the combination of a frequency-tunable optoelectronic oscillator (OEO) and a recirculating phase modulation loop (RPML) [80-83].

The SS-FTT method is based on an optical spectral shaper, made by a Sagnac loop, a Fourier transform pulse shaper and a fiber Bragg gratings, and a dispersive medium, to convert the shaped pulse into a time domain [80]. Although this approach is very simple to make, it shows values of TBWP in the order of tens, at central frequency larger than 20 GHz.

The self-heterodyne approach provides the chirped signal by beating the sweeping optical signal with a continuous wave light. The frequency-modulated optical pulse generated by a distributed feedback laser (DFB) is sent to an interferometer, as Mach-Zehnder [81], that generates two time-delayed replicas of the input signal. The chirped signal results by the beating of the two replicas. A TBWP of 4200 and a bandwidth of 4.2 GHz have been experimentally demonstrated [81]. Although the aforementioned performance, with a good tunability of the central frequency and the bandwidth, are compliant with SAR requirements, the use of a noncoherent light source involves a large phase noise of the chirped signal. The injected laser – based chirp generator is based on an

optically injected modulated laser [82] or a single monolithically integrated amplified feedback laser [83], exploiting the period-one dynamics or the dual-mode state, respectively. The optically injected modulator laser-based architecture suffers of a large volume, due to the use of discrete components, although with large values of TBWP, while, a monolithically approach ensures a very large TBWP (e.g. 5.159×10^5) with a bandwidth more than 5 GHz, in a compact size [83].

An innovative approach has been proposed, for the first time, in [84], to obtain a large TBWP with low phase noise of the generated chirped signal. In this system, the optoelectronic oscillator (OEO) and the recirculating phase modulation loop (RPML) are the key building blocks. The continuous wave, generated by a laser source, is split by a power splitter (PS). One replica is handled by the OEO to generate a high purity microwave signal, while, the other one is intensity modulated by a Mach-Zehnder interferometer, driven by a rectangular switching signal. Then, the chirp-free signal, at the MZI output, feeds the RPML, where the signal experiences multiple phase modulations, increasing its chirp rate. By beating the OEO and RPML outputs at a high-speed photodetector (PD), a linearly chirped microwave waveform (LCMW) is generated. In terms of phase noise, the performance of the chirped generator is strictly affected by the optoelectronic oscillator one.

As reported into the Chapter 3, the key element into the OEO is the notch photonic filter, whose *Q*-factor influences the oscillating signal purity.

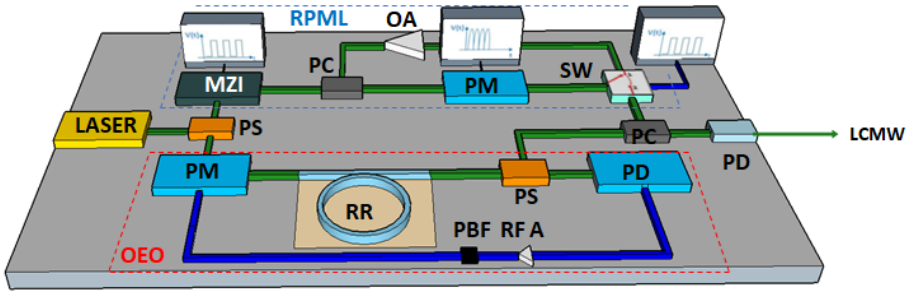

Fig.4.14. Design scheme of linearly chirped microwave waveform (*LCMW*) generator, (*PS*: power splitter, *MZI*: Mach-Zehnder modulator, *PC*: power combiner, *OA*: optical amplifier, *PM*: phase modulator, *SW*: switch, *PD*: photodiode, *RR*: ring resonator, *RF A*: electric amplifier, *RPML*: recirculating phase modulation loop, *OEO*: optoelectronic oscillator, *PBF*: pass-band filter). Optical connections are in green, electrical ones are in blue.

A phase shifter fiber Bragg grating has been used in [84] as optical notch filter, with a *Q*-factor of about 1000, and then, a noise of -130 dBm/Hz, at the expense of a bulky configuration.

An innovative photonic chirped generator (see Fig. 4.14), based on an ultra-high *Q*-factor silicon nitride-based ring resonator, has been designed with high spectral purity and high chip rate in a small footprint, exploiting the combination of OEO and RPML [21-22, 85-86]. In order to demonstrate the principle of operation of the proposed linear chirped generator, bulky devices currently on the market have been taken into account for the circuit simulations, carried out by using the licensed software *Optisystem* by *OptiWave Photonic Software*. This choice does not affect the possibility to deploy the entire circuit on a single chip by using a hybrid integration approach. In the following paragraphs, the design of the OEO and RPML is discussed, reporting also the simulated performance of the chirped generator.

4.3.3.1 Optoelectronic Oscillator

For most Space applications, the OEO should generate an output signal with a power of about 10 dBm, a phase noise as low as possible (< -100 dBc/Hz at 10 kHz from the carrier) and operate at high frequency (e.g. Ka- or X- band) [87]. Two different configurations of the OEO have been explored, according to the modulation approach. In particular, a phase or an intensity modulation could be used into the OEO scheme, by using a phase modulator (Fig. 4.15(a)) or a Mach-Zehnder interferometer (Fig. 4.15(b)), respectively. The latter one has been widely discussed into the Chapter 3.

As shown in Fig. 4.15(a), the input signal from the laser is phase modulated by a phase modulator (PM). The modulated signal is filtered by the ring resonator (RR) and electro-optical converted by a photodiode (PD). Its output is RF amplified, if necessary, filtered by a pass band filter (PBF), and then, drives the PM. The 50:50 power splitter (PS) have been inserted into the closed loop in order to plot the feedback signal on a spectrum analyser.

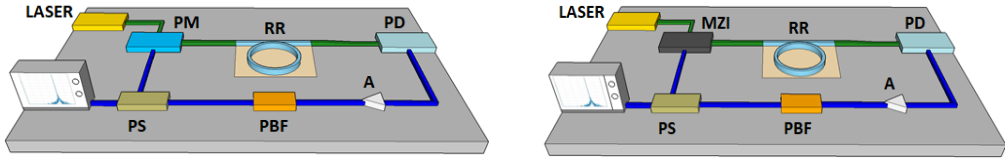

(a) (b)

Fig. 4.15. OEO based on a phase (a) or intensity (b) modulation approach (*PS*: power splitter, *MZI*: Mach-Zehnder modulator, *PM*: phase modulator, *PD*: photodiode, *RR*: ring resonator, *A*: electric amplifier, *PBF:* pass-band filter). Optical connections are in green, electrical ones are in blue [22].

After a brief transient, the positive feedback loop generates a sinusoidal signal with high spectral purity. The filtering window of the ring resonator affects the frequency of the sinusoidal output signal.

For the simulations, the frequency of the laser input signal has been tuned to generate an output signal frequency into the Ka-band (about 40 GHz). Further details of the OEO operation are reported into the Chapter 3. In contrast to the chip-scaled OEO reported in Chapter 3, the oscillator for LCMW generator has been designed by using bulky commercial devices.

For the OEO simulations, the NP Photonics *Rock ULTRA Module 1.55 μm* laser, with a linewidth < 700 Hz, a RIN value of -155 dB/Hz and an output power in the range 1 – 80 mW [88], has been used as optical source. The PM and PD used are the iXblue *MPZ-LN* [89] and Newport *104* [90], both able to operate at about 40 GHz. Furthermore, several RF amplifiers of the company SAGE millimeter have been explored.

In order to improve the spectral purity of the sinusoidal signal, the carrier suppression of the optical signal is required. Thus, the phase deviation of the phase modulator should be designed to maximize the first sideband and suppress the contribution of the optical carrier. The proper phase deviation φ_m of the PM has been calculated by using the Bessel functions [91]. In fact, the amplitude of the modulated signal could be expressed as:

$$E(t) = exp\left[i \cdot m \cdot cos\left(\omega_m t\right)\right] = \sum_{n=-\infty}^{\infty} i^n J_n(m) exp(in\omega_m t) \tag{4.12}$$

where m is the modulation index, ω_m is the angular frequency of the modulating signal, $J_n(m)$ is the Bessel function of the first kind with order n. The modulation

index m is strictly related to the amplitude of the modulating signal V_s and the half-wave voltage of the modulator V_π:

$$m=\left(\frac{V_s}{V_\pi}\right)\cdot\pi \tag{4.13}$$

The intensity of the phase modulator output signal I is:

$$I\approx 2I_0\left[1+J_0\left(2\varphi_m\right)+2J_1\left(2\varphi_m\right)\cos\omega_m t\right] \tag{4.14}$$

For the carrier suppression, the maximum value of the first kind Bessel function has been derived by Eq. (4.14):

$$J_1\left(2\varphi_m\right)=0.5819° \tag{4.15}$$

Then,

$$2\varphi_m=1.8412\ rad \tag{4.16}$$

$$\varphi_m=52.7465° \tag{4.17}$$

Furthermore, the optical output power of the laser and the RF amplifier gain have been designed, to comply the requirement of a signal output power of 10 dBm. About the photonic notch filter, as shown into the Chapter 2, a Q-factor into the range 1 x 10^9 – 1 x 10^{10}, with an extinction ratio (ER) of about 8 dB, could be obtained by properly designing the radius of the ring resonator and the bus-ring gap. Fig. 4.16 shows the phase noise trend, calculated at 10 kHz from the carrier at 40 GHz, for several values of ring resonator Q-factor, and laser output powers P_{laser} equal to 25 mW (blue curve) and 40 mW (red curve). For each value of P_{laser}, the RF amplifier has been chosen to obtain a value of the oscillating signal of about 10 dBm. In particular, an electric amplifier with a gain equal to 25 dB (noise figure = 3.5 dB) (SAGE millimeter *SBL-3634632535*) [92] and 20 dB (noise figure of 3 dB) (SAGE millimeter *SBL-2634032030*) [93] has been considered for an output laser power of 25 mW and 40 mW, respectively. As clearly shown in Fig. 4.16, an increase of the laser power involves a performance enhancement in terms of phase noise, requiring, also, a lower amplifier gain, and then, a better noise figure. Obviously, an increase of the Q-factor involves an improvement of the phase noise.

In order to choose the best OEO configuration for the LCMW generation, the intensity modulation approach, widely discussed into the Chapter 3, has been explored and compared to the phase modulation one, in terms of the signal output power and phase noise. The results of the comparison are reported into the Fig.

4.17, considering in both configurations a laser output power of 40 mW and an amplifier gain of 20 dB. An output power of the output signal of 3.9 dBm and 12.1 dBm has been simulated for the configuration with PM and MZI, respectively. Thus, besides a higher phase noise, the OEO with MZI shows a lower signal output power. This behavior causes the need of a higher gain of the RF amplifier, with a relative worsening of the phase noise. Then, the configuration with the PM seems to be the most performable.

As shown in Fig. 4.15, to further improve the phase noise value, a RF filter could be inserted after the RF amplifier. The RF filter selected is an *MMW-FilterFerrite-FIB* Millitech bandpass filter [94], characterized by a bandwidth of 2 GHz, an insertion loss of 1.4 dB and an attenuation factor of about 50 dB.

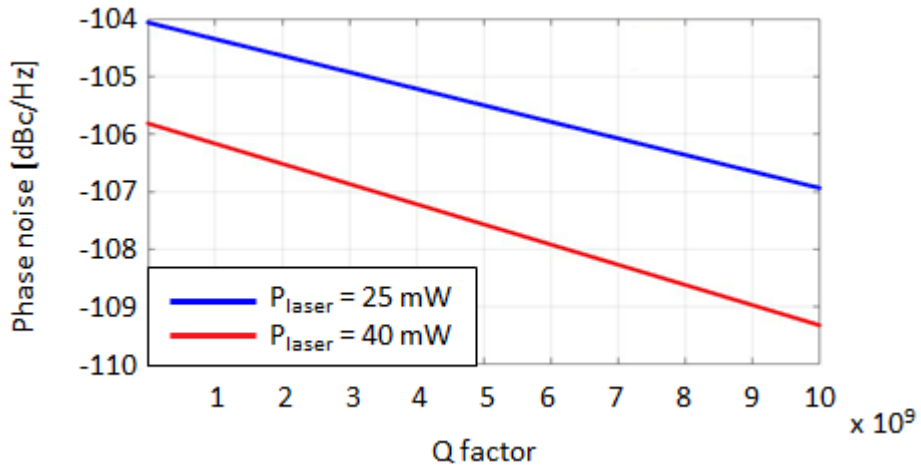

Fig.4.16. Phase noise trend of LCMW (output power ≈ 10 dBm) *vs* ring resonator Q-factor, for P_{laser} equal to 25 mW(blue) and 40 mW(red).

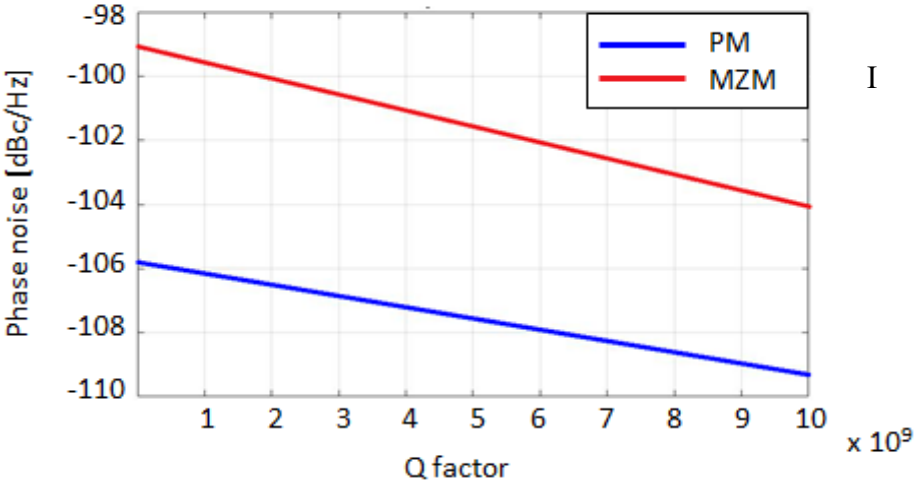

Fig. 4.17. Phase noise trend *vs* ring resonator *Q*-factor, for OEO configurations with PM (blue curve) and MZI (red curve).

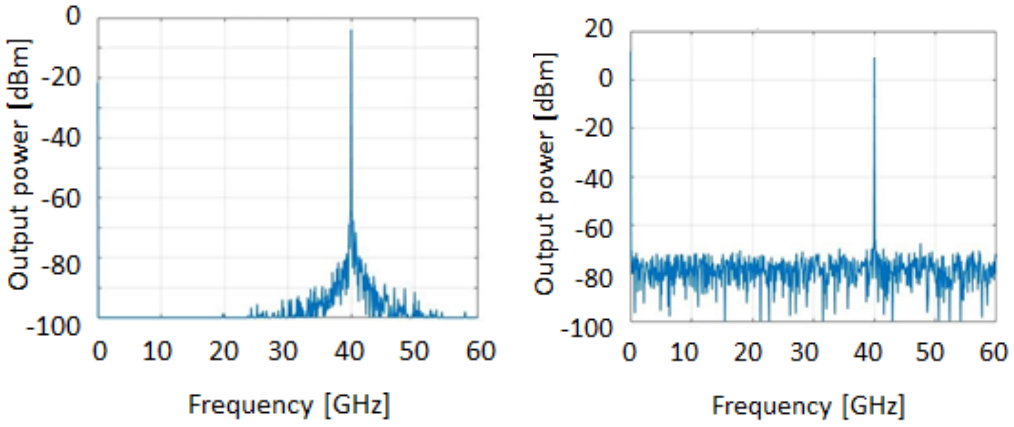

(a) (b)

Fig. 4.18. Output power of the OEO output signal for the configuration with (a) and without (b) the RF amplifier into the feedback loop.

The output signal spectra for the OEO configuration with and without the RF amplifier are reported in Fig. 4.18. A configuration with P_{laser} equal to 40 mW and an amplifier gain of 20 dB (noise figure = 3 dB) has been simulated. As shown in Fig. 4.18(a), the RF filter makes the spectrum more accurate, and therefore, a lower phase noise respect to Fig. 4.18(b), though, with a lower output power value at 40 GHz (≈ 11 dBm for (a) and ≈ -3 for (b)).

Aiming to obtain a phase noise at least equal to -110 dBc/Hz and an output power of 10 dBm, the configuration with the RF filter has been selected as optoelectronic oscillator. To increase the value of the signal output power and phase noise, P_{laser} equal to 40 mW, with a RF amplifier gain of 35 dB (SAGE millimeter *SBL-4034533540*) [95], and 80 mW, with a RF amplifier gain of 30 dB (SAGE millimeter *SBB-1834033022*) [96] have been considered (see Fig. 4.19).

A minimum phase noise of about -113 dBc/Hz with a signal output power of about 11 dBm have been simulated for the case P_{laser} = 40 mW. Instead, the case with P_{laser} = 80 mW shows a signal output power and a phase noise of 13.8 dBm and -119.2 dBc/Hz, respectively. Thus, the latter case has been chosen as final configuration of the designed OEO section.

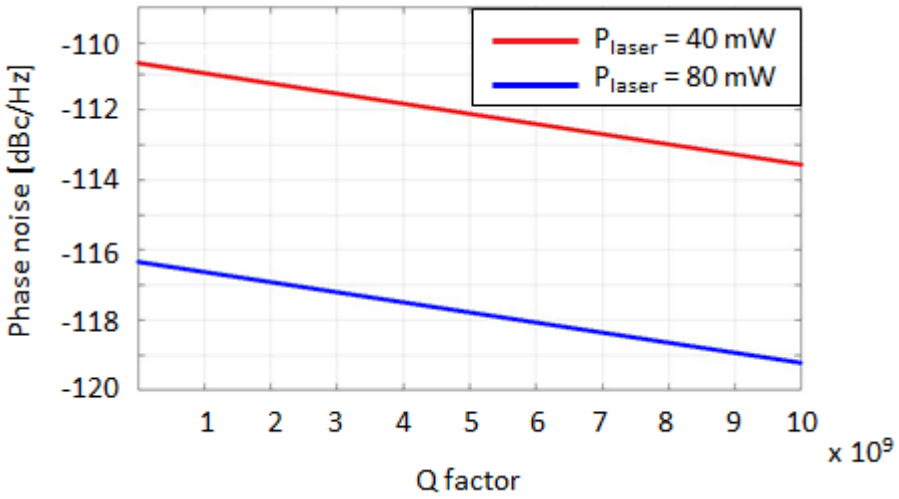

Fig. 4.19. Phase noise trend of OEO with PM and PBF *vs* ring resonator Q-factor, for P_{laser} = 40 mW (red curve) – 80 mW (blue curve).

4.3.3.2 Recirculating Phase Modulation Loop

Another key building block of the proposed LCMW generator is the RPML (see Fig. 4.14). The RPML block is the one responsible for the formation of the linear frequency modulation of the optical signal [84]. The signal emitted by the laser is amplitude modulated by an MZI driven by an electrical signal with a period T, and then phase modulated several times to increase the bandwidth. The electric field at the PM input could be expressed as:

$$E_{in,PM}=E_{in}exp\left(i2\pi f_c t\right) \tag{4.18}$$

where f_c (= 1/ T) and E_{in} are the frequency and the amplitude of the input optical signal, respectively. To obtain a linearly frequency modulated signal, a parabolic electric signal, expressed as Kt^2+1, drives the PM. Then, at the PM output, the field is equal to:

$$E_{out,PM}=E_{in}\cdot exp\left[i\left[\left(2\pi f_c t+\Delta\phi(Kt^2+1)\right)\right]\right] \tag{4.19}$$

where $\Delta\phi$ is a characteristic parameter of the phase modulator, called as modulation depth, equal to:

$$\Delta\phi=\frac{\pi V_{p\text{-}p}}{2V_\pi} \tag{4.20}$$

where V_{pp} is the peak-to-peak voltage of the driven signal.

Thus, the instant frequency at the PM output corresponds to:

$$f_{ist}=\frac{\partial[2\pi f_c t+\Delta\phi(Kt^2+1)]}{\partial t}=2\pi f_c+(2K\Delta\phi)t \tag{4.21}$$

The Eq. (4.21) shows a linear relationship between the frequency and the time. Each time the optical pulse recirculates in the RPML and it is again modulated by the PM, with a band enlargement equal to:

$$\Delta f=\frac{\Delta\phi}{T_0} \tag{4.22}$$

The expression of the main merit figure for linearly modulated frequency waveforms, the Time-Bandwidth Product is given by [84]:

$$TBWP=\frac{2N\cdot V_{p\text{-}p}}{V_\pi} \tag{4.23}$$

For the RPML simulations, the signal reported in Fig. 4.20 (a) and (b) are used as driven signal of the MZI and PM, respectively. As shown in Fig. 4.20 (b), a parabolic signal is used in order to obtain a linearly chirped microwave waveform. For both signals, a period *T* equal to 15 ns has been assumed.

The number of phase modulation cycles has been set, aiming to maximize the *TBWP* and generate a linear frequency modulated signal.

Although an enhancement of the *TBWP* requires an increase of the cycles number, a high value results in a distortion of the linear frequency modulated signal. Thus, the optimal number of cycles is 16. Since $V_{pp}=V_\pi$=6V for the iXBlue *MPZ-LN* Phase modulator [89], a *TBWP* equal to 32 has been calculated by Eq. (4.23). To further improve the *TBWP*, a decrease/increase of V_{pp}/V_π is required, fixing the number of cycles. Unfortunately, PMs with higher/smaller value of V_{pp}/V_π are not currently on the market.

4.3.3.3 Performance of LCMW generator

For the LCMW generation, the beating of the OEO and RPML signals at the photodiode give rise to a linearly chirped modulated frequency signal with very low phase noise. The amplitude of the LCMW could be expressed as:

$$i(t)=\begin{cases}cos\left[2\pi f_{osc}t+\frac{N\cdot\pi V_{p\text{-}p}}{V_\pi}\left(-\frac{t^2}{T^2}+1\right)\right] & |t|\le T\\ 0\end{cases} \tag{4.24}$$

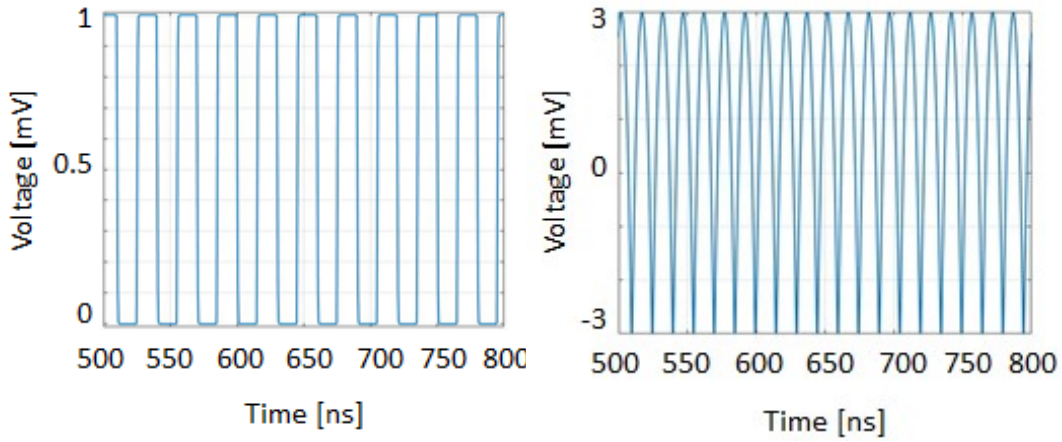

(a) (b)

Fig.4.20. Driven signal of the MZI (a) and PM (b) into the RPML, with a period of 15 ns.

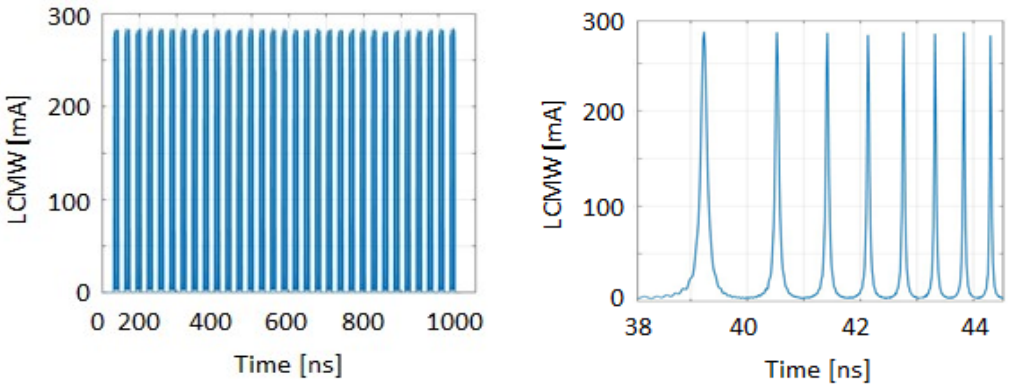

(a) (b)

Fig. 4.21. (a) LCMW amplitude for RPML configuration with PM driven by a parabolic waveform (see Fig. 4.20(b)); (b) Zoom on a single period of the LCMW.

The performance of the LCMW generator, based on the OEO and RPML designed, has shown in Fig. 4.21. For the simulations, a PhCRR with a *Q*-factor of 10^9, and ER of about 8 dB has been used.

Fig.4.21 shows a periodic linearly chirped waveform, and its zoom is reported in Fig. 4.21(b), where a *TBWP* of 32, with a phase noise of about -116 dBc/Hz, has been calculated.

To further improve the *TBWP* value, not changing the ratio V_{pp}/V_{π}, the engineering of the PM driven waveform is required. As example, a N-times stepped parabolic waveform [97] has been used. In Fig. 4.22, a 10 – times stepped parabolic waveform is reported.

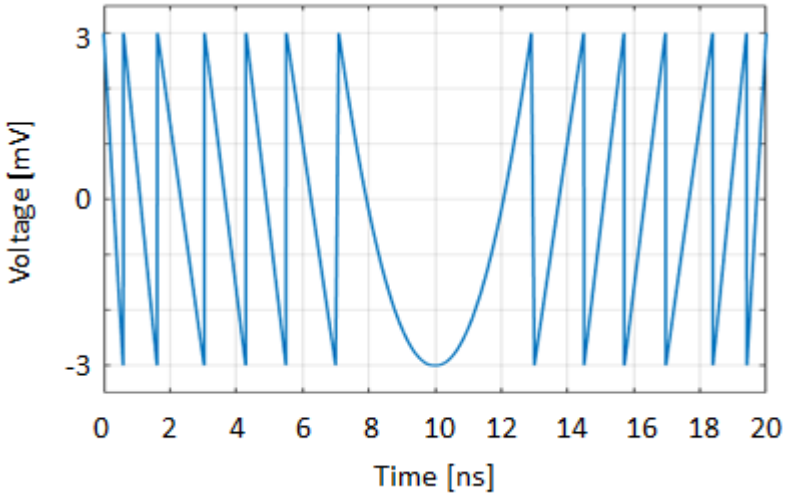

Fig.4.22. 10-times stepped parabolic waveform.

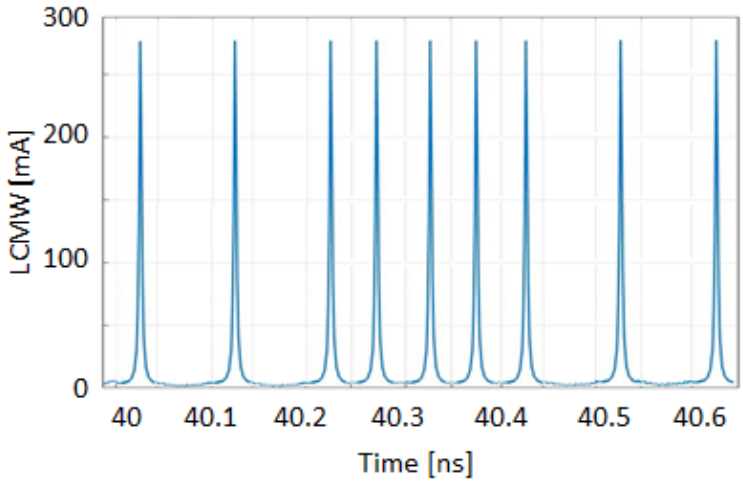

Fig.4.23. LCMW amplitude for RPML configuration with PM driven by a 10-times stepped parabolic waveform (see Fig. 4.22).

For this case, a *TBWP* of about 320 has been calculated, as shown in Fig. 4.23. In short, a *TBWP* of the order of thousands could be obtained by using complex waveforms to drive the PM into the RPML.

4.4 Conclusions

This Chapter is focused on the SAR systems for the Earth Observation. After highlighting the advantages of a photonic approach respect to the electronic one, the photonic-based SAR sub-systems have been discussed, e.g. analog-to-digital converters, beamforming and chirped signal generator. In particular, an optical

delay line with a tuning range of 200 ps, and then, an antenna steering angle of about ±15°, have been proposed, useful for beamsteering/beamforming in X-band. The delay line provides a flat bandwidth BW = 1.19 GHz, together with low value of delay loss 0.03 dB/ps and very small footprint (A ~1.3 x 10^{-3} mm^2). The integration of a graphene capacitor enables the electro-optic continuously tuning, fast switching time (t_{switch} < 8 ns) and very high-power efficiency (P_{eff} = 0.0006 mW/ps). Such high performance of the proposed resonant optical delay line is confirmed by the highest value of the figure of merit FOM = 1.54 x 10^5 ps/mm^2 , which represents an improvement of the state-of-the-art of integrated optical delay lines, together with very low delay loss, high power efficiency and short time switching values.

Furthermore, the microwave pulse compression has been investigated useful to improve the range resolution of SAR systems. In this context, an innovative architecture of a chirped generator has been reported. It is based on the ultra-high Q-factor ring resonator, based on a 1D photonic crystal waveguide, and bulky devices available in the market. By engineering the generator sections, e.g. RPML and OEO, a *TBWP* of 320 with phase noise of about -116 dBc/Hz has been simulated.

4.5 References

[1] S-E. Qian, *Optical payloads for space missions*, John Wiley & Sons, Montreal, Canada, 2015.

[2] P. Moreira, M. Prats-Iraola, G. Younis, I. Krieger, P. Hajnsek, and P. Papathanassiou, "A tutorial on synthetic aperture radar," IEEE Geoscience and remote sensing magazine, **1**, 1, pp. 6-43, 2013.

[3] Y. K. Chan, and V. C. Koo, "An introduction to synthetic aperture radar (SAR)," Progress In Electromagnetics Research, **2**, pp. 27-60, 2008.

[4] J. C. Curlander, and R. N. McDonough, *Synthetic aperture radar- Systems and signal processing*, New York: John Wiley & Sons, Inc, 1991.

[5] G. H. Born, J. A. Dunne, and D. B. Lame, "Seasat mission overview," Science, **204**, 4400, pp. 1405-1406, 1979.

[6] R. Francis, G. Graf, P. G. Edwards, M. McCaig, and C. McCarthy, "The ERS-1 Spacecraft and its Payload," ESA Bulletin, **65**, pp. 27-48, 1991.

[7] Y. Nemoto, H. I. D. E. O. Nishino, M. Ono, H. Mizutamari, K. Nishikawa, and K. Tanaka, "Japanese Earth Resources Satellite-1 Synthetic Aperture Radar," Proc. of the IEEE, **79**, 6, pp. 800-809, 1991.

[8] S. Ahmed, S. Parashar, E. Langham, and J. McNally, "RADARSAT Mission Requirements and Concept," Canadian Journal of Remote Sensing, **19**, 4, p. 280, 1993.

[9] M. Suess, S. Riegger, W. Pitz, and R. Werninghaus, "TerraSAR-X - Design and Performance," Proc. of EUSAR 2002, **2**, pp. 49-52, Cologne, Germany, June 4-6, 2002.

[10] M. Cossu, L. Corsano, M. L'Abbate, M. Mappini, R. Roscigno, M. Sacchettino, R. Sigismondi, and P. Venditti, "From large to small Earth Observation satellites: wide range of applications for Data Handling and Transmission Payload," Proc. of the 60th International Astronautical Congress (IAC), Daejeon, Korea, Oct. 12-16, 2009.

[11] M. W. J. Davidson, E. Attema, B. Rommen, N. Floury, L. Moreno Patricio, and G. Lerini, "ESA Sentinel-1 SAR mission concept," Proc. of EUSAR 2006, Dresden, Germany, May 16-18, 2006.

[12] P. Whittaker, M. Cohen, D. Hall, R. Bird, and L. Gomes, "NovaSAR – A Novel, Low Cost, Medium Resolution Spaceborne SAR System Development," Proc. of the 3rd Workshop on Advanced RF Sensors and Remote Sensing Instruments (ARSI), Noordwijk, The Netherlands, September 13-15, 2011.

[13] J. Lomba, R. Trigo, J. Ureña, E. Vez, M. López, F. Cerezo, M. Fernández, A. Borges, and J. Sánchez-Palma, "The Spanish Earth Observation Program," Proc. of the 2nd Workshop on Advanced RF Sensors and Remote Sensing Instruments 2009, Noordwijk, The Netherlands, Nov. 17-18, 2009.

[14] F. Covello, F. Battazza, A. Coletta, E. Lopinto, C. Fiorentino, L. Pietranera, G. Valentini, and S. Zoffoli, "COSMO-SkyMed an existing opportunity for observing the Earth," Journal of Geodynamics, **49**, 3-4, pp. 171-180, 2010.

[15] A. Moreira, "Synthetic Aperture Radar (SAR): Principles and Applications," Proc. of 4th Advanced Training Course in Land Remote Sensing, Athens, Greece, July 1-5, 2013.

[16] M. Cohen, A. Larkins, P. L. Semedo, and G. Burbidge, "NovaSAR-S Low Cost Spaceborne SAR Payload Design, development and deployment of a new benchmark in spaceborne radar," Proc. of IEEE Radar Conference (RadarConf), IEEE, pp. 0903-0907, Seattle, USA, May 8-12, 2017.

[17] C. Ciminelli, F. Dell' Olio, and M. N. Armenise, *Photonics in Space: Advanced Photonic Devices and Systems*, World Scientific, 2016.

[18] C. A. Wiley, "Pulsed doppler radar methods and apparatus," U.S. Patent 3 196 436, 1954.

[19] C. A. Wiley, "Synthetic aperture radars: A paradigm for technology evolution," IEEE Transaction on Aerospace and Electronic Systems, **21**, 3, pp. 440–443, 1985.

[20] W. A. Imbriale, S. S. Gao, and L. Boccia, *Space Antenna Handbook*, John Wiley & Sons, Chichester, United Kingdom, 2012.

[21] M. N. Armenise, F. Dell' Olio, C. Ciminelli, C. Galeone, and G. Brunetti, "Microphotonics-based architectures of mini-SAR payloads," Proc. of 21st International Conference on Transparent Optical Networks (ICTON 2019), IEEE, Angers, France, July 9-13, 2019. (INVITED).

[22] F. Dell' Olio, G. Brunetti, C. Galeone, D. Filippetto, N. Sasanelli, V. Stanzione, M. N. Armenise, and C. Ciminelli, "Microphotonic sub-systems for Synthetic Aperture Radar Payloads", Proc. of XXV International Congress Italian Association of Aeronautics and Astronautics (AIDAA 2019), Rome, Italy, September 9-12, 2019.

[23] D. Pilz, and P. Feldle, "RF-payload of TerraSAR-X," Proc. of German Microwave Conference (GeMiC), pp. 140-143, Stuttgart, Germany, April 5-7, 2005.

[24] N. Chantier, B. Dervaux, C. Lambert, V. Monier, C. Allene, and O. Bonnet, "Challenges of Mixed Signal Space grade ICs operating at Microwave frequencies," AMICSA 2012, ESA/ESTEC, Noordwijk, The Netherlands, August 26–28, 2012.

[25] P. Ghelfi, F. Laghezza, F. Scotti, G. Serafino, A. Capria, S. Pinna, D. Onori, C. Porzi, M. Scaffardi, A. Malacarne, V. Vercesi, E. Lazzeri, F. Berizzi, and A. Bogoni, "A fully photonics-based coherent radar system," Nature, **507**, 7492, pp. 341–345, 2014.

[26] G. C. Valley, "Photonic analog-to-digital converters," Optics Express, **15**, 5, pp. 1955–1982, 2007.

[27] A. Khilo S. J. Spector, M. E. Grein, A. H. Nejadmalayeri, C. W. Holzwarth, M. Y. Sander, M. S. Dahlem, M. Y. Peng, M. W. Geis, N. A. DiLello, J. U. Yoon, A. Motamedi, J. S. Orcutt, J. P. Wang, C. M. Sorace-Agaskar, M. A. Popovic, J. Sun, G.-R. Zhou, H. Byun, J. Chen, J. L. Hoyt, H. I. Smith, R. J. Ram, M. Perrott, T. M. Lyszczarz, E. P. Ippen, and F. X. Kartner, "Photonic ADC: Overcoming the bottleneck of electronic jitter," Optics Express, **20**, 4, pp. 4454–4469, 2012.

[28] F. Laghezza, F. Scotti, P. Ghelfi, A. Bogoni, and S. Pinna "Jitter limited photonic analog-to-digital converter with 7 effective bits for wideband radar applications, IEEE Radar Conference, Ottawa, ON, Canada, April 29–May 3, 2013.

[29] S. Pantoja, M. A. Piqueras, P. Villalba, B. Martínez, and E. Rico, "High performance photonic ADC for space applications," Proc. of International Conference on Space Optics—ICSO 2010, International Society for Optics and Photonics, **10565**, 1056511, Rhodes Island, Greece, October 4-8, 2010.

[30] M. A. Piqueras, P. Villalba, J. Puche, and J. Marti, "High performance photonic ADC for space and defence applications", Proc. of 2011 IEEE International Conference on Microwaves, Communications, Antennas and Electronic Systems (COMCAS 2011), IEEE, pp. 1-6, Tel Aviv, Israel, November 4-6, 2011.

[31] M. A. Piqueras, P. Villalba, V. Polo, A. Álvaro, J. M. Rodriguez, S. Lecomte, E. Portuondo-Campa, M. Maignan, and G. Spühler, "High speed, high frequency electro-photonic ADC for space enabled routers and flexible antennas," Proc. of International Conference on Space Optics—ICSO 2016, International Society for Optics and Photonics, **10562**, p. 105625U, Biarritz, France, October 18-21, 2016.

[32] J. Uher, C. Grenier, and G. Lefebvre, "RADARSAT-2 SAR," Canadian Journal of Remote Sensing, **30**, 3, pp. 287–294, 2004.

[33] A. Torre, and P. Capece, "COSMO-SkyMed: The advanced SAR instrument," Proc. of 5th International Conference on Recent Advances in Space Technologies (RAST), Istanbul, Turkey, June 9–11, 2011.

[34] W. Pitz, and D. Miller, "The TerraSAR-X Satellite," IEEE Transactions on Geoscience and Remote Sensing, **48**, 2, pp. 615–622, 2010.

[35] T. Tatoli, D. Conteduca, F. Dell'Olio, C. Ciminelli, and M. N. Armenise, "Graphene-based fine-tunable optical delay line for optical beamforming in phased-array antennas," Applied Optics, **55**, 16, pp. 4342-4349, 2016.

[36] R. D. Esman, M. Y. Frankel, J. L. Dexter, L. Goldberg, M. G. Parent, D. Stilwell, and D. G. Cooper, "Fiber-optic prism true time-delay antenna feed," IEEE Photonics Technical Letters, **5**, 11, pp. 1347–1349, 1993.

[37] P. Wu, S. Tang, and D. E. Raible, "A prototype high-speed optically steered X-band phased array antenna," Optics Express, **21**, 26, pp. 32599–32604, 2013.

[38] D. Dolfi, P. Joffre, J. Antoine, J. P. Huignard, D. Philippet, and P. Granger, "Experimental demonstration of a phased-array antenna optically controlled with phase and time delays," Applied Optics, **35**, 26, pp. 5293–5300, 1996.

[39] S. Li, X. Li, W. Zou, and J. Chen, "Rangeability extension of fiber-optic low-coherence measurement based on cascaded multistage fiber delay line," Applied Optics, **51**, 6, pp. 771–775, 2012.

[40] E. F. Burmeister, J. P. Mack, H. N. Poulsen, M. L. Mašanović, B. Stamenic, D. J. Blumenthal, and J. E. Bowers, "Photonic integrated circuit optical buffer for packet-switched networks," Optics Express, **17**, 8, pp. 6629-6635, 2009.

[41] H. Lee, T. Chen, J. Li, O. Painter, and K. J. Vahala, "Ultra-low-loss optical delay line on a silicon chip," Nature Communications, **3**, 867, pp. 1–7, 2012.

[42] I. Aryanfar, D. Marpaung, A. Choudhary, Y. Liu, K. Vu, D. Y. Choi, P. Ma, S. Madden, and B. J. Eggleton, "Chip-based Brillouin radio frequency photonic phase shifter and wideband time delay," Optics Letters, **42**, 7, pp. 1313-1316, 2017.

[43] R. Pant, A. Byrnes, C. G. Poulton, E. Li, D. Y. Choi, S. Madden, B. Luther-Davies, and B. J. Eggleton, "Photonic-chip-based tunable slow and fast light via stimulated Brillouin scattering," Optics Letters, **37**, 5, pp. 969-971, 2012.

[44] W. Shi, V. Veerasubramanian, D. Patel, and D. V. Plant, "Tunable nanophotonic delay lines using linearly chirped contradirectional couplers with uniform Bragg gratings," Optics Letters, **39**(3), pp. 701-703, 2014.

[45] N. Ishikura, R. Hosoi, R. Hayakawa, T. Tamanuki, M. Shinkawa, and T. Baba, "Photonic crystal tunable slow light device integrated with multi-heaters," Applied Physics Letters, **100**, 22, pp. 221110, 2012.

[46] X. Wang, L. Zhou, R. Li, J. Xie, L. Lu, K. Wu, and J. Chen, "Continuously tunable ultra-thin silicon waveguide optical delay line," Optica, **4**, 5, pp. 507-515, 2017.

[47] J. Yang, N. K. Fontaine, Z. Pan, A. O. Karalar, S. S. Djordjevic, C. Yang, W. Chen, S. Chu, B. E. Little, and S. J. B. Yoo, "Continuously tunable, wavelength-selective buffering in optical packet switching networks," IEEE Photonics Technology Letters, **20**, 12, pp. 1030–1032, 2008.

[48] N. Fontaine, J. Yang, Z. Pan, S. Chu, W. Chen, B. E. Little, and S. J. Ben Yoo, "Continuously tunable optical buffering at 40 gb/s for optical packet switching networks," Journal of Lightwave Technology, **26**, 23, pp. 3776–3783, 2008.

[49] A. Melloni, F. Morichetti, C. Ferrari, and M. Martinelli, "Continuously tunable 1 byte delay in coupled-resonator optical waveguides," Optics Letters, **33**, 20, pp. 2389–2391, 2008.

[50] P. A. Morton, J. Cardenas, J. B. Khurgin, and M. Lipson, "Fast thermal switching of wideband optical delay line with no long-term transient," IEEE Photonics Technology Letters, **24**, 6, pp. 512-514, 2012.

[51] Y. Xie, L. Zhuang, K. J. Boller, and A. J. Lowery, "Lossless microwave photonic delay line using a ring resonator with an integrated semiconductor optical amplifier," Journal of Optics, **19**, 6, pp. 065802, 2017.

[52] A. Meijerink, C. G. H. Roeloffzen, R. Meijerink, L. Zhuang, D. A. I. Marpaung, M. J. Bentum, M. Burla, J. Verpoorte, P. Jorna, A. Hulzinga,

and W. van Etten, "Novel ring resonator-based integrated photonic beamformer for broadband phased array receive antennas—Part I: design and performance analysis," Journal of Lightwave Technology, **28**, 1, pp. 3–18, 2010.

[53] J. Capmany, D. Domenech, and P. Munoz, "Silicon graphene reconfigurable CROWS and SCISSORS," IEEE Photonic Journal, **7**, 2, pp. 1 -9, 2015.

[54] D. Conteduca, F. Dell'Olio, C. Ciminelli, and M. N. Armenise, "Resonant graphene-based tunable optical delay line," IEEE Photonic Journal, **7**, 6, pp. 1-9, 2015.

[55] C. Ciminelli, D. Conteduca, F. Dell'Olio, and M. N. Armenise, "Novel graphene-based photonic devices for efficient light control and manipulation," Proc. of 17th International Conference on Transparent Optical Networks (ICTON 2015), IEEE, Budapest, Hungary, July 5-9, 2015.

[56] F. Zangeneh-Nejad, and R. Safian, "Significant enhancement in the efficiency of photoconductive antennas using a hybrid graphene molybdenum disulphide structure," Journal of Nanophotonics, **10**, 3, pp. 036005-036005, 2016.

[57] C. T. Phare, Y.-H. D. Lee, J. Cardenas, and M. Lipson, "Graphene electro-optic modulator with 30 GHz bandwidth," Nature Photonics, **9**, 8, pp. 511-514, 2015.

[58] M. Liu, X. Yin, E. Ulin-Avila, B. Geng, T. Zentgraf, L. Ju, F. Wang, and X. Zhang, "A graphene-based broadband optical modulator," Nature, **474**, 7349, p. 64, 2011.

[59] A. Phatak, Z. Cheng, C. Qin, and K. Goda, "Design of electro-optic modulators based on graphene-on-silicon slot waveguides," Optics Letters, **41**, 11, pp. 2501-2504, 2016.

[60] J. Wang, Z. Cheng, Z. Chen, X. Wan, B. Zhu, H. K. Tsang, C. Shu, and J. Xu, "High-responsivity graphene-on-silicon slot waveguide photodetectors," Nanoscale, **8**, 27, pp. 13206-13211, 2016.

[61] F. Xia, T. Mueller, Y.-M. Lin, A. Valdes-Garcia, and P. Avouris, "Ultrafast graphene photodetector," Nature Nanotechnology, **4**, 12, pp. 839-843, 2009.

[62] F. Zangeneh-Nejad, and R. Safian, "A Graphene-Based THz Ring Resonator for Label-Free Sensing," IEEE Sensors Journal, **16**, 11, pp. 4338-4344, 2016.

[63] A. K. Geim, and K. S. Novoselov, "The rise of graphene," Nature Materials, **6**, 3, pp. 183-191, 2007.

[64] F. Bonaccorso, Z. Sun, T. Hasan, and A. C. Ferrari, "Graphene photonics and optoelectronics," Nature Photonics, **4**, 9, pp. 611–622, 2010.

[65] G. Brunetti, D. Conteduca, F. Dell'Olio, C. Ciminelli,, and M. N. Armenise, "Design of an ultra-compact graphene-based integrated microphotonic tunable delay line," Optics Express, **26**, 4, pp. 4593-4604, 2018.

[66] C. Ciminelli, G. Brunetti, D. Conteduca, F. Dell'Olio,, and M. N. Armenise, "Integrated microphotonic tunable delay lines for beam steering in phased array antennas," Proc. of 20th International Conference on Transparent Optical Networks (ICTON 2018), IEEE, pp. 1-4, Bucharest, Romania, July 1-5, 2018. (INVITED).

[67] G. Brunetti, D. Conteduca, F. Dell'Olio, C. Ciminelli, and M. N. Armenise, "Silicon Electro-Optically Tunable Delay Line," Proc. of Integrated Photonics Research, Silicon and Nanophotonics (IPR), pp. IM3B-6, Zurich, Switzerland, July 2-5, 2018.

[68] Z. Sheng, C. Qiu, H. Li, L. Li, A. Pang, A. Wu, X. Wang, S. Zou, and F. Gan, "Low loss silicon nanowire waveguide fabricated with 0.13 μm CMOS technology," Proc. of IEEE Communications and Photonics Conference (ACP), IEEE, pp. 1-3, Guangzhou, China, November 7-10, 2012.

[69] M. Liu, X. Yin, and X. Zhang, "Double-layer graphene optical modulator," Nano Letters, **12**, 3, pp. 1482-1485, 2012.

[70] V. Sorianello, M. Midrio, and M. Romagnoli, "Design optimization of single and double layer Graphene phase modulators in SOI," Optics Express, **23**, 5, pp. 6478-6490, 2015.

[71] J. Capmany, D. Domenech, and P. Muñoz, "Silicon graphene Bragg gratings," Optics Express, **22**, 5, pp. 5283-5290, 2014.

[72] S. Bae, H. Kim, Y. Lee, X. Xu, J.-S. Park, Y. Zheng, J. Balakrishnan, T. Lei, H. R. Kim, Y. I. Song, Y.-J. Kim, K. S. Kim, B. Özyilmaz, J.-H. Ahn, B. H. Hong, and S. Iijima, "Roll-to-roll production of 30-inch graphene films for transparent electrodes," Nature Nanotechnology, **5**, 8, pp. 574–578, 2010.

[73] J. Feng, W. Li, X. Qian, J. Qi, L. Qi, and J. Li, "Patterning of graphene," Nanoscale, **4**,16, pp. 4883-4899, 2012.

[74] L. A. Coldren, S. W. Corzine, and M. L. Mashanovitch, *Diode lasers and photonic integrated circuits*, 2nd Edition, John Wiley & Sons, 2012.

[75] A. Vakil, and N. Engheta, "Transformation optics using graphene," Science, **332**, 6035, pp. 1291-1294, 2011.

[76] F. Z.-Nejad, S. A. Ramezani, K. Arik, and A. Khavasi, "Beam focusing using two-dimensional graphene-based meta-reflect-array," Proc. of 2016 24th Iranian Conference on Electrical Engineering (ICEE), pp. 613-616, Shiraz, Iran, May 10-12, 2016.

[77] E. Simsek, "A closed-form approximate expression for the optical conductivity of graphene," Optics Letters, **38**, 9, pp. 1437-1439, 2013.

[78] M. Y. Chua, and V. C. Koo, "FPGA-based chirp generator for high resolution UAV SAR," Progress in Electromagnetics Research, **99**, pp. 71-88, 2009.

[79] S. Srivastava, and P. Hobden, "5Ghz Chirp Signal Generator for Broadband FCMW Radar Applications," Proc. of 2018 IEEE International Symposium on Smart Electronic Systems (iSES), IEEE, pp. 152-155, Rourkela, India, 2018.

[80] C. Wang, and J. Yao, "Chirped Microwave Pulse Generation Based on Spectral Shaping and Wavelength-To-Time Mapping using a Sagnac Loop Mirror Incorporating a Chirped Fiber Bragg Grating," Journal of Lightwave Technology, **27**, 16, pp. 3336-3641, 2009.

[81] O. L. Coutinho, J. Zhang, and J. Yao, "Photonic generation of a linearly chirped microwave waveform with a large time-bandwidth product based

on self-heterodyne technique," Proc. of. 2015 International Topical Meeting on Microwave Photonics (MWP), IEEE, pp. 1-4, Paphos, Cyprus, 2015.

[82] P. Zhou, F. Zhang, Q. Guo, and S. Pan, "Linearly chirped microwave waveform generation with large time-bandwidth product by optically injected semiconductor laser," Optics Express, **24**, 16, pp. 18460-18467, 2016.

[83] J. Li, T. Pu, J. Zheng, Y. Zhang, Y. Shi, H. Zhu, Y. Li, X. Zhang, G. Zhao, Y. Zhou, and X. Chen, "Photonic generation of linearly chirped microwave waveforms using a monolithic integrated three-section laser," Optics Express, **26**, 8, pp. 9676-9685, 2018.

[84] W. Li, and J. Yao, "Generation of Linearly Chirped Microwave Waveform With an Increased Time-Bandwidth Product Based on a Tunable Optoelectronic Oscillator and a Recirculating Phase Modulation Loop," Journal of Lightwave Technology, **32**, 20, pp. 3573-3579, 2014.

[85] C. Ciminelli, F. Dell'Olio, G. Brunetti, N. Sasanelli, and M. N. Armenise, "Chirped Microwave Waveform Generation with High Spectral Purity," Proc. of 41st Photonics & Electromagnetics Research Symposium (PIERS 2019), Rome, Italy, September 17-20, 2019. (INVITED).

[86] C. Galeone, "Photonic architecture of SAR for Space applications", Politecnico di Bari, Master Thesis, 2017/2018.

[87] HI-Q™ Opto-Electronic Oscillators, OeWaves, https://oewaves.com/hi-q-oeo.

[88] The Rock OEM Module NP Photonics, http://www.npphotonics.com/rock-module.

[89] Phase modulator MPZ-LN iXBlue Photonics, https://photonics.ixblue.com/sites/default/files/2018-12/CBand%20Phase%20Modulators.pdf.

[90] Photodiode Newport 104, https://www.newport.com/medias/sys_master/images/images/h68/hba/8797113122846/High-Speed-Detectors-and-Receivers-User-s-Manual.pdf

[91] I. Kenyon, *The Light Fantastic: A Modern Introduction to Classical and Quantum Optics*, Oxford University Press, Inc., New York, 2008.

[92] RF amplifier SBL-3634632535 SAGE millimeter. https://www.sagemillimeter.com/content/datasheets/SBL-3634632535-2F2F-S1.pdf

[93] RF amplifier SBL-2634032030 SAGE millimeter. https://www.sagemillimeter.com/content/datasheets/SBL-2634032030-KFKF-S11111S1.pdf

[94] PBF filter MMW FIB Millitech. http://www.millitech.com/MMW-FilterFerrite-FIB.htm

[95] RF amplifier SBL-4034533540 Sage millimeter. https://www.sagemillimeter.com/content/datasheets/SBL-4034533540-2F2F-S1.pdf

[96] RF amplifier SBB-1834033022 SAGE millimeter. https://www.sagemillimeter.com/content/datasheets/SBB-1834033022-KFKF-E3.pdf

[97] K. Zhang, S. Zhao, Y. Yin, T. Lin, X. Li, W. Jiang, and G. Wang, "Photonic Generation and Transmission of Linearly Chirped Microwave Waveform With Increased Time-Bandwidth Product," IEEE Access, **7**, pp. 47461-47471, 2019.

Chapter 5

Conclusions

5.1 Summary of accomplishments

The thesis is focused on the demonstration of the potentiality of a photonic approach in the field of Space applications.

For the attitude and orbit control sub-system, the investigation of ultra-high *Q* ring resonator as sensitive element of an angular rate sensor, theoretically demonstrates the feasibility of a gyro on chip having a resolution less than 0.5 °/hr. The rate sensor exploits a Si_3N_4 based ring resonator with a quality factor exceeding 1,000,000,000. A so high *Q*-factor value has been achieved by integrating along the ring resonator optical path, a top grating, exploiting the slow light effect, forming the so-called photonic crystal ring resonator (PhCRR). Furthermore, the use of an ultra-low loss technology platform, as silicon nitride that exhibits waveguide loss value in the order of dB/m, assists to reach so high performance, providing also the capability to integrate all gyroscope devices in a single chip. The electromagnetic simulations aiming at the transmission spectra detection at the PhC band-edge has been performed by a self-made accurate mathematical model based on the coupled-mode theory. It results accurate, taking into account the waveguide curvature and the refractive index dispersion, and faster respect to the conventional well-known numerical approaches, e.g. 3D FEM, FDTD, SMT, Time Domain Equations.

The performance of the designed PhCRR results suitable for other Space applications. In the context of next generation telecom payload, the PhCRR has been designed as key building block of Ka-band optoelectronic oscillator. The theoretical analysis of the oscillator performance has been carried out,

demonstrating a remarkable improvement respect to the state of the art. Furthermore, the use of the PhCRR as key element of a microwave filter has been investigated. An accurate notch filter design has been carried out, aiming to obtain a Gaussian filtering shape continuously tuneable, according to the after-launch satellite reconfigurability requirement. The device has been studied by using a 2D FEM approach and a home-made mathematical model, based on the transmission matrices.

A fully photonics architecture of Synthetic Aperture Radar systems for Earth observation has been investigated, including the linearly chirped microwave generation and beamforming/beamsteering network.

The performance of the linearly chirped microwave generator, based on the designed PhCRR and electronic devices currently in the market, have been simulated by using the *OptiSystem* software.

To ensure a high-resolution of the SAR system, an optical delay line, useful for beamsteering application, has been designed. It is based on a graphene-pattern on a silicon waveguide. A mathematical model, based on the transmission matrix approach of the electromagnetic behaviour of both the graphene layers and the 1D-PhC structure, has been developed.

5.2 Critical issues

Main critical point of the PhCRR designed in thesis work regards the feasibility of its very accurate manufacture. Although the design has been carried out considering the constraints, i.e. e-beam resolution, the manufacturing of many periods along a circular path requires a very high fabrication effort. The insertion of defects inside the PhC, due to potential manufacturing issues, could affect the PhCRR behaviour, resulting in a performance worsening. Furthermore, although the grating losses have been supposed five (Chapter 2) and ten (Chapter 3) times larger than waveguide ones, not-optimized fabrication steps could involve very large value of grating losses, in the order of hundreds of dB/m, strongly affecting the PhCRR performance.

The direct measurement of a so ultra-high *Q*-factor requires a laser with an ultra-narrow linewidth (< 1kHz) and a high level of frequency stability, top quality into the worldwide market. Such lasers are not available in many laboratories. Recently, a nonlinear ring-down technique has been proposed in order to overcome the direct measurements limitations. It is based on a fast laser frequency sweeping across the resonance line. A part of light is detected by the resonance mode during the sweep and is reemitted in the direction of the detection, where interferes with the laser light, generating beatnote signals.

5.3 Future work

Prototypes of the designed devices, operating into the Space environment, may be the topic of the future experimental work. The proper operation of the proposed devices should be tested into the lab and in a harsh environment, as Space, aiming to reach a very high technology readiness level.

The fabrication of a photonic integrated circuit for angular rate sensing designed in this thesis and optimization of its performance is a short-term development of the research work reported here. To achieve this objective, techniques for hybrid integration of active and passive devices have to be experimentally investigated and improved.

The exploitment of the photonic benefits on new applications into the Space field is a medium-term target, as example, for the health monitoring of the astronauts during the Space missions.

Appendix A

Gyro performance parameters

The gyro technologies could be compared on basis of cost, power consumption, reliability, weight, volume, thermal stability, immunity to external disturbance [1-2].

The gyro performance parameters can be defined, such as scale factor, bias, input and output range, full range, resolution, dynamic range and dead band [3-4], from the gyroscope static input-output characteristic, as shown in Figure A.1.

Gyro scale factor is defined as the ratio between the change of the sensor output and the relevant angular velocity, evaluated as the slope of the straight line that can be obtained by linear fitting input-output data.

Bias is the average, over a certain time, of the gyro output when the device is not subject to rotation (expressed in °/h or °/s).

Input range is the range of input values within the angular velocity is measured. The difference between the extreme values of the input range is called full range.

Output range is the product of input range and scale factor.

Minimal detectable angular rate or resolution is the minimum angular velocity that can be detected (expressed in °/h or °/s). The ratio between full range and resolution is called dynamic range.

The dead band is a range of input values where the output is less than 10% of expected one.

The main noise contributions in a gyroscope are the quantization noise, the bias instability, and the Angle Random Walk (ARW).

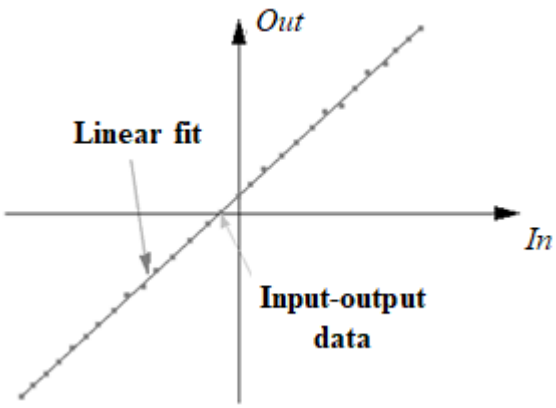

Fig. A.1. Gyroscope input-output static characteristic.

The bias instability and the ARW strictly depend on the gyro operating principle, while, the quantization noise is mainly due to analog-to-digital conversion of gyro output signal.

The ARW describes the average deviation of the rotation signal that will occur when the signal is integrated. The standard deviation of the noise observed in angle estimation is equal to:

$$\sigma_{rw}=W_{ARW}\sqrt{t} \tag{A.1}$$

where W_{ARW} is the angle random walk coefficient, usually called simply ARW (expressed in °/√h or °/√s).

Bias instability or drift is the peak-to-peak amplitude of the bias long term drift (expressed in °/s or °/h).

As shown in Fig. A.2, the bias drift evaluates the peak to-peak boundaries of the long-term variations of the mean value of the output signal, in contrast to the ARW that measures the white noise term.

Low values of ARW are crucial for fast response stabilization and control, while, the bias drift is a fundamental parameter mainly for navigation.

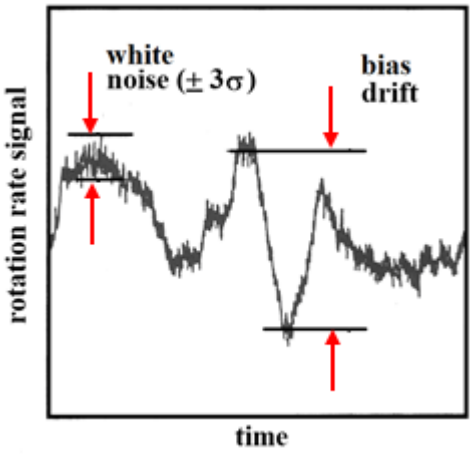

Fig. A.2. Typical output of a gyro at rest.

References

[1] M. N. Armenise, C. Ciminelli, F. Dell'Olio, and V. M. Passaro, *Advances in gyroscope technologies*, Springer Science & Business Media, 2010.

[2] C. Ciminelli, F. Dell' Olio, and M. N. Armenise, *Photonics in Space: Advanced Photonic Devices and Systems*, World Scientific, 2016.

[3] IEEE Standard for Inertial Sensor Terminology (Std 528-2001).

[4] ECSS-E-ST-60-21C – Gyro terminology and performance specification, https://ecss.nl/standard/ecss-e-st-60-21c-gyroterminology-and-performance-specification-15-february-2017/

Appendix B

Sagnac effect

The operating principle of all optical gyros is based on the Sagnac effect [1], according to which a phase shift $\Delta\varphi$, between two optical signals propagating in opposite directions (clockwise (CW) and counter-clockwise (CCW) directions) within a ring interferometer rotating along an axis perpendicular to the ring, or a frequency shift, between two resonant modes propagating in opposite CW and CCW directions within an optical cavity rotating around an axis perpendicular to it, are generated.

A simple cinematic approach can be used to derive analytic expression of rotation induced phase shift between CW and CCW beams [2]. As shown in Fig. B.1, a circular ring interferometer is considered. Laser light comes into the interferometer at point A and the CW and CCW propagating signals are generated by a beam splitter. When the interferometer is at rest with respect to a motionless inertial frame of references, the optical path lengths of the two optical signals propagating are equal, and their speed is equal to c (c is light speed in the free space). After a round-trip both waves come back into the beam splitter after a time interval τ equal to:

$$\tau = \frac{2\pi R}{c} \tag{B.1}$$

where R is ring interferometer radius.

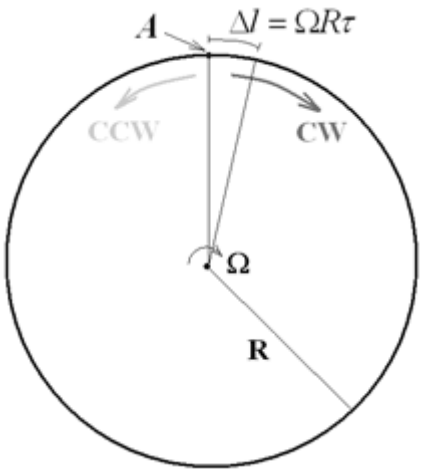

Fig. B.1. Sagnac ring interferometer.

In case of rotation of the ring interferometer with an angular rate Ω with respect to an observer which is in a motionless inertial frame of reference around an axis through the loop centre and perpendicular to the circular path plane, the beam splitter located in A in stationary condition has moved during the time interval τ through a length $\Delta l=\Omega R\tau$.

Since CW is co-directional with Ω according to the Fig. B.1, CW beam experiences a path length L_{CW} slightly greater than $2\pi R$ in order to reach the point A, while, CCW beam experiences a path length L_{CCW} slightly less than $2\pi R$ during one round trip. The difference between optical paths of CW and CCW waves could be expressed as:

$$\Delta L=L_{CW}-L_{CCW}=2\cdot\Delta l=2\cdot\Omega\cdot R\cdot\tau=\frac{4\pi\cdot\Omega\cdot R^2}{c} \tag{B.2}$$

Since CW and CCW waves propagate at the same speed, the CCW wave reaches the beam splitter located in A before than CW waves. Thus, the delay Δt and the relevant phase shift $\Delta\varphi$, induced by the rotation, between the two optical signals are equal to:

$$\Delta t=\frac{\Delta L}{c}=\frac{4\pi\cdot\Omega\cdot R^2}{c^2} \tag{B.3}$$

$$\Delta\phi=\Delta t\cdot\omega=\frac{4\pi\cdot\omega\cdot\Omega\cdot R^2}{c^2}=\frac{8\pi^2\cdot R^2}{c\cdot\lambda}\Omega \tag{B.4}$$

where λ is the optical signals wavelength and ω is the optical signals angular frequency. Eq. (B.4) is valid for one loop circular interferometer. If CW and CCW beams optical paths travel k circular loops, phase shift $\Delta\varphi$ is equal to:

$$\Delta\phi=\frac{8\pi^2\cdot R^2}{c\cdot\lambda}\cdot k\cdot\Omega \tag{B.5}$$

The time delay expression reported in Eq. (B.3) can be also derived in the framework of special relativity [3]. The mathematical approach just outlined has concerned the propagation of optical beams in vacuum. For a general purpose, now a similar interferometer based on a dielectric medium having a refractive index equal to n is considered. While the interferometer is at rest, light travels at the speed c/n in both directions with a propagation round-trip time of $n\cdot\tau$.

If the interferometer is rotating, the beam splitter located in A has moved through a length $n\cdot\Delta l$ in the propagation time $n\cdot\tau$. So, the optical path length of CW wave in one round-trip is equal to:

$$L^*_{CW}=2\pi R+n\Delta l=2\pi R+\frac{2\pi\cdot n\cdot\Omega\cdot R^2}{c} \tag{B.6}$$

whereas the optical path length of CCW wave in one round trip is given by:

$$L^*_{CCW}=2\pi R-n\Delta l=2\pi R-\frac{2\pi\cdot n\cdot\Omega\cdot R^2}{c} \tag{B.7}$$

Furhtermore, the speed of CW wave is equal to:

$$v_{CW}=\frac{c}{n}+\alpha\cdot\Omega\cdot R \tag{B.8}$$

and the speed of CCW wave is equal to:

$$v_{CCW}=\frac{c}{n}-\alpha\cdot\Omega\cdot R \tag{B.9}$$

where α is the Fresnel-Fizeau drag coefficient, which is equal to [4]:

$$\alpha=1-n^{-2} \tag{B.10}$$

The additive terms in light speed expressions reported in Eqs. (B.8) and (B.9) are due to the drag of light propagating in a uniformly moving medium [5].

The CW and CCW waves reach the point A in different instants, with a delay Δt^* equal to:

$$\Delta t^*=\frac{L^*_{CW}}{v_{CW}}-\frac{L^*_{CCW}}{v_{CCW}}=\frac{2\pi R+\frac{2\pi\cdot n\cdot\Omega\cdot R^2}{c}}{\frac{c}{n}+\alpha\cdot\Omega\cdot R}-\frac{2\pi R-\frac{2\pi n\cdot\Omega\cdot R^2}{c}}{\frac{c}{n}-\alpha\cdot\Omega\cdot R} \tag{B.11}$$

Rearranging Eq. (B.11) and supposing that $\frac{c^2}{n^2} >> \alpha\Omega^2R^2$, Δt^* becomes:

$$\Delta t^* \cong \frac{4\pi \cdot R^2 \cdot n^2 \cdot \Omega \cdot (1-\alpha)}{c^2} = \frac{4\pi \cdot R^2 \cdot \Omega}{c^2} \tag{B.12}$$

Comparing Eqs. (B.12) and (B.3), it is evident that $\Delta t = \Delta t^*$, then, the phase shift induced by rotation is equal either when the optical propagation takes place in a homogeneous medium with refractive index equal to n and when optical propagation takes place in vacuum or when. The same result has been demonstrated by using a more rigorous relativistic electrodynamic approach [6], that requires the derivation of the equation describing the optical propagation in a rotating frame and the application of a perturbation method to calculate the rotation induced phase shift [6].

As previously reported, the rotation induces a frequency difference between two counter-propagating resonant modes excited in an optical ring cavity. In particular, an optical resonator supports optical modes whose resonance frequencies v_q satisfy the following relation:

$$q \cdot c = v_q \cdot L \tag{B.13}$$

where q is an integer number and L is the optical path length of resonant modes when the ring cavity is at rest. If two qth order counter-propagating resonant modes are excited in a ring cavity, their resonance frequencies experience a frequency shift, and their resonant frequency are being equal to:

$$v_q^{CW} = \frac{q \cdot c}{L_+} \tag{B.14}$$

and

$$v_q^{CCW} = \frac{q \cdot c}{L_-} \tag{B.15}$$

where L_+ and L_- are the optical path lengths experienced by the two resonant modes.

The frequency difference Δv between the two qth order resonant modes is given by:

$$\Delta v = v_q^{CW} - v_q^{CCW} = q \cdot c \left(\frac{1}{L_-} - \frac{1}{L_+}\right) \cong q \cdot c \frac{\Delta L}{L^2} \tag{B.16}$$

The $q \cdot c$ product can be written as:

$$q \cdot c = L \cdot v_{q,0} \tag{B.17}$$

where $v_{q,0}$ is the resonance frequency of the q-th order resonant mode when the optical resonator is at rest. Combining Eq. (B.16) and Eq. (B.17), the following expression can be obtained:

$$\Delta v = v_{q,0}\frac{\Delta L}{L} \tag{B.18}$$

Using Eq. (B.2) and Eq. (A.18), Δv can be written as:

$$\Delta v = v_0\frac{2R}{c}\Omega \tag{B.19}$$

where R is the resonator radius.

For an arbitrary geometry of the optical cavity, frequency difference Δv between the two qth order resonant modes is given by [7]:

$$\Delta v = \frac{4\cdot a\cdot v_0}{p\cdot c}\Omega \tag{B.20}$$

where a is the area enclosed by the light path and p is the perimeter of the light path.

References

[1] G. Sagnac, "L'èther lumineux dèmontrè par l'effet du vent relatif d'èther dans un interfèromètre en rotation uniforme," CR Academic Science, **157**, pp. 708-710, 1913.

[2] H. J. Arditty, and H. C. Lefevre, "Sagnac effect in fiber gyroscopes," Optics Letters, **6**, 8, pp. 401-403, 1981.

[3] G. Rizzi, and M. L. Ruggiero, "A Direct Kinematical Derivation of the Relativistic Sagnac Effect for Light or Matter Beams," General Relativity and Gravitation, **35**, 12, pp. 2129-2136, 2003.

[4] V. Vali, R. W. Shorthill, and M. F. Berg "Fresnel-Fizeau effect in a rotating optical fiber ring interferometer," Applied Optics **16**, 10, pp. 2605-2607, 1977.

[5] A. Drezet, "The physical origin of the Fresnel drag of light by a moving dielectric medium," European Physical Journal B-Condensed Matter and Complex Systems, **45**, 1, pp. 103-110, 2005.

[6] H. C. Lefevre, and H. J. Arditty, “Electromagnetisme des milieux dielectriques lineaires en rotation et application a la propagation d'ondes guidees,” Applied Optics, **21**, 8, pp. 1400-1409, 1982.

[7] F. Jacobs, and R. Zamoni, “Laser ring gyro of arbitrary shape and rotation axis,” American Journal of Physics, **50**, 7, pp. 659-660, 1982.

List of publications on optoelectronic and photonic devices for Space applications

International journals with referee

[1] G. Brunetti, D. Conteduca, F. Dell'Olio, C. Ciminelli, and M. N. Armenise, "Design of an ultra-compact graphene-based integrated microphotonic tunable delay line," Optics Express, **26**, 4, pp. 4593-4604, 2018.

[2] F. Dell'Olio, D. Conteduca, G. Brunetti, M. N. Armenise, and C. Ciminelli, "Novel CMOS-Compatible Athermal and Polarization-Insensitive Ring Resonator as Photonic Notch Filter," Photonics Journal, **10**, 6, pp. 1-11, 2018.

[3] G. Brunetti, F. Dell' Olio, D. Conteduca, M. N. Armenise, and C. Ciminelli, "Ultra-compact tuneable notch filter using silicon photonic ring resonator," Journal of Lightwave Technology, **37**, 13, pp. 2970-2980, 2019.

[4] G. Brunetti, I. McKenzie, F. Dell'Olio, M. N. Armenise, and C. Ciminelli, "Measured radiation effects on InGaAsP/InP ring resonators for space applications," Optics Express, **27**, 17, pp. 24434-24444, 2019.

[5] G. Brunetti, D. Conteduca, F. Dell' Olio, C. Ciminelli, and M. N. Armenise, "Comprehensive Mathematical Modelling of Ultra-high *Q* Grating-Assisted Ring Resonators," Journal of Optics, 2020, https://doi.org/10.1088/2040- 8986/ab71eb.

International Book Chapters

[6] C. Ciminelli, G. Brunetti, F. Dell'Olio, F. Innone, D. Conteduca, and M.N. Armenise, "Emerging applications of Whispering Gallery Mode photonic resonators," Lecture Notes in Electrical Engineering, **429**, pp. 185-191, 2017.

[7] F. Dell'Olio, G. Brunetti, D. Conteduca, N. Giovinazzi, N. Sasanelli, C. Ciminelli, and M. N. Armenise, "Integrated microwave photonics: overview and promising space applications," Lecture Notes in Electrical Engineering, **512**, pp. 107-112, 2018.

Proceedings of international conferences

[8] F. Dell'Olio, G. Brunetti, D. Conteduca, N. Sasanelli, C. Ciminelli, and M. N. Armenise, "Planar Photonic Gyroscopes for Satellite Attitude Control," Proc. of 7th International Workshop on Advances in Sensors and Interfaces (IWASI), pp. 167-169, Vieste, Italy, June 15-16, 2017.

[9] C. Ciminelli, F. Dell'Olio, G. Brunetti, D. Conteduca, and M. N. Armenise, "New microwave photonic filters based on resonant structures with engineered the spectral reflectance," Proc. of 19th International Conference on Transparent Optical Networks (ICTON 2017), pp. 1-4, Girona, Spain, July 2-6, 2017. (INVITED).

[10] F. Dell'Olio, G. Brunetti, D. Conteduca, N. Giovinazzi, N. Sasanelli, C. Ciminelli, and M.N. Armenise, "Integrated Microwave Photonics: Overview and Promising Space Applications," Proc. of ApplePies International Conference (Applications in Electronics Pervading Industry, Environment and Society), Rome, Italy, September 21-22, 2017.

[11] C. Ciminelli, F. Dell'Olio, G. Brunetti, D. Conteduca, N. Sasanelli, and M. N. Armenise, "Photonic technologies for nanosatellites", Proc. of Italy – Israel Workshop On Nanosatellite Technologies, Rome, Italy, April 9-10, 2018.

[12] C. Ciminelli, G. Brunetti, D. Conteduca, F. Dell'Olio, and M. N. Armenise, "Integrated microphotonic tunable delay lines for beam steering in phased

array antennas," Proc. of 20th International Conference on Transparent Optical Networks (ICTON 2018), pp. 1-4, Bucharest, Romania, July 1-5, 2018. (INVITED).

[13] C. Ciminelli, F. Dell'Olio, G. Brunetti, D. Conteduca, and M. N. Armenise, "Graphene/Silicon Schottky Junction Solar Cells," Proc. of 20th International Conference on Transparent Optical Networks (ICTON 2018), pp. 1-4, Bucharest, Romania, July 1-5, 2018. (INVITED).

[14] G. Brunetti, D. Conteduca, F. Dell'Olio, C. Ciminelli, and M. N. Armenise, "Silicon Electro-Optically Tunable Delay Line," Proc. of Integrated Photonics Research, Silicon and Nanophotonics (IPR), pp. IM3B-6, Zurich, Switzerland, July 2-5, 2018.

[15] G. Brunetti, F. Dell'Olio, D. Conteduca, M. N. Armenise, and C. Ciminelli, "Photonic Devices for Space Applications," Proc. of 26th Annual International Conference on Composites/Nano Engineering (ICCE-26), Paris, France, July 15-21, 2018. (INVITED).

[16] C. Ciminelli, F. Dell'Olio, G. Brunetti, and M. N. Armenise, "Microwave Photonics: An Opportunity for Space Systems and 5G Networks," Proc. of 1st International Conference on Dieletric Photonic Devices and Systems Beyond Visible (D-PHOTON 2018), Bari, Italy, October 1-2, 2018. (INVITED).

[17] C. Ciminelli, F. Dell'Olio, G. Brunetti, N. Sasanelli, and M. N. Armenise, "Chirped Microwave Waveform Generation with High Spectral Purity," Proc. of 41st Photonics & Electromagnetics Research Symposium (PIERS 2019), Rome, Italy, September 17-20, 2019. (INVITED).

[18] C. Ciminelli, F. Dell' Olio, G. Brunetti, A. Di Benedetto, and M. N. Armenise, "Integrated Microphotonic Switching Matrices for Flexible and Broadband Telecom Satellite Payloads," Proc. of 21st International Conference on Transparent Optical Networks (ICTON 2019), Angers, France, July 9-13, 2019. (INVITED).

[19] M. N. Armenise, F. Dell' Olio, C. Ciminelli, C. Galeone, and G. Brunetti, "Microphotonics-based architectures of mini-SAR payloads," Proc. of 21st

International Conference on Transparent Optical Networks (ICTON 2019), Angers, France, July 9-13, 2019. (INVITED).

[20] F. Dell' Olio, G. Brunetti, M. N. Armenise, and C. Ciminelli, "Ka-band optoelectronic oscillator based on ultra-high *Q* ring resonator," accepted by European Frequency and Time Forum (EFTF 2020), Noordwijk, The Netherlands, April 21-23, 2020.

Proceedings of national conferences

[21] F. Dell'Olio, G. Brunetti, D. Conteduca, N. Giovinazzi, C. Ciminelli, and M. N. Armenise, "Integrated microwave photonic devices and circuits in space," Proc. of 49th Annual Meeting of the Associazione Società Italiana di Elettronica (SIE), Palermo, Italy, June 21-23, 2017.

[22] G. Brunetti, F. Dell'Olio, D. Conteduca, M. N. Armenise, and C. Ciminelli, "Tuneable Gaussian-Shaped Photonic Notch Filter", Proc. of 51th Annual Meeting of the Associazione Società Italiana di Elettronica (SIE), Rome, Italy, June 26-28, 2019.

[23] F. Dell' Olio, G. Brunetti, C. Galeone, D. Filippetto, N. Sasanelli, V. Stanzione, M. N. Armenise, and C. Ciminelli, "Microphotonic sub-systems for Synthetic Aperture Radar Payloads", Proc. of XXV International Congress Italian Association of Aeronautics and Astronautics (AIDAA 2019), Rome, Italy, September 9-12, 2019.

Complete list of publications

International journals with referee

[1] G. Brunetti, D. Conteduca, F. Dell'Olio, C. Ciminelli, and M. N. Armenise, "Design of an ultra-compact graphene-based integrated microphotonic tunable delay line," Optics Express, **26**, 4, pp. 4593-4604, 2018.

[2] F. Dell'Olio, D. Conteduca, G. Brunetti, M. N. Armenise, and C. Ciminelli, "Novel CMOS-Compatible Athermal and Polarization-Insensitive Ring Resonator as Photonic Notch Filter," IEEE Photonics Journal, **10**, 6, pp. 1-11, 2018.

[3] G. Brunetti, F. Dell' Olio, D. Conteduca, M. N. Armenise, and C. Ciminelli, "Ultra-compact tuneable notch filter using silicon photonic ring resonator," Journal of Lightwave Technology, **37**, 13, pp. 2970-2980, 2019.

[4] D. Conteduca, G. Brunetti, F. Dell'Olio, M. N. Armenise, T. F. Krauss, and C. Ciminelli, "Monitoring of individual bacteria using electro-photonic traps," Biomedical Optics Express, **10**, 7, pp. 3463-3471, 2019.

[5] G. Brunetti, I. McKenzie, F. Dell'Olio, M. N. Armenise, and C. Ciminelli, "Measured radiation effects on InGaAsP/InP ring resonators for space applications," Optics Express, **27**, 17, pp. 24434-24444, 2019.

[6] G. Brunetti, D. Conteduca, F. Dell' Olio, M. N. Armenise, and C. Ciminelli, "Comprehensive Mathematical Modelling of Ultra-high *Q* Grating-Assisted Ring Resonators," Journal of Optics, 2020. https://doi.org/10.1088/2040- 8986/ab71eb.

International Book Chapters

[7] C. Ciminelli, G. Brunetti, F. Dell'Olio, F. Innone, D. Conteduca, and M.N. Armenise, "Emerging applications of Whispering Gallery Mode photonic resonators," Lecture Notes in Electrical Engineering, **429**, pp. 185-191, 2017.

[8] F. Dell'Olio, G. Brunetti, D. Conteduca, N. Giovinazzi, N. Sasanelli, C. Ciminelli, and M. N. Armenise, "Integrated microwave photonics: overview and promising space applications," Lecture Notes in Electrical Engineering, **512**, pp. 107-112, 2018.

[9] F. Dell'Olio, D. Conteduca, M. Cito, G. Brunetti, C. Ciminelli, T. F. Krauss, and M. N. Armenise, "Electro-photonic chip-scale microsystem for label-free single bacteria monitoring," Lecture Notes in Electrical Engineering, **550**, pp. 53-58, 2019.

Proceedings of international conferences

[10] F. Dell'Olio, G. Brunetti, D. Conteduca, N. Sasanelli, C. Ciminelli, and M. N. Armenise, "Planar Photonic Gyroscopes for Satellite Attitude Control," Proc. of 7th International Workshop on Advances in Sensors and Interfaces (IWASI), pp. 167-169, Vieste, Italy, June 15-16, 2017.

[11] C. Ciminelli, F. Dell'Olio, G. Brunetti, D. Conteduca, and M. N. Armenise, "New microwave photonic filters based on resonant structures with engineered the spectral reflectance," Proc. of 19th International Conference on Transparent Optical Networks (ICTON 2017), pp. 1-4, Girona, Spain, July 2-6, 2017. (INVITED).

[12] C. Ciminelli, D. Conteduca, F. Dell'Olio, G. Brunetti, T. F. Krauss, and M. N. Armenise, "Photonic, plasmonic and hybrid nanotweezers for single nanoparticle trapping and manipulation," Proc. of 19th International Conference on Transparent Optical Networks (ICTON 2017), pp. 1-4, Girona, Spain, July 2-6, 2017. (INVITED).

[13] F. Dell'Olio, G. Brunetti, D. Conteduca, N. Giovinazzi, N. Sasanelli, C. Ciminelli, and M.N. Armenise, "Integrated Microwave Photonics:

Overview and Promising Space Applications," Proc. of ApplePies International Conference (Applications in Electronics Pervading Industry, Environment and Society), Rome, Italy, September 21-22, 2017.

[14] C. Ciminelli, F. Dell'Olio, G. Brunetti, D. Conteduca, N. Sasanelli, and M. N. Armenise, "Photonic technologies for nanosatellites", Proc. of Italy – Israel Workshop On Nanosatellite Technologies, Rome, Italy, April 9-10, 2018.

[15] D. Conteduca, F. Dell'Olio, G. Brunetti, T.F. Krauss, C. Ciminelli, and M.N. Armenise, "High-efficiency optoelectronic system for monitoring of antimicrobial resistance (AMR) in bacteria", Proc. of 20th Italian National Conference on Photonic Technologies (FOTONICA 2018), Lecce, Italy, May 23-25, 2018.

[16] C. Ciminelli, G. Brunetti, D. Conteduca, F. Dell'Olio, and M. N. Armenise, "Integrated microphotonic tunable delay lines for beam steering in phased array antennas," Proc. of 20th International Conference on Transparent Optical Networks (ICTON 2018), pp. 1-4, Bucharest, Romania, July 1-5, 2018. (INVITED).

[17] C. Ciminelli, F. Dell'Olio, G. Brunetti, D. Conteduca, and M. N. Armenise, "Graphene/Silicon Schottky Junction Solar Cells," Proc. of 20th International Conference on Transparent Optical Networks (ICTON 2018), pp. 1-4, Bucharest, Romania, July 1-5, 2018. (INVITED).

[18] G. Brunetti, D. Conteduca, F. Dell'Olio, C. Ciminelli, and M. N. Armenise, "Silicon Electro-Optically Tunable Delay Line," Proc. of Integrated Photonics Research, Silicon and Nanophotonics (IPR), pp. IM3B-6, Zurich, Switzerland, July 2-5, 2018.

[19] G. Brunetti, F. Dell'Olio, D. Conteduca, M. N. Armenise, and C. Ciminelli, "Photonic Devices for Space Applications," Proc. of 26th Annual International Conference on Composites/Nano Engineering (ICCE-26), Paris, France, July 15-21, 2018. (INVITED).

[20] F. Dell'Olio, D. Conteduca, G. Brunetti, M. N. Armenise, and C. Ciminelli, "Photonic devices for biosensing and trapping at nanoscale," Proc. of 26th

Annual International Conference on Composites/Nano Engineering (ICCE-26), Paris, France, July 5-21, 2018. (INVITED).

[21] C. Ciminelli, D. Conteduca, F. Dell'Olio, M. Cito, G. Brunetti, M. Armenise, and T. Krauss, "Optoelectronic microsystem for quick and label-free bacteria detection," Proc. of ApplePies International Conference (Applications in Electronics Pervading Industry, Environment and Society), Pisa, Italy, September 26-27, 2018.

[22] C. Ciminelli, F. Dell'Olio, G. Brunetti, and M. N. Armenise, "Microwave Photonics: An Opportunity for Space Systems and 5G Networks," Proc. of 1st International Conference on Dieletric Photonic Devices and Systems Beyond Visible (D-PHOTON 2018), Bari, Italy, October 1-2, 2018. (INVITED).

[23] C. Ciminelli, F. Dell'Olio, G. Brunetti, N. Sasanelli, and M. N. Armenise, "Chirped Microwave Waveform Generation with High Spectral Purity," Proc. of 41st Photonics & Electromagnetics Research Symposium (PIERS 2019), Rome, Italy, September 17-20, 2019. (INVITED).

[24] C. Ciminelli, F. Dell' Olio, G. Brunetti, A. Di Benedetto, and M. N. Armenise, "Integrated Microphotonic Switching Matrices for Flexible and Broadband Telecom Satellite Payloads," Proc. of 21st International Conference on Transparent Optical Networks (ICTON 2019), Angers, France, July 9-13, 2019. (INVITED).

[25] M. N. Armenise, F. Dell' Olio, C. Ciminelli, C. Galeone, and G. Brunetti, "Microphotonics-based architectures of mini-SAR payloads," Proc. of 21st International Conference on Transparent Optical Networks (ICTON 2019), Angers, France, July 9-13, 2019. (INVITED).

[26] F. Dell' Olio, G. Brunetti, M. N. Armenise, and C. Ciminelli, "Ka-band optoelectronic oscillator based on ultra-high *Q* ring resonator," accepted by European Frequency and Time Forum (EFTF 2020), Noordwijk, The Netherlands, April 21-23, 2020.

Proceedings of national conferences

[27] F. Dell'Olio, G. Brunetti, D. Conteduca, N. Giovinazzi, C. Ciminelli, and M. N. Armenise, "Integrated microwave photonic devices and circuits in space," Proc. of 49th Annual Meeting of the Associazione Società Italiana di Elettronica (SIE), Palermo, Italy, June 21-23, 2017.

[28] D. Conteduca, C. Reardon, M. G. Scullion, F. Dell'Olio, G. Brunetti, C. Ciminelli, T. Krauss, and M. N. Armenise, "Photonic/plasmonic nanotweezer for high-efficiency single nanoparticle trapping," Proc. of 49th Annual Meeting of the Associazione Società Italiana di Elettronica (SIE), Palermo, Italy, June 21-23, 2017.

[29] F. Dell'Olio, G. Brunetti, D. Conteduca, M. Cito, N. Sasanelli, C. Ciminelli, and M. N. Armenise, "CMOS-Compatible Ring Resonators for Biosensing and Space Applications", Proc. of 50th Annual Meeting of the Associazione Società Italiana di Elettronica (SIE), Naples, Italy, June 20-22, 2018.

[30] D. Conteduca, G. Brunetti, F. Dell'Olio, M. N. Armenise, T. F. Krauss, and C. Ciminelli, "Chip-scale electro-photonic system for antimicrobial susceptibility testing", Proc. of 51th Annual Meeting of the Associazione Società Italiana di Elettronica (SIE), Rome, Italy, June 26-28, 2019.

[31] G. Brunetti, F. Dell'Olio, D. Conteduca, M. N. Armenise, and C. Ciminelli, "Tuneable Gaussian-Shaped Photonic Notch Filter", Proc. of 51th Annual Meeting of the Associazione Società Italiana di Elettronica (SIE), Rome, Italy, June 26-28, 2019.

[32] F. Dell' Olio, G. Brunetti, C. Galeone, D. Filippetto, N. Sasanelli, V. Stanzione, M. N. Armenise, and C. Ciminelli, "Microphotonic sub-systems for Synthetic Aperture Radar Payloads", Proc. of XXV International Congress Italian Association of Aeronautics and Astronautics (AIDAA 2019), Rome Italy, September 9-12, 2019.